CRS4 - Centre for Advanced Studies,
Research and Development in Sardinia

Thermal and Mechanical Analyses of the LHC injection Beam Stopper (TDI)

L. Massidda and F. Mura

Solid and Structural Mechanics Area
Computational Methods for Engineering Department

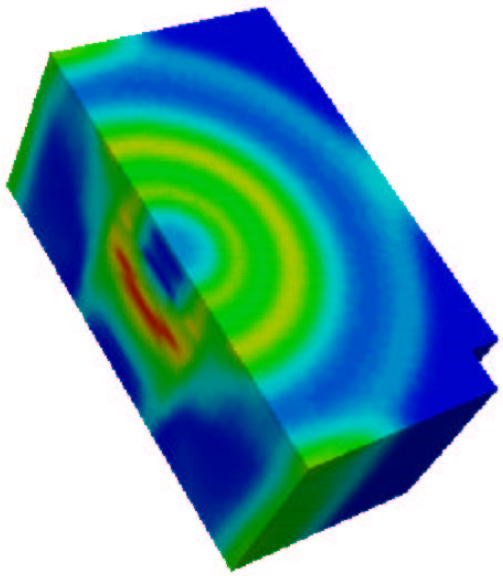

CRS4 S.C.ar.l.
Loc. Pixina Manna Edificio 1
C.P. n. 25 09010 Pula (CA - Italy)
tel +39 07092501, fax +39 0709250216
http://www.crs4.it

Computational Methods for Engineering Department
http://www.crs4.it/ cme-ssm/cm4e/

Solid and Structural Mechanics Area
http://www.crs4.it/ cme-ssm/

This document has been revised on 30th June 2003
previous revisions are superseded and must be destroyed or clearly marked

Authors: L. Massidda, F. Mura
Checked: F. Maggio
Approved: G. Fotia

This document contains 191 pages

Contents

Chapter 1

Introduction

In this report we present the results of the analyses performed in the frame of the contract K777/SL. The object of the work is the study of the mechanical behavior of beam obstacles due to the interaction with the high energy particle beam of the new Large Hadron Collider (LHC). This includes several numerical analyses of the mechanical behavior of the TDI beam stopper under normal operating conditions.

The TDI (Injection Stoppers) for LHC are mobile obstacles intended to be used during the adjustment of the injection trajectory in order to protect the superconducting machine elements in the event of a malfunctioning of the injection kicker.

It has been decided together with the SL/BT Group at CERN to investigate this problem by new numerical simulation techniques developed at CRS4, based on the *spectral element method*. This is similar to the well known *finite element method*, inheriting its flexibility in dealing with complex geometries and its proved efficiency in the simulation of structural dynamics phenomena, but is an high order method: it makes use of a reacher set of functions to describe fields in the computational domain, and provide accuracies beyond standard methods, especially when simulating wave propagation.

These methods are being developed from several years up to now, and have been applied with success in different fields including structural dynamics, acoustics and seismic waves propagation [1][2][3].

The spectral element code ELSE, developed at CRS4, has been modified and further developed to efficiently treat the problem at hand. Some new features have been added (e.g. the thermoelastic coupling) and the interface with the Monte Carlo code FLUKA ([4][5]) has been implemented. In the present work we started using ELSE for a 2D parametric study of the influence of the point of impingement of the particle beam in a semi infinite plane, simulating a generic graphite absorbing block under standard loading conditions. Then the TDI design problem has been considered, and several target configurations with different materials and geometries have been throughly analyzed, under several loading conditions. It was therefore possible to verify the performance of the adopted design. A number of simulations both in 2D and with the real 3D model were performed.

This report is organized as follows. First, a detailed problem formulation of the

problem at hand is given, followed by the description of the numerical technique adopted for the simulation. Then, the results for the 2D parametric analyses are presented and discussed, and finally the results of the simulations performed on the TDI are illustrated.

Chapter 2

Beam dump analysis method

2.1 Problem Formulation

The absorption of high-energy and well focalised proton beams for a duration of a few microseconds causes a considerable temperature increase in the solid obstacle. During this short period the thermal expansion is partly prevented by the inertia properties of the beam obstacle structure. This gives rise to dynamic stresses which propagate through the material in form of elastic waves [6].

Our attention is focused on the interaction of the beam with the material, and its possible consequences on the structural integrity of the beam obstacle. The coupled thermo-elastic problem will be analyzed calculating how the temperature profile varies in time and how the stress wave propagates in the structure.

First we present a general formulation of a coupled thermoelastic problem [7]. We consider a body occupying at initial time $t = 0$ the finite region $\Omega \subset R^d$ (with d = 2 or 3, number of space dimensions) with boundary Γ. The body is subject to the momentum balance equation and the energy balance equation:

$$\rho \ddot{u}_i = \sigma_{ji,j} + \rho f_i \qquad \text{in } \Omega \times (0, T_f) \quad \forall i = 1, \ldots, d \tag{2.1}$$

$$\rho c \dot{\theta} = \rho Q - q_{i,i} - T_0 \gamma \dot{e} \qquad \text{in } \Omega \times (0, T_f) \tag{2.2}$$

Where T_f is the final time. The body status is described by the values of the displacements u_i and the relative temperature $\theta = T - T_0$, being T_0 the stress free initial temperature expressed in the Kelvin scale.

In the previous equations a cartesian reference system is assumed and vector and tensor components are identified by the index. Time derivatives are denoted by overlying dots, spatial derivatives are denoted by the comma associated with the index of the spatial direction of derivation; repeated indexes mean summation.

In the momentum balance equation σ_{ij} are the coefficients of the Cauchy stress tensor, f_i are the components of external distributed body forces, ρ is the density, u_i is the displacement component in the i-th direction. In the energy balance equation c is the specific heat, Q is the external heat source per unit volume, q_i are the components of the heat flux vector.

The body is supposed to be a linear isotropic elastic solid, and to conduct heat according to the Fourier's law:

$$\sigma_{ij} = \lambda\delta_{ij}e + 2\mu\epsilon_{ij} - \gamma\delta_{ij}\theta \tag{2.3}$$

$$q_i = -k\theta_{,i} \tag{2.4}$$

Equation (2.3) is the Hooke's law expressed by means of the Lamé coefficients λ and μ, where ϵ_{ij} are the coefficients of the deformations tensor; e is the volumetric expansion and the modulus γ is related to thermal expansion and elastic coefficients as expressed in the following. In the equation equation (2.4) k is the heat conductivity. We also define:

$$\begin{aligned} \epsilon_{ij} &= \frac{1}{2}(u_{i,j} + u_{j,i}) \\ e &= div(\mathbf{u}) \\ \gamma &= \alpha(3\lambda + 2\mu) \end{aligned}$$

The coupling between the standard elastodynamics problem and the thermal problem is given by the last term in (2.3), representing the stresses due to the thermal expansions, and by the last term in (2.2) accounting for the internal heat source due to the rate of elastic volumetric deformation.

The boundary Γ is subjected to mechanical and thermal boundary conditions. In general we have

$$\Gamma = \Gamma_D^{el} \cup \Gamma_N^{el} \cup \Gamma_A^{el} = \Gamma_D^{th} \cup \Gamma_N^{th} \cup \Gamma_C^{th} \tag{2.5}$$

where the elastic sub-boundaries do not overlay on each other, as well as the thermal ones.

On Γ_D^{th} Dirichlet boundary conditions are applied and the temperature value is imposed; Γ_N^{th} is a Neumann boundary, where a fixed value for heat flux across the boundary is assigned; Γ_C^{th} represents an heat convection surface, where heat flux depends from an external medium temperature, from an heat exchange coefficient, but also from the surface temperature value. Thermal radiation is not included in this formulation: it would determine a nonlinear boundary condition and may be approximated with an equivalent heat convection. In the following only the Dirichlet and Neumann boundary conditions will be discussed, for the sake of simplicity:

$$\begin{aligned} \theta &= \theta_D && \text{on } \Gamma_D^{th} \times (0, T_f) \\ q_i n_i &= q_N && \text{on } \Gamma_N^{th} \times (0, T_f) \quad \forall i = 1, \ldots, d \end{aligned}$$

It is also necessary to specify the initial conditions for the temperature in Ω:

$$\theta(t = 0) = \theta^{(0)} \qquad \text{in } \Omega \tag{2.6}$$

The boundary is also subjected to elastic boundary conditions, expressed in the form:

$$\begin{aligned} u_i &= \phi_i && \text{on } \Gamma_D^{el} \times (0, T_f) \quad i = 1, \ldots, d \\ \sigma_{ij} n_j &= t_i && \text{on } \Gamma_N^{el} \times (0, T_f) \quad i = 1, \ldots, d \end{aligned}$$

On Γ_D^{el} prescribed values of the i component of displacements are imposed, on Γ_N^{el} known tractions are applied. Apart from these, an absorbing boundary condition has been implemented to approximate the infinite media behavior; this will not be discussed here and the interested reader may refer to [1][2][3]. The initial conditions for the elastodynamics problem should be provided as well:

$$\begin{aligned} u_i(t=0) &= u_i^{(0)} \qquad \text{in } \Omega \\ \dot{u}_i(t=0) &= \dot{u}_i^{(0)} \qquad \text{in } \Omega \end{aligned}$$

Through the principle of virtual work, the dynamic equilibrium problem can be stated in the following *weak* or variational form [8]:
if $\mathbf{v}$ is generic function candidate to represent a possible solution and vanishing on Γ_D^{el}, find $\mathbf{u} = \mathbf{u}(\mathbf{x}, t)$ such that $u_i = \phi_i$ on $\Gamma_D^{el} \times (0, T_f)$ and, $\forall t \in (0, T_f)$:

$$\int_\Omega \rho v_i \ddot{u}_i \, d\Omega + \int_\Omega v_{i,j}\sigma_{ij} \, d\Omega = \int_\Omega v_i f_i \, d\Omega + \int_{\Gamma_N^{el}} v_i t_i \, d\Gamma \qquad \forall \mathbf{v} \tag{2.7}$$

Similarly, for the thermal problem, we denote by $\tilde{\theta}$ a generic function candidate to represent a possible solution and vanishing on Γ_D^{th}, and we look for $\theta = \theta(\mathbf{x}, t)$ such that $\theta = \theta_D$ on $\Gamma_D^{th} \times (0, T_f)$ and $\forall t \in (0, T_f)$:

$$\int_\Omega \tilde{\theta}\rho c\dot{\theta} \, d\Omega + \int_\Omega \tilde{\theta}_{,i} k \theta_{,i} \, d\Omega = \int_\Omega \tilde{\theta}\rho Q \, d\Omega - \int_\Omega \tilde{\theta} T_0 \gamma \dot{e} \, d\Omega - \int_{\Gamma_N^{th}} \tilde{\theta} q_N \, d\Gamma \qquad \forall \tilde{\theta} \tag{2.8}$$

If we split the thermal component of the stress:

$$\begin{aligned} \sigma_{ij} &= \sigma_{ij}^* - \sigma_{ij}^{th} \\ \sigma_{ij}^* &= \lambda e \delta_{ij} + 2\mu\epsilon_{ij} \\ \sigma_{ij}^{th} &= \gamma\theta\delta_{ij} \end{aligned}$$

then the we can formulate the thermoelastic problem as follows:
Find $\mathbf{u} = \mathbf{u}(\mathbf{x}, t)$ and $\theta = \theta(\mathbf{x}, t)$ such that $\forall t \in (0, T_f)$ and $\forall \mathbf{v}$, $\forall \tilde{\theta}$:

$$\begin{aligned} \int_\Omega \rho v_i \ddot{u}_i \, d\Omega + \int_\Omega v_{i,j}\sigma_{ij}^* \, d\Omega &= \int_\Omega v_i f_i \, d\Omega + \int_\Omega v_{i,j}\sigma_{ij}^{th} \, d\Omega + \int_{\Gamma_N^{el}} v_i t_i \, d\Gamma \\ \int_\Omega \tilde{\theta}\rho c\dot{\theta} \, d\Omega + \int_\Omega \tilde{\theta}_{,i} k_i \theta_{,i} \, d\Omega &= \int_\Omega \tilde{\theta}\rho Q \, d\Omega - \int_\Omega \tilde{\theta} T_0 \gamma \dot{e} \, d\Omega - \int_{\Gamma_N^{th}} \tilde{\theta} q_N \, d\Gamma \end{aligned}$$

This is the weak form expression of the fully coupled thermoelastic problem, in which not only the deformations and the stresses depend on the solution of the thermal problem but the latter also depends on the rate of volumetric deformation and hence on the solution of the elastic problem. Anyway, due to the characteristics of the problem under exam and to the common properties of the materials adopted for these equipments, several simplifications of the general form of this problem are possible.

2.2 Problem simplification

The thermal problem, in particular, may be simplified. First of all, it is a common practice to discard the coupling term in the heat balance equation, to obtain

$$\rho c\dot{\theta} = \rho Q - q_{i,i} \qquad \text{in } \Omega \times (0, T_f) \tag{2.9}$$

By means of this decoupling, the thermal problem is no longer influenced by the elastic problem: it can be solved independently and its results may be used as input when simulating the wave propagation. This popular approach brings negligible approximations in the final result, at least for the most common thermal load characteristics and structural materials.

Considering that typical durations of the particle bursts available from accelerators have order of magnitude of microseconds or even shorter, during the heating of the irradiated material heat conduction may be neglected and the temperature rise is governed by the thermal capacity only. This approximation is usually accepted in numerical analysis of beam obstacles [6][9].

Both approximations introduced have the effect to increase safety: in fact, in common problems they increase the steepness of thermal and displacement gradients, therefore increasing the resulting stresses in the material, the most crucial quantity in these simulations [10].

So the heat equation reduces to:

$$\rho c\dot{\theta} = \rho Q \qquad \text{in } \Omega \times (0, T_f) \tag{2.10}$$

The problem is now greatly simplified: the temperature is easily calculated, by integrating in time the thermal power supplied, and does not depend by the temperature of the surrounding points, or by the thermal boundary conditions.

The momentum and thermal energy balance equation may be rewritten as:

$$\rho \ddot{u}_i = \sigma_{ji,j} + \rho f_i \qquad \text{in } \Omega \times (0, T_f) \quad \forall i = 1, \ldots, d \tag{2.11}$$

$$\rho c\dot{\theta} = \rho Q \qquad \text{in } \Omega \times (0, T_f) \tag{2.12}$$

The solid obeys to Hooke's law and is here considered isotropic for simplicity; moreover it is subjected to mechanical boundary conditions only:

$$u_i = \phi_i \qquad \text{on } \Gamma_D^{el} \times (0, T_f) \quad i = 1, \ldots, d$$

$$\sigma_{ij} n_j = t_i \qquad \text{on } \Gamma_N^{el} \times (0, T_f) \quad i = 1, \ldots, d$$

Initial conditions are specified in terms of temperature, displacement and velocity:

$$\begin{cases} \theta(t=0) = \theta^{(0)} \\ u_i(t=0) = u_i^{(0)} \\ \dot{u}_i(t=0) = \dot{u}_i^{(0)} \end{cases} \qquad \text{in } \Omega, i = 1, \ldots, d \tag{2.13}$$

Finally the variational form reads:
Find $\mathbf{u} = \mathbf{u}(\mathbf{x}, t)$ and $\theta = \theta(\mathbf{x}, t)$ such that $u_i = \phi_i$ on $\Gamma_D^{el} \times (0, T_f)$, $\theta = \theta_D$ on $\Gamma_D^{th} \times (0, T_f)$, and $\forall t \in (0, T_f)$:

$$\begin{cases} \int_\Omega \rho v_i \ddot{u}_i \, d\Omega + \int_\Omega v_{i,j} \sigma_{ij} \, d\Omega = \int_\Omega v_i f_i \, d\Omega + \int_{\Gamma_N^{el}} v_i t_i \, d\Gamma & \forall \mathbf{v} \\ \int_\Omega \tilde{\theta} \rho c \dot{\theta} \, d\Omega = \int_\Omega \tilde{\theta} \rho Q \, d\Omega & \forall \tilde{\theta} \end{cases} \tag{2.14}$$

Traditionally, this problem has been solved using different numerical techniques, including the well known finite differences and finite element method. We are using a spectral element approach. The reason for our choice is the following: spectral elements are more suited the treatment of large scale problems (such as beam obstacles analysis) than traditional techniques. In the following the spectral element method as implemented in the ELSE code will be briefly discussed.

2.3 Spectral Element Method

The Spectral Element Method (SEM) may be considered as a generalization of standard finite elements, using high order piecewise polynomial functions [1][2][3].

It is an *h-p* method, since the accuracy of the numerical solution may be increased through a mesh refinement, reducing element mean size as in a standard finite element method, or enhancing the algebraic degree of the piecewise polynomial functions used to approximate the solution. This latter opportunity results very useful to the final user who simply has to set the desired spectral degree at runtime to obtain the needed accuracy, whereas no time consuming meshing or re-meshing process is required.

To obtain an approximate numerical solution for the thermal and elastic problems we divide the computational domain Ω in a number of subdomains, the spectral elements, namely quadrilaterals in 2D problems and hexahedra in 3D, denoted by $\Omega_1, \Omega_2, \ldots, \Omega_K$.

Each element Ω_k is obtained mapping a reference (or "master") domain $\hat{\Omega} = [-1, 1]^d$, $(d = 2, 3)$ with a transformation $\mathbf{x} = \mathbf{F}_k(\hat{\mathbf{x}})$ where $\mathbf{x}$ and $\hat{\mathbf{x}}$ refer to Ω_k and $\hat{\Omega}$, respectively.

The simplest transformation is the Q_1 mapping that associates the vertex of Ω_k with those of $\hat{\Omega}$ and is linear in each space coordinate. The transformation is sub-parametric, but this does not affect the convergence behavior, and positively reduces the grid generation effort.

Nodes on each local axis of the reference domain are defined as the cartesian product of the roots of the one dimensional polynomial $(1 - \xi)(1 + \xi)L'_N(\xi)$, where L_N is the Legendre polynomial of degree N and ξ is the coordinate in the reference domain [-1,1]. Figure 2.1 illustrates the procedure.

Defining:

$$Q_N(\Omega_k) = \left\{ v = \hat{v} \circ \mathbf{F}_k^{-1}, \hat{v} \in \mathbf{Q}_N(\hat{\Omega}) \right\} \tag{2.15}$$

the mapping $\mathbf{Q}_N(\hat{\Omega})$ of the space of polynomials with degree less than or equal to N,

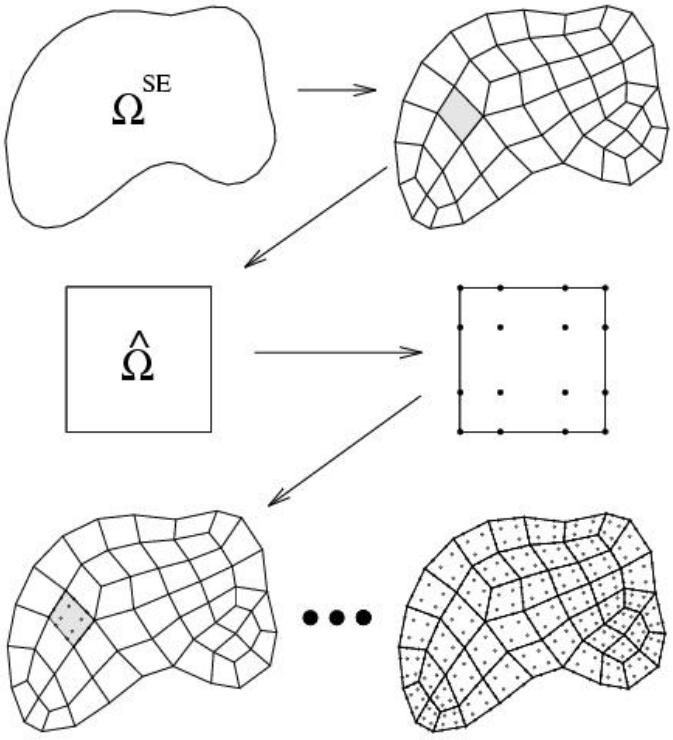

Figure 2.1: Spectral grid construction

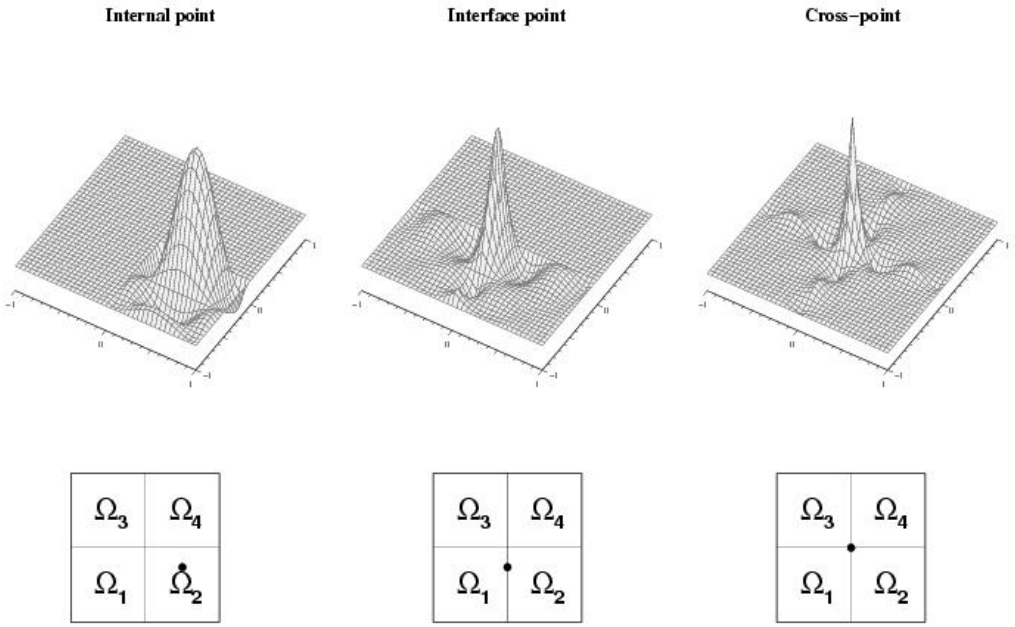

Figure 2.2: Spectral basis functions

with respect to each variable, then the space of admissible displacement components and temperature (v_i and $\tilde{\theta}$ in section 2.1) is

$$X_N(\Omega) = \{v_N \in C^0(\Omega) \mid v_N|_{\Omega_k} \in Q_N(\Omega_k), \forall \Omega_k\} \tag{2.16}$$

along with its subset V_N which is a finite dimensional approximation of $H_0^1(\Omega)$:

$$V_N = \{v_N \in X_N(\Omega) \mid v_N = 0 \text{ on } \Gamma_D\} \tag{2.17}$$

Functions v_N may be expressed as

$$v_N(\mathbf{x}, t) = \sum_{q=1}^{Nnodes} \tilde{v}_q(t)\psi_q(\mathbf{x}) \tag{2.18}$$

where $\tilde{v}_q(t)$ are the actual unknowns of our problem, being either a component of the displacement vector or the temperature value at any node q. The restrictions of the ψ_q's on the element Ω_k is a subparametric mapping of the Lagrange polynomials of degree N which are equal to one at the q-th node and vanish at all other nodes ($\tilde{v}_q(t) = v_N(\mathbf{x}_q, t)$).

Different ψ_q's for simple four element mesh of 2D elements of spectral degree 4, are shown in Figure 2.2

Integration is performed element-wise, the integrals being evaluated numerically by an accurate quadrature formula, namely the Gauss-Lobatto (GL) one:

$$\int_{\Omega_k} f \, d\Omega \simeq \sum_q f(\mathbf{x}_q^{(k)})\omega_q^{(k)} \tag{2.19}$$

where $\mathbf{x}_j(k)$ is the vector of coordinates of the Legendre-Gauss-Lobatto (LGL) nodes in Ω_k and the ω_q are the corresponding weights (see [11]).

According to the well known strategy of the standard finite elements, integrations are performed over the reference domain $\hat{\Omega}$, thus:

$$\int_{\Omega_k} f \, d\Omega \simeq \sum_q f(\hat{\mathbf{x}}_q^{(k)}) J_k(\hat{\mathbf{x}}_q) \hat{\omega}_q \tag{2.20}$$

where $\mathbf{x}_q$ are the images of $\hat{\mathbf{x}}_q$ through $\mathbf{F}_k$ and J_k is the determinant of the Jacobian of $\mathbf{F}_k$.

Such approach provides a property known in literature as *spectral accuracy*: being u the "exact" regular solution, then the numerical solution $u_{h,N}$ will converge to the exact one according to the following law:

$$\| u - u_{h,N} \| \leq C h^N exp(-N) \tag{2.21}$$

where $\| \cdot \|$ is th H^1 norm and the constant C is independent from element size h and spectral degree N, exhibiting an exponential decay of the error with respect to the spectral degree. Moreover the computational effort in evaluating the integrals and solving the resulting system is minimized, since matrices for inertia and heat capacity terms are naturally diagonal and no lumping procedure is required.

2.4 Matrix formulation

Equations (2.14) are the weak formulation of the thermal and elastic problem. There, the *test* displacement v_i and temperature $\tilde{\theta}$ may be chosen arbitrarily in the functional space V_N. Taking ψ_k's as test functions for the displacement and temperature, the thermoelastic problem may be formulated in a matrix form:

$$\begin{cases} \mathbf{M}\ddot{\mathbf{u}} + \mathbf{K}\mathbf{u} = \mathbf{f} + \mathbf{f}^{\theta} \\ \mathbf{C}\dot{\theta} = \mathbf{q} \end{cases} \tag{2.22}$$

where $\mathbf{u}$ is the vector of nodal displacements and θ the vector of nodal temperature (the actual unknowns of the problem), and $\ddot{\mathbf{u}}$ is the vector of nodal accelerations. Mechanical loads are described by the vector $\mathbf{f}$ that includes contributions form the body forces and Neumann boundary condition, and the vector $\mathbf{f}^{\theta}$ taking into account the effect of the thermal expansion as an equivalent internal pressure; thermal power is applied by the nodal vector $\mathbf{q}$.

The inertia or mass matrix is denoted by $\mathbf{M}$ and the stiffness matrix by $\mathbf{K}$, for the elastic problem; for the thermal problem only the thermal capacity matrix $\mathbf{C}$ is necessary.

Vectors and matrices in the previous system of equations refer to the whole model, nodal unknowns are shared by the different elements and assure the continuity of displacement and temperature throughout the model and across element interfaces. Matrices are assembled adopting the standard technique of the finite element by summing the contributions coming from the element matrices.

$$\mathbf{M} = \mathcal{A}_{k=1}^{Nel} \mathbf{M}^{(k)} \qquad \mathbf{K} = \mathcal{A}_{k=1}^{Nel} \mathbf{K}^{(k)} \qquad \mathbf{f} = \mathcal{A}_{k=1}^{Nel} \mathbf{f}^{(k)} \tag{2.23}$$

$$\mathbf{C} = \mathcal{A}_{k=1}^{Nel}\mathbf{C}^{(k)} \qquad \mathbf{q} = \mathcal{A}_{k=1}^{Nel}\mathbf{q}^{(k)} \tag{2.24}$$

where N_{el} is the total number of elements. The assembly procedure is extended to all the elements Ω_k and the element matrices are defined as follows, where p and q are nodal indexes $(p, q = 1, \ldots, N_{nodes})$, i, j, I and m denote vector component $(i, j, I, m = 1, \ldots, d)$:

$$M^{(k)}_{(i-1)N_{nodes}+p \;\; (j-1)N_{nodes}+q} = \delta_{ij} \int_{\Omega_k} \psi_p \rho \psi_q d\Omega \tag{2.25}$$

$$K^{(k)}_{(i-1)N_{nodes}+p \;\; (j-1)N_{nodes}+q} = \int_{\Omega_k} \sigma_{Im}(\psi_q \hat{e}_j)\epsilon_{Im}(\psi_p \hat{e}_i) d\Omega \tag{2.26}$$

$$f^{(k)}_{(i-1)N_{nodes}+p} = \int_{\Omega_k} f_i \psi_p d\Omega + \int_{\Gamma_N}^{el} t_i \psi_p d\Gamma \tag{2.27}$$

$$f^{\theta(k)}_{(i-1)N_{nodes}+p} = \int_{\Omega_k} \psi_p \gamma \theta d\Omega \qquad i = 1, \ldots, d \tag{2.28}$$

where $\hat{e}_i$ is the i-th unit base vector. The thermal problem has similar expressions for element thermal capacity matrix and element internal heat:

$$C^{(k)}_{pq} = \int_{\Omega_k} \psi_p \rho c \psi_q d\Omega \tag{2.29}$$

$$q^{(k)}_{p} = \int_{\Omega_k} \psi_p Q d\Omega \tag{2.30}$$

Alternative orderings of indexes i,j,I,m are possible. Integrals (2.25) - (2.30) are actually evaluated by means of formula (2.20).

In addition to space discretization, it is necessary to specify a time advancing algorithm to allow the solution of the coupled system. Several approaches have been proposed in literature based on implicit and explicit schemes; most of them require the assembly and subsequent solution of the composite system of equations, with both the elastic and thermal terms, to allow the correct calculation of the coupling effects. This approach, anyway, may lead to ill-conditioned linear systems, with poor results and low computational efficiency.

We found more suitable to treat the elastic and the thermal system separately, with different approaches for time integration. The thermal problem has to be solved first, since its results, in terms of nodal temperatures are an input for the mechanical problem. A simple first order forward Euler scheme may be adopted to time-advance the second equation of (2.22), thus enjoying stability thanks to the lack of the conductivity terms.

Then the elastic problem is solved by an explicit second order *leap-frog* scheme, a well known central difference method commonly used for wave propagation and fast transient mechanical problems.

This method must satisfy the Courant-Friedrichs-Levy (CFL) condition on the time step:

$$\Delta t \leq \zeta \frac{\Delta x_{min}}{c_{max}} \tag{2.31}$$

where Δx_{min} is the minimum spacing in the spectral grid and c_{max} is the maximum wave propagation velocity; finally $\zeta \in (0, 1)$ is a stability parameter. The Δx_{min} in the LGL points distribution corresponds to the nodes near the border of the sub-domain, where the grid spacing is proportional to L/N^2, L being the characteristic element size and N the polynomial order.

The interval $(0, T_f)$ is divided in a finite number n_T of time steps Δt, with $T_f = n_T \Delta t$ and Δt satisfying the stability condition for the elastic problem. The solution of the thermal and elastic problem is calculated at times $t_n = n\Delta t$.

For the heat transfer problem, knowing the temperature vector θ_n and the external heat source $\mathbf{q}_n$ at time $t_n = n\Delta t$, it is possible to calculate the vector of the temperature θ_{n+1} at time t_{n+1} by solving:

$$\theta_{n+1} = \theta_n + \Delta t \mathbf{C}^{-1} \mathbf{q}_n \tag{2.32}$$

For the elastodynamics problem, knowing the displacements $\mathbf{u}_n$ and $\mathbf{u}_{n+1}$ and the external forces $\mathbf{f}_{n+1}$, from the results of the thermal problem it is possible to calculate the load vector due to the thermal expansion $\mathbf{f}^{\theta}_{n+1}$, and finally to calculate the nodal displacements $\mathbf{u}_{n+2}$:

$$\mathbf{u}_{n+2} = \Delta t^2 \mathbf{M}^{-1} (\mathbf{f}_{n+1} + \mathbf{f}^{\theta}_{n+1} - \mathbf{K}\mathbf{u}_{n+1}) + 2\mathbf{u}_{n+1} - \mathbf{u}_n \tag{2.33}$$

Since both matrices $\mathbf{C}$ and $\mathbf{M}$ are diagonal, their inversion is straightforward, no system solving is required and the computation may be very quick for each time step. The drawback is that the number of time steps may become exceedingly large because of the limitation to the time step due to the stability requirements (2.31). Anyway, for this class of problems the value of time step that has to be chosen to obtain a good approximation has the same order of magnitude of that imposed by the stability limit: if the mesh is sufficiently regular the CFL condition does not bring a severe limit.

It is worth here to remind a difference from standard finite element methods: no lumping process is required to diagonalize inertia and heat capacity matrices, they are naturally diagonal due to the choice of the integration rule and of the functional space.

2.5 Temperature dependent properties

Apart from a gain in CPU-time, the use of the explicit time stepping procedure previously described may reduce memory occupation, thanks to the fact that the stiffness matrix (or better the elastic reaction term in the dynamic equilibrium equation) may be calculated at each time step without assembly. This allows a straightforward treatment of the non linearities due to material properties depending on the temperature value, a key aspect for this kind of problems.

The elastic problem may be formulated again in matrix form as follows:

$$\mathbf{M}\ddot{\mathbf{u}} = \mathbf{f}^{ext} - \mathbf{f}^{int} \tag{2.34}$$

and the time advancing scheme may be rewritten as:

$$\mathbf{u}_{n+2} = \Delta t^2 \mathbf{M}^{-1}(\mathbf{f}^{ext}_{n+1} - \mathbf{f}^{int}_{n+1}) + 2\mathbf{u}_{n+1} - \mathbf{u}_n \tag{2.35}$$

Here $\mathbf{f}^{ext}$ is the vector of external nodal forces, including body loads and tractions on the boundary; $\mathbf{f}^{int}$ is the vector of nodal elastic reaction forces, and merges the stiffness term and the thermal expansion forcing term: $\mathbf{f}^{int} = \mathbf{K}\mathbf{u} - \mathbf{f}^{\theta}$.

This vector is calculated and assembled on an *element by element* basis at each time step. Knowing the displacement configuration at a given time step, say $\mathbf{u}_{n+1}$, and the temperature distribution at the same time θ_{n+1}, it is possible to compute the internal stresses for each spectral element from the thermoelastic constitutive law.

$$\epsilon_{ij} = \frac{1}{2}(u_{i,j} + u_{j,i}) \qquad e = \nabla \cdot u \tag{2.36}$$

$$\sigma_{ij} = \delta_{ij}\lambda e + 2\mu\epsilon_{ij} - \delta_{ij}(3\lambda + 2\mu)\epsilon^{th} \tag{2.37}$$

Here the elastic moduli and the thermal expansion ϵ^{th} may be a property of the local temperature:

$$\lambda = \lambda(\theta) \qquad \mu = \mu(\theta) \qquad \epsilon^{th} = \epsilon^{th}(\theta)$$

and their values may be calculated on the basis of the nodal temperature configuration.

Once the stress distribution in each element has been determined, each component of the stress tensor has been calculated on the spectral node position, the vector of internal reaction forces may be assembled as follows:

$$\mathbf{f}^{int} = \mathcal{A}_{k=1}^{Nel}\mathbf{f}^{int(k)} \tag{2.38}$$

$$f^{int(k)}_{(i-1)N_{nodes}+p} = \int_{\Omega_k} \epsilon_{lm}(\psi_p \hat{e}_i)\sigma_{lm}(\mathbf{u}_{n+1})d\Omega \tag{2.39}$$

This method is perfectly equivalent to that described in the previous paragraph, expressed in terms of stiffness matrix. The only difference is the computation of nodal reaction, either as the result of a matrix vector product, or by direct element by element integration: in our view the second approach is more flexible for the problem under exam. The inertia term - not modified - remains constant throughout the simulation, since effective density is assumed constant with time and temperature.

The specific heat c may also depend on temperature, therefore it is necessary to recalculate at each time step the thermal capacity diagonal matrix.

We provide some further detail on material properties. These are defined in the code in a tabular form, as a function of the temperature; linear interpolation is then adopted for intermediate temperatures. Material properties may vary from point to point: it has been assumed for the sake of simplicity that these properties are constant within each

element. When integrating the internal force term, for example, first a mean element temperature is calculated (over each element nodes), then the material properties are determined with respect to the mean temperature and kept constant on the element. We believe that the approximation induced by this approach is limited and is a minor drawback when compared with the computational efficiency it brings.

The thermal expansion ϵ^{th} can be simply calculated as long as the thermal expansion coefficient remains constant:

$$\epsilon^{th}(\theta) = \alpha\theta$$

If α is a function of the temperature, then

$$\frac{d\epsilon^{th}}{d\theta} = \alpha(\theta)$$

and

$$\epsilon^{th}(\theta) = \int_{T_o}^{T} \alpha(T)dT \tag{2.40}$$

The thermal expansion coefficient used in the previous equation is known as the *tangent* expansion coefficient; it may be expressed more conveniently as:

$$\epsilon^{th}(\theta) = \frac{\int_{T_0}^{T} \alpha(T)dT}{T - T_0}(T - T_0) = \alpha_m(\theta)\theta \tag{2.41}$$

α_m is called the *secant* or mean thermal expansion coefficient: it allows to calculate a given set of values of this coefficient before the time loop, and to evaluate the thermal expansion as a simple product rather than by numerical integration.

2.6 Yield condition

The analyses of the beam dumping in different loading conditions have been performed under the hypothesis of linear elasticity, so no yielding of the material has been considered. Anyway, a measure of the criticity of a given loading condition can be obtained by comparing the point stress of the model at a given time with a reference yielding condition.

2.6.1 Stassi Yield Criterion

Brittle materials are normally tested under bending condition, and results on the material yielding stress at different temperatures are available. Yielding criteria are necessary to compare the available experimental results on axial tension to the general stress state, for which all the components of the stress tensor are available.

A widely used criterion for ductile materials as a metallic alloy, for example, is the Von Mises yield criterion, where the yield stress determined in the tensile stress is compared

with an equivalent stress, function of the components of the stress tensor calculated as follows:

$$\sigma_{vm} = \sqrt{\sigma_1^2 + \sigma_2^2 + \sigma_3^2 - (\sigma_1\sigma_2 + \sigma_2\sigma_3 + \sigma_3\sigma_1)} \tag{2.42}$$

where $\{\sigma_i\}$'s are the principal components of the stress in the intrinsic reference system.

It is assumed that the material has the same behavior in tensile and compressive stress states: this may be reasonable in metallic alloys, but is a poor approximation of the real behavior of most brittle materials, like polycrystalline graphite. These materials have a different resistance in tension and in compression, typically showing better performances when subject to compressive stress states. A different yielding criterion is therefore necessary for these materials: we used the Stassi yield criterion, which may be figured out as a modified Von Mises criterion (see e.g. [12]).

After introducing the ratio k between compressive and tensile strength:

$$k = \frac{\sigma_c}{\sigma_t} \tag{2.43}$$

we can define the Stassi tensile equivalent stress σ_{teq} as:

$$k\sigma_{teq}^2 + 3(k-1)p\sigma_{teq} - \sigma_{vm}^2 = 0 \tag{2.44}$$

the pressure p being defined as:

$$p = -\frac{1}{3}(\sigma_1 + \sigma_2 + \sigma_3) \tag{2.45}$$

The Stassi compressive equivalent stress σ_{ceq} is then equal to $\sigma_{ceq} = -k\sigma_{teq}$. To verify the resistance in any point of the structure it is then sufficient to compare the tensile equivalent stress σ_{teq} with the tensile admissible stress or, equivalently, to compare the compressive equivalent stress with the compressive admissible stress, being the admissible stress the ratio of the tensile or compressive strength with respect to a chosen safety factor η.

Therefore the Stassi yield criterion reads:

$$\sigma_{teq} \leq \sigma_{tadm} \tag{2.46}$$

where

$$\sigma_{tadm} = \frac{\sigma_t}{\eta} \tag{2.47}$$

The Stassi criterion has been applied to the entire set of simulations presented in this report in which an isotropic material, as Graphite is analyzed. We remark that it is perfectly equivalent to a Von Mises criterion when the compressive and tensile strength of the material are equal.

Another useful quantity is the Stassi ratio ε_{teq} defined as:

$$\varepsilon_{teq} = \frac{\sigma_{teq}}{\sigma_t} \tag{2.48}$$

The safety of the structure may be checked by verifying that everywhere in the model:

$$\varepsilon_{teq} \leq \frac{1}{\eta} \tag{2.49}$$

thus allowing an immediate view of the criticity of a given state of stress.

2.6.2 Maximum stress yield Criterion

The previously discussed Stassi Yield criterion may be figured out as an improvement of the Von Mises Yield criterion for those materials in which the compressive and tensile strength are different. This criterion is anyway applicable to isotropic materials only.

The Von Mises equivalent stress loses much of its significance when anisotropic materials have to be analyzed, since different stiffness, as well as different tensile and compressive strength, have to be considered along the different directions; it is therefore difficult to identify a single quantity giving a significant measure of a stress state.

For anisotropic materials the Maximum Stress criterion has been applied. The resistance of the material is verified by checking that for each point each component of the stress is lower than a corresponding rupture stress [13]. A Maximum stress Ratio may be defined as:

$$\varepsilon_{MS} = \text{max. of} \begin{cases} \frac{\sigma_{xx}}{\sigma^{rt}_{xx}} \text{ or } \frac{-\sigma_{xx}}{\sigma^{rc}_{xx}} \\ \frac{\sigma_{yy}}{\sigma^{rt}_{yy}} \text{ or } \frac{-\sigma_{yy}}{\sigma^{rc}_{yy}} \\ \frac{\sigma_{zz}}{\sigma^{rt}_{zz}} \text{ or } \frac{-\sigma_{zz}}{\sigma^{rc}_{zz}} \\ \frac{|\sigma_{yz}|}{\sigma^{r}_{yz}} \\ \frac{|\sigma_{zx}|}{\sigma^{r}_{zx}} \\ \frac{|\sigma_{xy}|}{\sigma^{r}_{xy}} \end{cases} \tag{2.50}$$

The normal stresses in the three directions are compared to the tensile or compressive strength depending on their sign: if it is positive the ratio is made with the tensile strength, if negative, the compressive strength is considered.

It is sometimes hard to obtain tested values of the shear resistance of the materials, most of the times only normal stresses failure values are available, shear failure stresses have to be estimated in some way.

If a material may be assumed to be fragile, the Galileo-Rankine criterion is considered (it corresponds to the maximum stress criterion for an isotropic material): for this criterion it turns out that the failure stress in shear is equal to the failure stress in tension.

This is overestimating for the resistance to shear of a ductile material. However it does not put excessive limits in stress conditions for which the correct values of the limits are not available, and furthermore gives reasonable results when applied to the problem at hand.

2.7 Beam loading

The loading on the beam obstacles is due to the energy deposition of the LHC beam in the material.

As a consequence of the assumptions made (i.e. neglecting heat conduction and the elastic deformation effect on heat balance), neither Dirichlet nor Neumann boundary

conditions for the temperature are applied: the boundary is not subjected to given temperature values, convection or imposed heat fluxes.

In a first approximation, the effect of the beam energy deposition is simulated by directly imposing the structural temperature, assuming it has a known time-varying distribution. In this way no thermal problem has to be solved, and the temperature can be regarded as a given parameter.

In the first simulations (see chapter 3) we adopted the following distribution for the temperature:

$$\theta(\mathbf{x}, t) = \theta_M e^{-b\left[(x-x_0)^2+(y-y_0)^2\right]} g(t) \tag{2.51}$$

where θ_M is the maximum temperature increase on the beam axis; the latter is parallel to the z axis and the distribution is constant along z. The time-history has the following form:

$$g(t) = \begin{cases} 0 & 0 \leq t < t_0 \\ \frac{t-t_0}{\Delta t_{bd}} & t_0 \leq t < t_0 + \Delta t_{bd} \\ 1 & t_0 + \Delta t_{bd} \leq t \end{cases} \tag{2.52}$$

where t_0 and Δt_{bd} represent the initial time and the duration of the beam deposition.

Expressions 2.51 and 2.51 are an approximation of the real condition and give a schematic representation of the real time function of the energy deposition.

This method applies reasonably to parametric studies, as for the first 2D examples proposed. For real 3D simulations, a more sophisticated approach shall be chosen.

The internal heating due to the energy deposition of the beam Q may be expressed as follows:

$$Q(\mathbf{x}, t) = E_d(\mathbf{x}) \dot{n}_p(t) \tag{2.53}$$

where $E_d(\mathbf{x})$ is the energy deposited in the material surrounding a single proton of given energy or a given set of particles, and $\dot{n}_p(t)$ gives deposition rate of protons, or particle set, per unit time.

The energy deposition E_d, is an input for the elastic code and is calculated with a Monte Carlo method, implemented in the FLUKA code [4][5]. The rate of deposited particles depends on the beam time structure and is provided as input in form of a temporal function.

The following subsections give more details on the FLUKA interface and the distribution of particles. This is anyway an approximated approach since a more realistic model should take into account the full coupling between the energy deposition and the thermo-elastic phenomenon.

Energy deposition causes a temperature increase and a thermal expansion in the solid material, modifying the local density and affecting the energy deposition; if high amounts of energy are deposited and/or the beam is particularly focused, the beam obstacle may undergo changes in the phase, from solid to liquid up to a gas, with important effects on real energy deposition.

The one-way coupling described before may be considered sufficiently accurate for the problem at hand, where materials remain solid, but constitutes an interesting and possible improvement for the future.

2.7.1 FLUKA interface

Numerical philosophies underlying Monte Carlo methods and spectral elements are quite different, and such are implementations of FLUKA and ELSE.

In the spectral element approach the computational domain is split in a given number of non overlapping elements, following a completely unstructured pattern. On the other hand, FLUKA calculations are made on a set of regular, structured grids of cells, which can overlap each other and may cover a computational domain different from that considered in the mechanical simulations. The data structures are therefore completely different. Consequently the output of FLUKA cannot be read directly in ELSE unless some kind of interface is built.

Internal heating is the required input for the thermal - mechanical simulation: it has to be integrated over each element to obtain a vector of nodal heat power, used in the calculation as described in the previous paragraphs.

As mentioned, the integration for spectral elements requires the knowledge of the exact value of the quantity to be integrated at each nodal position. The ELSE code has therefore been improved by adding a numerical tool in charge of interpreting the FLUKA output and computing the correct input at each nodal position.

To perform this task, the interface first reads the FLUKA output file and generates the different grids used by FLUKA; then, for each spectral node, determines the grid that has the maximum accuracy near that point and the subset of cells surrounding the point of interest; finally the interface calculates the value of internal heating by interpolating the values of these cells. It should be remarked that the numerical models used in ELSE and in FLUKA may be (and normally are) completely different, in terms of the number and size of the grids adopted, but also in terms of the reference system used.

The simple example in Figure 2.3 may be useful in clarifying this procedure. Three FLUKA grids are shown, all of these belonging to the same set of data. These grids are regular and structured, but also overlapping and non matching. An ELSE grid is shown too. FLUKA data is defined on the cells whereas ELSE data has to be defined on nodes. For each spectral node in the ELSE grid, such as nodes A, B and C shown in Figure 2.3, the interface takes care of evaluating which of the FLUKA grids offers the maximum precision in the proximity of the point of interest, and interpolates the results of the FLUKA cells. So in the figure the value in node A is calculated interpolating the results of FLUKA grid 1; node B depends on the results of the cells of the second FLUKA grid and, finally, node C is associated to the third, coarser, FLUKA grid.

In this way, the internal heating is calculated with the maximum possible accuracy for all the nodes, and may be integrated over the entire model. This procedure is fully

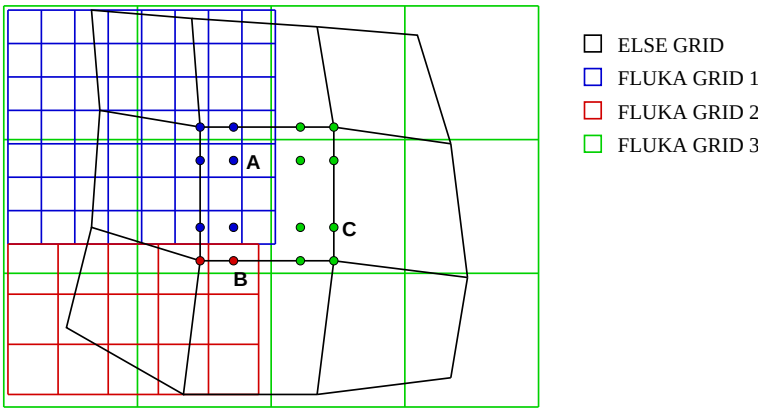

Figure 2.3: Matching between ELSE and FLUKA grids

automatic and the user only has to specify the FLUKA output file to be used in the simulation.

2.7.2 Particle distribution

In order to complete the definition of the internal heating in the beam obstacle it is necessary to define exactly the rate of particle deposition on the target as a function of time.

The deposition is not continuous in time: the LHC protons are grouped in 39 distinct trains; all trains are equal, each of them containing the same number of protons and having the same duration of $1.8\mu s$ as shown in Figure 2.4. Each of the rectangles in the figure is a train and is in turn composed by 72 bunches of protons $25ns$ distant in time [14].

The frequency content is not limited and it is possible to distinguish between several time scales. It is practically impossible, due to the actual limits of the computational resources available, to analyze all the time scales of the problem: the smallest ones are discarded in our simulations. In particular, while it is possible to describe the time structure of the batches, present computer performance do not allow to investigate the effects of the bunch time scale. In fact, this would bring a time step lower than $25ns$ and a consequent number of total time steps exceedingly large for the duration of the simulation required by the dimension of the structure, not to mention the enormous number of nodes required to efficiently describe those wave lengths.

We do not expect discarding higher frequency could significantly affect results: higher frequency should be compared with the characteristic frequency of the system under exam, that are related to the mechanical properties of the material adopted (wave speed) and to the mean dimension of the energy deposition profile.

The minimum resolvable time scales of the model are related with the adopted time step, that in turn depends from the wave propagation speed and from the minimum inter-nodal distance; this characteristic length has been chosen considering the necessity to

Figure 2.4: Bunch disposition inside the LHC

represent the energy deposition profile of the beam with a good approximation. The nodal distance has been chosen such that a sufficiently high number of elements and nodes is available to represent correctly the energy profile. The resulting time scales are comparable with batch duration, and the smaller time scale of the bunches are neglected.

The effect of this approximation on the results is negligible, also considering that the effect of energy deposition rate on the thermal stresses is averaged by the time integration procedure.

The model acts as a low-pass filter on the resolvable frequency. If simulation of smaller time scales or higher frequencies is required, then finer grids are necessary and the cut off frequency is limited by computational resources available: the higher the frequency one wants to calculate, the higher the number of unknowns, the lower the resulting time step, and, finally, the longer the CPU time required.

2.8 TDI Beam Obstacle design

The TDI (Injection Stoppers) for LHC are mobile obstacles intended to be used during the adjustment of the injection trajectory in order to protect the superconducting machine elements in the event of a malfunctioning of the injection kicker. The most sensitive downstream element to be protected being the separation dipole D1, that is placed 10 meters after the TDI end [14].

This structure must extend above and below the beam position to account for all the possible operating conditions leaving a gap of the order of $10mm$ for the beam.

The beam obstacle design consists of several absorber blocks suspended or sustained by two beam supports. Some detail of the structure is shown in Figure 2.5. Two long support beams are bolted to a set of aluminum jaws: this in turn contains the absorber blocks, made of different materials with a constant section, held in place and pressed against the aluminum support by bearing plates and a system of precompressed springs that push the copper plate against the block. The whole length of this system

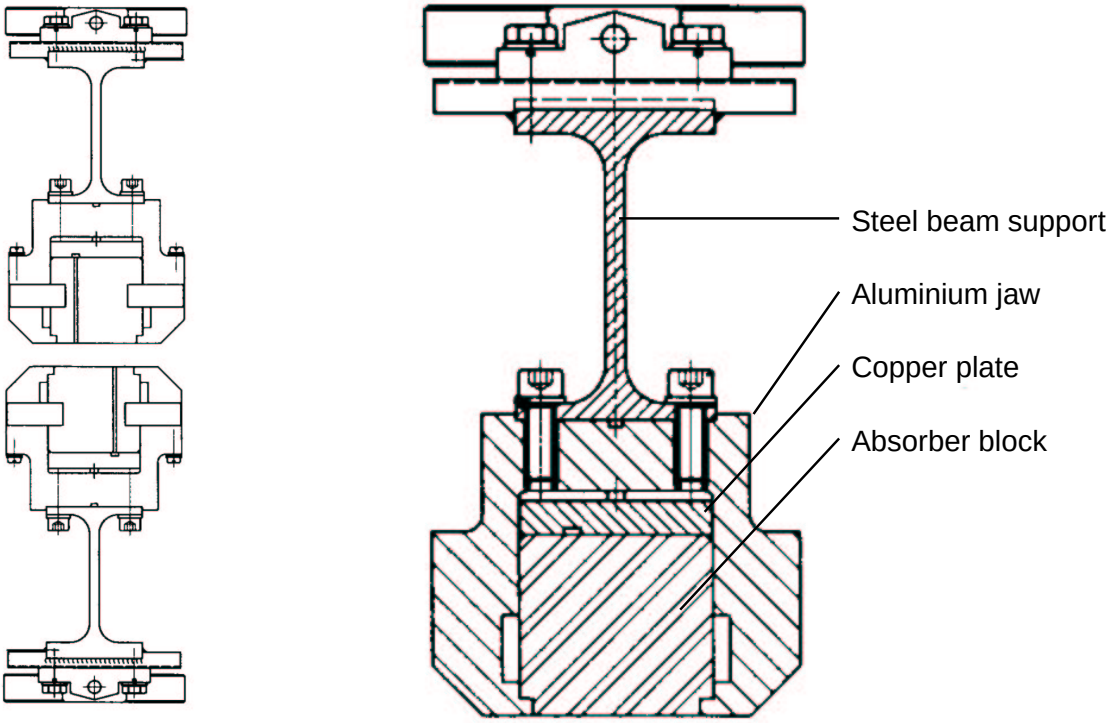

Figure 2.5: frontal view and section of the TDI

equals $4185mm$: 20 absorber blocks are used consisting, in the latest optimization of the design, of 18 Boron Nitride absorber blocks, whose length is equal to $157.7mm$, an Aluminum block $600mm$ long, and a $700mm$ long Beryllium-Copper alloy block at the end. The proton beam hits first the Boron Nitride blocks and then the Aluminum and Beryllium-Copper ones. The section is rectangular with a width of $58mm$ and an height of $54mm$.

The tolerances on the constructive dimensions are chosen such that a permanent gap is present between the vertical surfaces of the assembly, both on the sides between the jaw and the absorber block and the plate, as well as for the front and rear surfaces where the jaws and the blocks are separated: in this way the thermal expansions do not cause any undesired longitudinal compression. The absorber blocks are held in place by the friction forces against the teeth of the jaw, due to the above mentioned pressure of the copper plate, and by two sets (front and rear) of security plates.

This obstacle may receive single SPS bunches up to an ultimate intensity of $1.7 \cdot 10^{11}$ protons per bunch during the setting up of the injection. It is also necessary to consider some exceptional modes of operation in which more bunches could be involved, up to the full injected beam batch of $4 \times 72 = 288$ bunches of ultimate intensity.

The different operating conditions have been summarized in the following:

- **Case 1 (Normal):** the normal dumping of the beam. In this case the beam hits the TDI at the center of its upper block with a displacement $\Delta y = 34mm$ from the plane of the beam orbit. This is the normal operation mode during injection setup, with pilot bunches every $16s$. In exceptional cases a full train dumping may be also envisaged. The expected rate of these normal conditions is several per year.

- **Case 2 (Sweep):** this happens in case of a wrong MKI timing or of prefire of one module. When the passage of injected or circulating beam coincides with the rise or fall slope of the kicker pulse, part of the bunches will be swept over the TDI, either above or below the nominal orbit. The estimated rate of this event is several per year.

- **Case 3 :** this corresponds to the failure of one of the MKI modules, with the full batch hitting the block at a distance $\Delta y = 9.16mm$ from the orbit, at the expected rate of once a year.

- **Case 4 (Grazing):** the beam hits the TDI just on one of its edges so that part of it continues its trajectory grazing the horizontal surface: the distance from the plane of the beam orbit is approximately $\Delta y = 5mm$. This event may concern a bulk of bunches (with an initial sweep) in the case of internal fault of a module and estimated rate of a single event once every ten years.

The intent of this report is to analyze the normal condition (case 1) for the most critically loaded absorber block: this include several parametric studies performed on simplified 2D models to get a better insight. The analysis were performed during the design and

optimization phase for the TDI design to provide to the designers some information on the mechanical behavior; hence, the results presented in the first chapters of this report regard models having small discrepancies from the final design previously described, and adopting different materials, such as standard graphite.

Chapter 3

Preliminary analyses

3.1 Introduction

In this chapter, the results of two analyses are shown: a infinite plane under a perfectly centered thermal load and a semi infinite plane under a thermal load near the free edge. These simulations were performed mainly to calibrate the numerical model for the specific problem of the LHC.

For the first problem (the infinite plane case), the thermal load is analyzed also in static conditions. The reasons behind this test are:

- The possibility to make comparison between numerical and analytical results provided by Sievers ([6]), concerning the elastic stress due to a rapid heating by a particle beam.
- The necessity to find the 'optimal' size of the mesh to be used for dynamic analyses.

The interest of the first test is mainly on a conceptual ground, and the infinite plane approximation is well suited only for the very first instants of the thermal load. The experience on similar problems has shown that wave reflections on the boundaries of the structure should be regarded as a serious source of stress increase.

This is the motivation for the second set of analyses, where the effect of the proximity of a free wall is studied. Indeed, it may happen in real conditions that the impingement of the particle beam is not centered in the beam stopper but falls in the proximity of one of its borders. This may result in a critical condition for the beam obstacle design.

3.2 Properties of the material

A standard Graphite is initially used: its properties as a function of temperature are shown in Table 3.1, see [15].

Through this chapter the properties of the material are assumed independent from temperature. The values adopted are those relative at $20°C$.

T	ρ	E	ν	σ_t	σ_c	α	c	k
[°C]	$[Kg/m^3]$	$[GPa]$		$[MPa]$	$[MPa]$	$[\mu m\ /m\ °C]$	$[J/Kg\ °C]$	$[W/m\ °C]$
0	1850	9.96	0.15	27	90	2.97	510	93
20	1850	10.00	0.15	27	90	3.00	650	90
100	1850	10.16	0.15	27	90	3.13	1010	81
300	1850	10.57	0.15	27	90	3.46	1400	62
500	1850	10.97	0.15	27	90	3.79	1590	49
750	1850	11.47	0.15	27	90	4.06	1750	38
1000	1850	11.98	0.15	27	90	4.23	1880	31
1250	1850	12.48	0.15	27	90	4.40	2000	27
1500	1850	12.99	0.15	27	90	4.57	2050	24
2000	1850	14.00	0.15	27	90	4.91	2130	20
2500	1850	9.50	0.15	27	90	5.24	2200	19
3000	1850	5.00	0.15	27	90	5.00	2270	18

Table 3.1: Properties of standard Graphite

3.3 Thermal load

The beam energy deposition is simulated by means of a thermal gaussian load, in the form:

$$\theta(\mathbf{x}, t) = \theta_0 e^{-br^2} f(t) \tag{3.1}$$

with $r = \sqrt{x^2 + y^2}$ and θ_0 being the maximum temperature at the center of the section of energy deposition, $\theta_0 = 653.7°C$. The parameter b gives a measure of the steepness of temperature variation with the radius: for $r = 1/\sqrt{b}$ it turns out $\theta \cong 0.3\theta_0$. For the assumed value $b = 0.106 \cdot 10^6\ m^{-2}$, representative of the condition in the beam stopper, the temperature decreases to a 30% of the maximum value at a distance $r \cong 3mm$.

The maximum temperature is reached in $7.8\mu s$: the time function used is the ramp shown in Figure 3.1 (left). The Figure 3.1 (right) shows the snapshot of the temperature distribution when the maximum value is reached.

3.4 Infinite plane

The numerical model is a $75 \times 75mm^2$ graphite slice with absorbing conditions on the edges and a perfectly centered load. The absorbing conditions are necessary to simulate an infinite surface.

Every element is $1.5 \times 1.5mm^2$, therefore the temperature variation from its maximum to a value equal to θ_0/e is contained in two spectral elements along the radius. Several spectral degrees are used: depending on the chosen value of the spectral degree, a different number of spectral nodes are subjected to a temperature increase, different number of unknowns are involved, and different accuracies could be obtained. A tuning

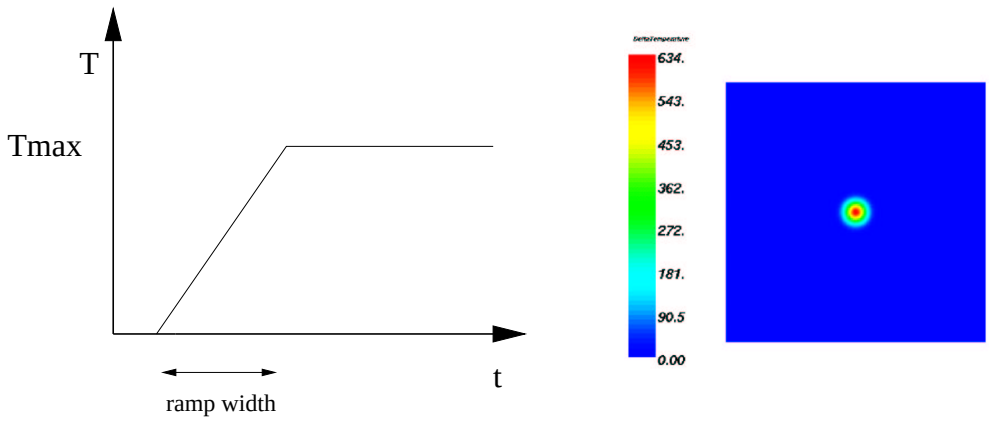

Figure 3.1: Temporal function and snapshot of the temperature

is therefore required to obtain a satisfactory precision within acceptable values of CPU time.

3.4.1 Static analysis

In this problem the thermal load is applied statically: the temperature increase in the material is theoretically realized in a infinite time. Several simulations are made varying spectral degree and the results are compared with those obtained analytically, see Table 3.2. For spectral degree 3, the mesh has 2500 elements and 22801 spectral nodes.

The stress values are calculated in three different nodes: in the load point ($r = 0$), at $r = 1.5mm$ and at $r = 3mm$. The difference between numerical and analytical value is plotted in Figure 3.2. The error decreases rapidly with the increase of the spectral degree being almost negligible, for engineering design purposes, when the spectral degree is set to 3.

3.4.2 Dynamic analysis with constant properties

The same problem, an infinite graphite plane subjected to a localized temperature increase, is now analyzed as a dynamic problem. Since particle deposition in beam obstacles is characterized by a very low deposition time, dynamic effects are very important. To be more precise, deposition and temperature rise time should be considered *slow* or *quick* depending on the dynamic effects they produce, which are related to the dimensions of the energy spot and to the wave propagation speed. A simple indication of the importance of dynamic effects is the comparison between temperature rise time and the time required for a wave to cover the length of the heated part.

In our model the temperature varies in time following a ramp of finite width; dynamic effects depend from the width of the ramp: the steeper is the ramp, the bigger is the dynamic part of the stress. To show this, we compare the results of two loads sharing the same temperature distribution of the static problem, but with different width of the

$r = 0mm$

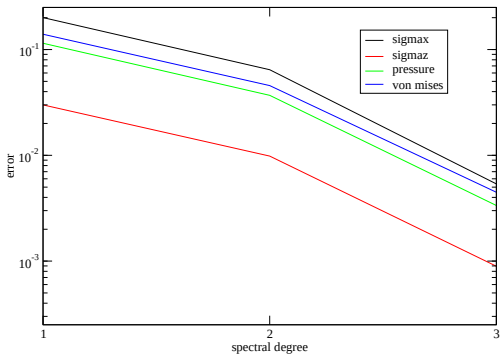

$r = 1.5mm$

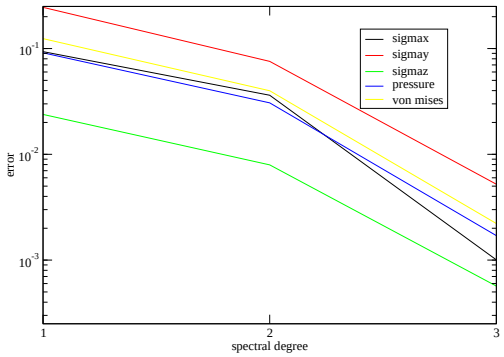

$r = 3mm$

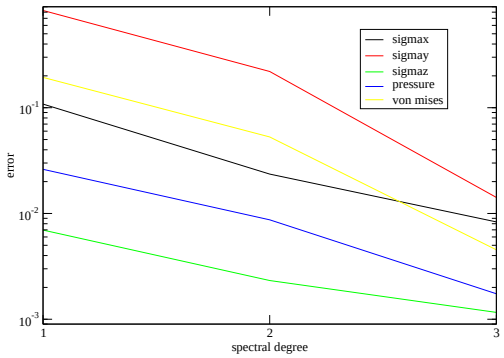

Figure 3.2: The error between numerical (static) and analytical stress evaluated in the load point for $r = 1.5mm$ and $r = 3mm$ (from top to bottom).

$r = 0$	N = 1	N = 2	N = 3	analytical
$\sigma_x[MPa]$	13.42	10.46	11.12	11.18
$\sigma_y[MPa]$	13.42	10.46	11.12	11.18
$\sigma_z[MPa]$	23.04	22.15	22.35	22.37
$p[MPa]$	16.62	14.36	14.86	14.91
$\sigma_{vm}[MPa]$	9.62	11.69	11.23	11.18
$r = 1.5mm$	N = 1	N = 2	N = 3	analytical
$\sigma_x[MPa]$	10.88	9.59	9.94	9.95
$\sigma_y[MPa]$	9.55	7.09	7.63	7.67
$\sigma_z[MPa]$	18.04	17.48	17.61	17.62
$p[MPa]$	12.82	11.39	11.73	11.75
$\sigma_{vm}[MPa]$	7.91	9.39	9.05	9.03
$r = 3mm$	N = 1	N = 2	N = 3	analytical
$\sigma_x[MPa]$	6.43	7.38	7.27	7.21
$\sigma_y[MPa]$	2.58	1.10	1.39	1.41
$\sigma_z[MPa]$	8.67	8.59	8.62	8.61
$p[MPa]$	5.89	5.69	5.75	5.74
$\sigma_{vm}[MPa]$	5.34	6.97	6.65	6.62

Table 3.2: Static analysis: numerical results, varying the spectral degree, and analytical solution

ramp, and the static results. The first ramp, which better approximates the real TDI behavior, is characterized by a rise time of $7.8\mu s$; the rise time of the second is equal to $0.1\mu s$. The maximum stress values at different distances from the center of the loaded area are compared in Table 3.3.

It is apparent that the first ramp may be considered *slow* for the material considered, since the resulting stress values are comparable with those obtained by the static analysis. In fact a stress wave starting from the center of the energy deposition area may cover almost $20mm$ during the rise time of the temperature, a path significantly higher than the mean energy deposition area size. On the contrary, the second ramp is very *quick*, since a wave may travel only for $0.24mm$ in the rise time of the temperature.

The Figure 3.3 shows the displacement of different points for the first and second ramp. The initial rise time for the second ramp is set to $9.9\mu s$ so that the temperature reaches the maximum value at $t = 10.0\mu s$ in both cases.

In the second one, the displacement is bigger at the beginning, but after the initial transient the two results are coincident, and equal to the static part of the stress.

The Figure 3.4 displays different snapshots of the displacement for the first ramp ($7.8\mu s$); the results at the same instants for the second ramp are shown in Figure 3.5

The displacement for the two ramps have a similar profile but, evidently, the circular wavefront departing from the center has a much steeper profile for the second ramp.

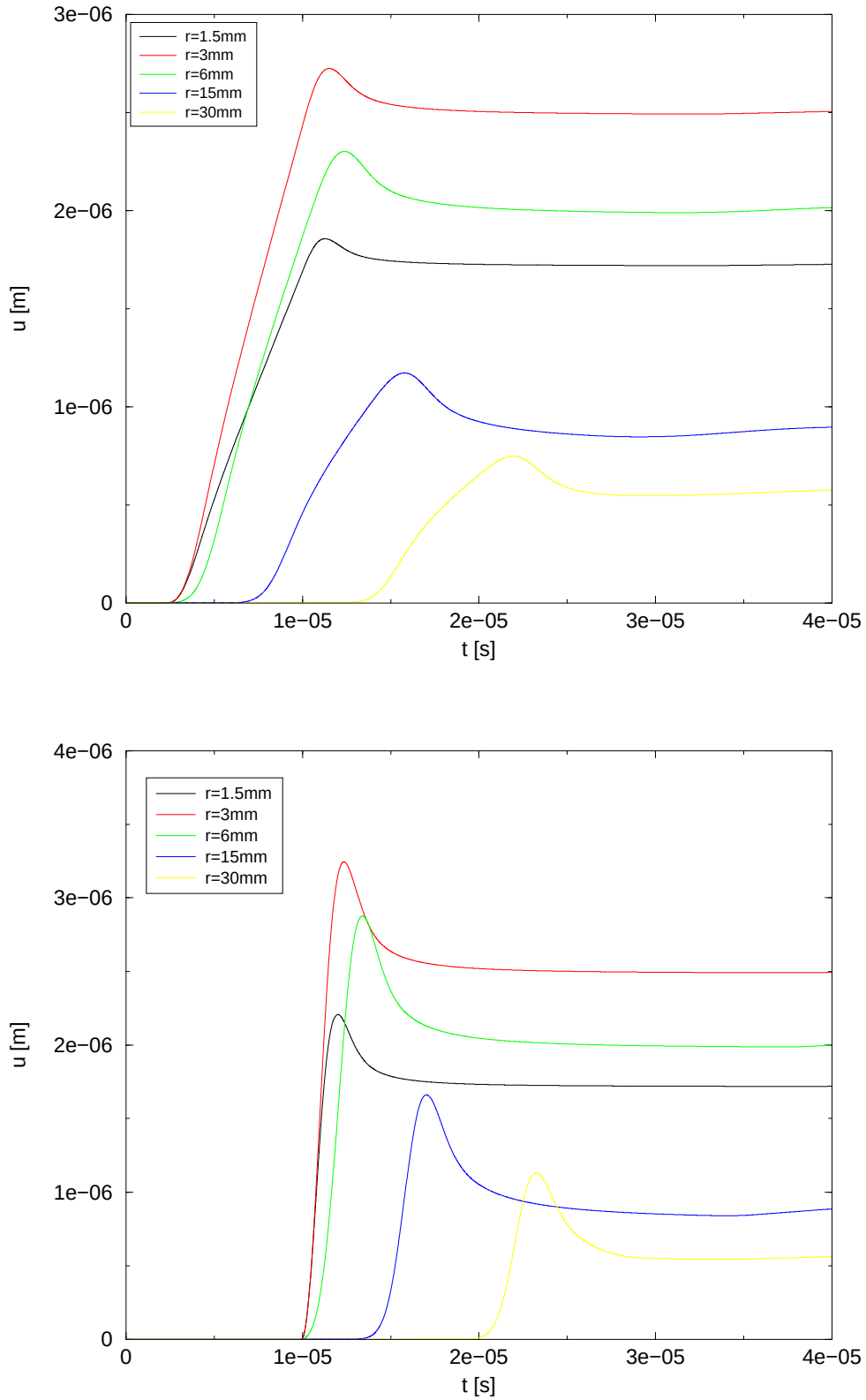

Figure 3.3: Displacement of different points when the ramp is 7.8μs long (top) and when it is 0.1μs long (bottom)

$t = 10.0\mu s$

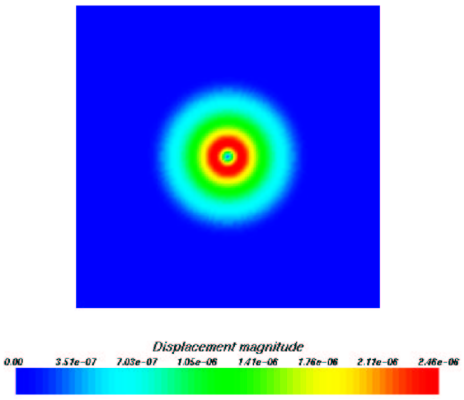

$t = 15.0\mu s$

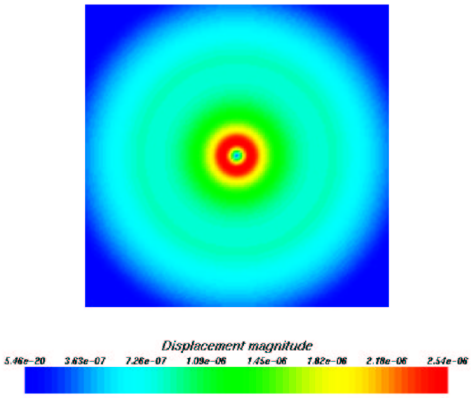

$t = 20.0\mu s$

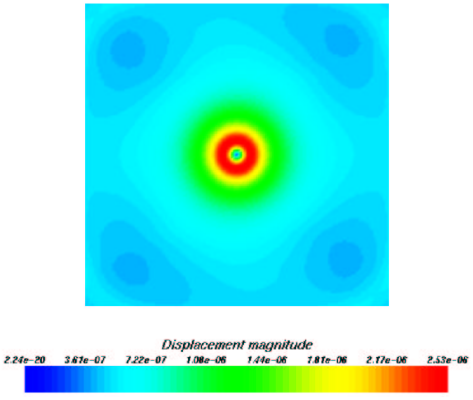

Figure 3.4: Snapshots of the displacement magnitude when the ramp is $7.8\mu s$ long

$t = 10.0\mu s$

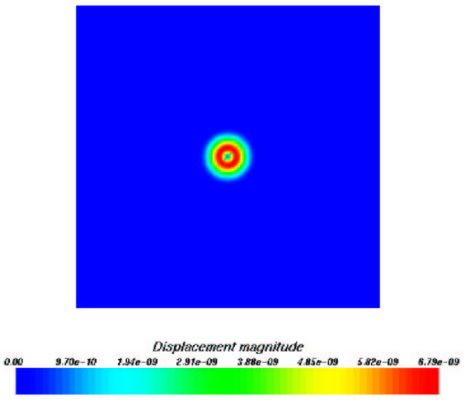

$t = 15.0\mu s$

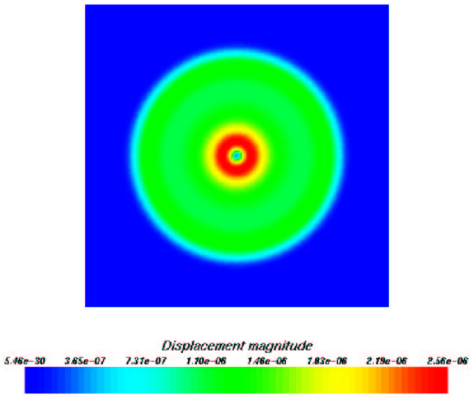

$t = 20.0\mu s$

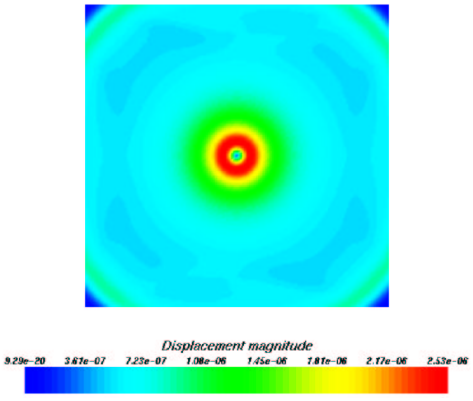

Figure 3.5: Snapshots of the displacement when the ramp is $0.1\mu s$ long

$r = 0$	ramp 1	ramp 2	static
$\sigma_x[MPa]$	11.34	27.09	11.12
$\sigma_y[MPa]$	11.34	27.09	11.12
$\sigma_z[MPa]$	22.41	27.14	22.35
$p[MPa]$	15.03	27.11	14.86
$\sigma_{vm}[MPa]$	11.08	0.47	11.23
$r = 1.5mm$	ramp 1	ramp 2	static
$\sigma_x[MPa]$	10.16	21.37	9.94
$\sigma_y[MPa]$	7.84	21.35	7.63
$\sigma_z[MPa]$	17.68	21.38	17.61
$p[MPa]$	11.89	21.37	11.73
$\sigma_{vm}[MPa]$	8.91	0.32	9.05
$r = 3mm$	ramp 1	ramp 2	static
$\sigma_x[MPa]$	7.46	10.48	7.27
$\sigma_y[MPa]$	1.61	10.44	1.39
$\sigma_z[MPa]$	8.68	10.46	8.62
$p[MPa]$	5.92	10.46	5.75
$\sigma_{vm}[MPa]$	6.55	0.31	6.65

Table 3.3: Dynamic analysis: comparison between stress values when the load is applied statically and with different ramps

3.4.3 Dynamic analysis with temperature dependent properties

As mentioned before, the analyses discussed so far were performed adopting material properties referred to the standard graphite at $20°C$. This was necessary in order to make a comparison with an analytical solution, and to get a first look at a reference problem with simplified physics.

A step toward a more accurate description can be done by considering temperature dependent material properties. In Figure 3.6, the results in terms of Stassi equivalent stress are shown for the problem with constant material properties (top) and that with temperature dependent properties (bottom), with the standard ramp, having a rise time of $7.8\mu s$. The state of stress is more critical for the problem with temperature dependent material. The reason is clearly the thermal expansion coefficient that increases with temperature for the material considered.

3.4.4 Results analysis

The Stassi equivalent stress above tensile strength is shown in Figure 3.7 at different instants.

It is possible to notice that the maximum value of the ratio between the Stassi equivalent stress and the tensile limit for the graphite, is reached at $r \cong 5.5mm$ and $t \cong 12\mu s$. It is worthwhile to remark that the gaussian parameters affect the position and the instant of the maximum Stassi stress value. A test with a different gaussian

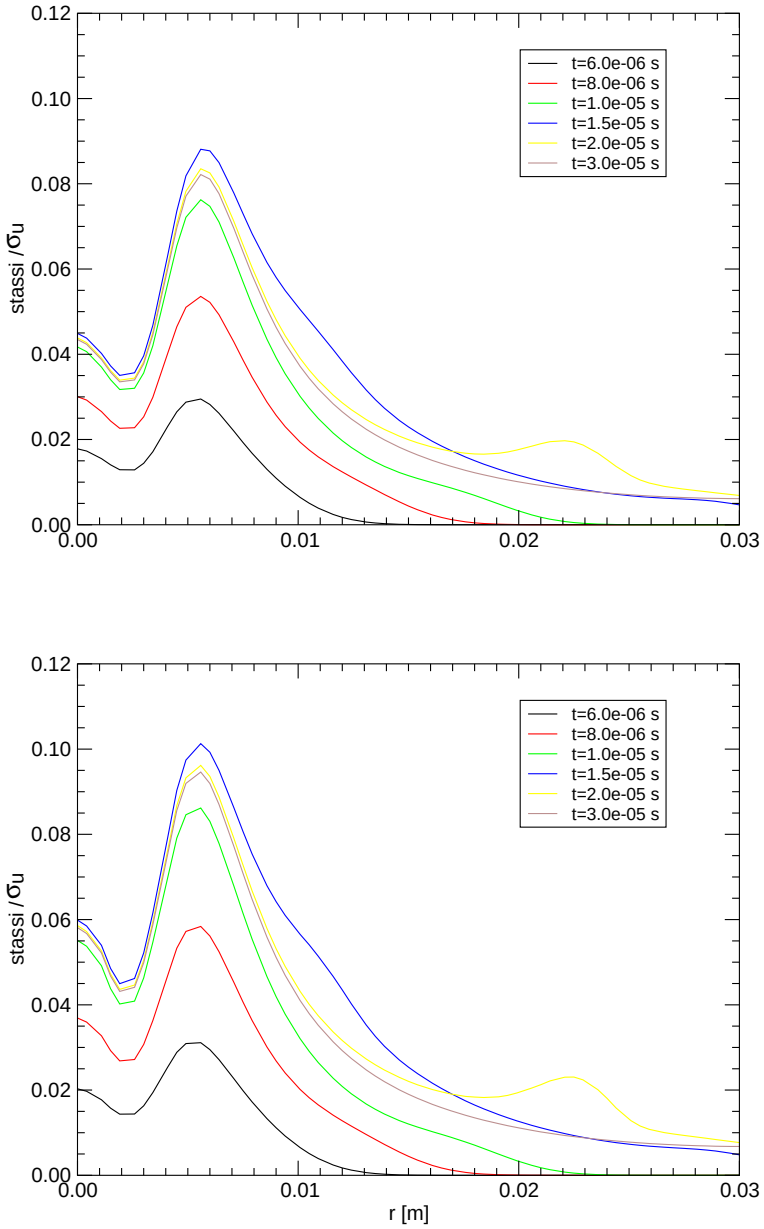

Figure 3.6: Stassi ratio for constant property material (top) and for a temperature dependent material (bottom)

load (where only the parameter b is changed) is done and the results obtained are shown in the Figure 3.8.

More in detail, in the new test, the parameter b of the gaussian load is set to one tenth of the original value, and this brings a bigger σ; the maximum of temperature does not change, so the energy deposited and the stress values are greater. We remark that the position of the maximum stress value is now at $r = 18mm$.

In another test, the ramp width is changed (precisely it is halved), while all the other parameters are kept constant. The results are shown in Figure 3.9. In this second test, the position and the instant of maximum stress remain the same, the stress values are greater since the dynamic part is increased.

From these and other results, it seems that keeping the same form of the temperature profile, and varying temperature and width of the heated area, the stress pattern in the quasi static approximation keeps the same form, and stress values are approximately proportional to the maximum temperature value. Moreover, the radius at which the critical stress condition is reached is approximately proportional to the σ parameter of the temperature function, the ratio between the two being approximately equal to 0.54.

The dynamic effects are superposed to the static stress distribution: they are related to the temperature increase, the lower the rise time of the temperature the higher the resulting dynamic stress. It is not easy to relate the rise time to the maximum value of the dynamic stress, reference to more detailed analytical works can be made [6]. Here we conclude that the dynamic stresses may almost double the stress induced by a static temperature distribution; as mentioned before, a way to check the importance of the dynamic effects may be the comparison of the rise time of the temperature and the time required by the elastic wave to cover a characteristic length of the temperature distribution (say σ as defined before). This is quite obvious indeed, but gives a quick rule of thumb useful in material selection.

It should be also noticed that the dynamic stress waves are characterized by two maximum values, corresponding to the two changes in slope of the time function adopted (i.e. the beginning and the end of the period in which the material is subjected to the heating).

Not surprisingly, the time at which the most critical stress condition is reached does coincide with the time at which the second circular wavefront, the one arising from the center of the heated area at the end of the heating period, reaches the radius of the maximum static stress: due to the superposition of these effects, the most critical condition is obtained. Therefore, given the characteristics of the heating curve and the material properties, it is possible to get an idea of the point and the time in which the beam stopper is subjected to the most critical stress condition.

Stresses however may increase a lot in case the heating spot falls near a free surface of the material: this situation is studied in the following paragraph.

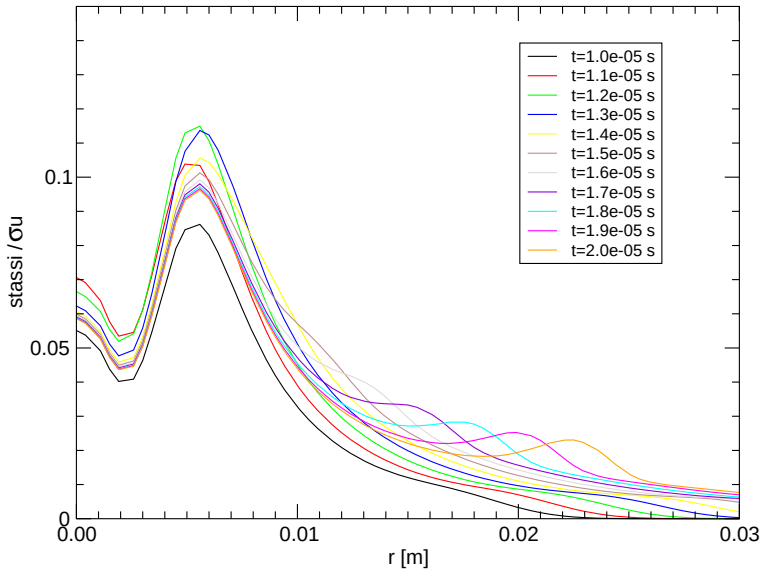

Figure 3.7: Stassi ratio in standard conditions

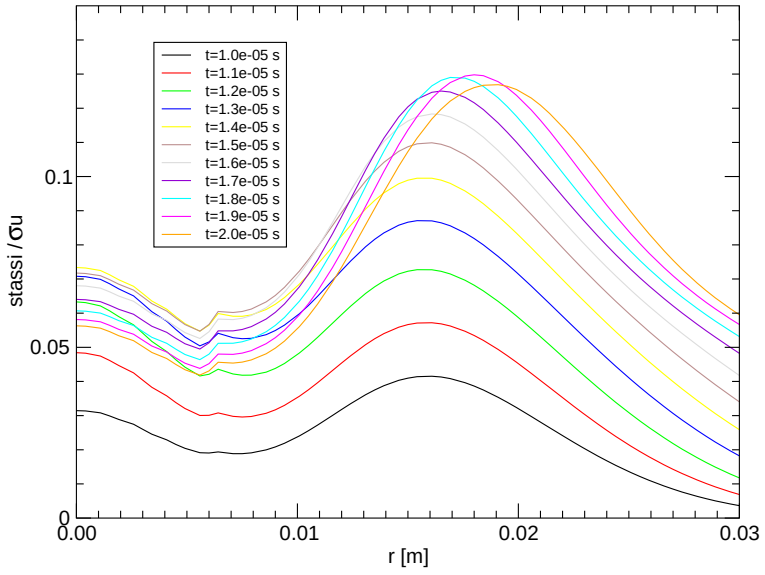

Figure 3.8: Stassi ratio ($\sigma = 9.7mm$)

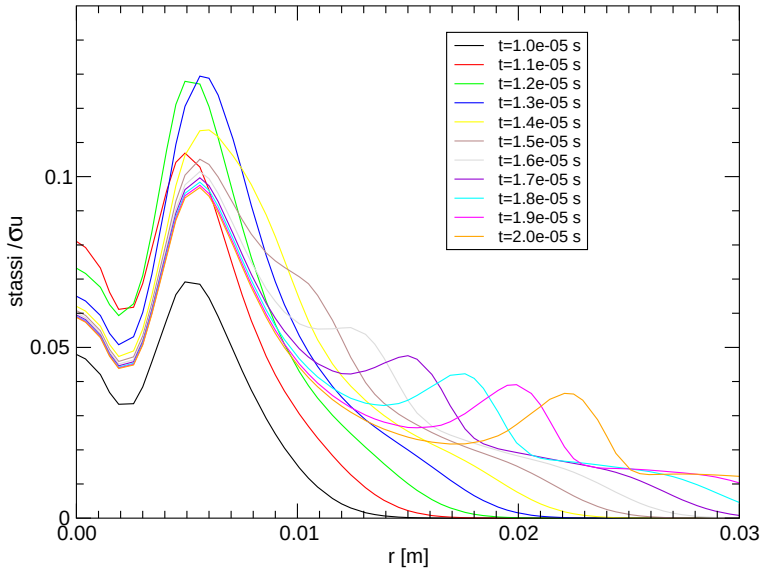

Figure 3.9: Stassi ratio: ramp width 3.9μs

3.5 Semi infinite plane

A semi infinite plane under the thermal gaussian load near the free edge is now analyzed. In the Figure 3.10 the model is shown: it is a $75 \times 39mm$ plane with a free surface condition on the bottom edge and absorbing conditions in the rest of the boundary. The thermal load and the mesh are exactly the same used in previous sections. The material properties are variable with temperature in the area surrounding the load point.

The proximity of the hot spot to the free edge leads to an increase of stresses with a stress concentration on the free edge. It may be important to determine which is the critical distance of the heat area from the free edge, the distance at which the most

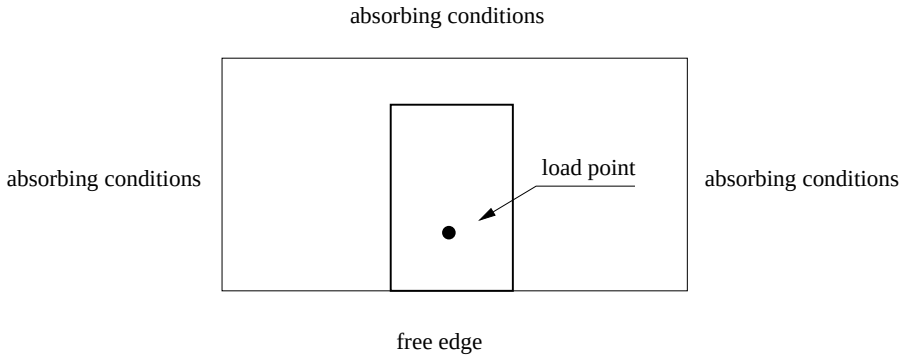

Figure 3.10: Model approximation for the semi infinite plane

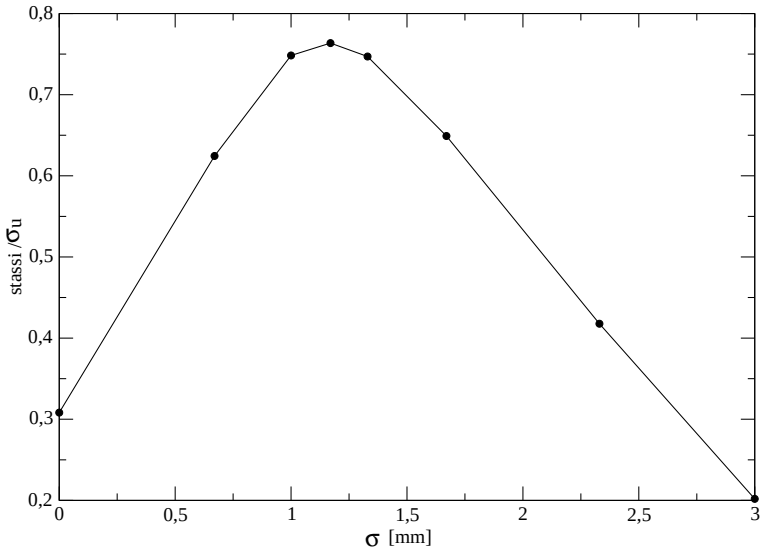

Figure 3.11: Maximum Stassi ratio varying the distance of the load point from the free edge

dangerous stress condition appears at any time for the given temperature profile and temperature rise time.

Different tests are made varying the load point: the results are summarized in Figure 3.11, where the maximum Stassi ratio found at any instant of the simulation in any point of the model is plotted as a function of the distance of the center of the heated area from the free edge. It is possible to see that the more critical condition takes place when the load point is $3.5mm$ (i.e. 1.167σ) far from the free edge. In fact, since $\sigma = 3mm$, in this case the total load energy is deposited very near to the free edge. Further approaching the beam deposition point to the free edge would cause part of the thermal energy to fall outside of the plane.

Figures 3.12, 3.13 and 3.14 show several snapshots of the stress wave represented in form of Stassi ratio, for different load conditions, with the center of the heated area located at $7mm$, $3.5mm$ and on the free edge, respectively.

The Figures 3.15, 3.16 and 3.17 show the Stassi equivalent stress varying the load position. For every graph the distance of the load point from the free edge is indicated.

The Figures 3.18, 3.19 and 3.20 show the radial displacement, the radial stress and tangential stress respectively.

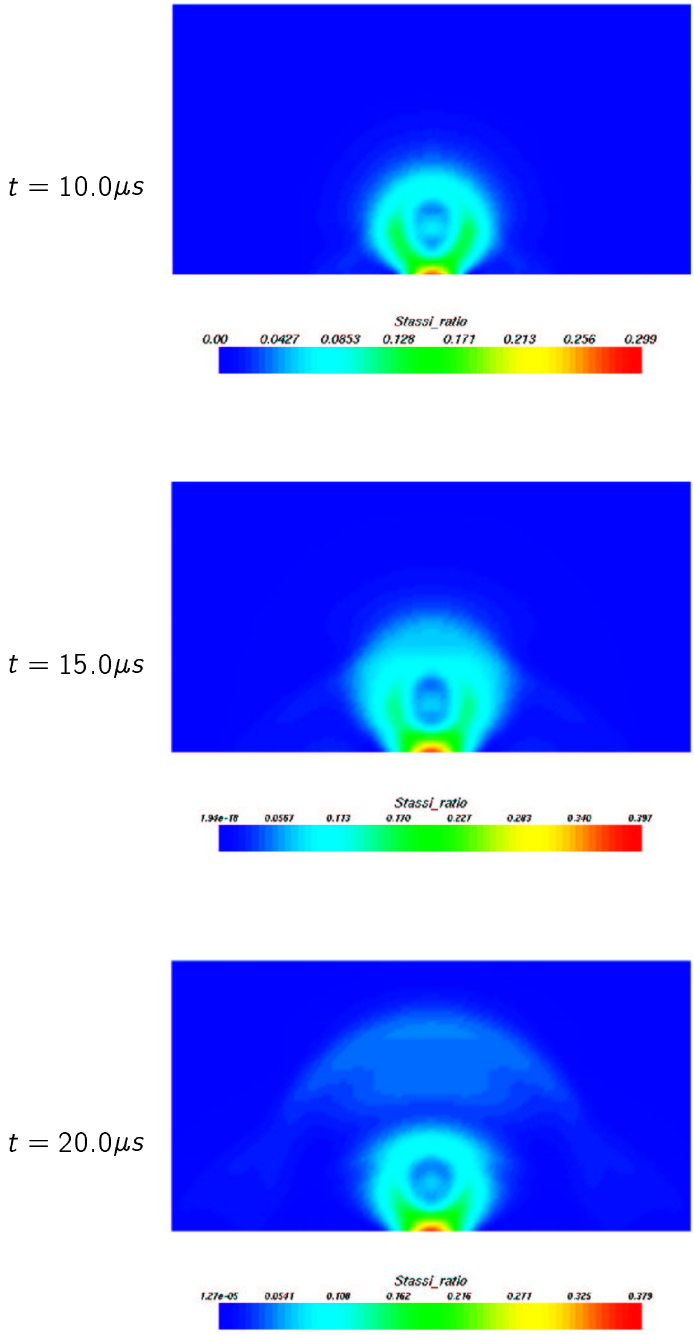

Figure 3.12: Snapshots of the Stassi ratio when the load center is $7mm$ distant from the free edge

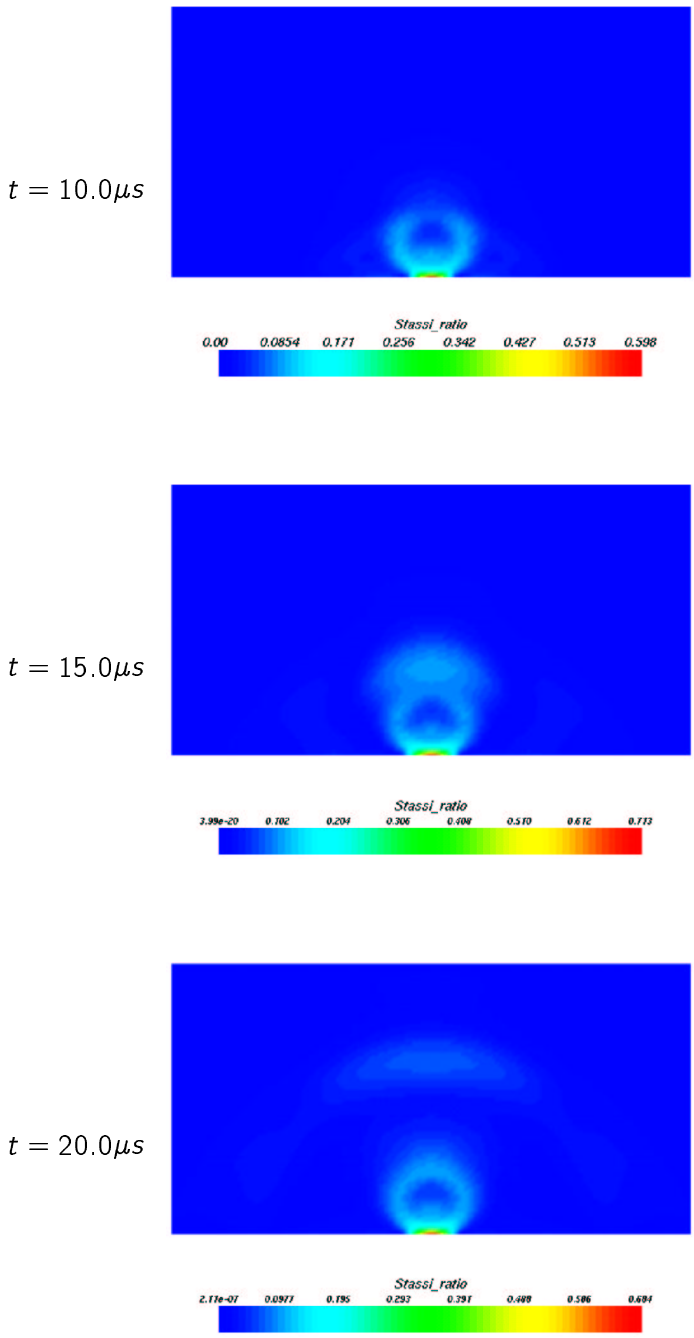

Figure 3.13: Snapshots of the Stassi ratio when the load center is 3.5mm distant from the free edge

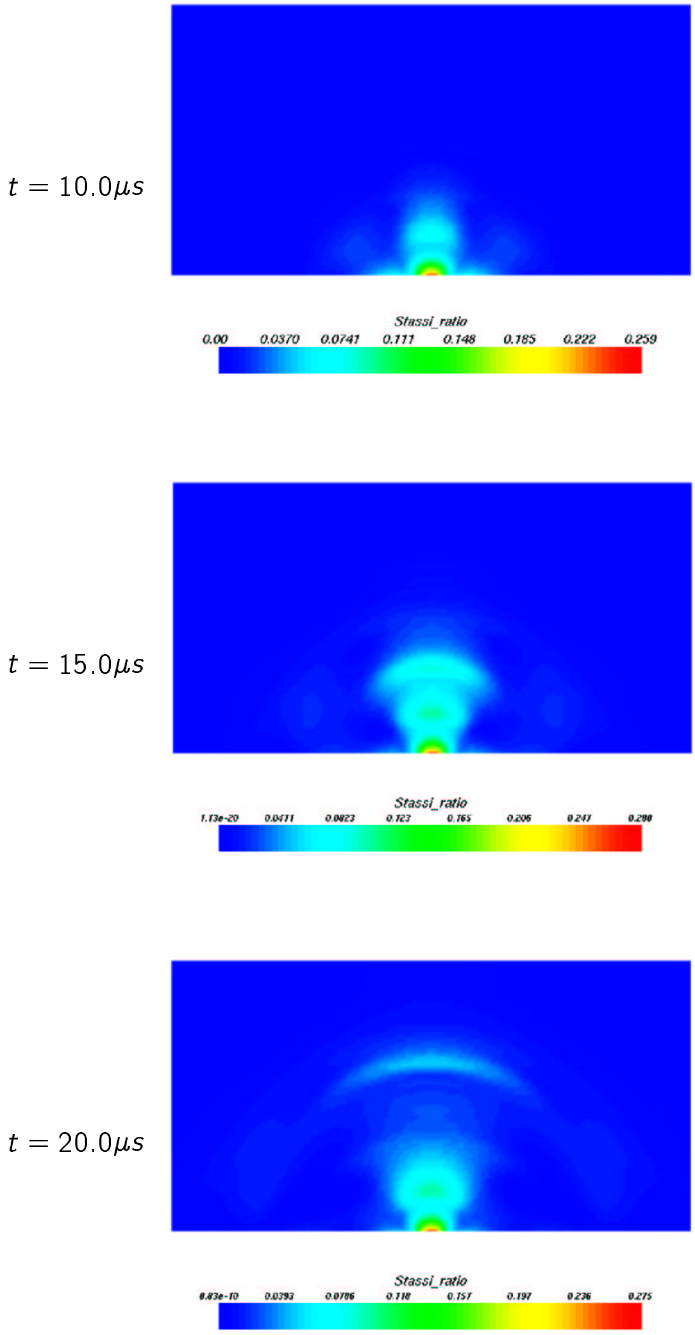

Figure 3.14: Snapshots of the Stassi ratio when the load center is on the free edge

0*mm*

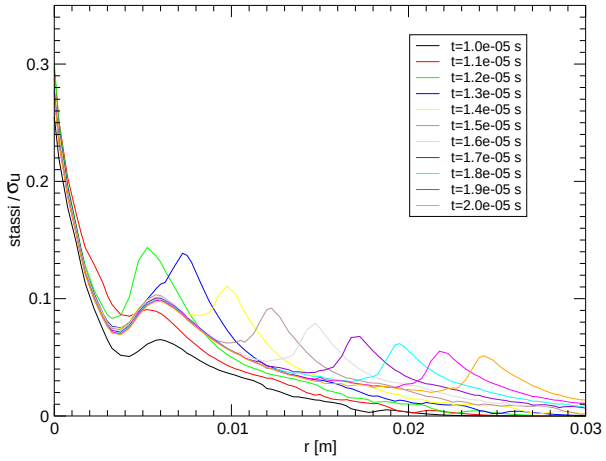

2*mm*

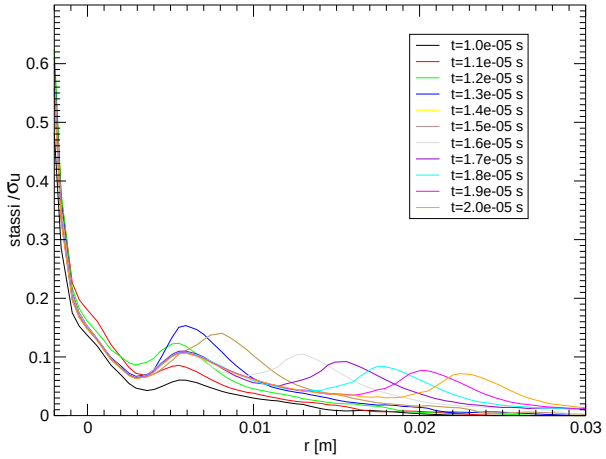

3*mm*

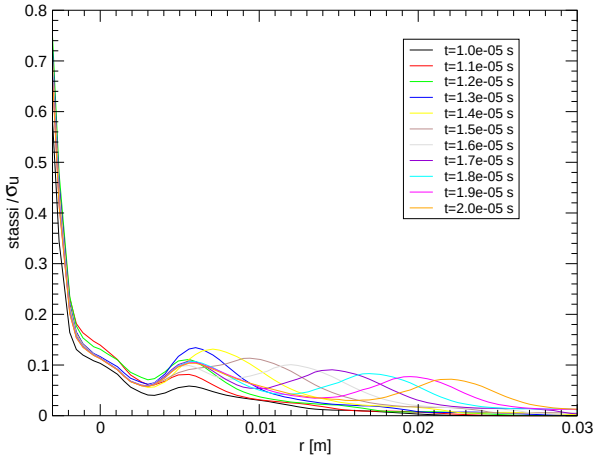

Figure 3.15: Stassi ratio along the normal to the free edge for different load distances and different times

3.5*mm*

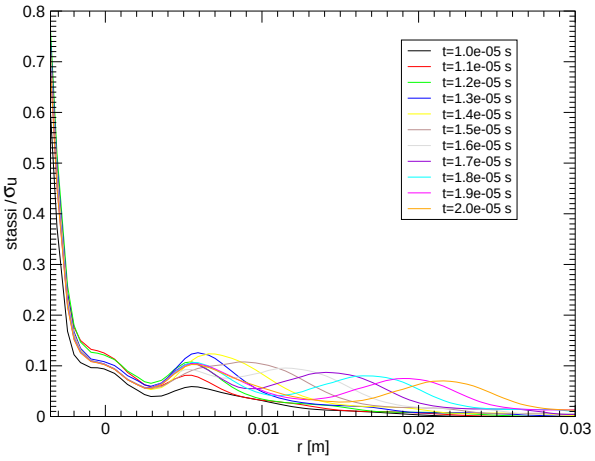

4*mm*

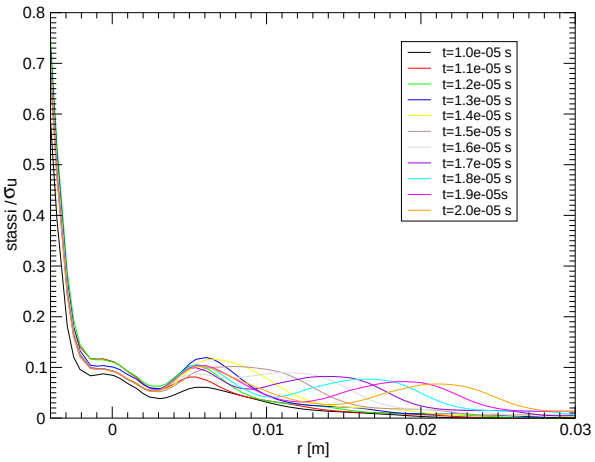

5*mm*

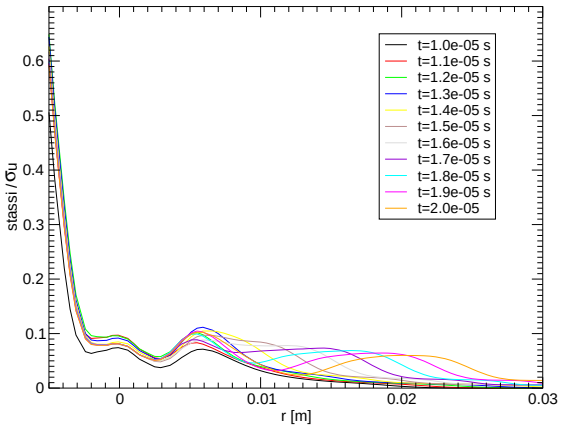

Figure 3.16: Stassi ratio along the normal to the free edge for different load distances and different times

7*mm*

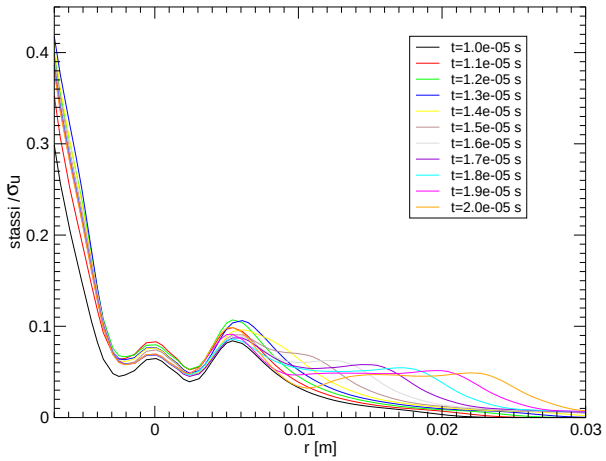

9*mm*

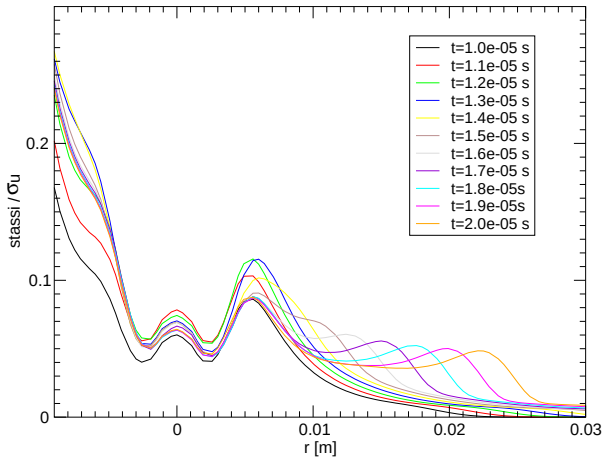

Figure 3.17: Stassi ratio along the normal to the free edge for different load distances and different times

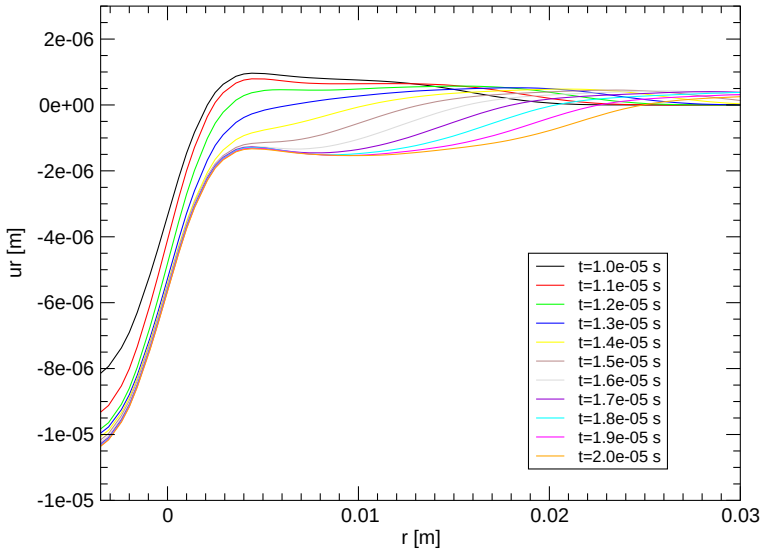

Figure 3.18: Radial displacements along the normal to the free surface for the maximum stress load condition

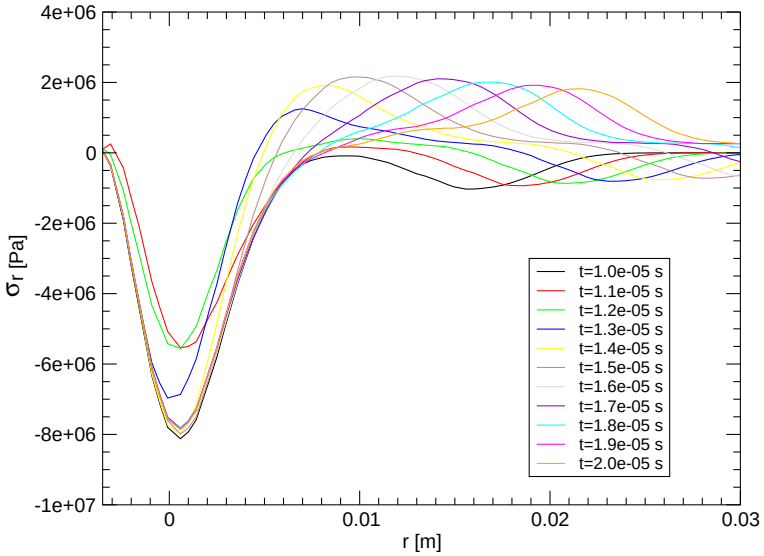

Figure 3.19: Radial stresses along the normal to the free surface for the maximum stress load condition

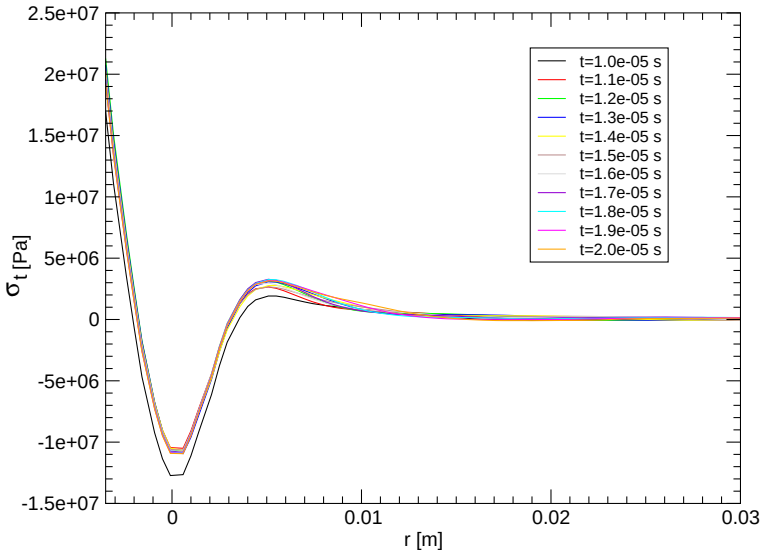

Figure 3.20: Tangential stresses along the normal to the free surface for the maximum stress load condition

Chapter 4

TDI 2D analysis

4.1 Introduction

In this chapter we analyze a 2D model of a TDI section under the same loading conditions discussed previously. Some details of construction drawings of these parts are presented in Figure 4.1. The thickness of each block is greater than its plane dimensions, hence we expect the plane strain hypothesis to be a good approximation of the real conditions, at least within the limits of a 2D analysis.

The analysis is performed on a section of the block and its neighboring elements, to evaluate the loads transferred to these parts and the critical state of stress thus induced. The graphite absorber block is in fact held in place by an aluminum support and by an overlying copper plate pressed over it, as shown in the drawings.

It is therefore crucial for a correct preparation of the model to properly determine the contact, gap and interference condition between the different parts of this assembly. Constructive drawings have been analyzed to verify the coupling specifications and measure tolerances between the different parts. It has been verified that the specified dimensions and relative tolerances realize an interface with a permanent gap within each of the parts, and in particular for the vertical surfaces between the graphite core and the aluminum support and between the latter and the copper plate. Moreover, even in the worst case for the as built dimensions, the permanent gap between the parts is still higher than the maximum displacement due to heating and elastic wave propagation.

Referring now to the horizontal surfaces, the different parts are pushed together by a set of pre-stressed springs: a constant pressure is therefore applied on the small contact horizontal areas between the graphite core and the aluminium jaw and between the copper plate and the upper surface of the graphite block.

Thus, the model of the TDI section has been prepared avoiding the continuity between the vertical surfaces, and the nodes of the two parts may share the same position but do not coincide. For the horizontal surfaces a non linear contact condition could be applied, at the expenses a worsening of the computer time requirements: in our opinion this is not worthwhile, due to the limited dimension of the contact area between graphite and aluminum and the different acoustic admittance of the materials of the different

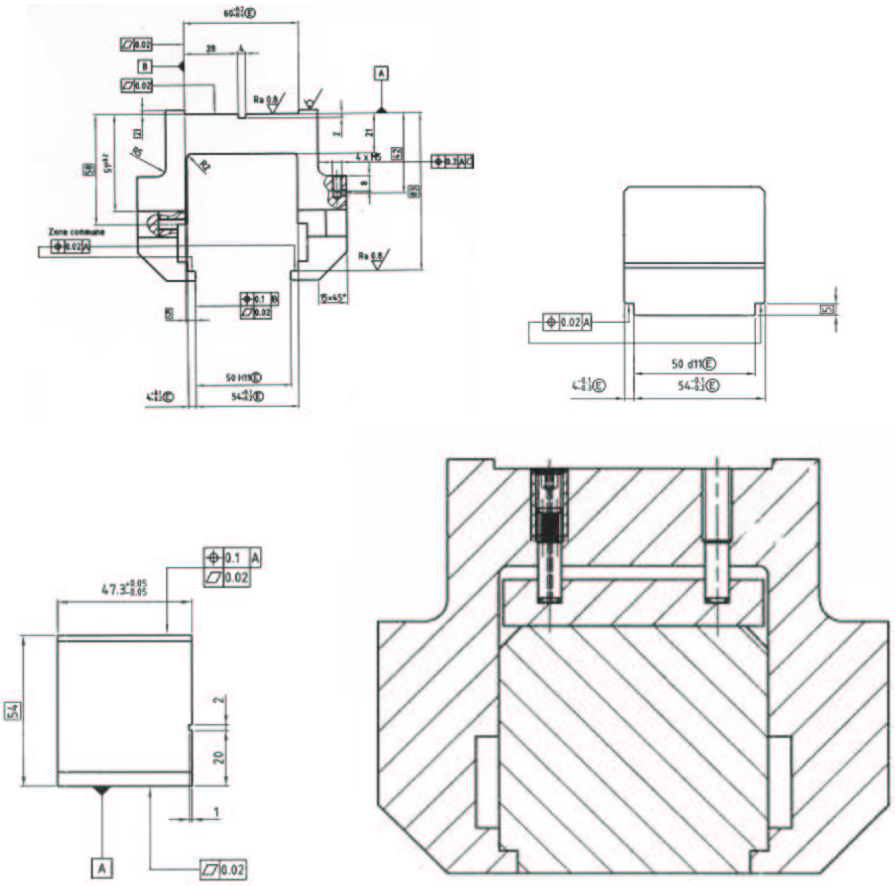

Figure 4.1: TDI drawing

T	ρ	E	ν	σ_t	σ_c	α	c	k
$[°C]$	$[Kg/m^3]$	$[GPa]$		$[MPa]$	$[MPa]$	$[\mu m\ /m\ °C]$	$[J/Kg\ °C]$	$[W/m°C]$
20	8960	110	0.343	33.3	33.3	16.4	385	385
250	8960	110	0.343	33.3	33.3	18.5	385	385
500	8960	110	0.343	33.3	33.3	20.2	385	385
1000	8960	110	0.343	33.3	33.3	24.8	385	385

Table 4.1: Copper mechanical properties

T	ρ	E	ν	σ_t	σ_c	α	c	k
$[°C]$	$[Kg/m^3]$	$[GPa]$		$[MPa]$	$[MPa]$	$[\mu m\ /m\ °C]$	$[J/Kg\ °C]$	$[W/m\ °C]$
20	2710	68	0.33	35	35	24	900	210
250	2710	68	0.33	35	35	25.5	900	210
500	2710	68	0.33	35	35	27.4	900	210

Table 4.2: Aluminum mechanical properties

parts. Continuity is imposed on these surfaces, so matching surfaces share the same nodes.

This test is useful since provide an upper approximation of the energy transferred from the block to the surrounding parts and the stress state induced on them. In the following we consider a stand-alone block (i.e. we neglect the surrounding components) in such a way that the whole energy of the beam dumping is confined inside the block itself.

The features of the thermal load are the same used in the first analyses: a temperature variation is imposed first on the center of the block, and then near the lower border. The temperature variations undergoes the following law:

$$\theta(\mathbf{x}, t) = \theta_M e^{-b((x-x_0)^2+(y-y_0)^2)} g(t) \tag{4.1}$$

where $\theta_M = 635°C$ is the maximum temperature increase, (x_0, y_0) are the coordinates of the center of the heated area and $g(t)$ gives the temperature time-history. The temperature is equal to zero until $t = 2.14\mu s$, then grows linearly to reach the maximum at time $10.0\mu s$. This law approximates the deposition of the energy of four trains of protons, as an impulse of finite length $\Delta t_{bd} = 7.86\mu s$.

4.2 Material properties

The properties of Copper and Aluminum adopted for this simulation are indicated in Tables 4.1 and 4.2. Standard Graphite properties are used for the absorber block, reference may be made to the previous chapters for details on graphite properties.

Wave speed, as well as the material density, should be carefully taken into account. The speed values of the pressure waves for the different materials at $t = 20°C$, are

Material	Speed [m/s]
graphite	2389
copper	4373
aluminum	6097

Table 4.3: Pressure wave speed for the different materials

indicated in the Table 4.3. Propagation velocity also drives the choice of the element size through the wave length resulting for a given frequency or, if the element size is given, determines the time step size via the stability requirements.

4.3 TDI grid

The Figure 4.2 shows the mesh used in the simulation. Different colors are used to indicate the different materials: red for copper, fucsia for aluminum, black for graphite with constant properties at $t = 20°C$, and blue for graphite with properties varying with temperature.

The model is described by 6340 elements. The element size is not constant: as a term of comparison, in the graphite core each element is $1 \times 1mm^2$. A spectral degree equal to three is chosen constant for all the model, and the total number of spectral nodes is 58059.

4.4 Results analysis

In the following, results are presented in the form of color plots of kinetic energy density, and several measures of the state of stress for a relevant number of instants, to better follow the propagation of the wave through the structure.

Figures from 4.3 to 4.6 show the kinetic energy density in the structure, giving a straightforward view of how energy propagates in the beam obstacle.

Figure 4.3 top is relative to the time when the temperature stops its growth: it is clearly visible that a circular wave front has already left from the center of the block, $7.8\mu s$ before, when beam deposition began. The energy density is initially concentrated in the area around the center but rapidly propagates in the rest of the obstacle. The bottom Figure refers to $12\mu s$: the first wavefront has not yet reached the borders of the block and clearly the final front of the wave has already left the center.

The wave propagates and reaches the horizontal border first (see Figure 4.4) and then the lateral surfaces. A different behavior is put in evidence in these pictures: on the lower border and the lateral surfaces (free edges) a maximum elongation is recorded. The upper surface is in contact with a material that is more rigid and has an higher density than graphite of the absorber block, and seems to act approximately like a rigid wall.

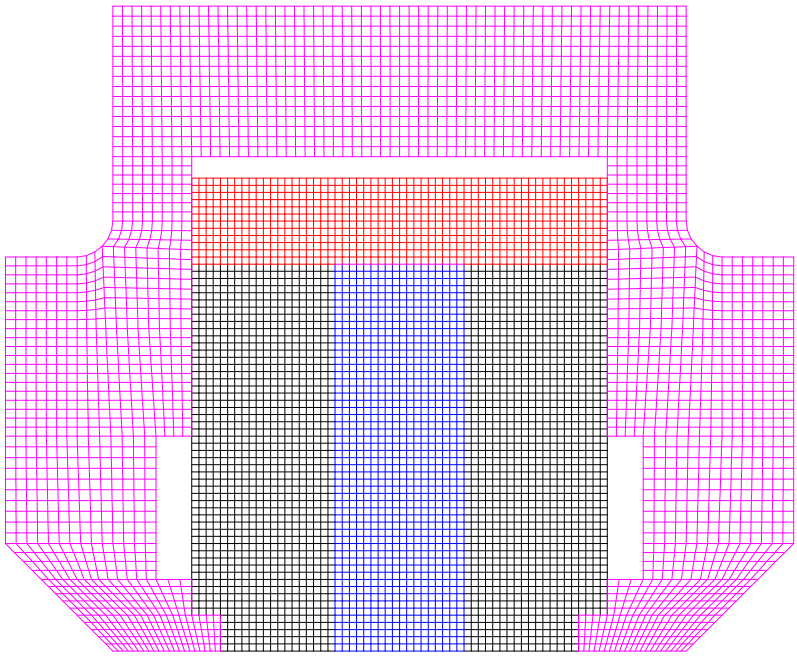

GIBI FECIT

Figure 4.2: TDI 2D mesh

Figure 4.5 shows snapshots taken at $t = 18\mu s$ and $t = 20\mu s$: some border effects are particularly evident on the sides near the aluminum support of the lower surface of the absorber block. It is interesting to see that the kinetic energy seems to be confined mostly inside the absorber block and just a limited portion seems to pass to the rest of the structure.

Proceeding in time, multiple reflections take place inside the block, the energy distribution and wavefronts become difficult to distinguish as shown in Figure 4.6; in the upper one it is anyway possible to see the energy distribution in the rest of the structure, with a much lower density than in the absorber block.

Figures 4.7-4.12 show the Von Mises equivalent stress and internal pressure at several instants. The results suggest that the state of stress induced by the load condition are mostly due to the static part, the beam deposition time being long enough for dynamic components of the state of stress to be small when compared to the static part. Therefore, the stress and pressure distribution in the structure seem to remain constant with stresses concentrated near the beam deposition area with the exception of limited area near the borders where notches are present.

This indication is partly confirmed by the most important results, those of Figures 4.13 - 4.17 that show the ratio of the Stassi tensile equivalent stress with the tensile rupture stress, giving a direct measure of the criticality of a stress configuration (a unitary ratio means rupture).

It is evident that an annular area around the beam deposition center maintains an high value during all the simulation. Anyway a circular stress wave propagating in the absorber block is now clearly visible along with its reflections in Figure 4.14, and the stress concentration near the notch of the contact area become more evident, but stress values appear still far from critic conditions. The stress configuration worsens in the next Figure 4.15 where stress concentrations on the notch are even more evident but still not critic.

From the last Figure 4.17 we can observe how the surrounding structure is loaded by the absorber block; stresses are evident but limited in value due to the material properties and the form and function of the structures involved. So the stresses in the bearing plate appear to have limited importance and those on the aluminum jaw seem confined to the lower teeth, near the contact area, and appear tolerable at least in these load conditions.

$t = 10\mu s$

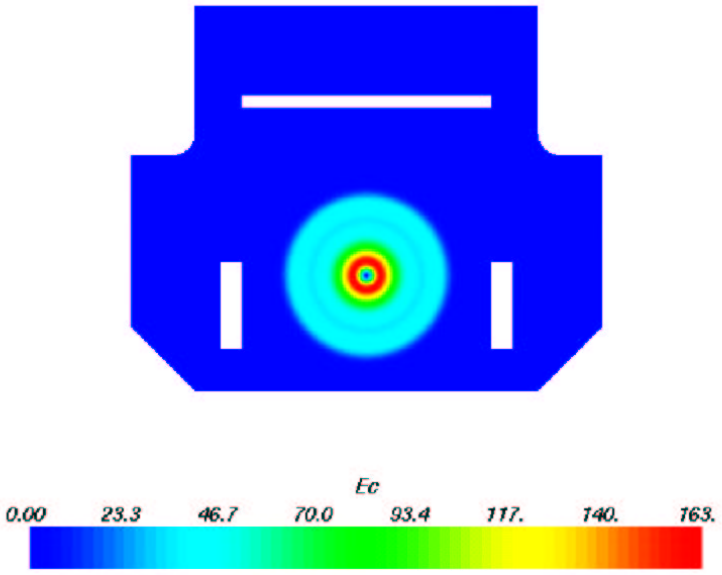

$t = 12\mu s$

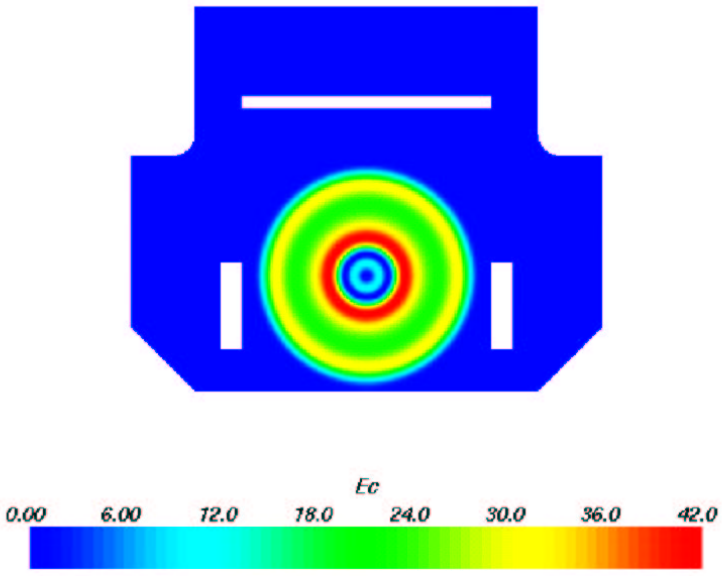

Figure 4.3: Kinetic energy density $[J/m^3]$

$t = 14\mu s$

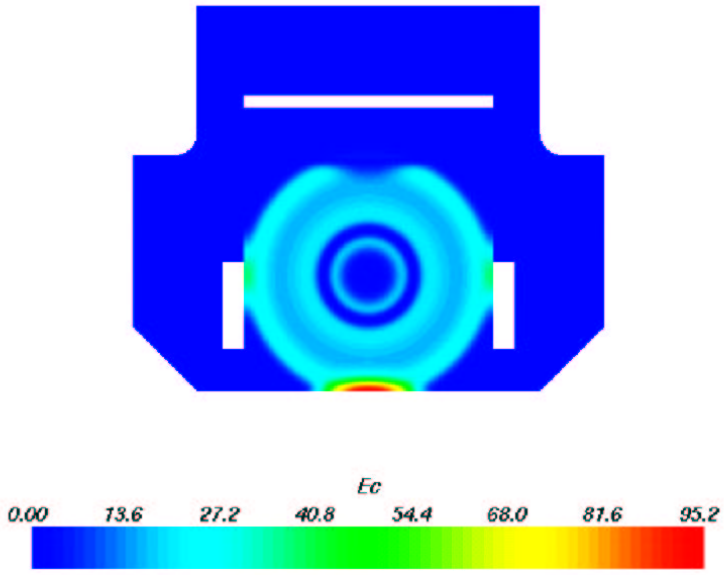

$t = 16\mu s$

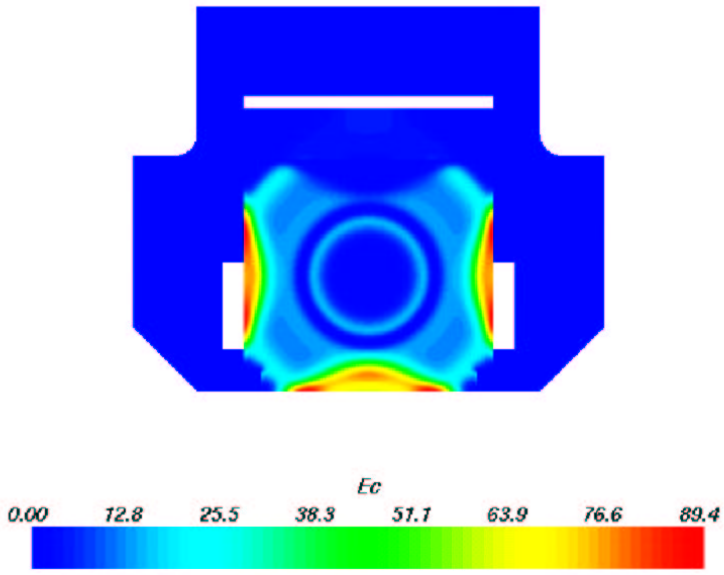

Figure 4.4: Kinetic energy density $[J/m^3]$

$t = 18\mu s$

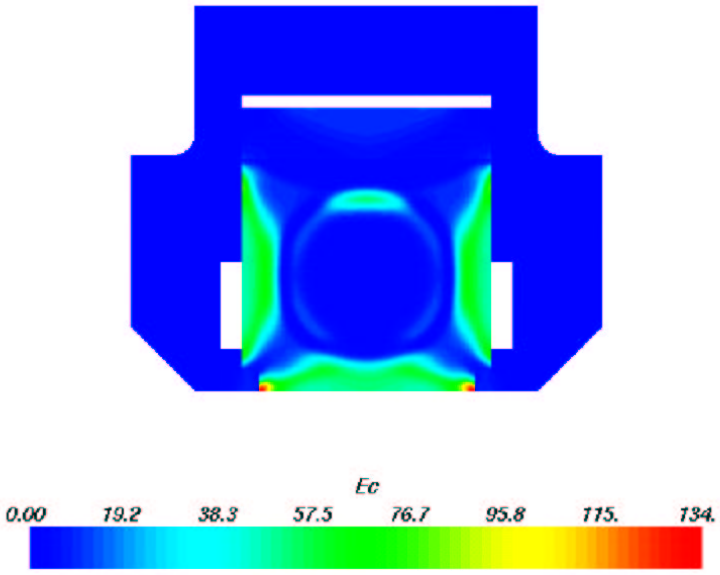

$t = 20\mu s$

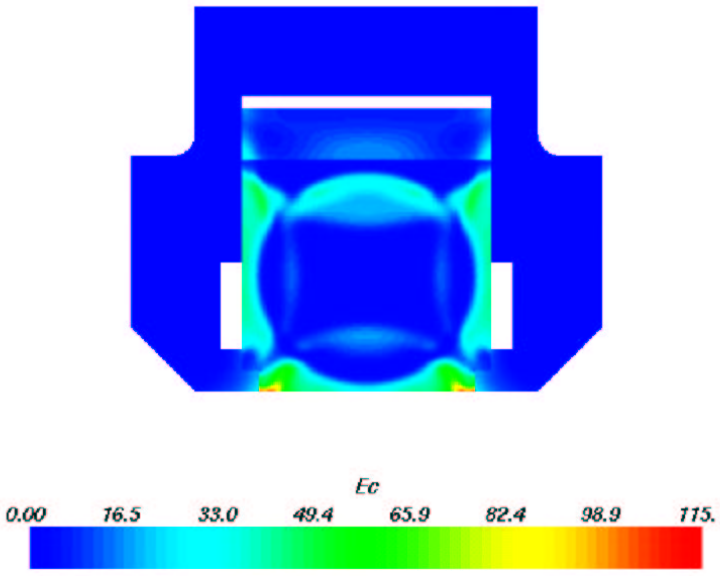

Figure 4.5: Kinetic energy density $[J/m^3]$

$t = 30\mu s$

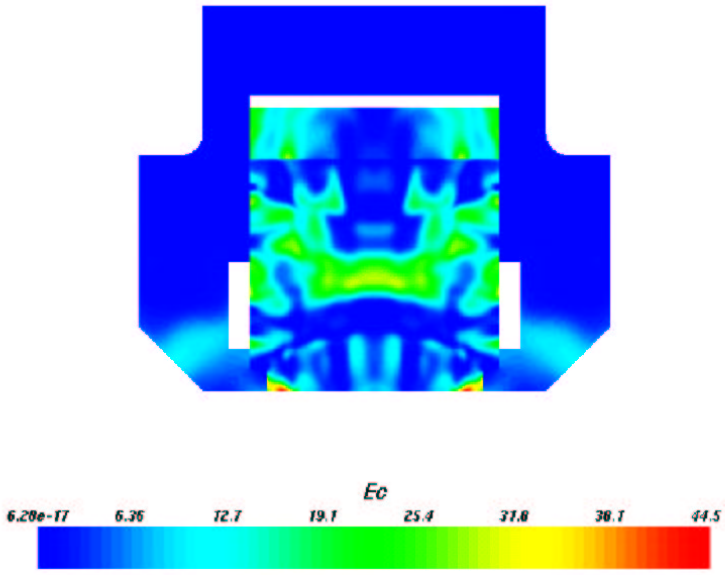

$t = 40\mu s$

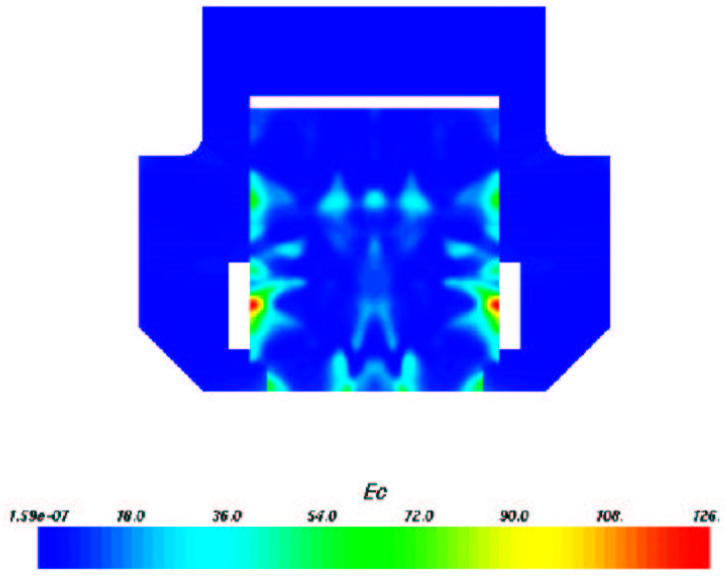

Figure 4.6: Kinetic energy density $[J/m^3]$

$t = 10\mu s$

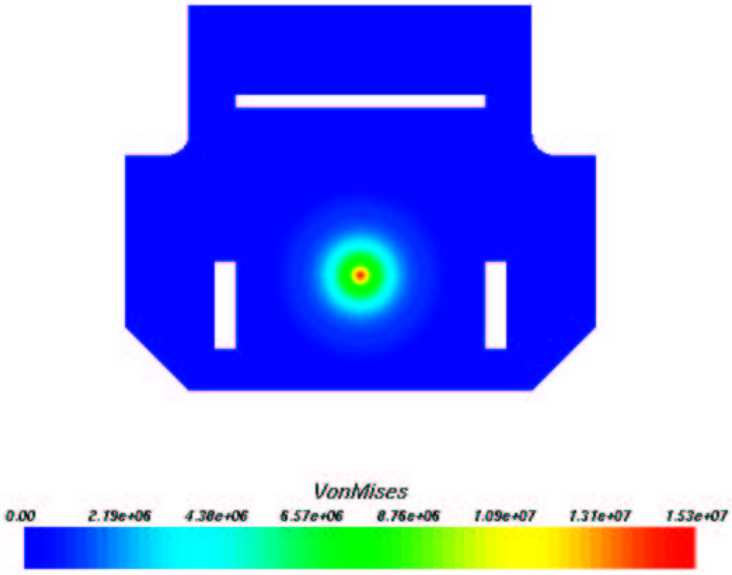

$t = 14\mu s$

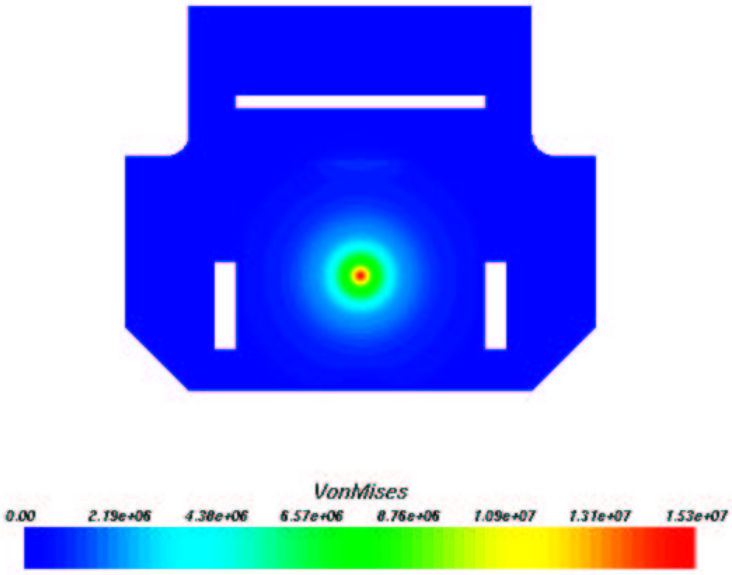

Figure 4.7: Von Mises equivalent stress [Pa]

$t = 18\mu s$

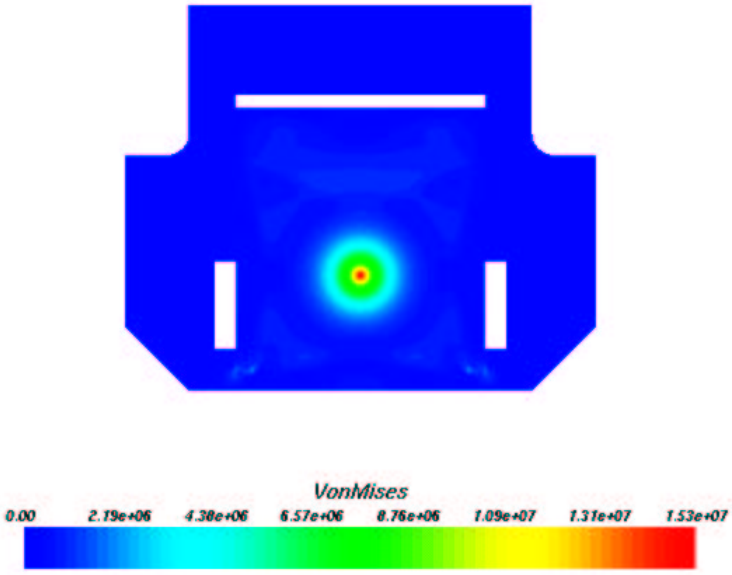

$t = 22\mu s$

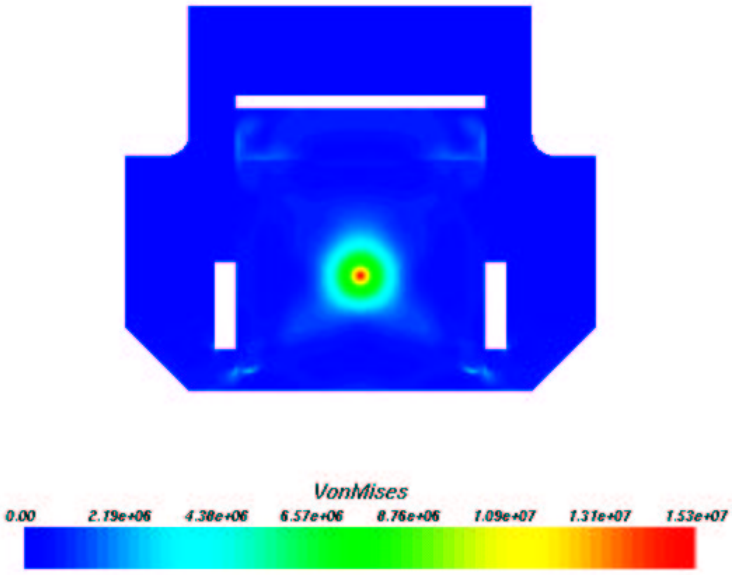

Figure 4.8: Von Mises equivalent stress [Pa]

$t = 26\mu s$

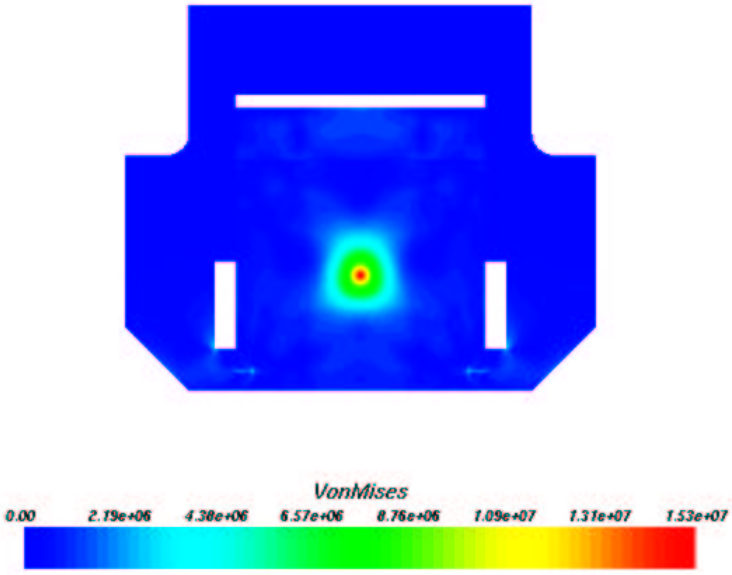

$t = 30\mu s$

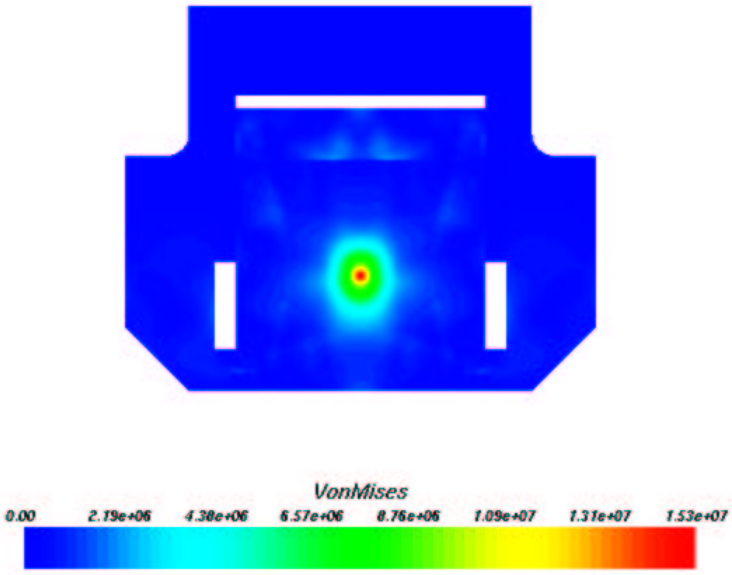

Figure 4.9: Von Mises equivalent stress [Pa]

$t = 10\mu s$

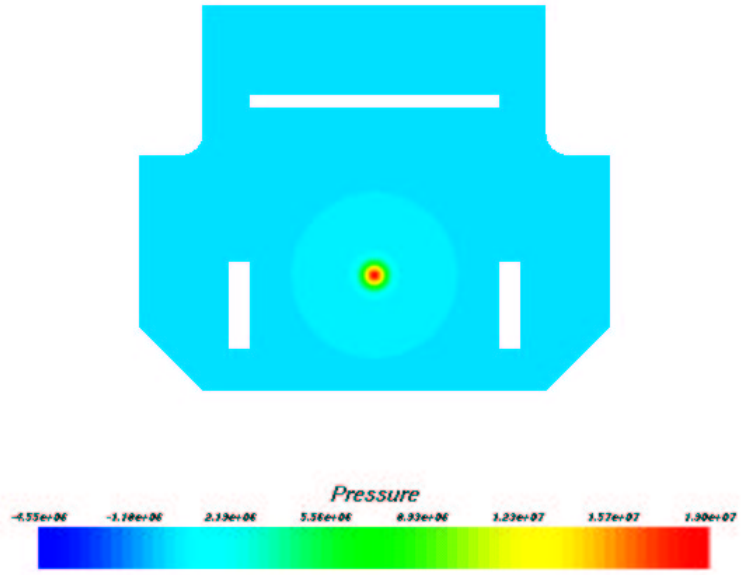

$t = 14\mu s$

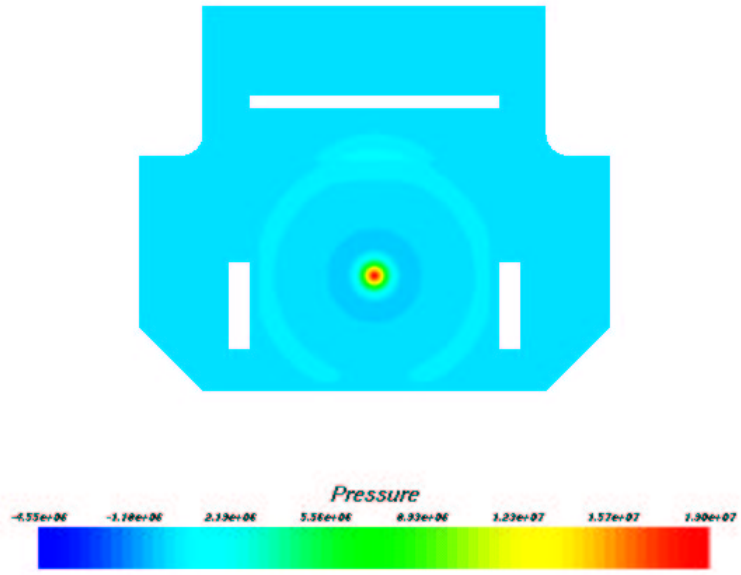

Figure 4.10: Internal pressure [Pa]

$t = 18\mu s$

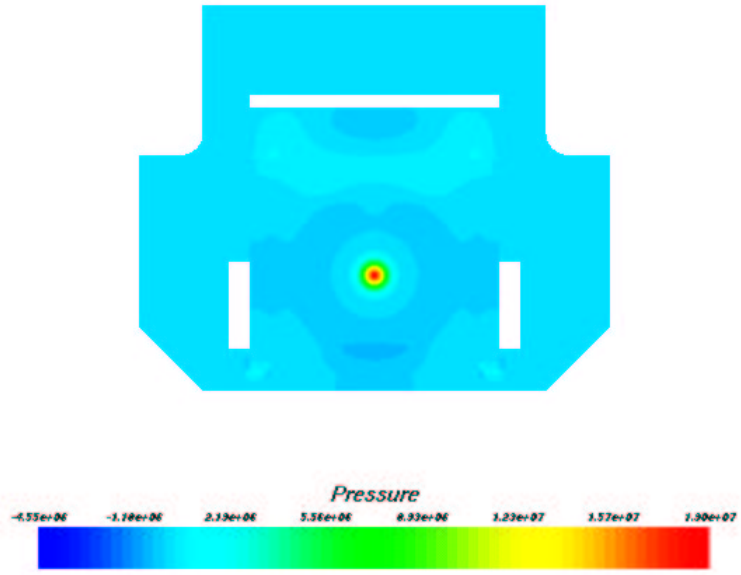

$t = 22\mu s$

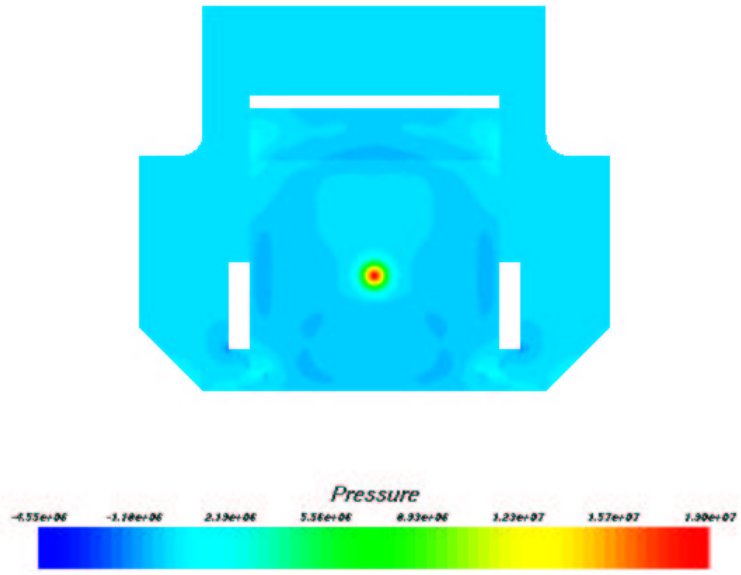

Figure 4.11: Internal pressure [Pa]

$t = 26\mu s$

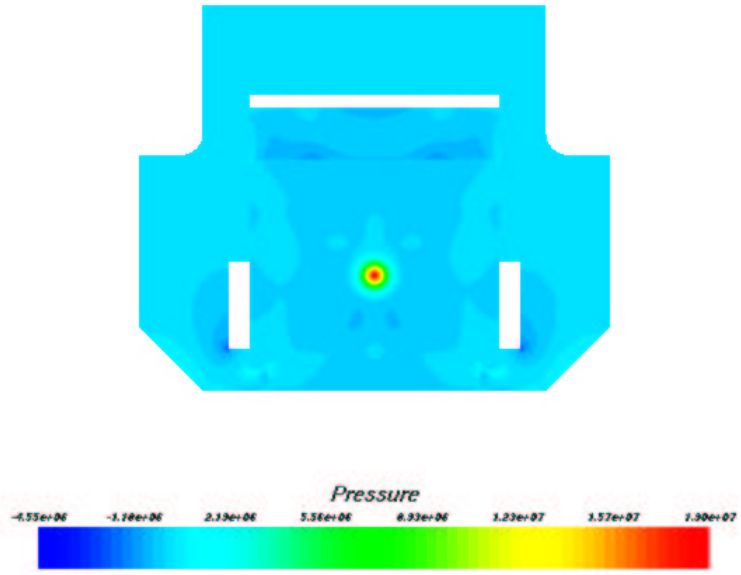

$t = 30\mu s$

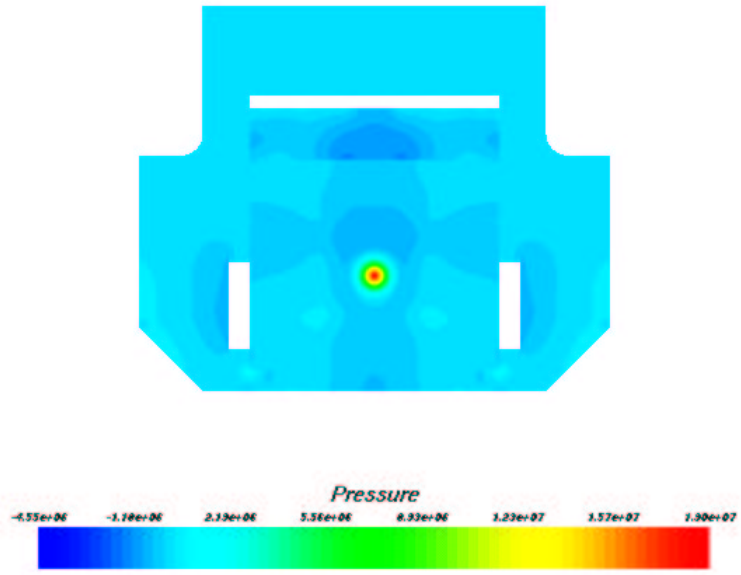

Figure 4.12: Internal pressure [Pa]

$t = 10\mu s$

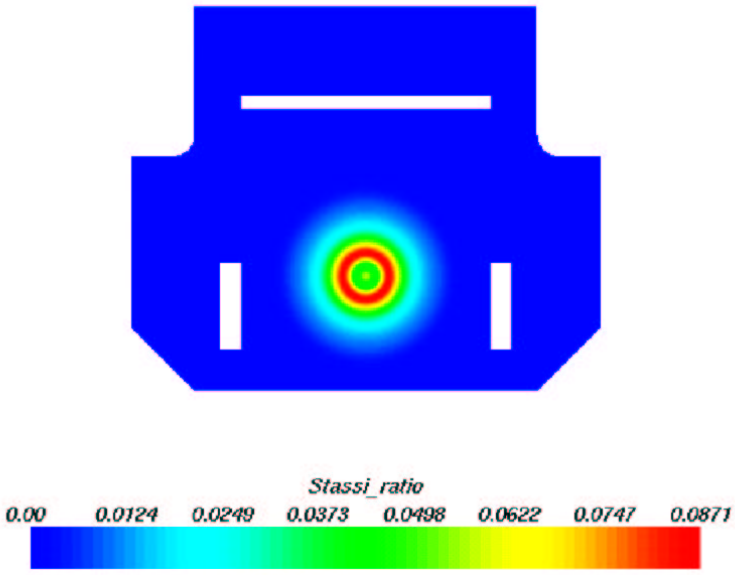

$t = 12\mu s$

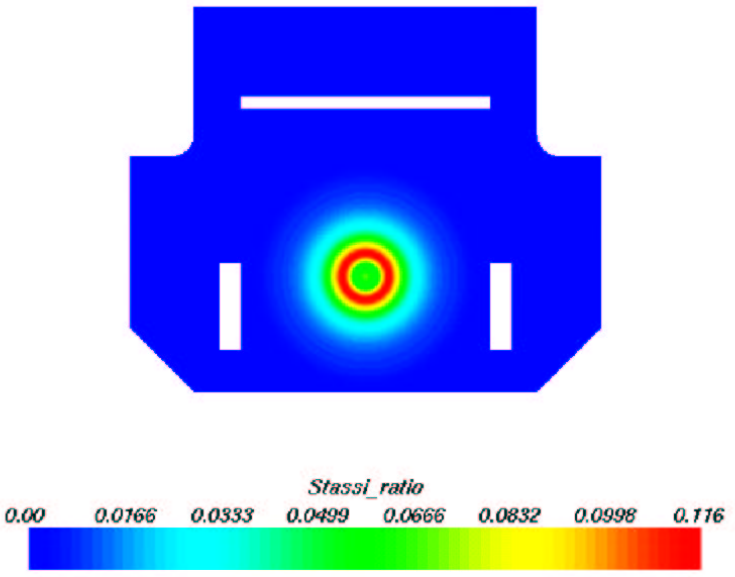

Figure 4.13: Stassi ratio

$t = 14\mu s$

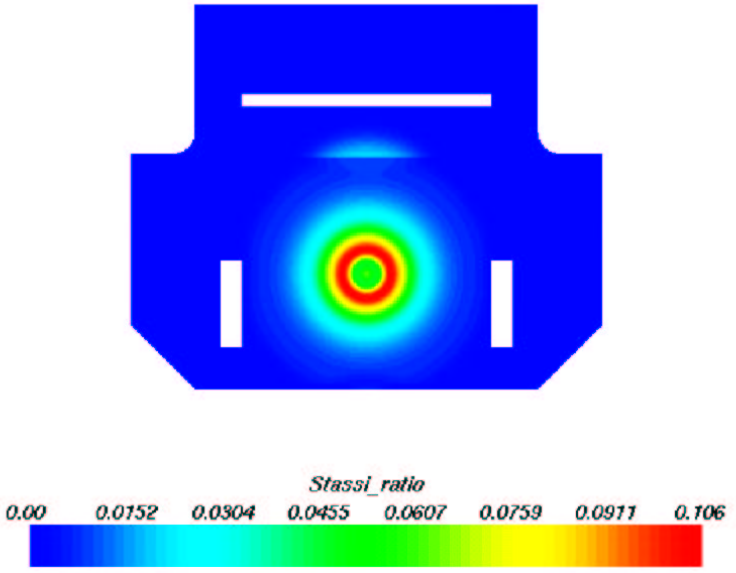

$t = 16\mu s$

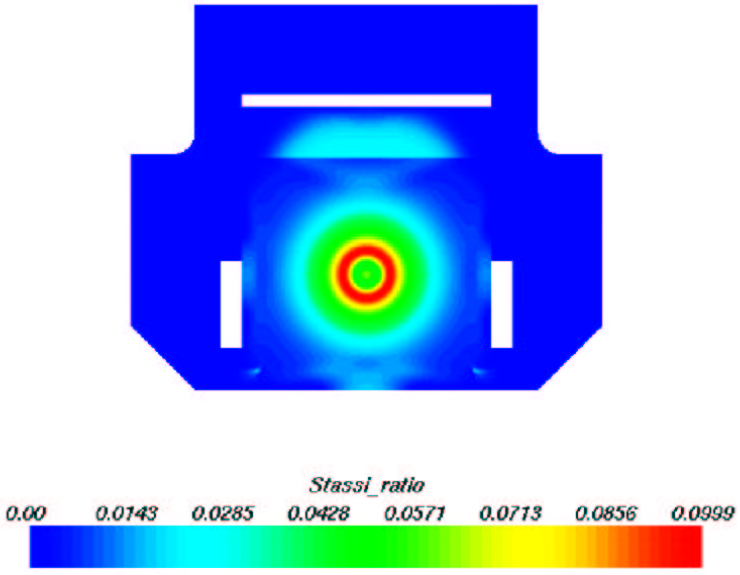

Figure 4.14: Stassi ratio

$t = 18\mu s$

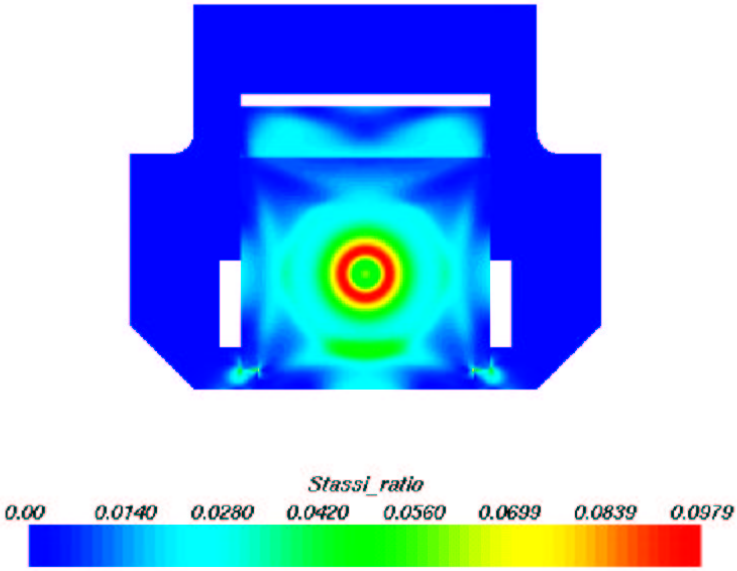

$t = 20\mu s$

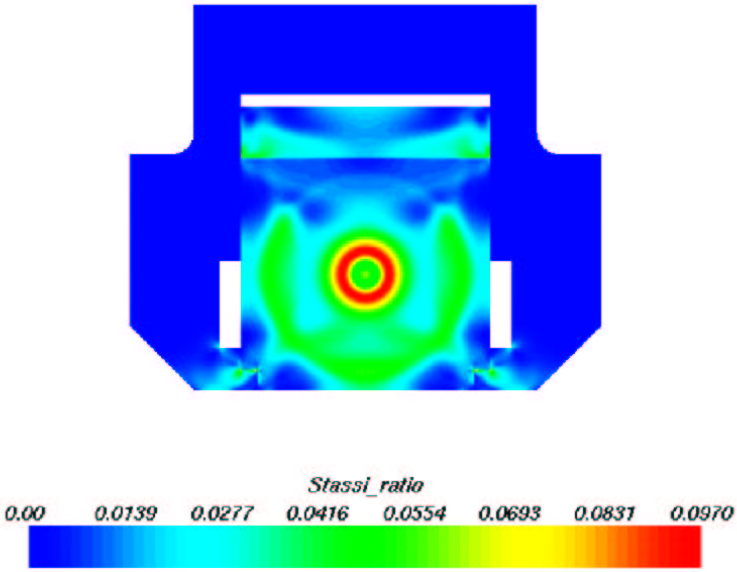

Figure 4.15: Stassi ratio

$t = 22\mu s$

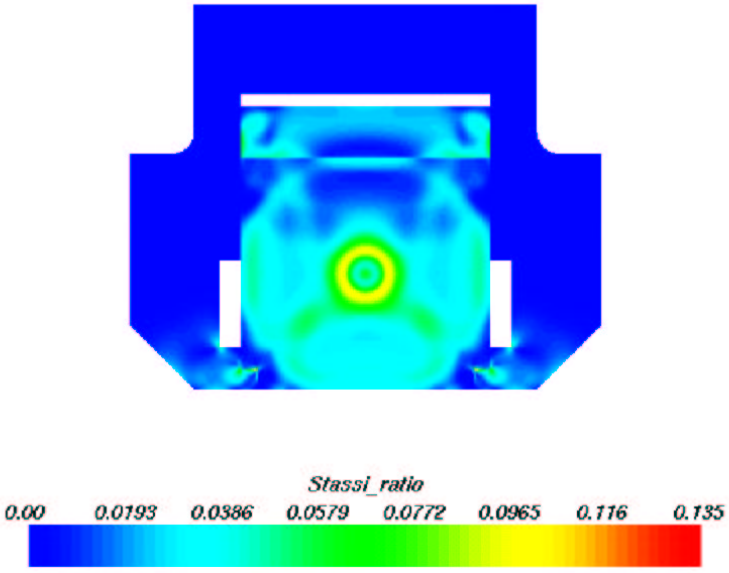

$t = 24\mu s$

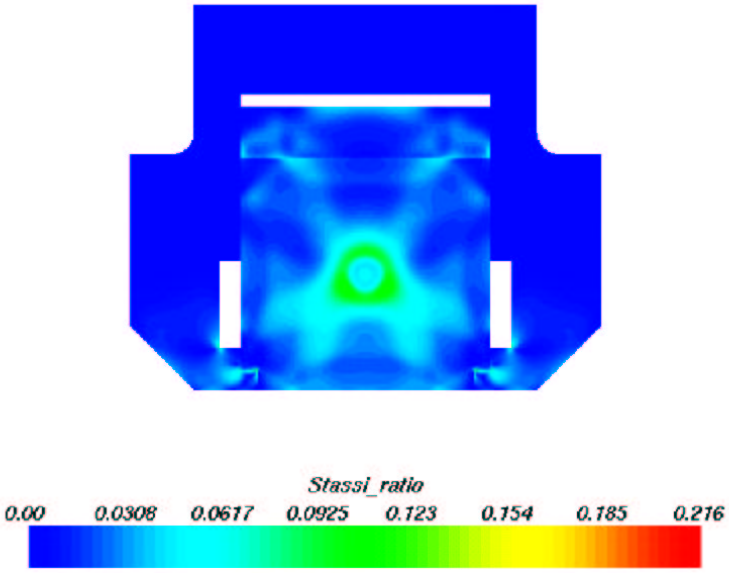

Figure 4.16: Stassi ratio

$t = 26\mu s$

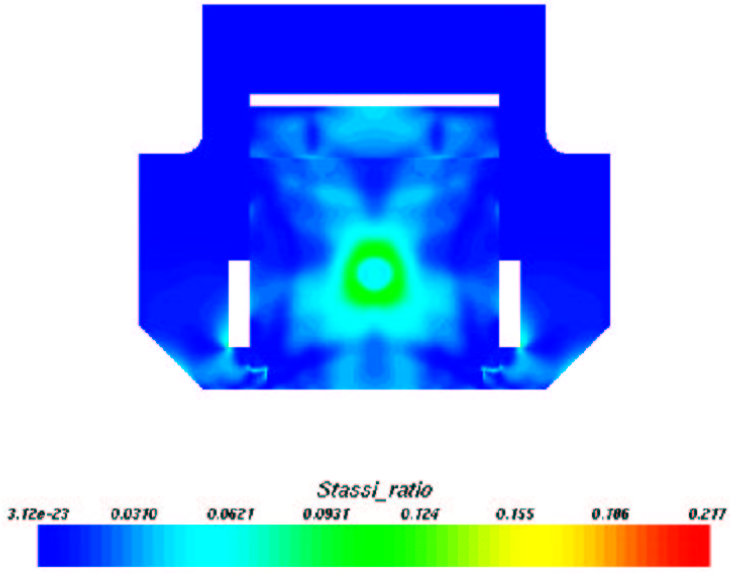

$t = 30\mu s$

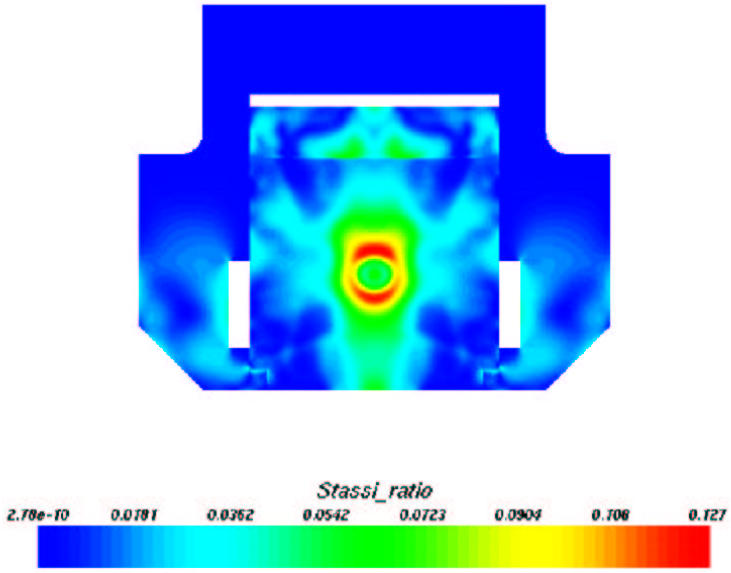

Figure 4.17: Stassi ratio

4.5 TDI 2D analysis with near surface load

In this section, we investigate the near surface load: the mesh of the TDI model is the same used in the previous section, while load conditions change.

The analyses described in the previous chapter, have shown that the beam deposition located at the center of the absorber block is not the worse one: stresses become more critical when the heated area is located near the free edge of the block.

In particular, the parametric analysis has shown that the maximum stress values are found on the free edge when the heated area center is located $3.5mm$ (1.17σ) above it. The same load conditions are applied in TDI 2D model; we want to verify if those results are still valid or if the real boundary conditions of the absorber block may lead significant changes.

Figures from 4.18 to 4.20 show the results of the simulation, in terms of the Stassi equivalent stresses. The distance of the load point from the free edge is $3.5mm$. The maximum value is 0.76 and it is concentrated in the lower edge (see the top snapshot of the Figure 4.18). This value is the same obtained in the first analyses for the semi infinite case (Figure 3.11). In the snapshots of Figure 4.19 and 4.20 it is possible to observe an increase of stresses concentrated in the edges, but the absolute value is always lower than that obtained on the lower surface at the first instants.

The propagation of the stress wave is visible too, but its intensity is limited when compared to the maximum stress concentration. The duration of the beam deposition is in fact the same and is therefore *slow* for the given the properties of the material; so the dynamic part has limited interest when compared with the static part of the stresses. This is even more evident for those results where a stress concentration, mostly static, is present on the lower face and *hides* the stresses in the rest of the structure. The stresses on the border are anyway really critic and demand a serious attention. On the basis of this simulation, with the load conditions and the adopted materials, the Stassi ratio reaches a value of 0.76, meaning that the safety factor with respect to the rupture is lower than 1.5.

We remind that these analyses do not include the longitudinal stress waves, which are expected to bring a worsening of the results.

$t = 12\mu s$

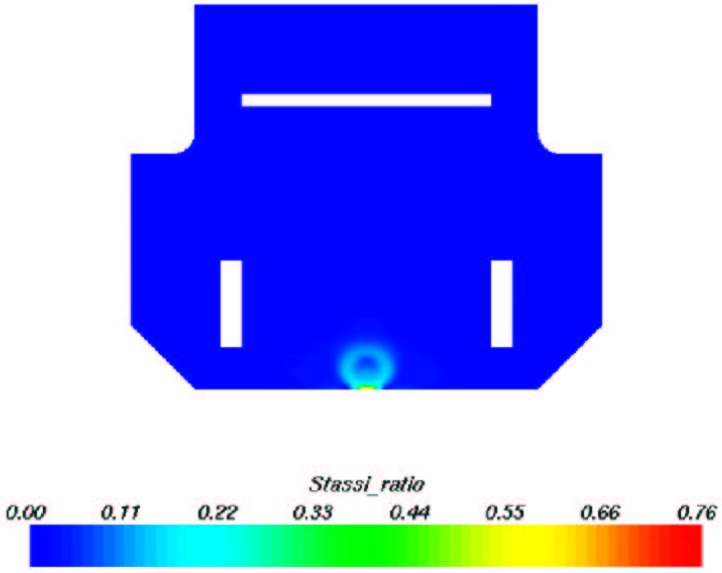

$t = 15\mu s$

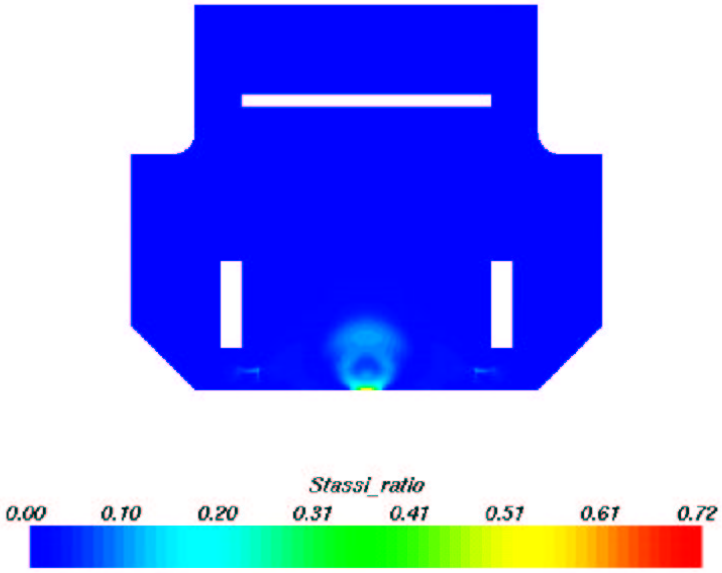

Figure 4.18: Stassi stress ratio

$t = 18\mu s$

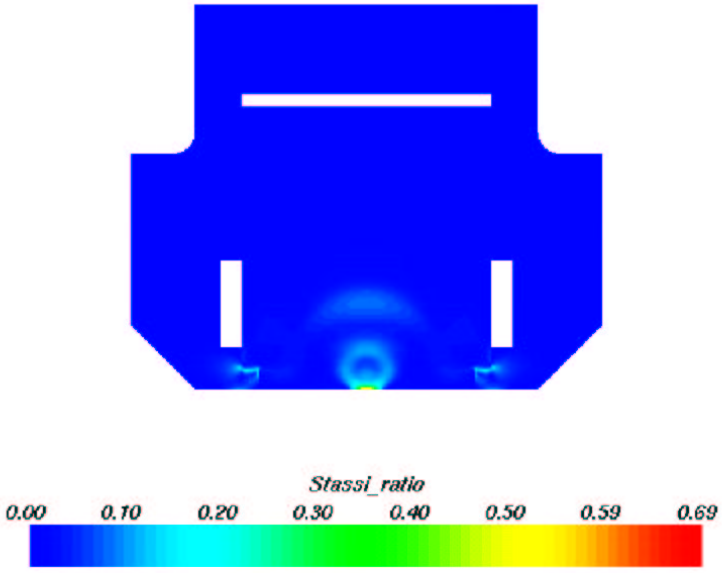

$t = 20\mu s$

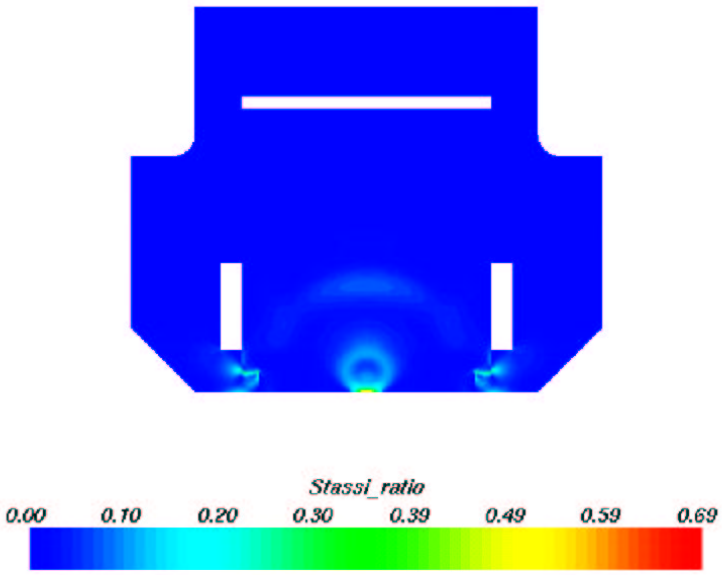

Figure 4.19: Stassi stress ratio

$t = 22\mu s$

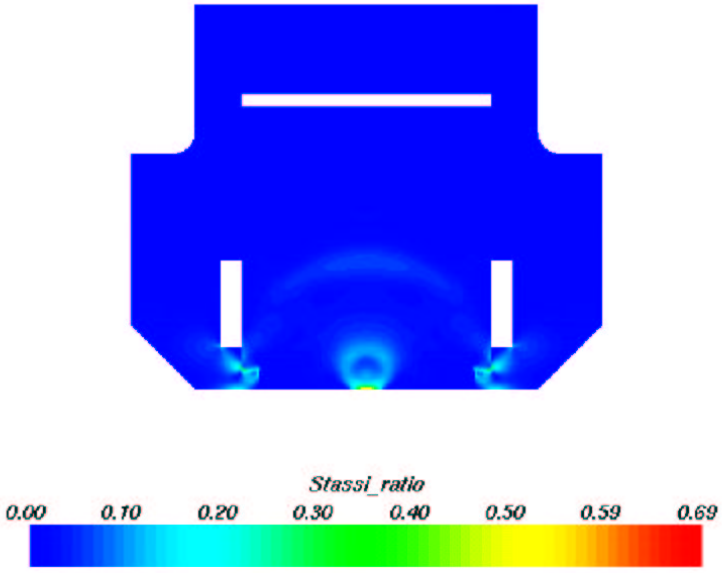

$t = 26\mu s$

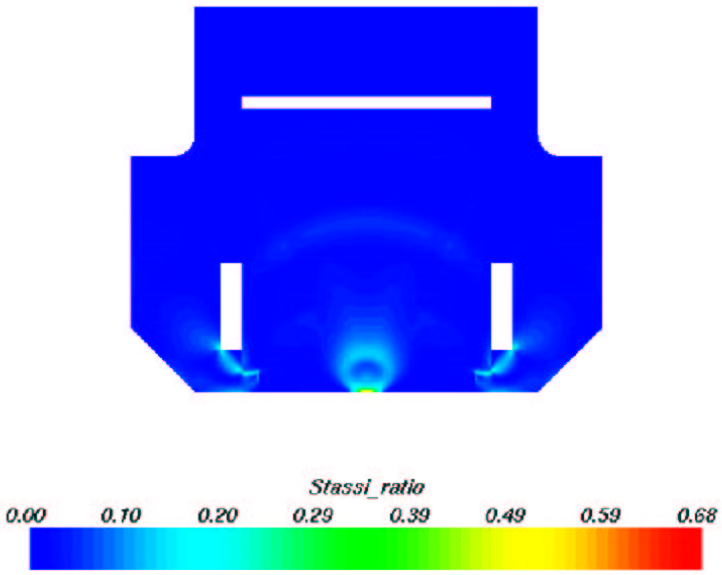

Figure 4.20: Stassi stress ratio

Chapter 5

Graphite TDI 3D analysis

5.1 Introduction

This chapter is devoted to a 3D analysis of the graphite TDI. The analysis is limited to a graphite block, since it has been agreed that in this way the energy deposited by the proton beam remains inside the absorber block; furthermore, it has been verified in the previous chapter that only the graphite block is really interested by the wave propagation and stress values inside the aluminum jaw and the copper top are negligible.

Properties of the standard graphite and the thermal load have been already introduced. In these 3D analyses a temperature increase is a priori imposed (no thermal problem is solved), with temperature constant along the z axis. The temperature enjoys the same time function and a value constant along the z direction, as in the previous chapters.

Since the finite length in z direction is the main difference respect to TDI 2D analyses, it is interesting to highlight the behavior in this direction. Initially, some tests are made to identify the grid size bringing the optimal ratio between accuracy and computational effort.

5.2 Symmetry conditions check

This first analysis refers to a test model with the same section of the previous examples and a length fixed to a value of $20mm$, due to a preliminary design. The analysis was run with a low spectral degree with the aim of verifying the validity of some approximations, rather than obtaining accurate results. All the external surfaces are supposed to be free from any imposed boundary condition, so that the energy arising from the interaction with the proton beam is kept inside the absorber block.

Figure 5.1 shows the grid of the model. The model is $58 \times 54 \times 20mm^3$, and the element size is $1mm$ along x and y and $5mm$ along z. The spectral degree is equal to 1, and the number of elements and nodes are 12368 and 16025, respectively. The blue portion of the block indicate the zone where material properties are varying with temperature.

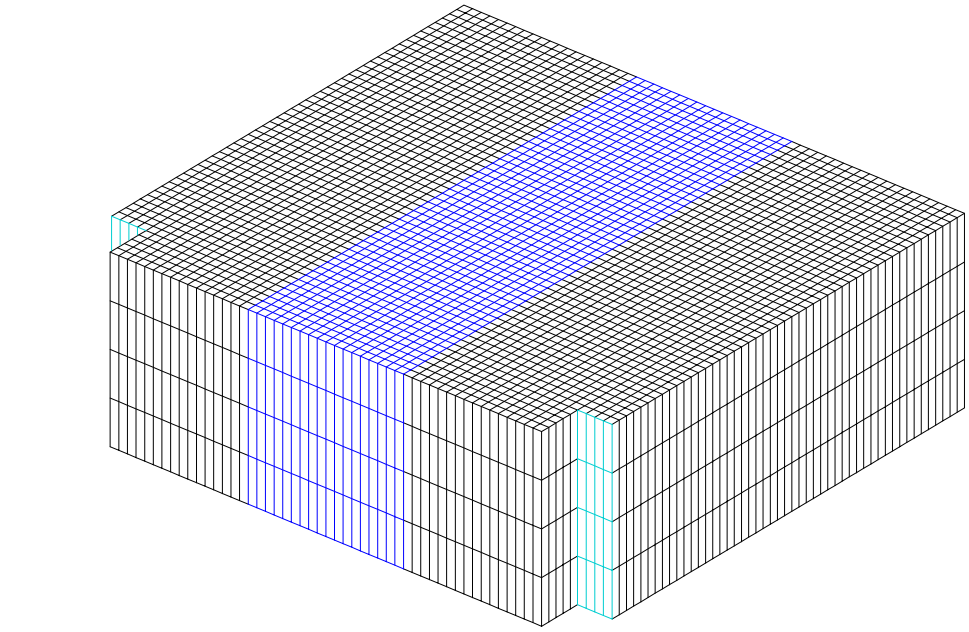

Figure 5.1: TDI 3D grid

Figures 5.2 and 5.3 show the simulation results. More precisely, the first one displays the Stassi stress ratio at $t = 15\mu s$ in the external surface and in a centered section lying in the yz plane; in the second one the Stassi stress ratio in x direction for different z values are reported.

As clearly suggested from the figures, an higher spectral degree would be preferable when running a real test.

The structure under exam is characterized by a symmetry along two planes: the central section of the block perpendicular to the z axis and the vertical plane passing through the center of the section and normal to x axis. Again, the boundary conditions are symmetric with respect to the afore mentioned planes, as well as the thermal load. A reduction of problem's unknowns may thus be obtained exploiting the symmetry in x and in z direction: this is made in the next tests. Here the complete model is analyzed to check the validity of this assumption.

It turns out that this approximation works fine, as graphically evident in Figure 5.2, and more in detail in the graphs of Figure 5.3: the results are clearly symmetric with respect to r and to the plane at $z = 10mm$.

From these first simulations it is evident that the stresses in the frontal and rear free surfaces are higher than those on the center, where we may assume that the plane strain conditions are approximately verified; evidence of a longitudinal stress wave is being given in the following tests.

5.3 Non uniform mesh check

A second test is made to verify if adopting a non isotropic mesh density would lead to a worsening in the quality of the results.

The model studied represents one quarter of the whole structure; the material adopted is graphite with the standard properties of the first chapter, and the imposed thermal load has a gaussian profile on any x-y section and is constant along the z axis.

When the first analyses on a 2D plane structure were presented, it was discussed how the mean dimension of the temperature distribution profile and the time scales of energy deposition may influence the choice of the element mean size and the spectral degree. Since the temperature profile is assumed constant along the z axis, it is therefore possible to reduce the number of unknowns by selecting a non uniform mesh with element mean size higher in the z direction. Results obtained with the uniform mesh will be compared with those obtained with a coarser mesh.

In the Figure 5.4, the two grids are shown. The models have the same dimensions, $29 \times 27 \times 23.5mm^3$, and symmetry conditions in the light blue surface (yz plane) and in the red surface (xy plane). Free surface conditions are applied to the external surfaces of the model. The simulation is made, for both cases, using a spectral degree equal to 3.

The first grid is almost uniform, every element is $2 \times 2 \times 2.14mm^3$ (slightly longer in the z direction). The elements are 2926 and the spectral nodes are 118660. For the

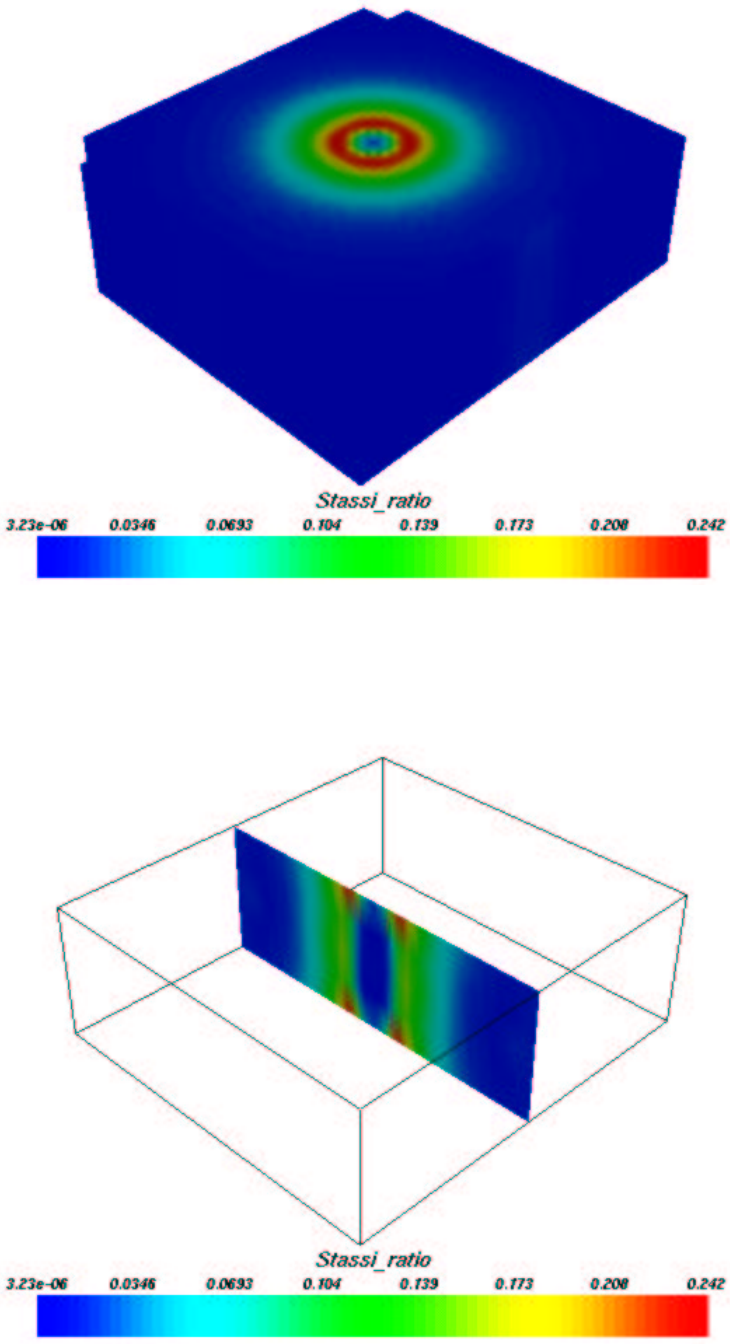

Figure 5.2: Stassi stress ratio at $t = 15\mu s$

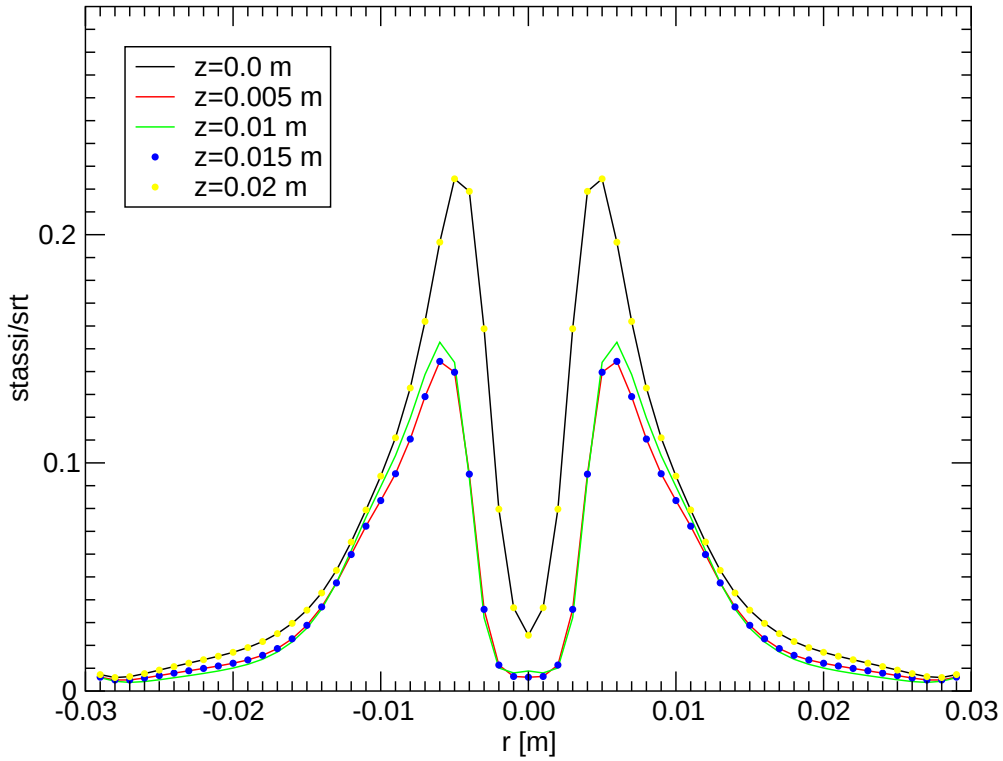

Figure 5.3: Stassi stress ratio at $t = 15\mu s$ and for different z values

second grid, every element is $2 \times 2 \times 4.7mm^3$, the number of elements is 1330 and the spectral nodes are 55840.

In the Figure 5.5 the snapshots of Stassi stress ratio at $t = 10\mu s$ are shown. The differences between the two results are negligible and the stress values are quite similar. In the Figure 5.6 the z component of the displacement in z direction in different instants is shown.

From these comparisons, it is possible to conclude that the use of a grid with double element size in z direction with respect to the mean element size in the section plane is reasonable: the results of the uniform and coarser grids are similar, but the latter model may be preferred due to the lower CPU time and memory requirement.

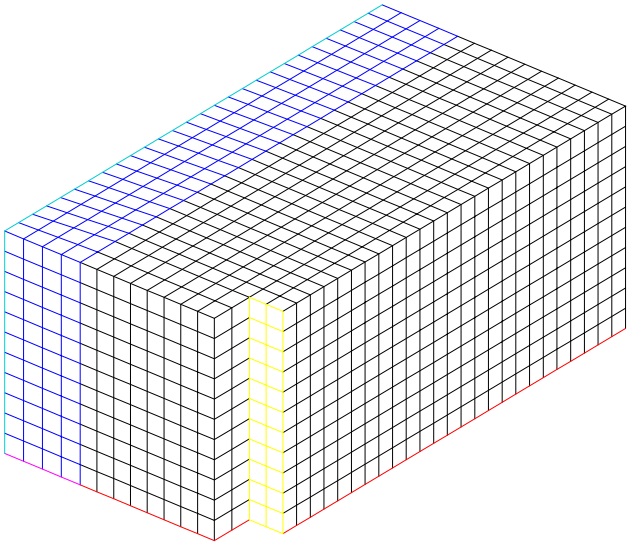

GIBI FECIT

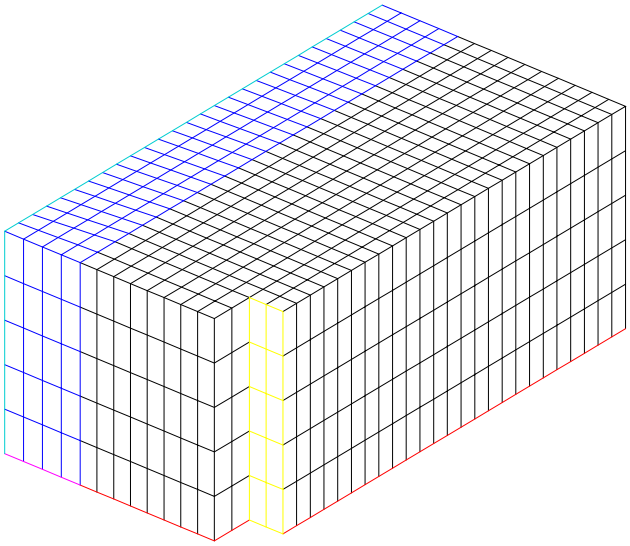

GIBI FECIT

Figure 5.4: Model with 11 and 5 elements in z direction, respectively

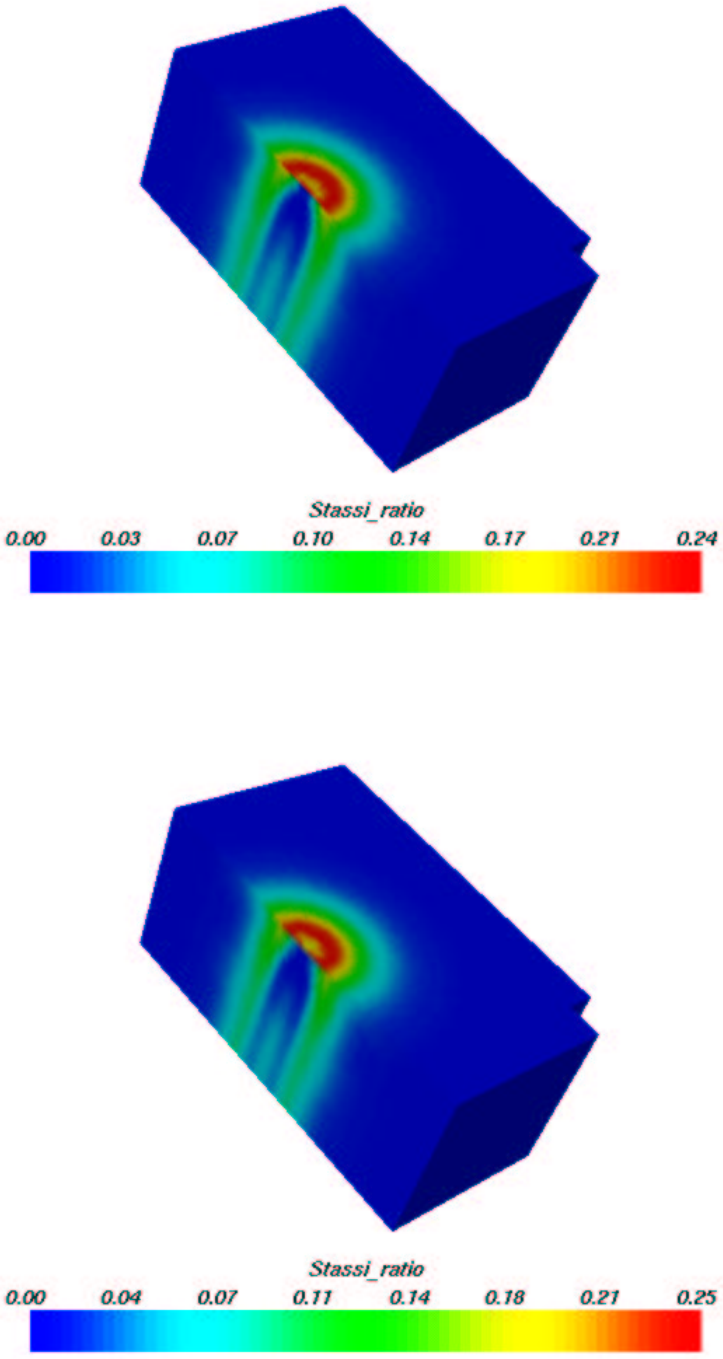

Figure 5.5: Snapshots of Stassi stress ratio for the model with 11 and 5 elements in z direction

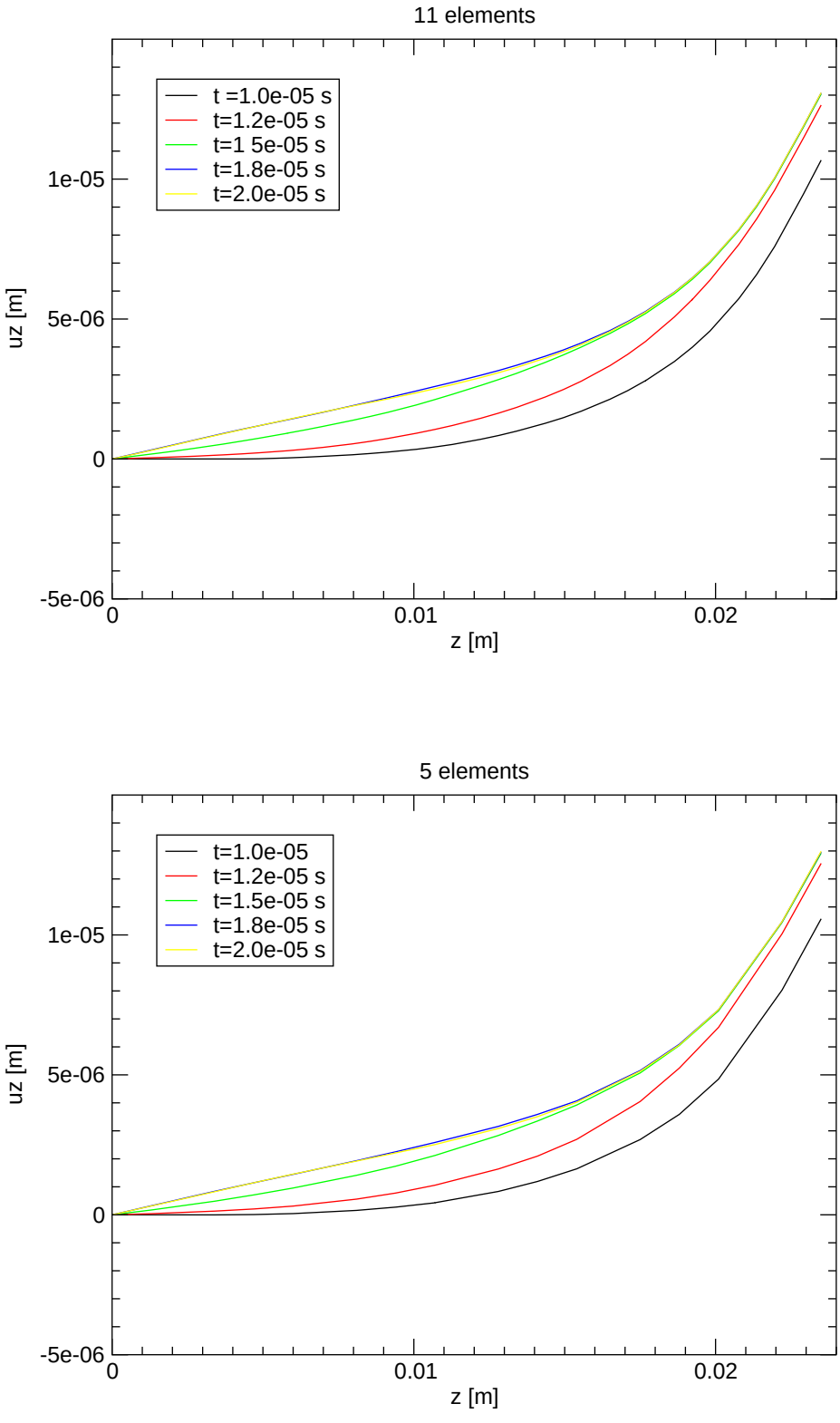

Figure 5.6: z component of displacement in z direction in different instants

5.4 Graphite block 3D analysis

According to the results shown in the previous paragraph, the non uniform grid has been selected for the 3D analysis of the graphite absorber block. The block is $58mm$ wide and $54mm$ high (the section is not perfectly rectangular); the thickness of the block is $47.3mm$.

Symmetry conditions are adopted: one quarter of the structure is analyzed and suitable boundary conditions are imposed on the xy section located at the middle of the block, and on the yz plane passing through the center and containing the beam axis. As usual, z axis does coincide with the proton beam, the y axis is vertical and x direction horizontal.

Several colors indicate different formulations adopted in different areas of the grid: temperature variable properties are adopted for the elements shown in blue, whereas constant with temperature properties are used for the elements shown in black. The second ones are obviously more efficient on the computational side.

A temperature variation is imposed first on the center of the block, with the following law:

$$\theta(\mathbf{x}, t) = \theta_M e^{-b((x-x_0)^2+(y-y_0)^2)} g(t) \tag{5.1}$$

where θ_M is the maximum temperature increase $\theta_M = 635°C$, (x_0, y_0) is the center of the heated area and $g(t)$ gives the variation of temperature in time, the parameter $b = 0.106 \cdot 10^6 m^{-2}$ corresponds to $\sigma \cong 3mm$. The temperature is initially equal to zero until time $t = 2.14\mu s$, then its value grows linearly to reach the maximum at $10.0\mu s$. This law approximates the deposition of the energy of four batches of protons, as an impulse of finite length $\Delta t_{bd} = 7.86\mu s$.

In Figures from 5.7 to 5.14, kinetic energy is displayed on the cross section in the middle of the block, corresponding to the back surface of the model. Figures from 5.15 to 5.22 show kinetic energy density with a view of the external front surface and the longitudinal section.

On the middle section, it is possible to recognize the same behavior found in the 2D analyses commented previously. Figure 5.7 and 5.8 show snapshots of the time interval in which temperature is growing to reach its maximum at $10.0\mu s$. Here, the rise and propagation of a cylindrical wave are clearly visible, with a wavefront leaving the center of the structure at the beginning of the energy deposition, at $t = 2.14\mu s$.

In the Figures 5.9 through 5.14 the wave propagates inside the structure reaching the external reflecting borders, with a behavior's that is very similar to that found in the 2D analyses, as expected. The legend of the color plot is kept constant for all the snapshots, while this was not possible for Figures from 5.15 to 5.22, due to extremely variable energy range.

These figures exhibit a phenomenon not arguable from a 2D analysis: the propagation of a longitudinal wave in the block. Figures from 5.15 to 5.16 show how the central part of the front surface is subjected to an increase of the kinetic energy during the

beam dump; after that, a longitudinal, almost hemispherical, wave departs. As visible in pictures taken after $t = 10\mu s$, the radius of this wavefront seems comparable to that of the in-plane circular wave.

The cylindrical wave propagating radially and the hemispherical wave superpose, resulting in higher energy densities that are evident in the front surface.

Figures 5.23 through 5.27 show the Von Mises stress in the central section of the graphite absorber block. The stress pattern is similar to that found in the 2D analyses: it has an axial symmetry with respect to the center of the block where the heated region is located, reaches its maximum at the center of this region, and gradually decreases to zero. The value at the center gradually rises up to $t = 12.0\mu s$. It is interesting to note that no wave propagation is visible by the analysis of these pictures only: the dynamic effects on the stresses are limited, since the stress configuration is dominated by its static part, at least for this central section.

Figures from 5.28 to 5.32, showing the equivalent stress on the front surface and on the longitudinal section, put in evidence different stress distributions with lower values on the axis of the beam. The stress value grows with the temperature and reaches its maximum at $t = 12\mu s$. It is interesting to notice that the maximum is still on the central section. From the kinetic energy results it was shown how the maximum densities are reached on the front surface, therefore it is not surprising to see that this time a stress wave propagation is visible in terms of Von Mises equivalent stress, on the front surface, especially in the Figure 5.31.

Similar analyses can be made on the pressure results. It is shown for the central section in Figures 5.33 - 5.37: it has a very sharp distribution around the beam axis, with a maximum at $t = 12.0\mu s$. This time, a pressure circular wave departing from the center is visible (especially in Figures 5.34 and 5.35) corresponding to the stress wave generated by the beginning of the temperature rise at $t = 2.14\mu s$ and reaching the lateral surface at $t = 14.0\mu s$; a second pressure wavefront, with opposite phase, originates at $t = 10.0\mu s$ and is visible in Figures 5.35 and 5.36.

Figures from 5.38 to 5.42 show pressure values on longitudinal section and front surface. The results are similar to those discussed previously for the central section; the pressure value is maximum on the beam axis and decreases rapidly with the radius. Pressure waves are visible on the longitudinal section and also on the front surface, giving a view of the cylindrical waves propagating from the beam axis. The pressure decreases rapidly when reaching the front surface where, due to the boundary conditions adopted, only plane stresses are present. This can lead to a misunderstanding on the concept of pressure, here intended as an internal pressure equal to one third of the first invariant of the stress tensor, giving a measure of the state of stress immediately under the surface. On the center of the front surface the material is pull out by the thermal expansion in the beam axis, high value of the stress components in the plane of the front surface should therefore be present around that area, as visible in the plots of the equivalent stress.

The material adopted has different values of the compressive and tensile strength:

this is accounted for by the Stassi equivalent stress. The Figures from 5.43 to 5.50 give the results of the ratio of the Stassi tensile equivalent stress with the tensile rupture stress, for the points of the central section of the absorber block. These results are similar to those found with the 2D analysis: the stress wave is visible, but the Stassi ratio is almost constant in this section, with the maximum in the annular area around the axis center.

Figures 5.51 through 5.58 show that a stress increment is present on the front surface, as expected, and is maximum on the area around beam axis where the material is forced to pull out, for $t \cong 12.0\mu s$ (see Figure 5.53). The stress wave is not clearly visible on the front surface but is more evident inside the material, in the section plane in particular, as shown in Figure 5.54.

The analysis of this 3D model suggests that the most critical portions of the structure - in this load - condition are the front and rear surfaces of the block near the beam axis, where the Stassi equivalent ratio reaches values clearly superior than those found on the central section and in the previous 2D tests. Even higher values may be expected when the beam hits the block near its lower surface. The analysis of the results of this simulation therefore suggests a change in the design of the absorber block, and/or in the material adopted for its construction.

$t = 4\mu s$

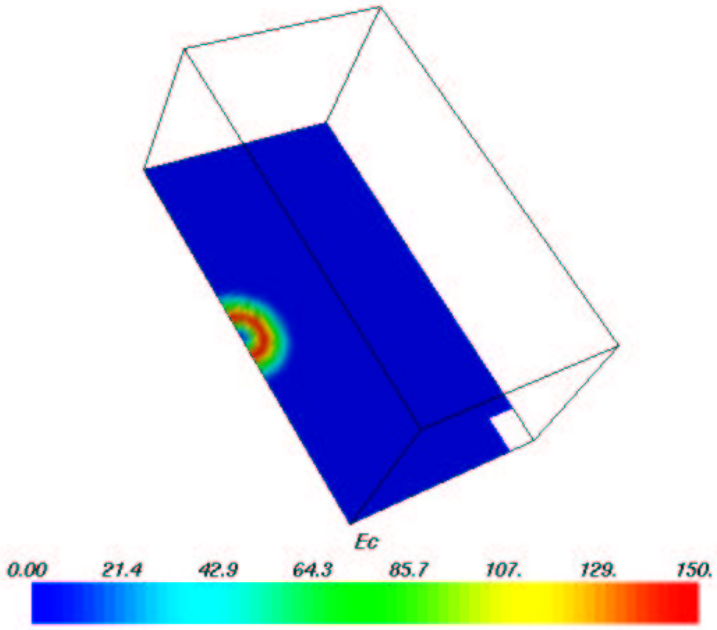

$t = 6\mu s$

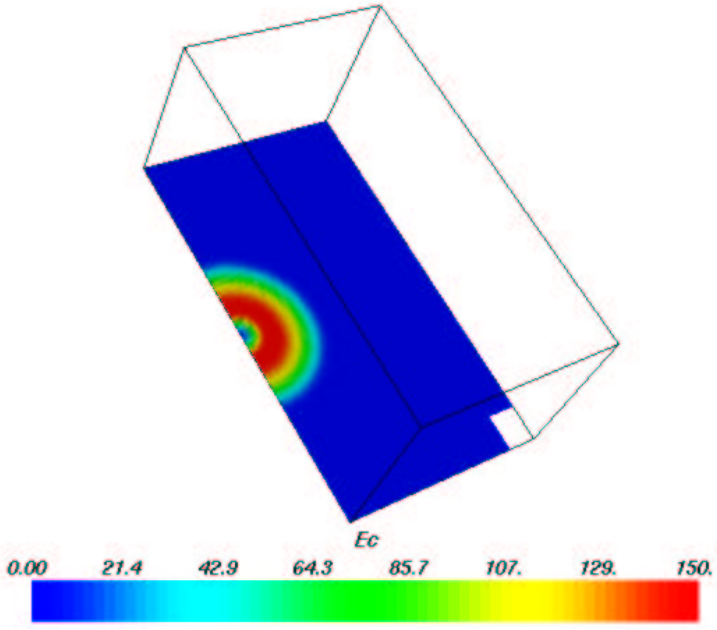

Figure 5.7: Kinetic energy density on the central section $[J/m^3]$

$t = 8\mu s$

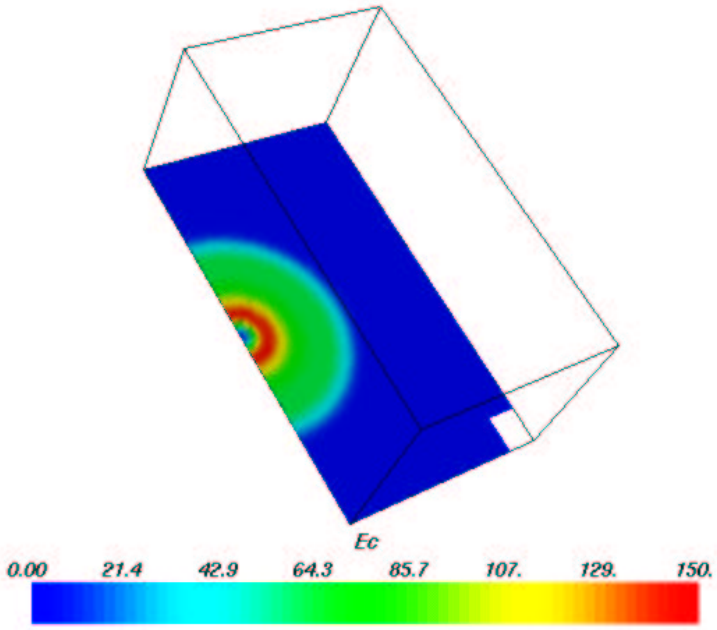

$t = 10\mu s$

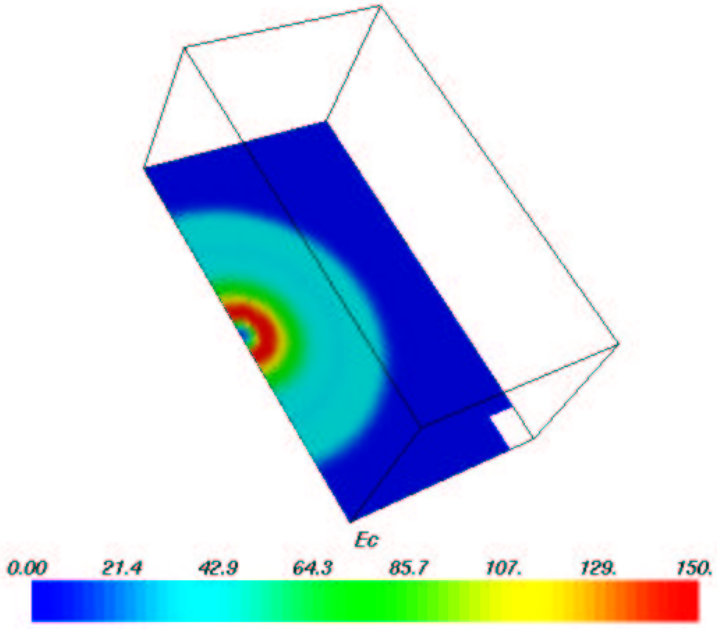

Figure 5.8: Kinetic energy density on the central section $[J/m^3]$

$t = 12\mu s$

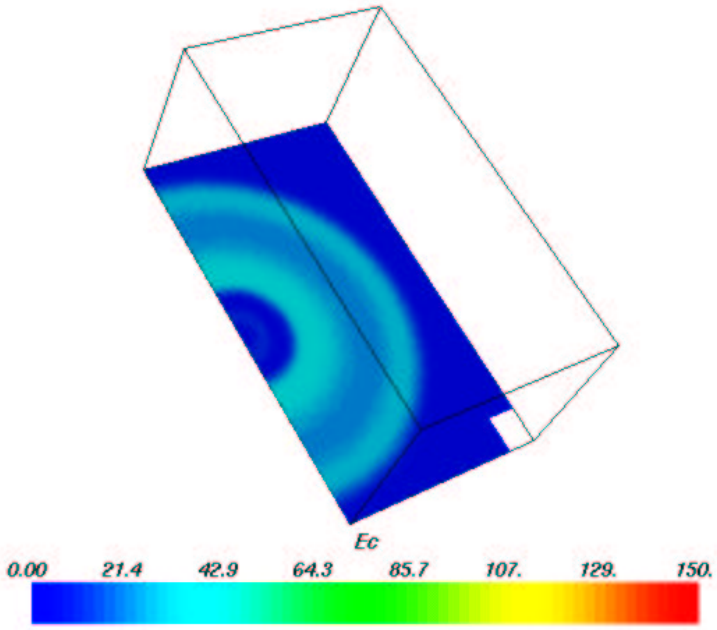

$t = 14\mu s$

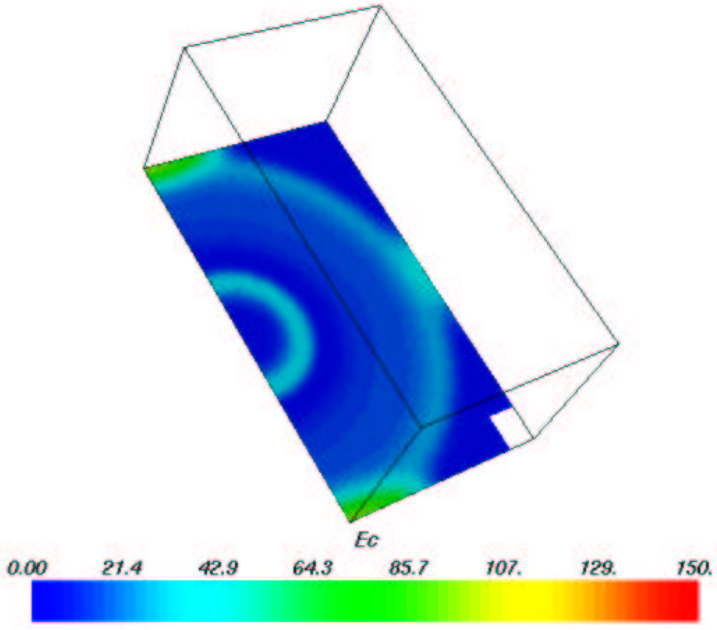

Figure 5.9: Kinetic energy density on the central section $[J/m^3]$

$t = 16\mu s$

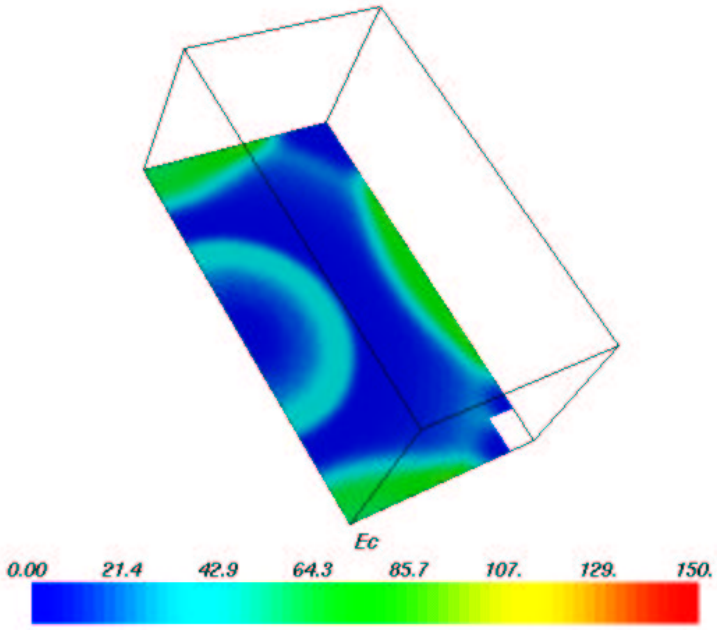

$t = 18\mu s$

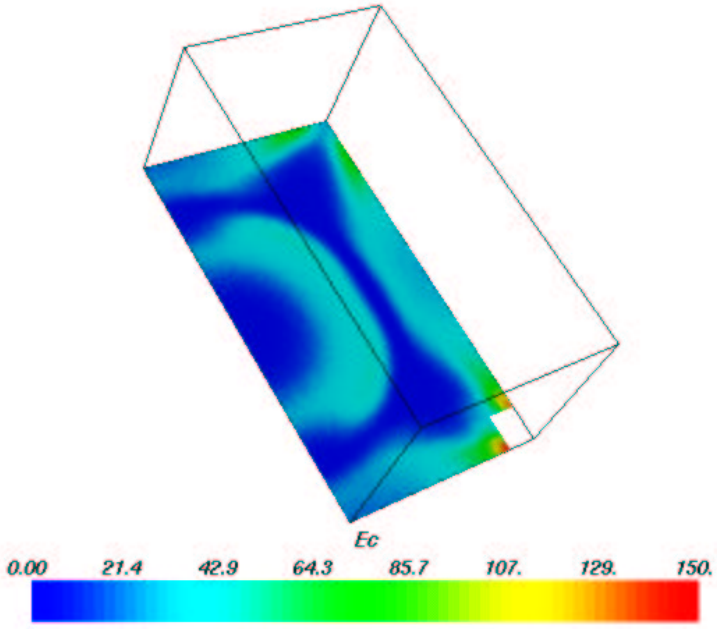

Figure 5.10: Kinetic energy density on the central section $[J/m^3]$

$t = 20\mu s$

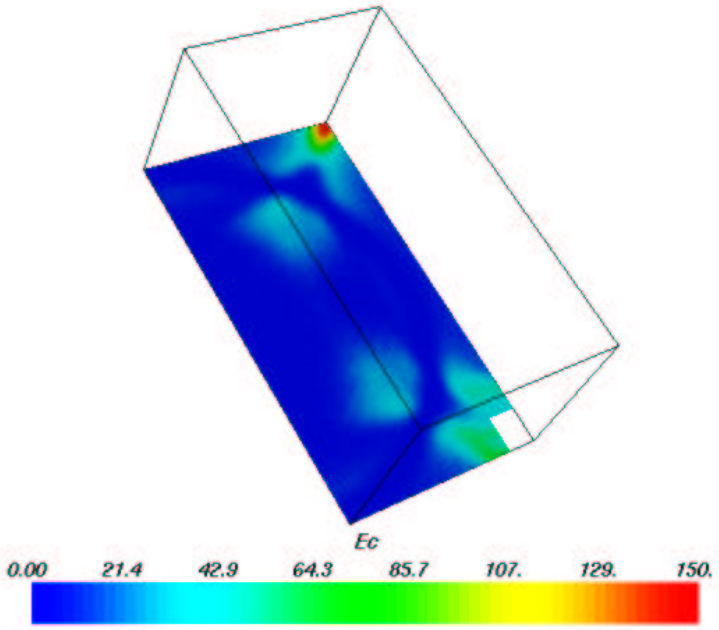

$t = 22\mu s$

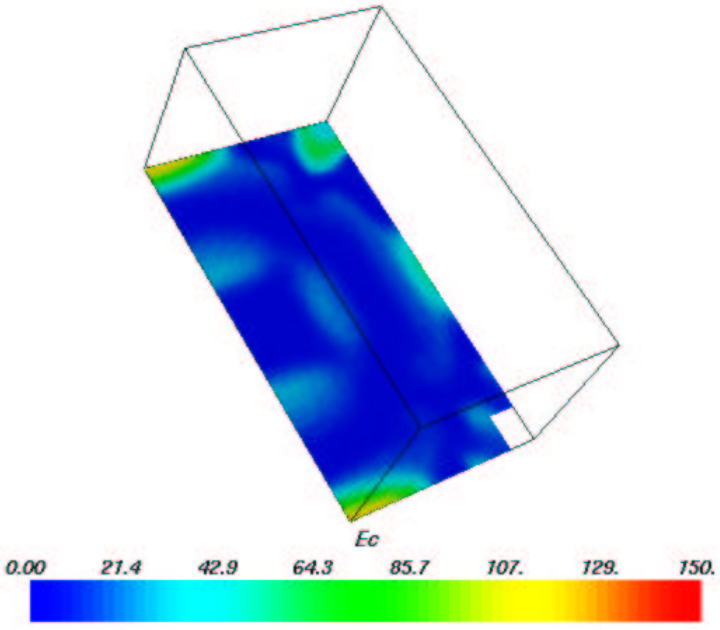

Figure 5.11: Kinetic energy density on the central section $[J/m^3]$

$t = 24\mu s$

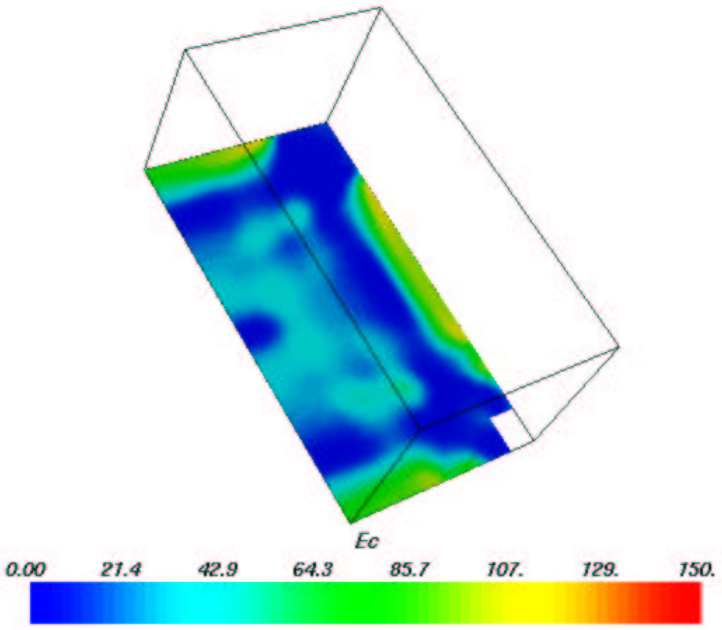

$t = 26\mu s$

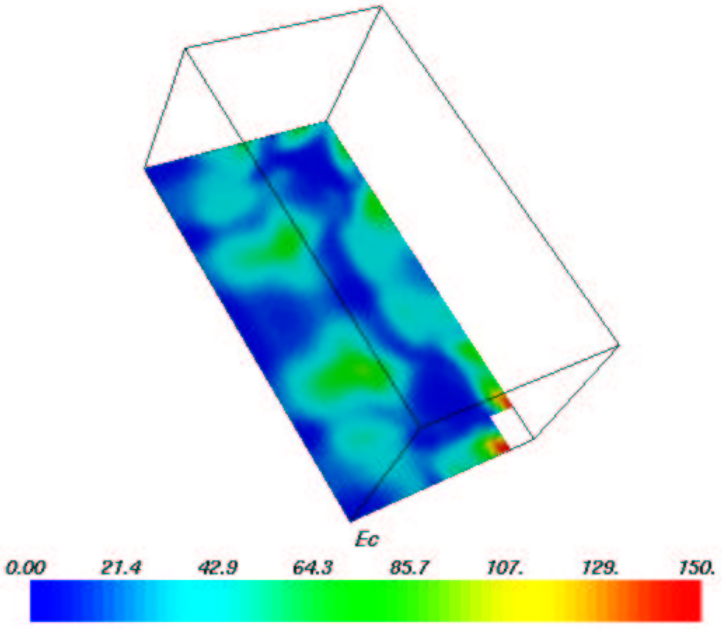

Figure 5.12: Kinetic energy density on the central section $[J/m^3]$

$t = 28\mu s$

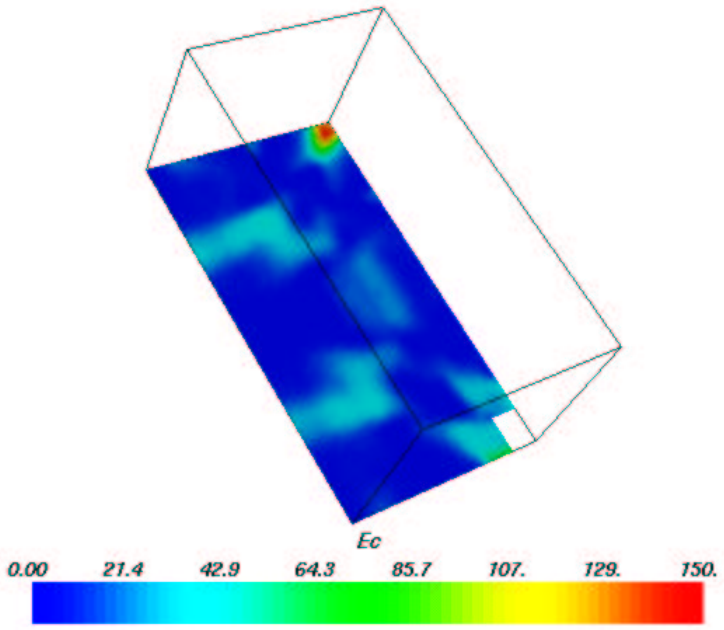

$t = 30\mu s$

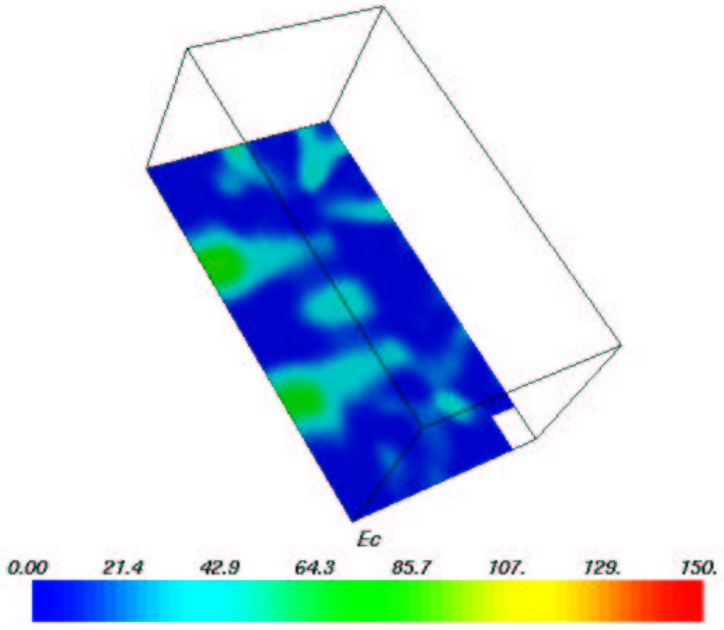

Figure 5.13: Kinetic energy density on the central section $[J/m^3]$

$t = 35\mu s$

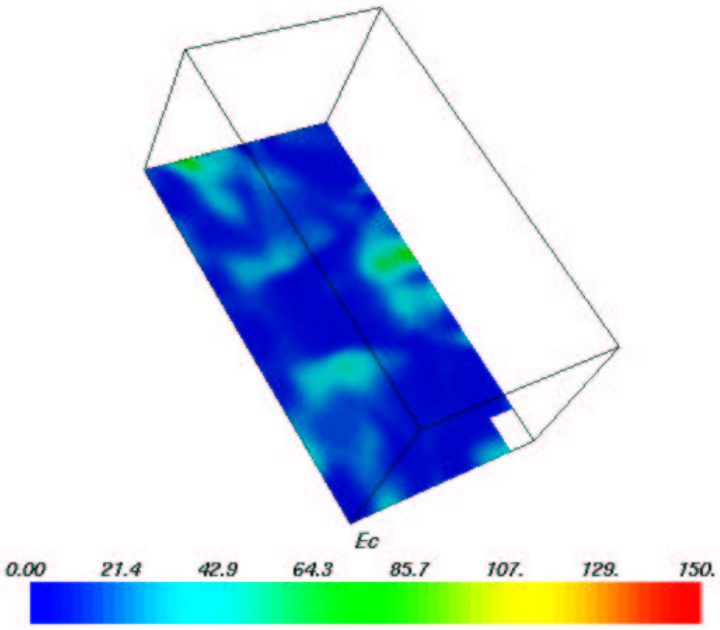

$t = 40\mu s$

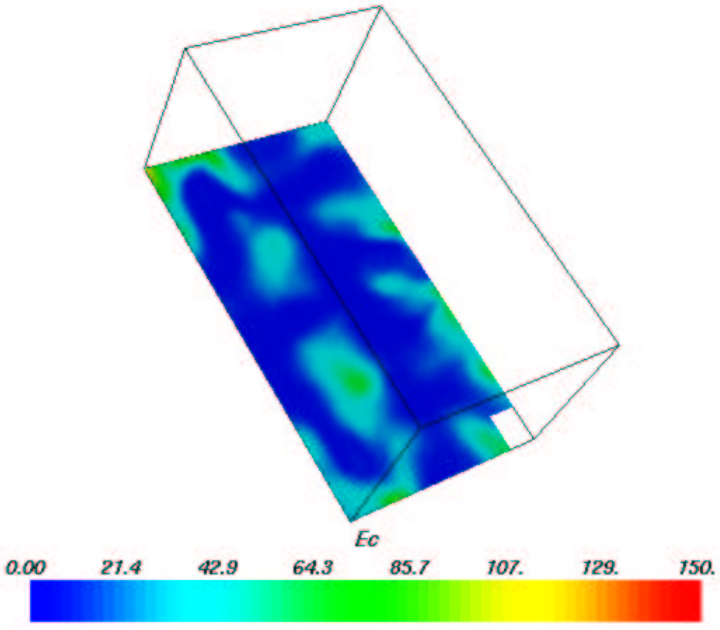

Figure 5.14: Kinetic energy density on the central section $[J/m^3]$

$t = 4\mu s$

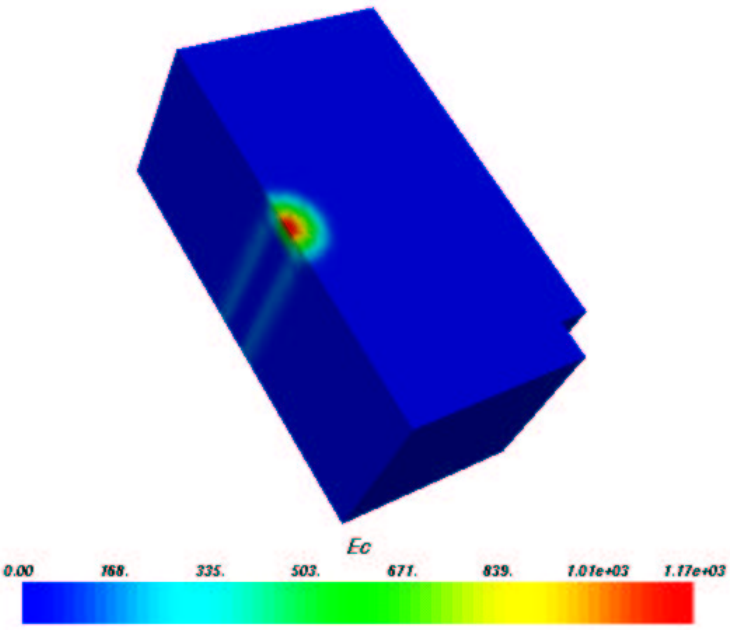

$t = 6\mu s$

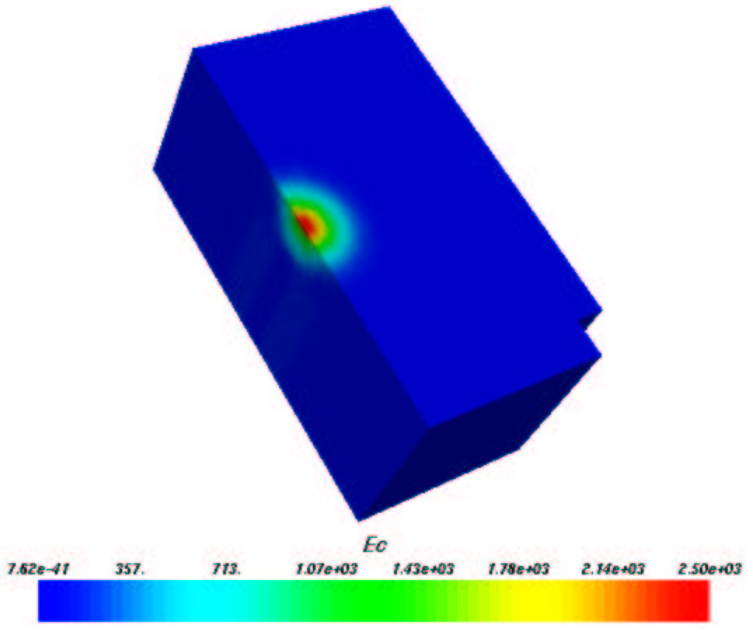

Figure 5.15: Kinetic energy density on the outside surface $[J/m^3]$

$t = 8\mu s$

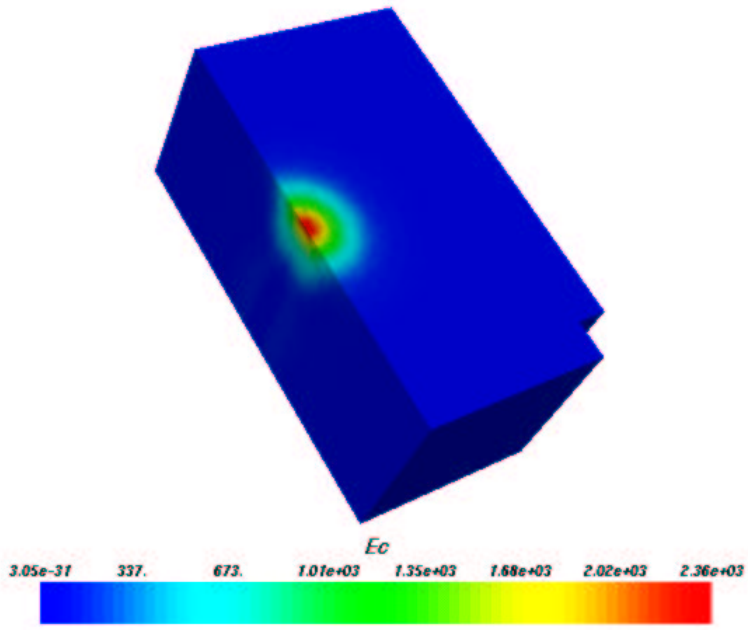

$t = 10\mu s$

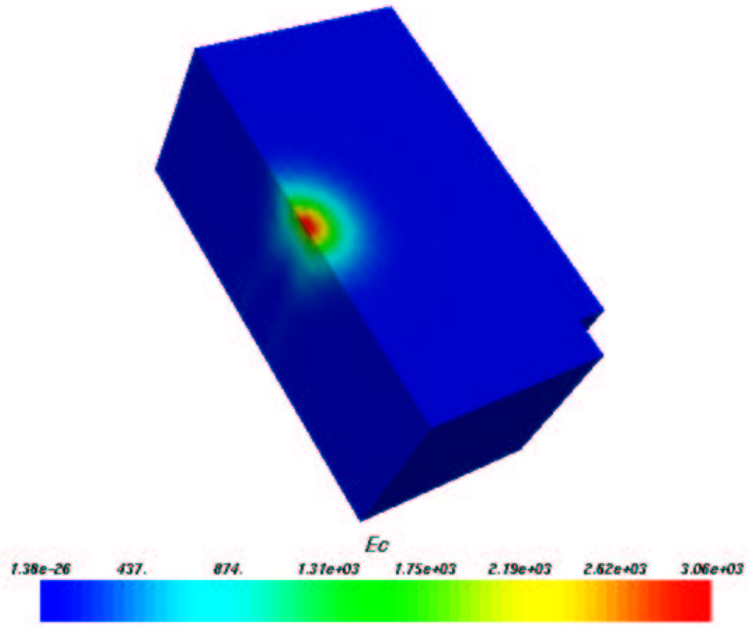

Figure 5.16: Kinetic energy density on the outside surface $[J/m^3]$

$t = 12\mu s$

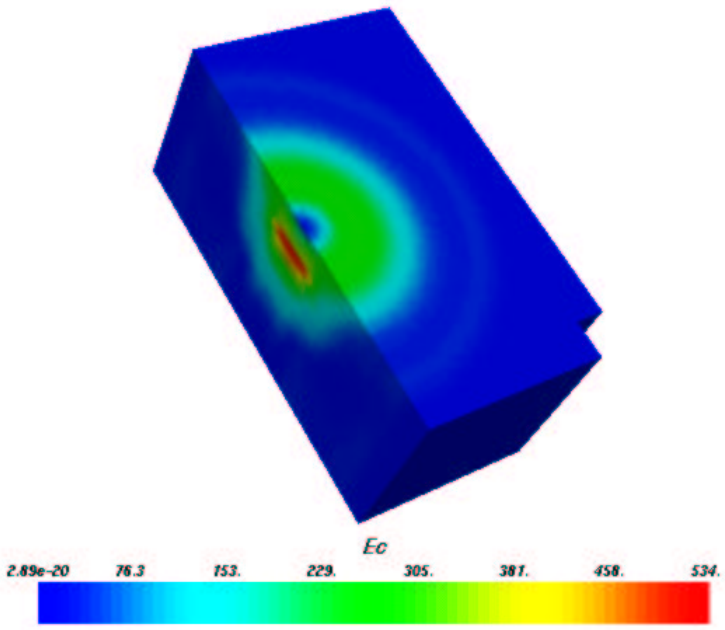

$t = 14\mu s$

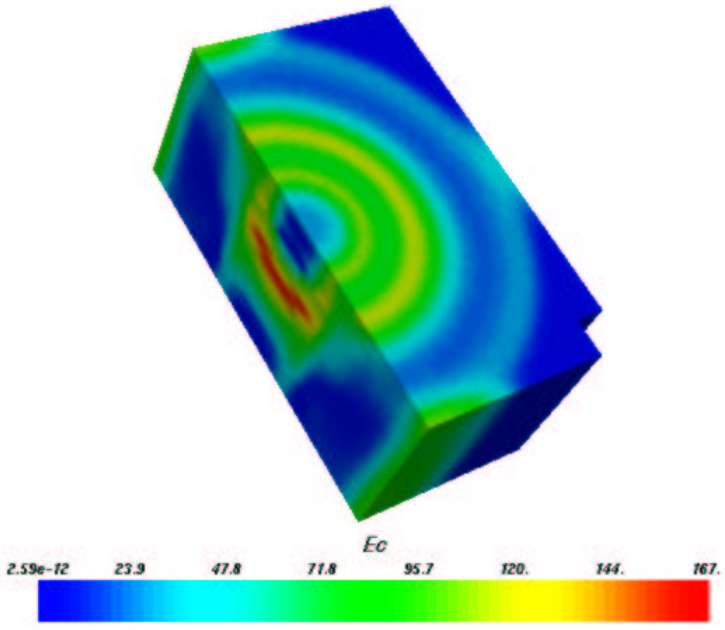

Figure 5.17: Kinetic energy density on the outside surface $[J/m^3]$

$t = 16\mu s$

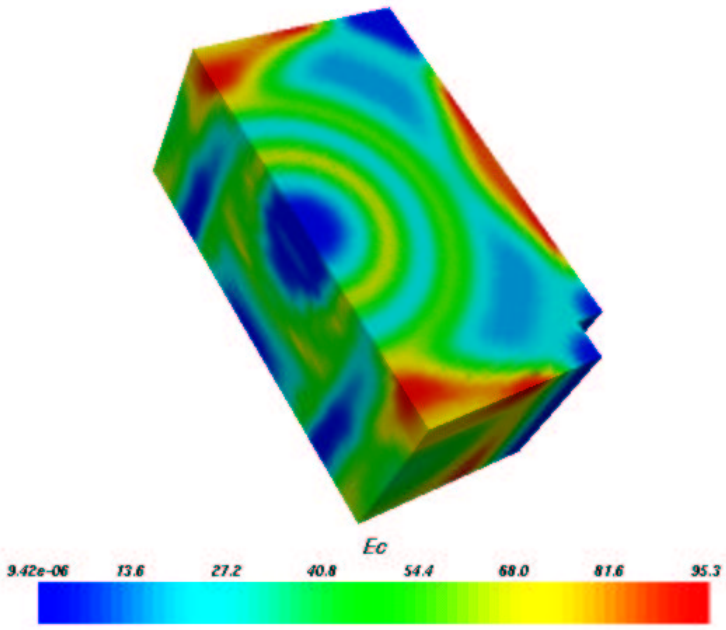

$t = 18\mu s$

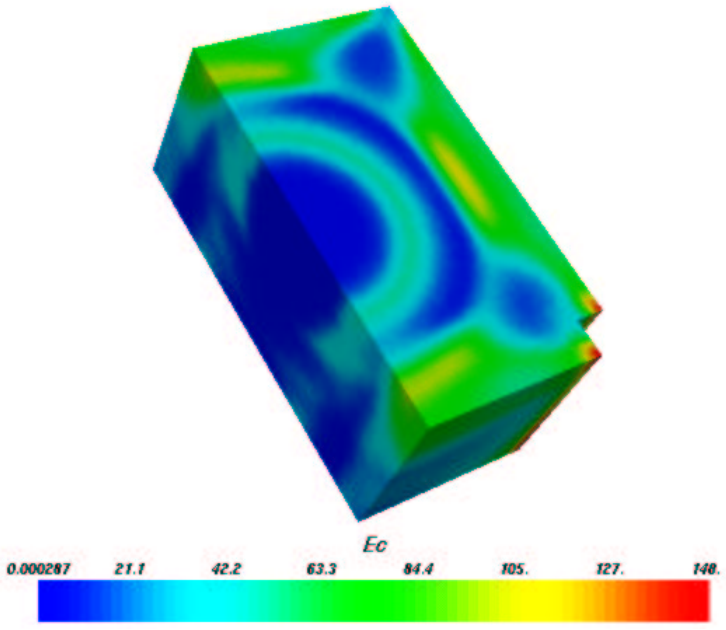

Figure 5.18: Kinetic energy density on the outside surface $[J/m^3]$

$t = 20\mu s$

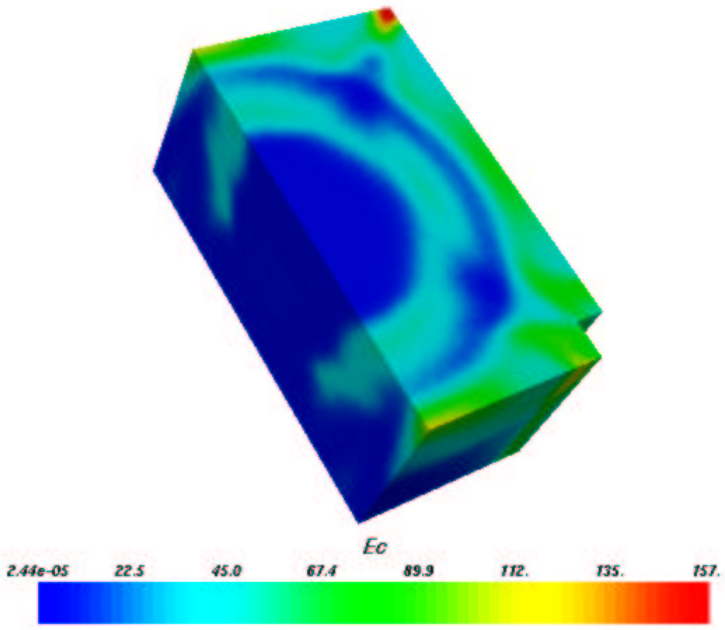

$t = 22\mu s$

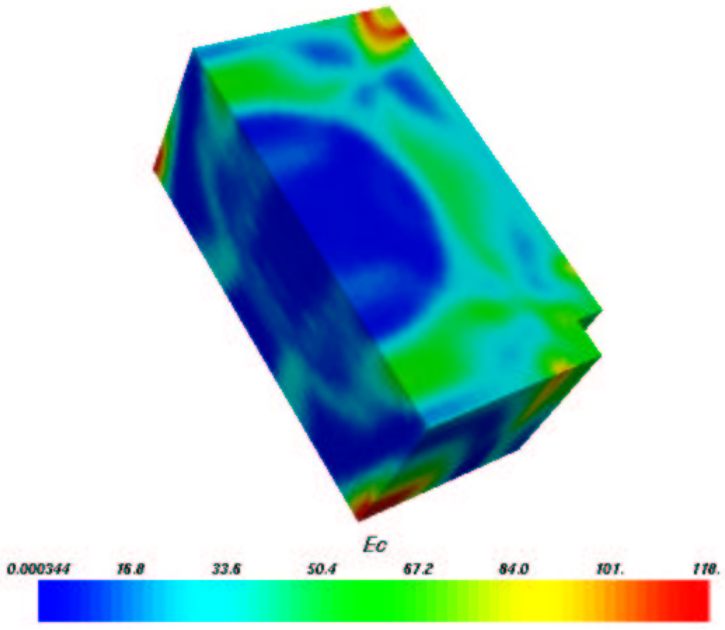

Figure 5.19: Kinetic energy density on the outside surface [J/m^3]

$t = 24\mu s$

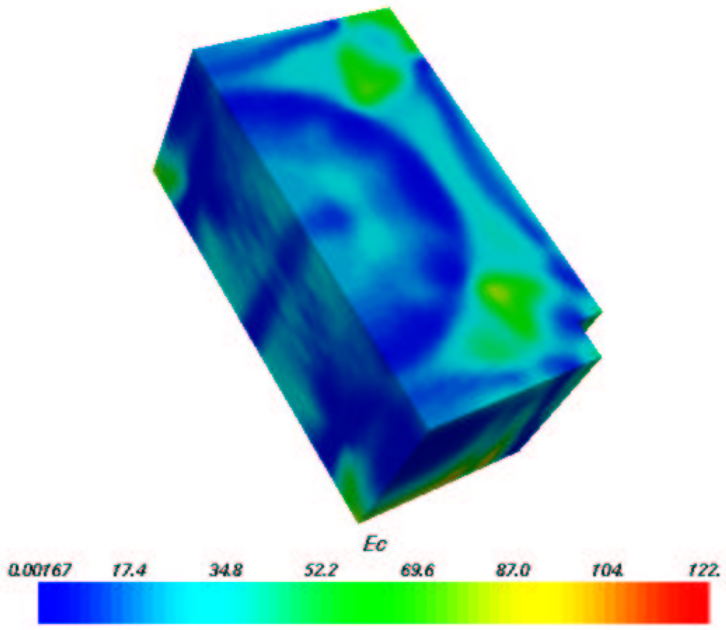

$t = 26\mu s$

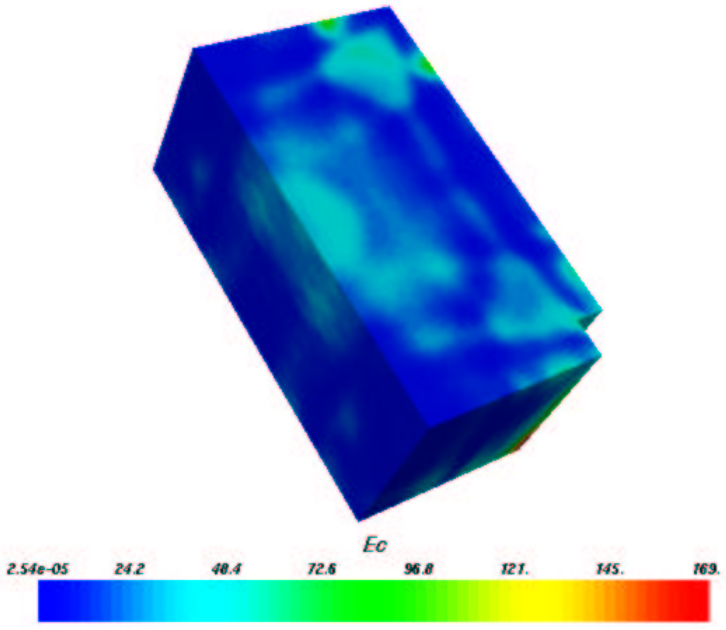

Figure 5.20: Kinetic energy density on the outside surface [J/m^3]

$t = 28\mu s$

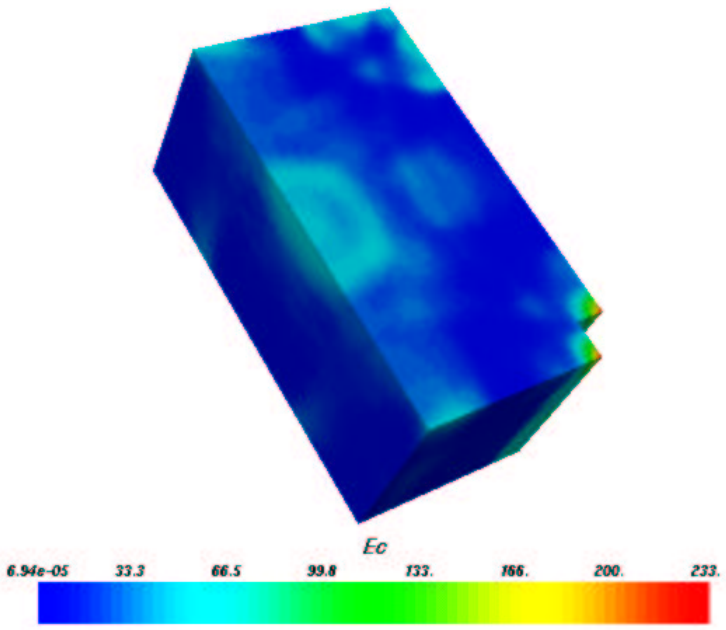

$t = 30\mu s$

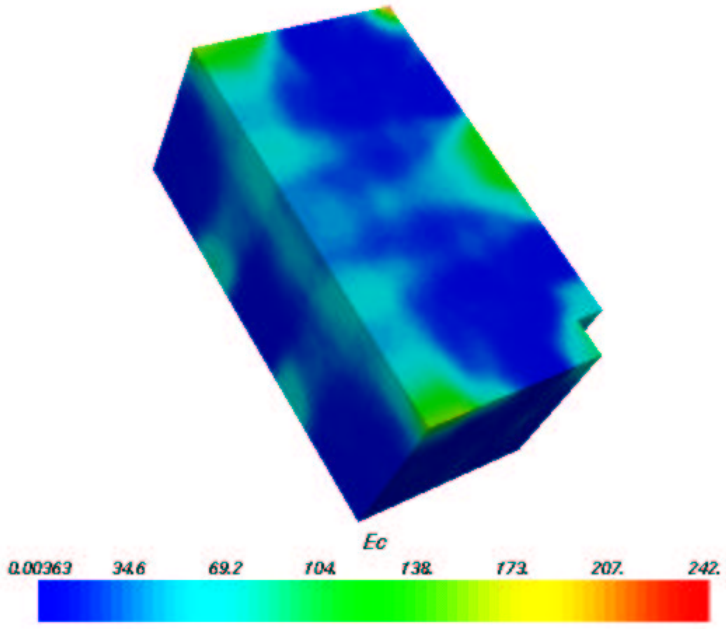

Figure 5.21: Kinetic energy density on the outside surface $[J/m^3]$

$t = 35\mu s$

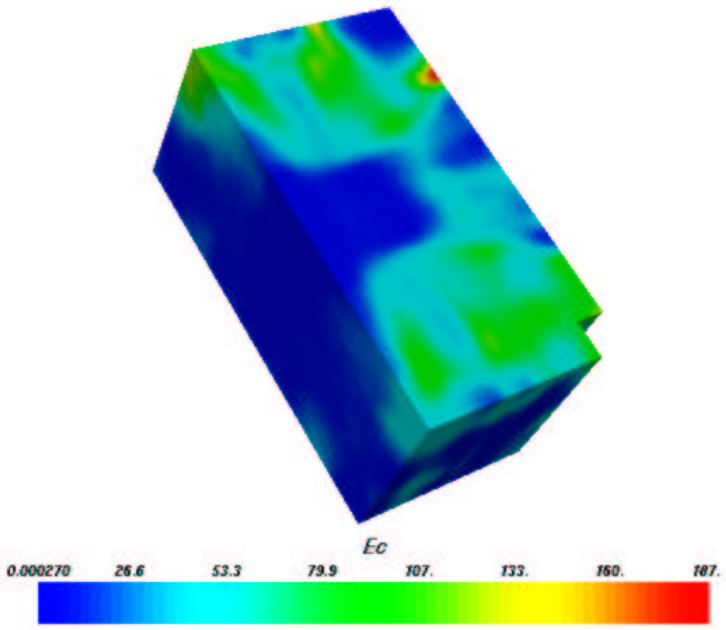

$t = 40\mu s$

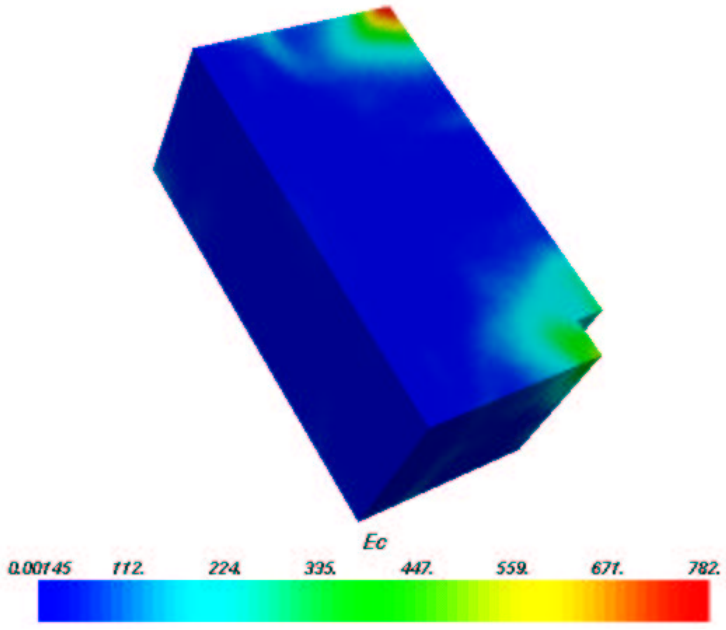

Figure 5.22: Kinetic energy density on the outside surface [J/m^3]

$t = 4\mu s$

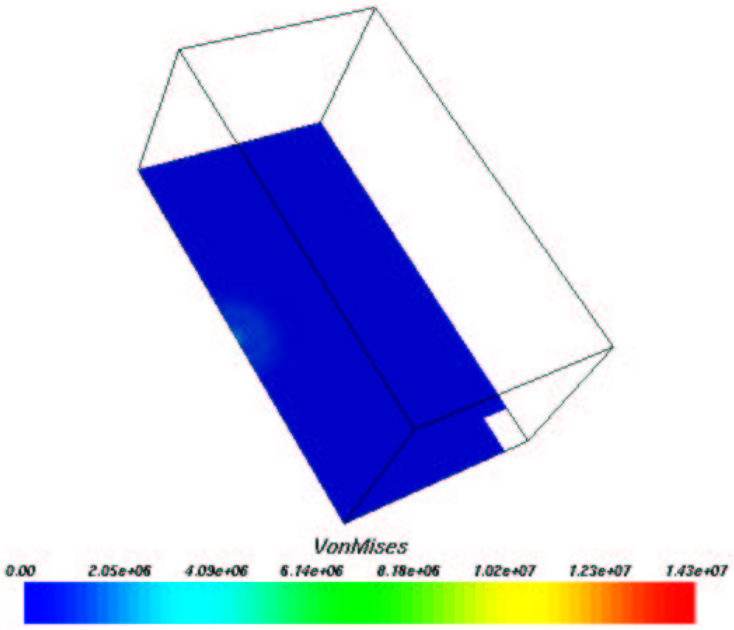

$t = 6\mu s$

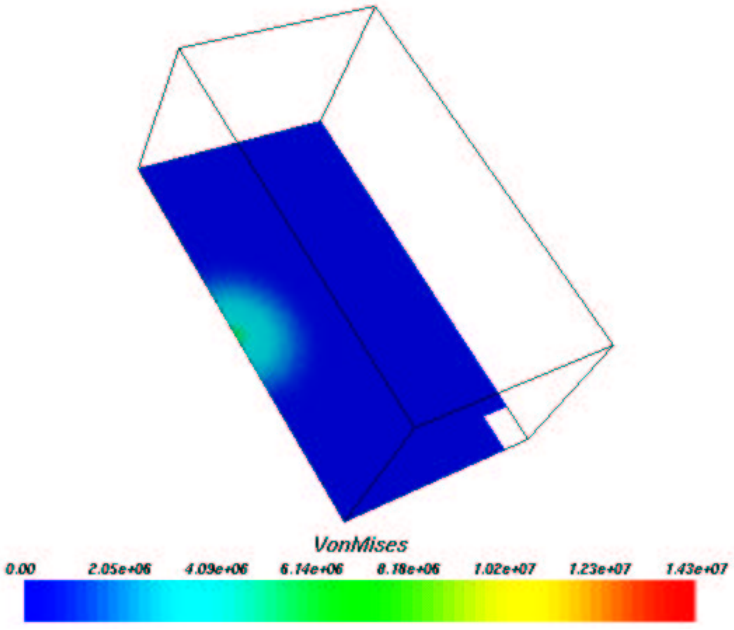

Figure 5.23: Von Mises stress on the central section [Pa]

$t = 8\mu s$

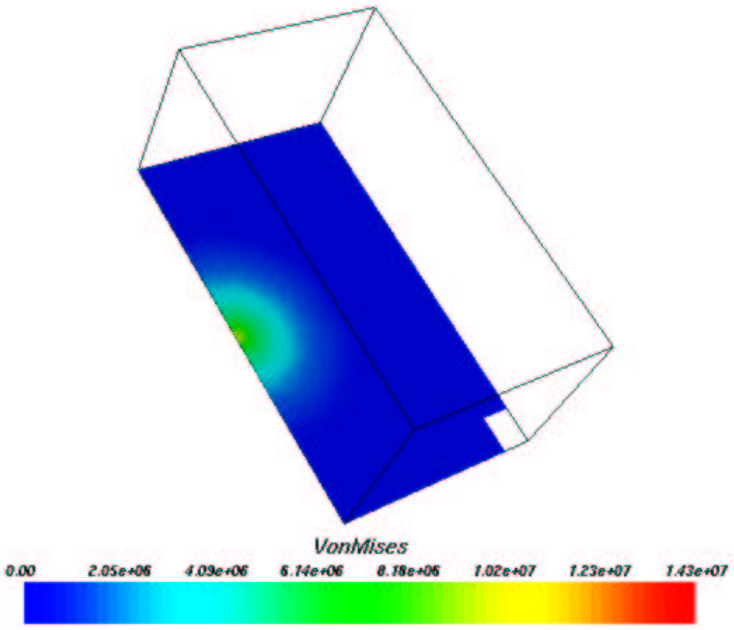

$t = 10\mu s$

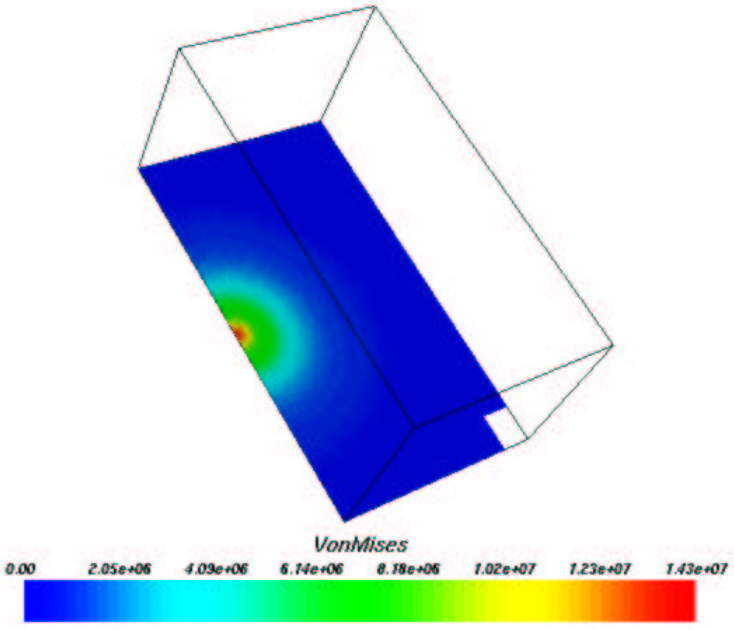

Figure 5.24: Von Mises stress on the central section [Pa]

$t = 12\mu s$

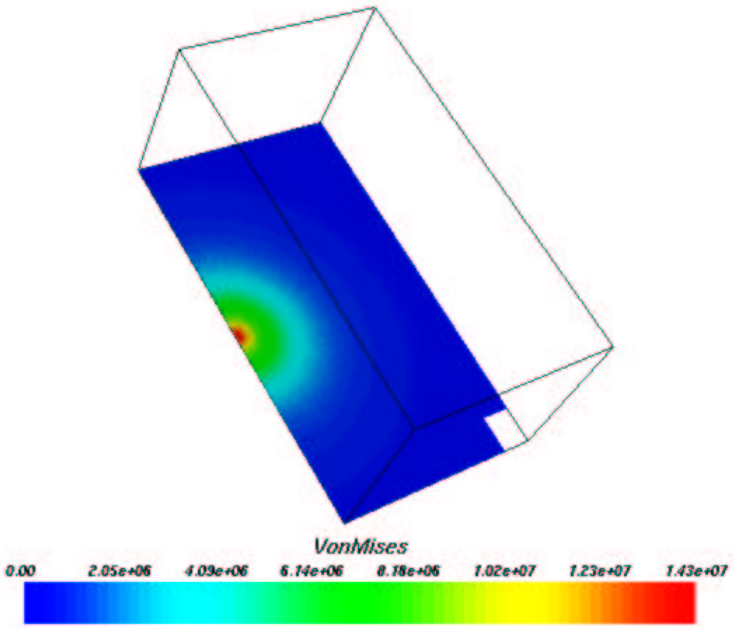

$t = 14\mu s$

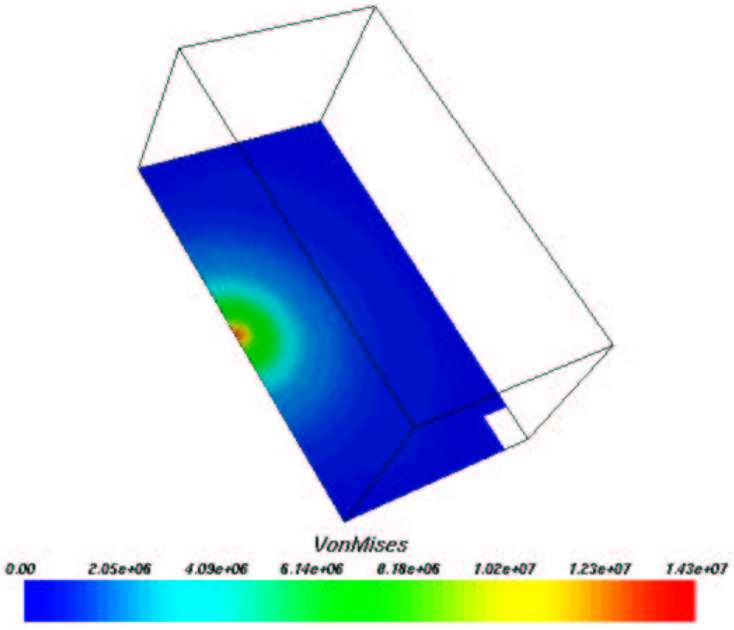

Figure 5.25: Von Mises stress on the central section [Pa]

$t = 16\mu s$

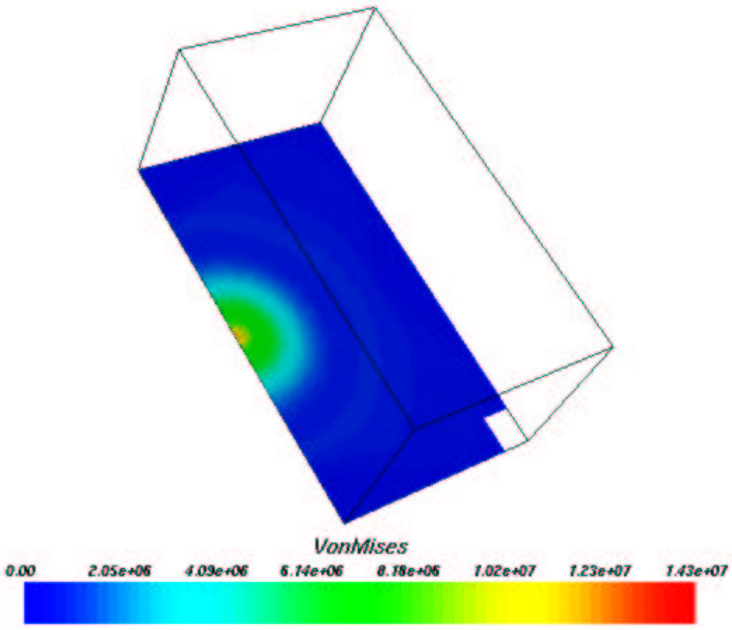

$t = 18\mu s$

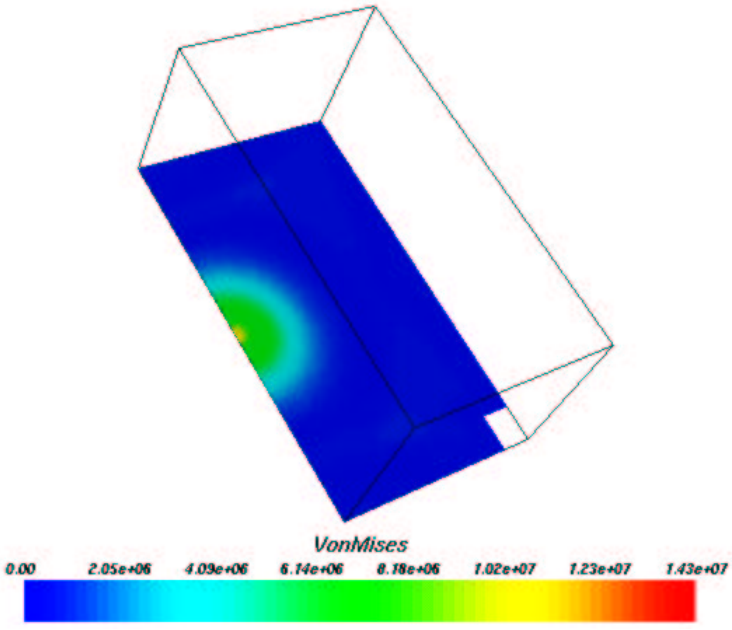

Figure 5.26: Von Mises stress on the central section [Pa]

$t = 20\mu s$

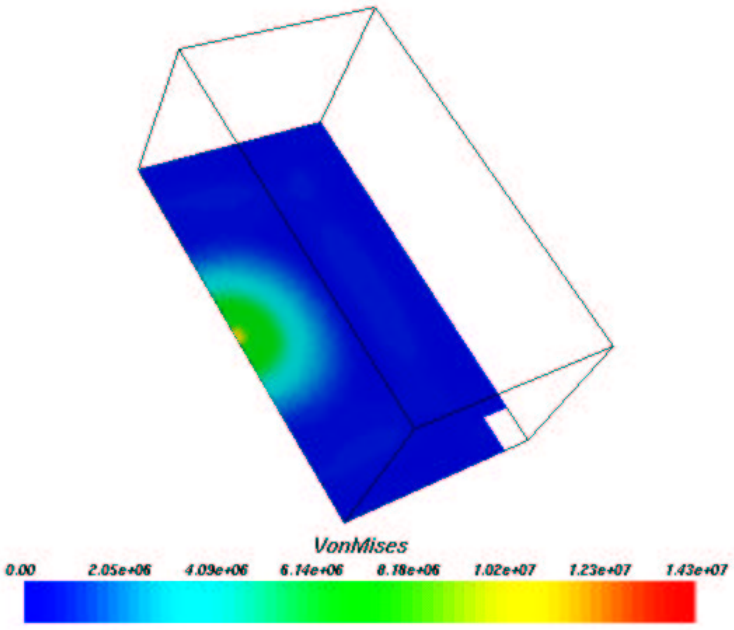

Figure 5.27: Von Mises stress on the central section [Pa]

$t = 4\mu s$

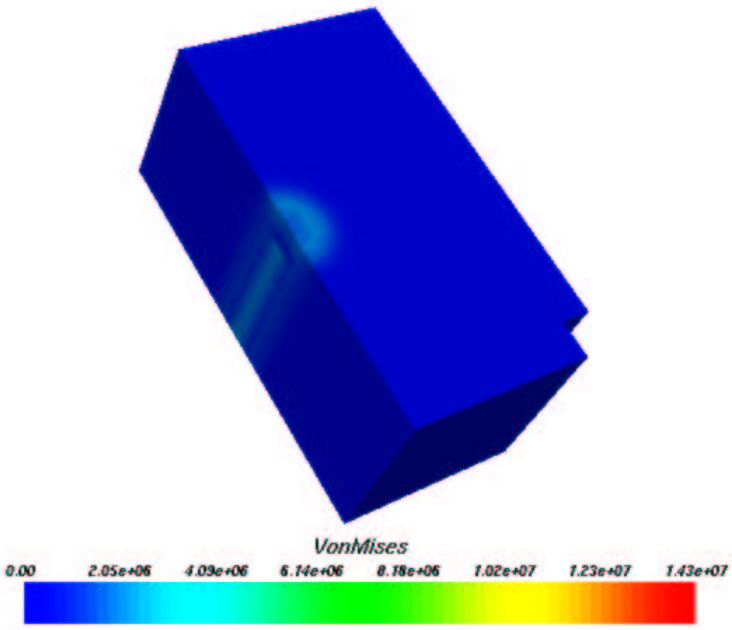

$t = 6\mu s$

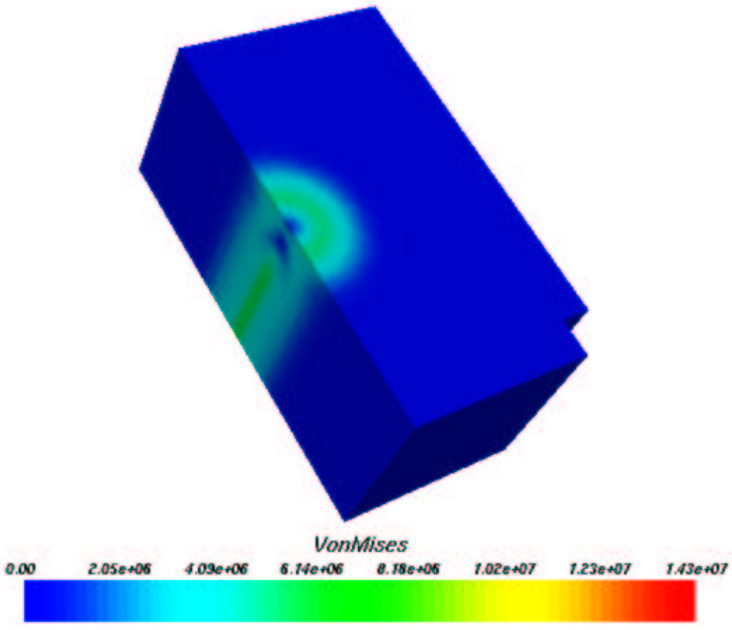

Figure 5.28: Von Mises stress on the outside surface [Pa]

$t = 8\mu s$

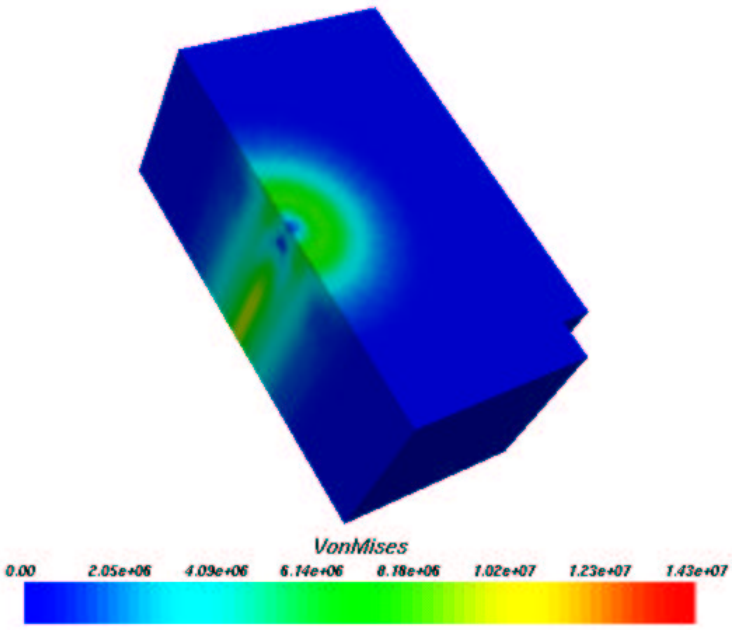

$t = 10\mu s$

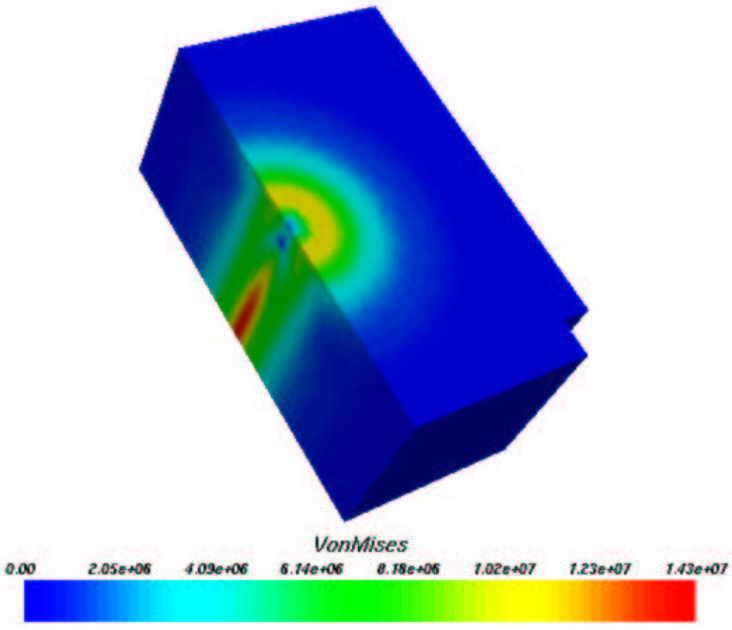

Figure 5.29: Von Mises stress on the outside surface [Pa]

$t = 12\mu s$

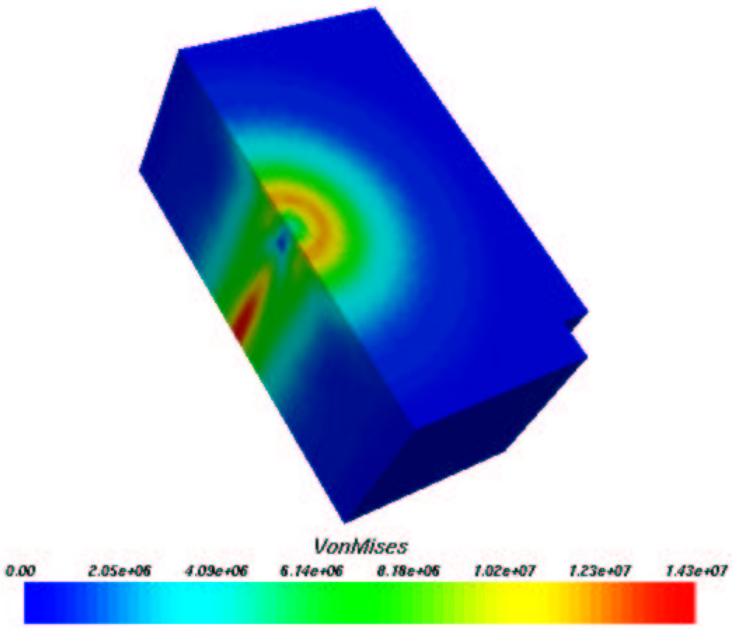

$t = 14\mu s$

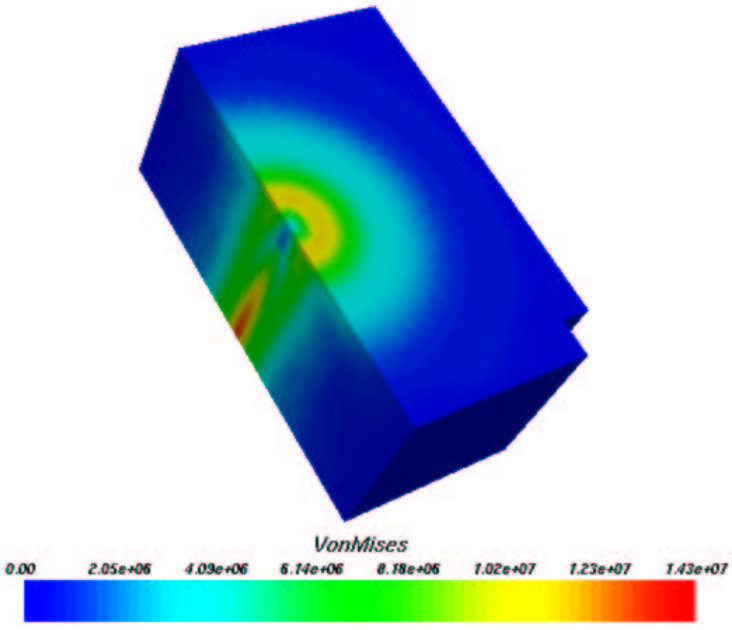

Figure 5.30: Von Mises stress on the outside surface [Pa]

$t = 16\mu s$

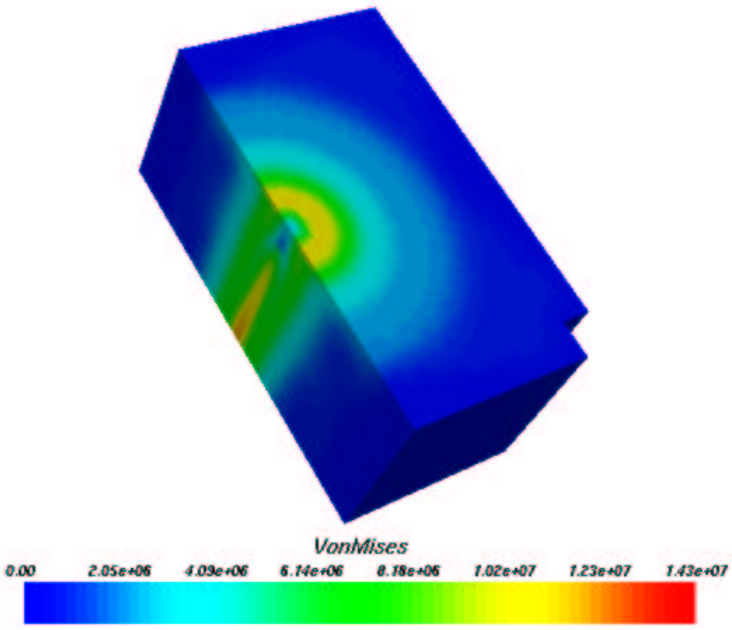

$t = 18\mu s$

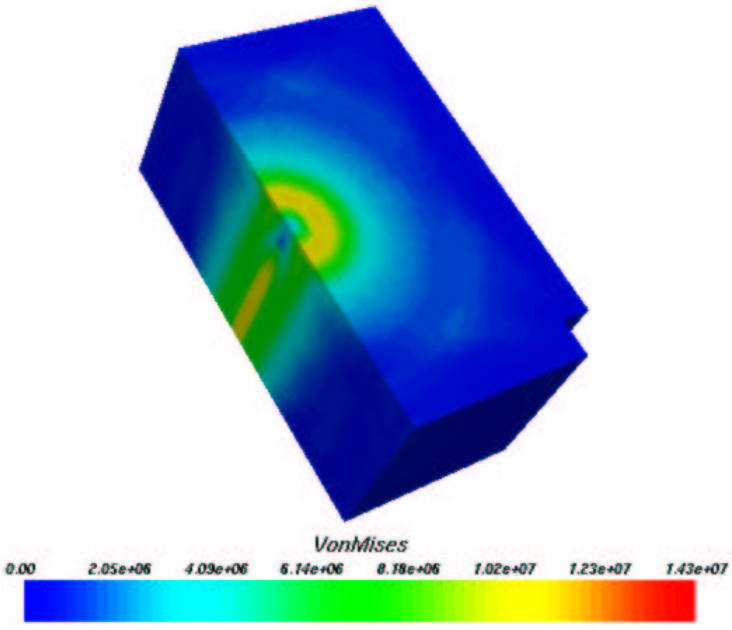

Figure 5.31: Von Mises stress on the outside surface [Pa]

$t = 20\mu s$

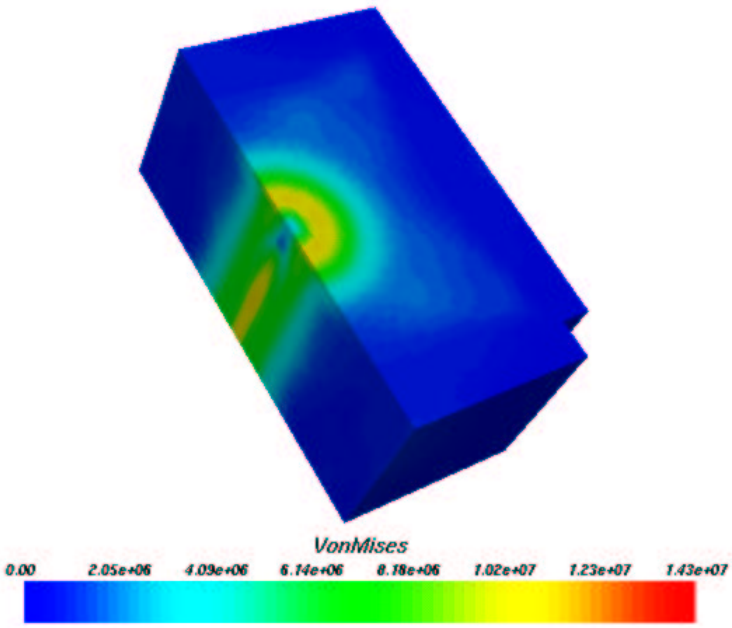

Figure 5.32: Von Mises stress on the outside surface [Pa]

$t = 4\mu s$

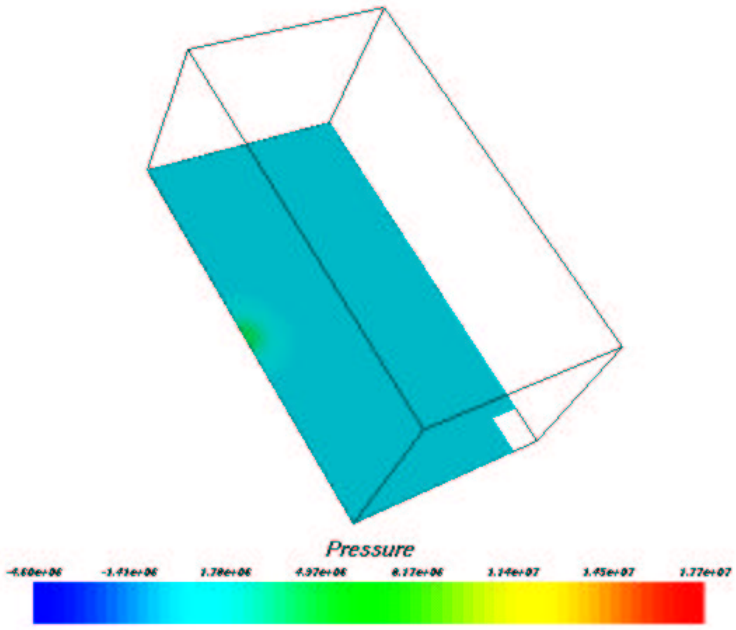

$t = 6\mu s$

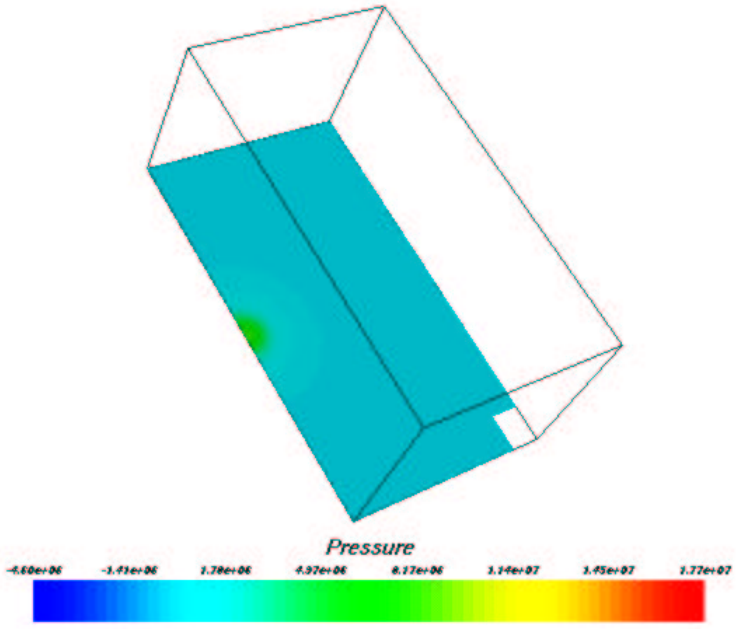

Figure 5.33: Pressure value on the central section [Pa]

$t = 8\mu s$

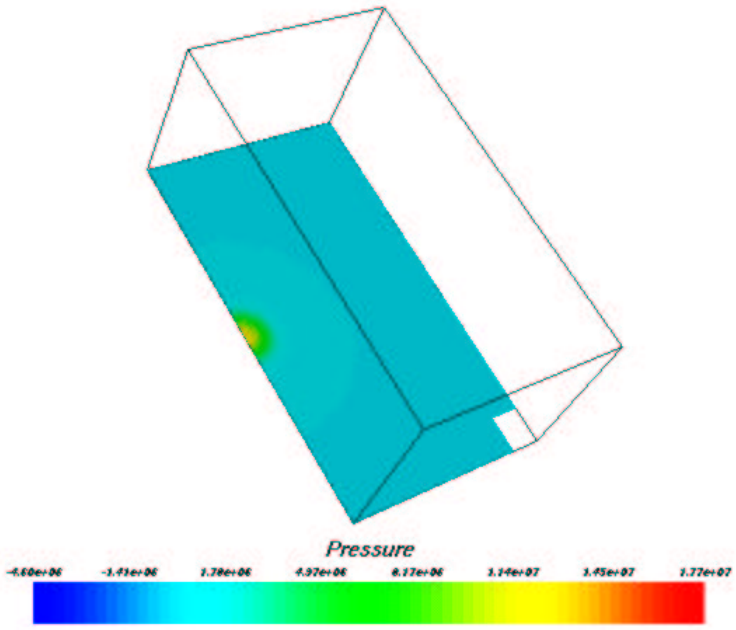

$t = 10\mu s$

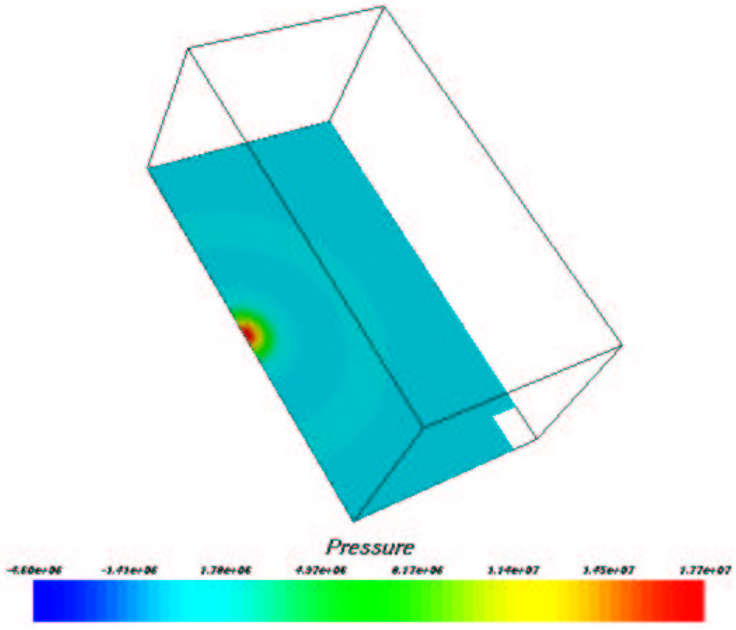

Figure 5.34: Pressure value on the central section [Pa]

$t = 12\mu s$

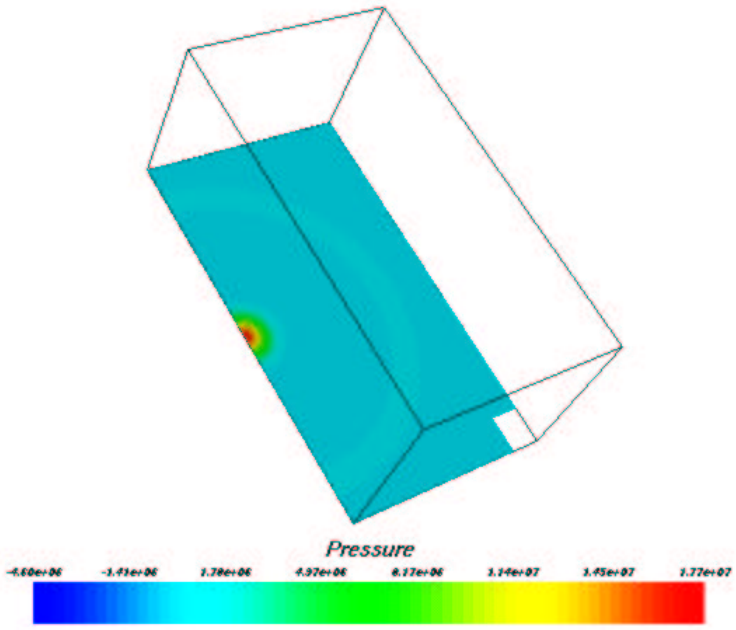

$t = 14\mu s$

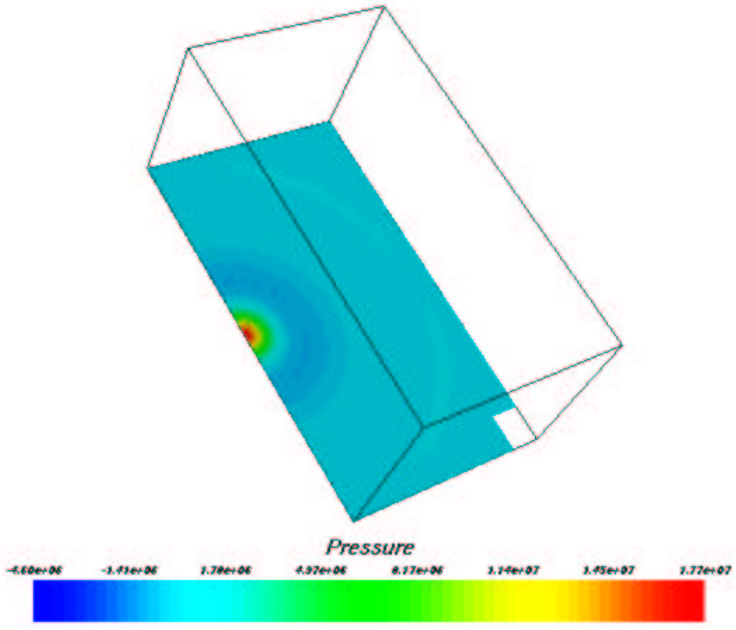

Figure 5.35: Pressure value on the central section [Pa]

$t = 16\mu s$

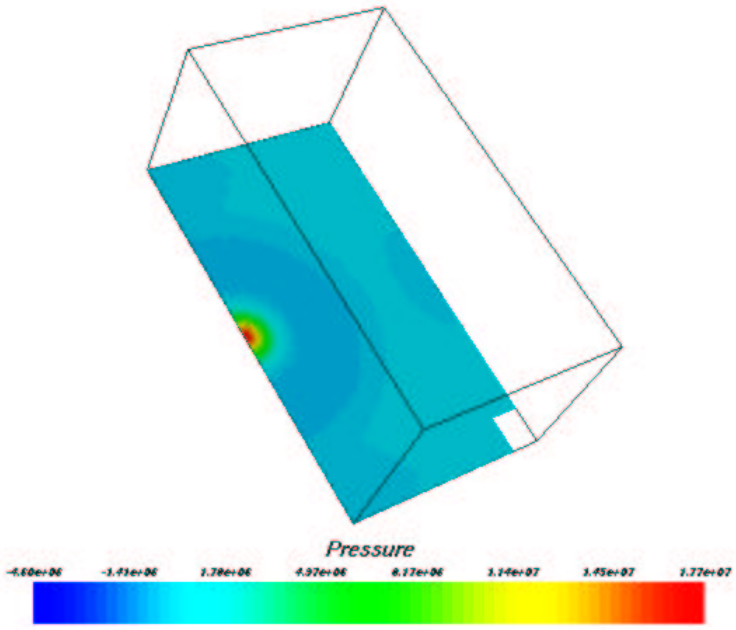

$t = 18\mu s$

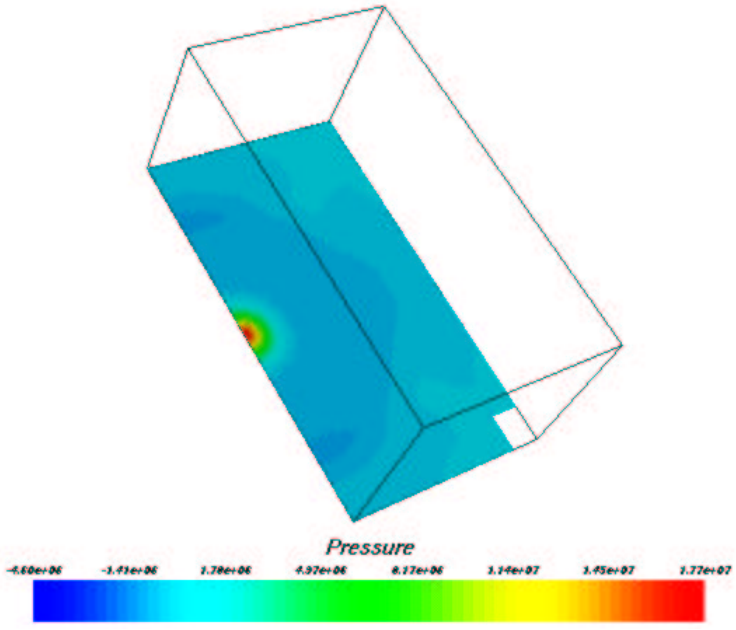

Figure 5.36: Pressure value on the central section [Pa]

$t = 20\mu s$

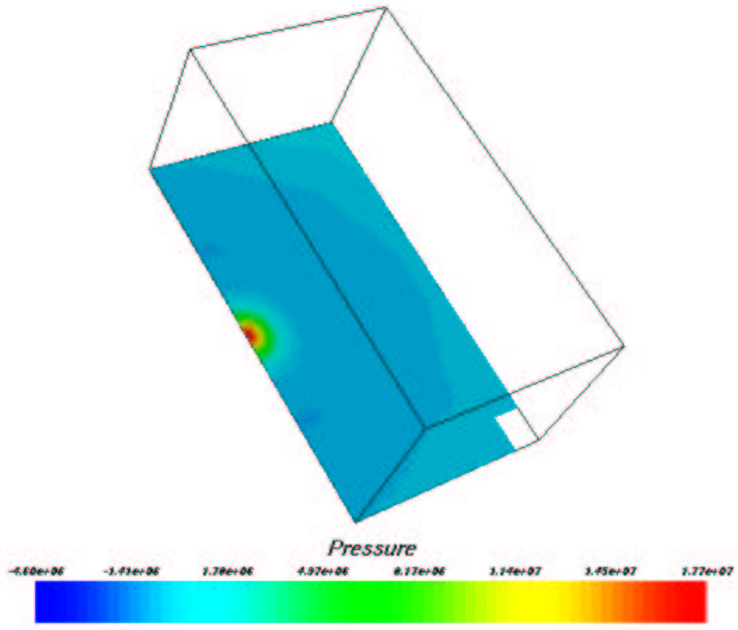

Figure 5.37: Pressure value on the central section [Pa]

$t = 4\mu s$

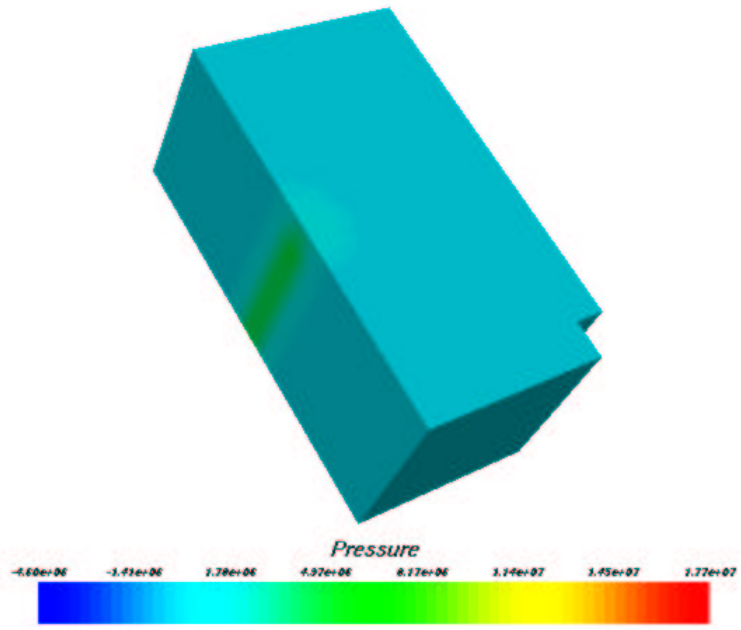

$t = 6\mu s$

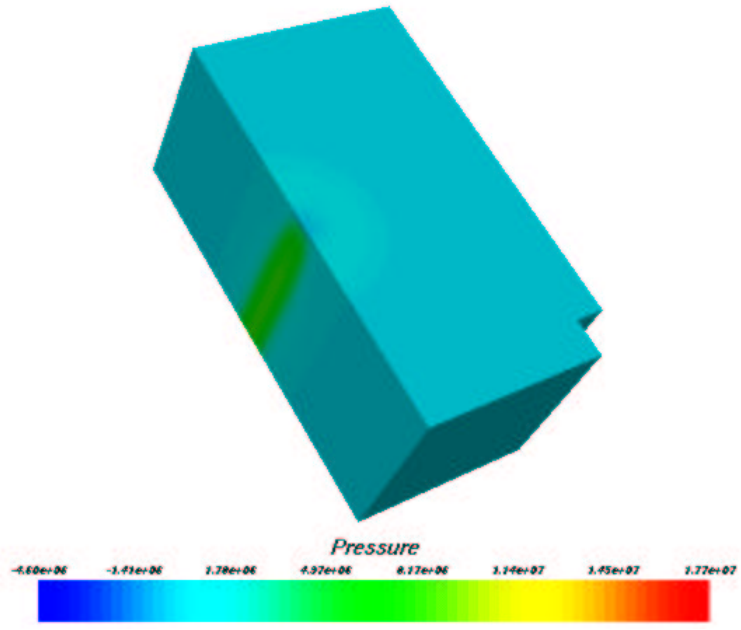

Figure 5.38: Pressure value on the outside surface [Pa]

$t = 8\mu s$

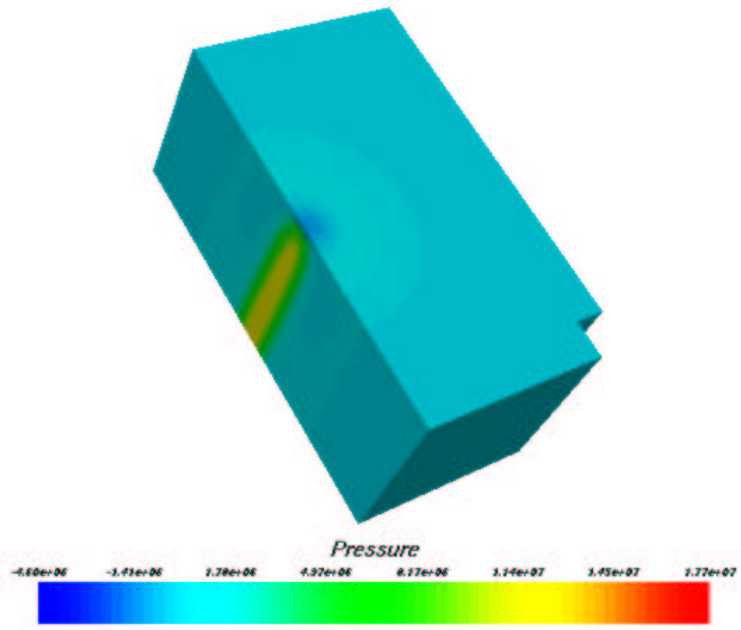

$t = 10\mu s$

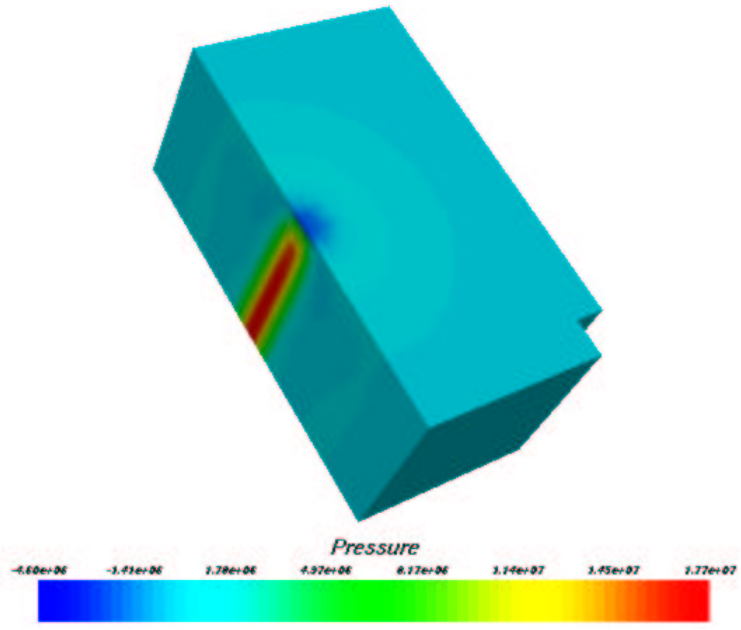

Figure 5.39: Pressure value on the outside surface [Pa]

$t = 12\mu s$

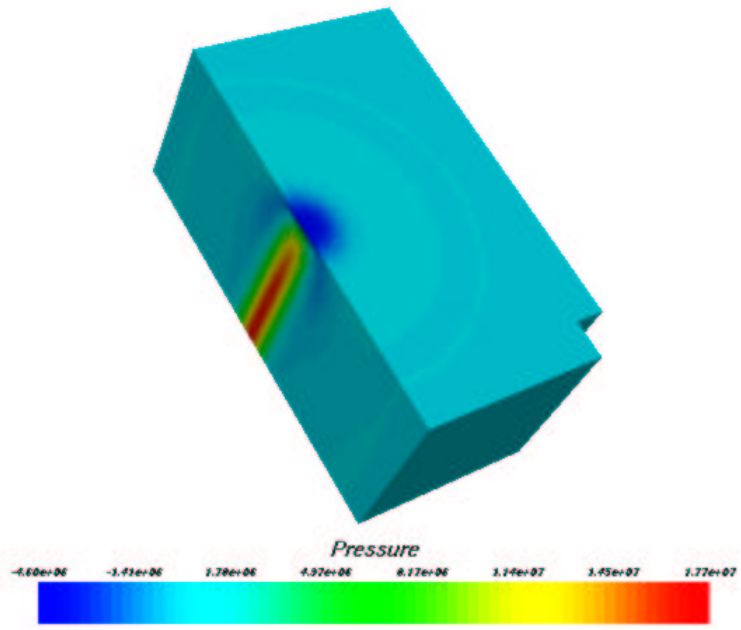

$t = 14\mu s$

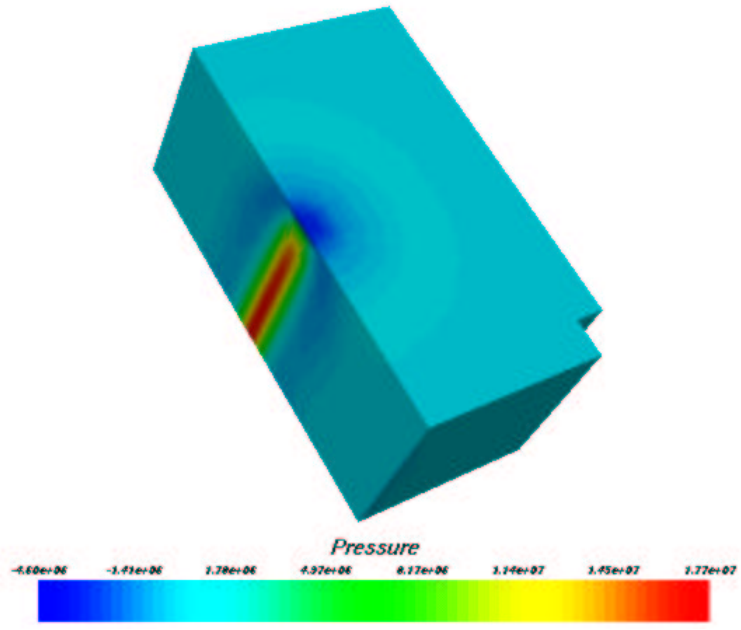

Figure 5.40: Pressure value on the outside surface [Pa]

$t = 16\mu s$

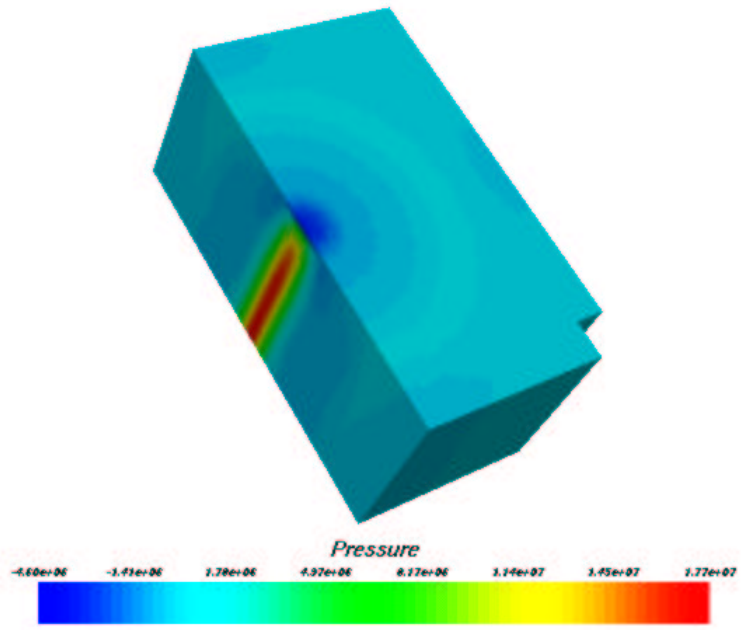

$t = 18\mu s$

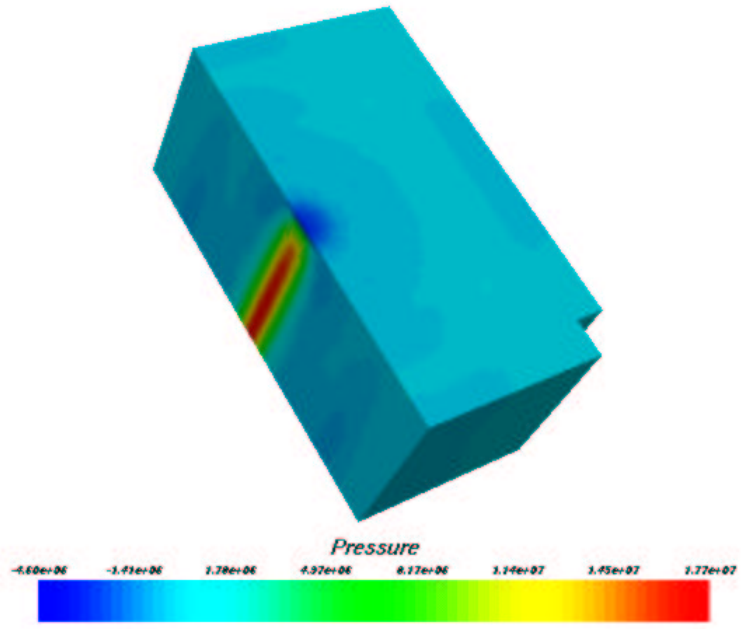

Figure 5.41: Pressure value on the outside surface [Pa]

$t = 20\mu s$

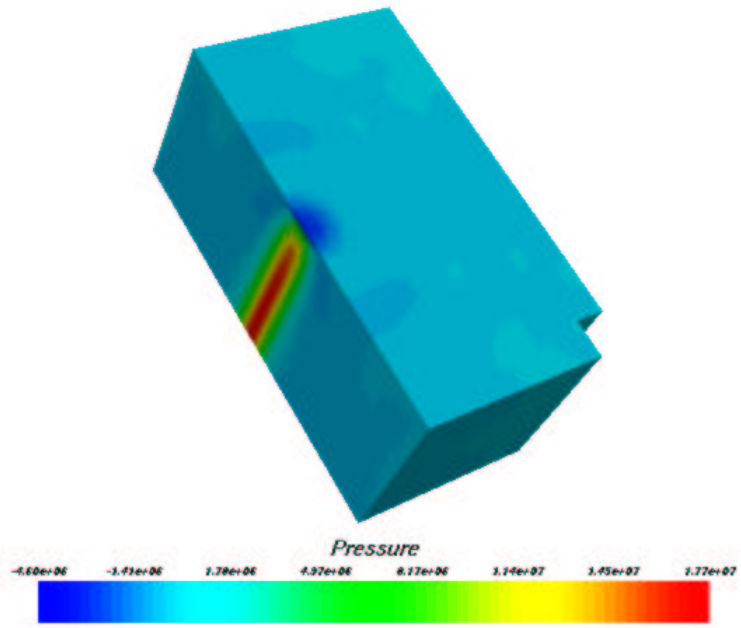

Figure 5.42: Pressure value on the outside surface [Pa]

$t = 4\mu s$

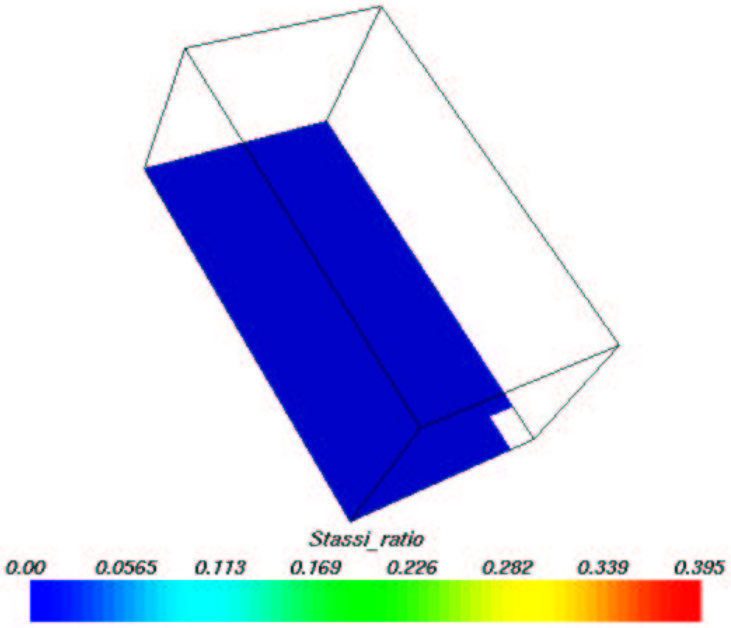

$t = 6\mu s$

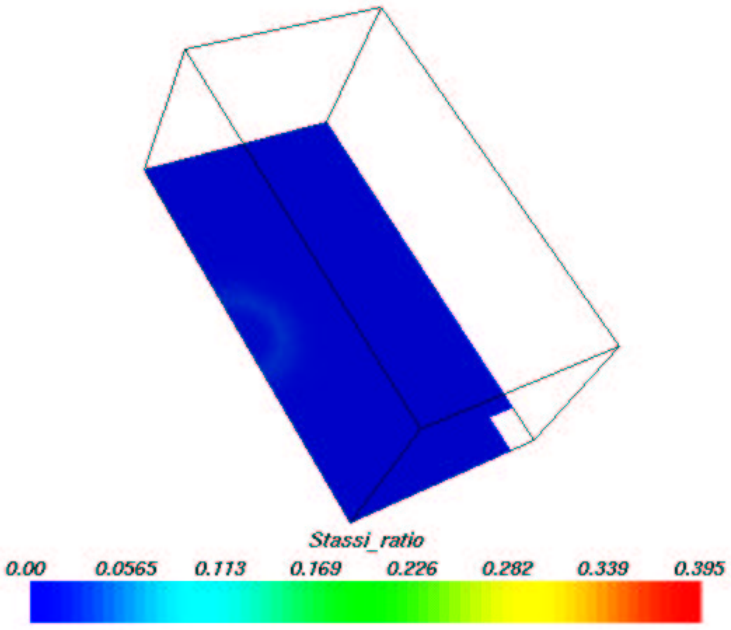

Figure 5.43: Stassi ratio on the central section

$t = 8\mu s$

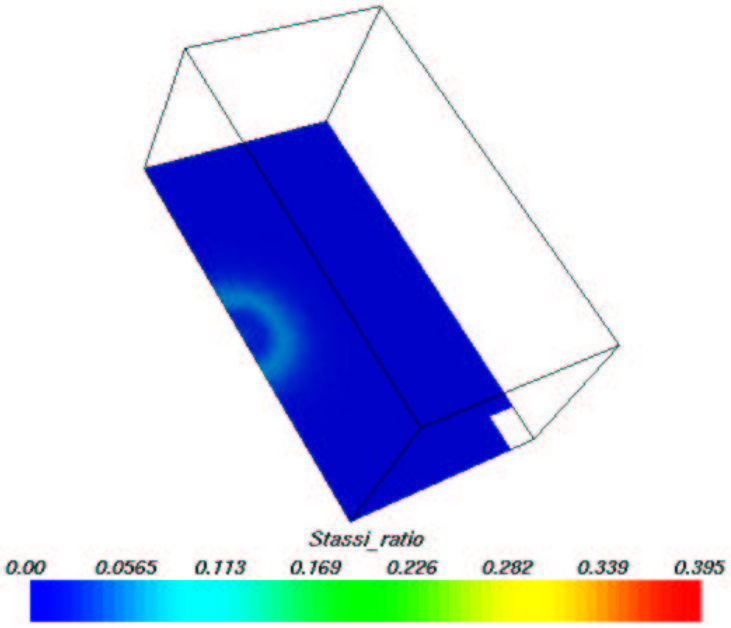

$t = 10\mu s$

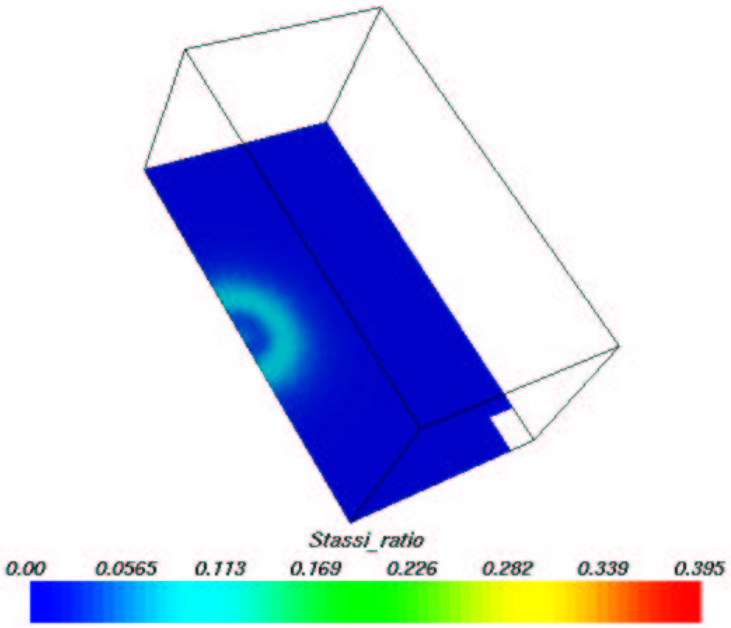

Figure 5.44: Stassi ratio on the central section

$t = 12\mu s$

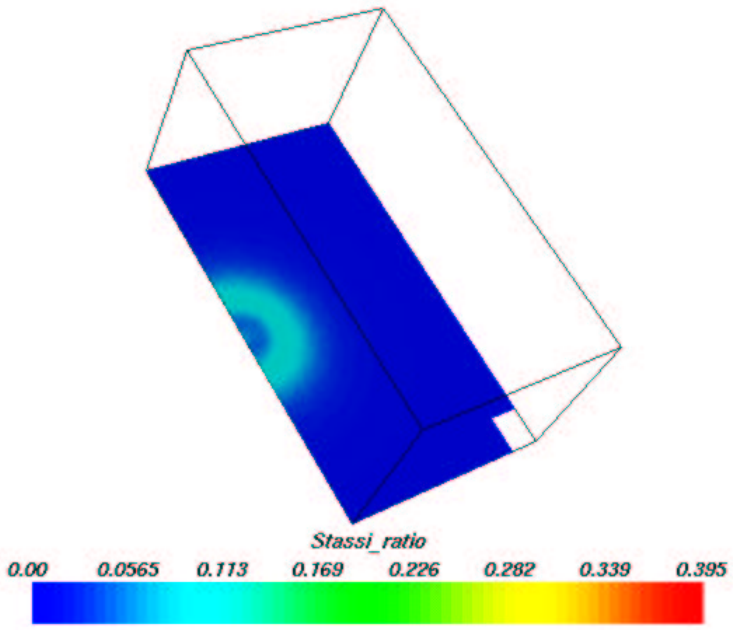

$t = 14\mu s$

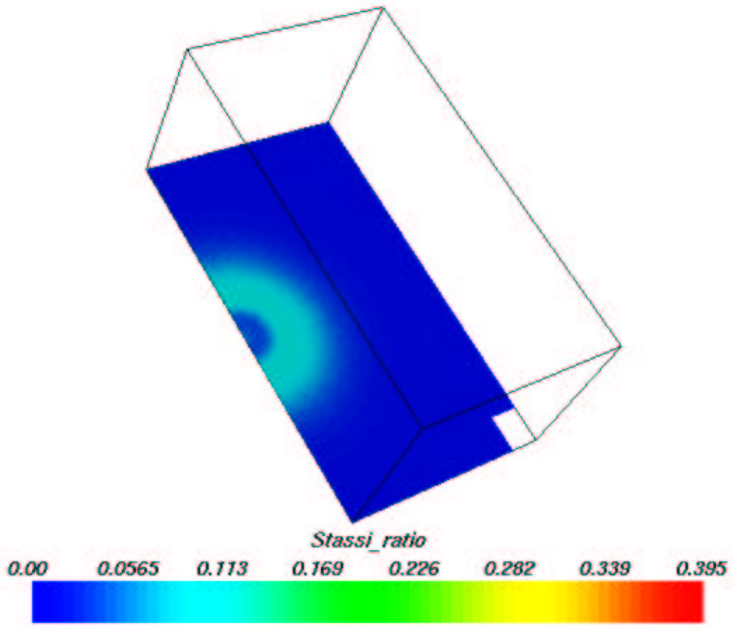

Figure 5.45: Stassi ratio on the central section

$t = 16\mu s$

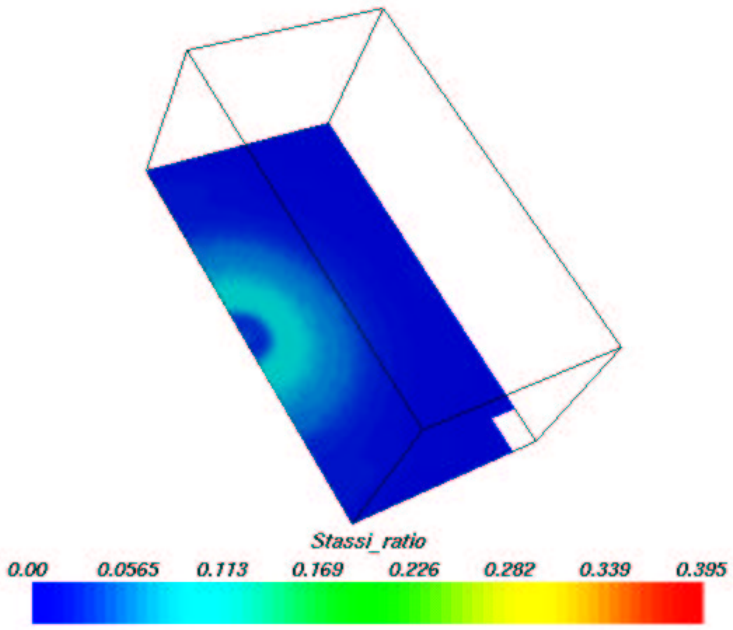

$t = 18\mu s$

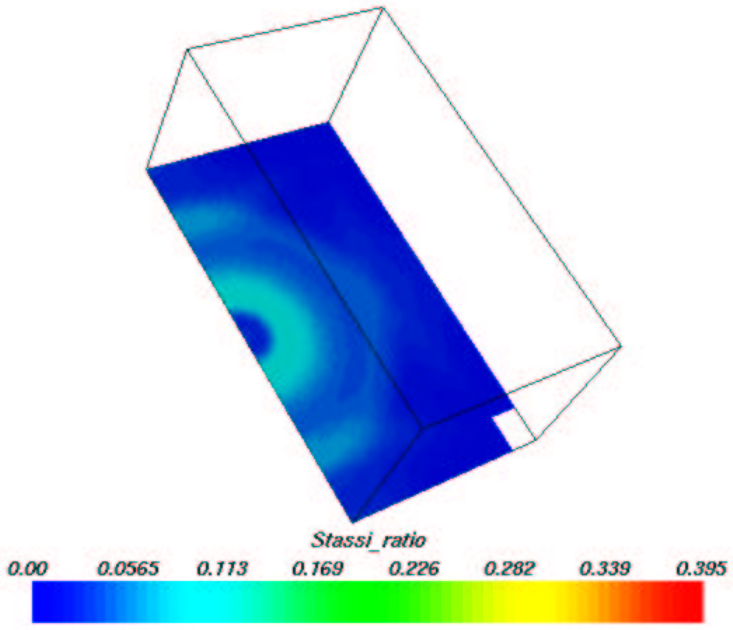

Figure 5.46: Stassi ratio on the central section

$t = 20\mu s$

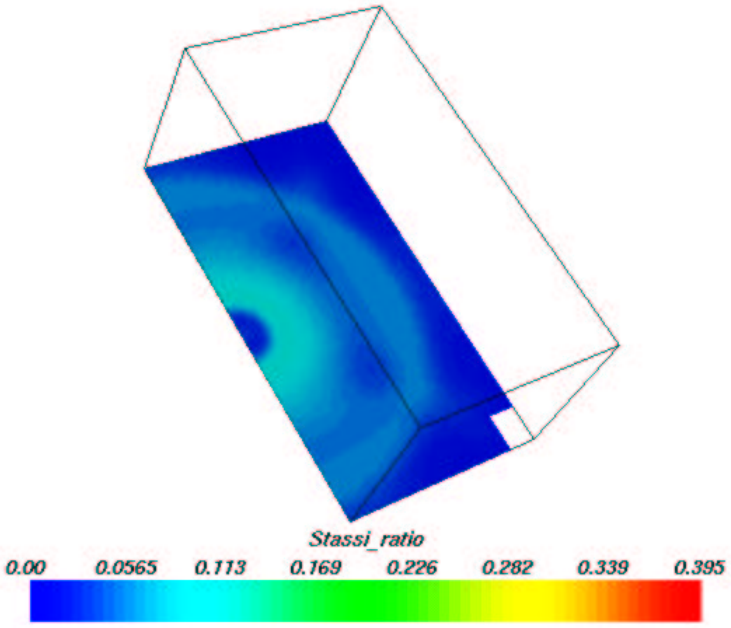

$t = 22\mu s$

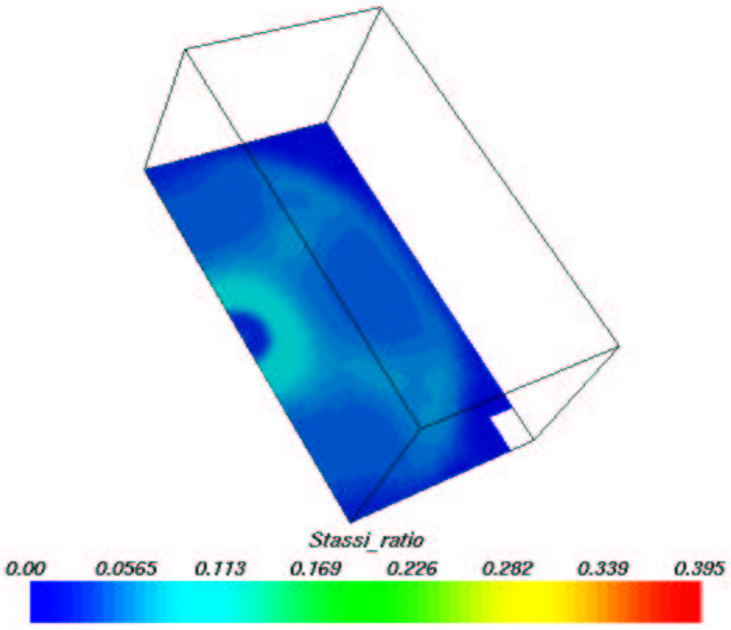

Figure 5.47: Stassi ratio on the central section

$t = 24\mu s$

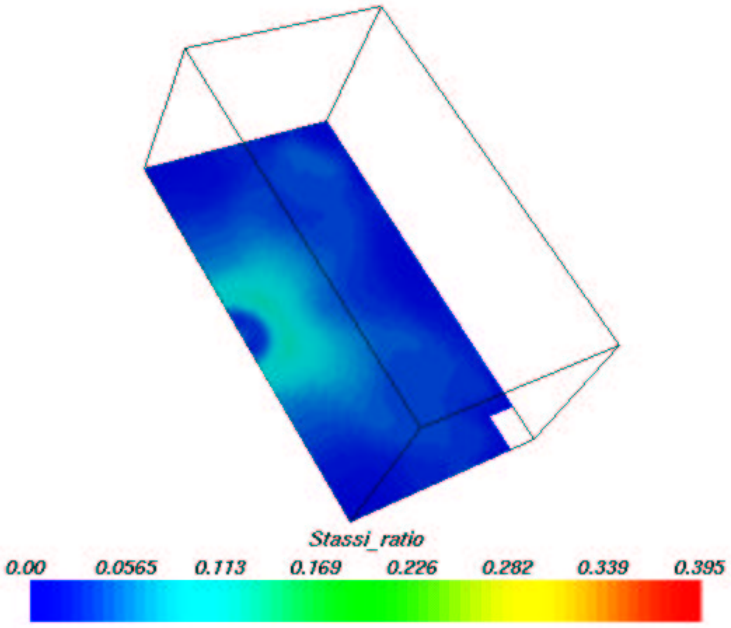

$t = 26\mu s$

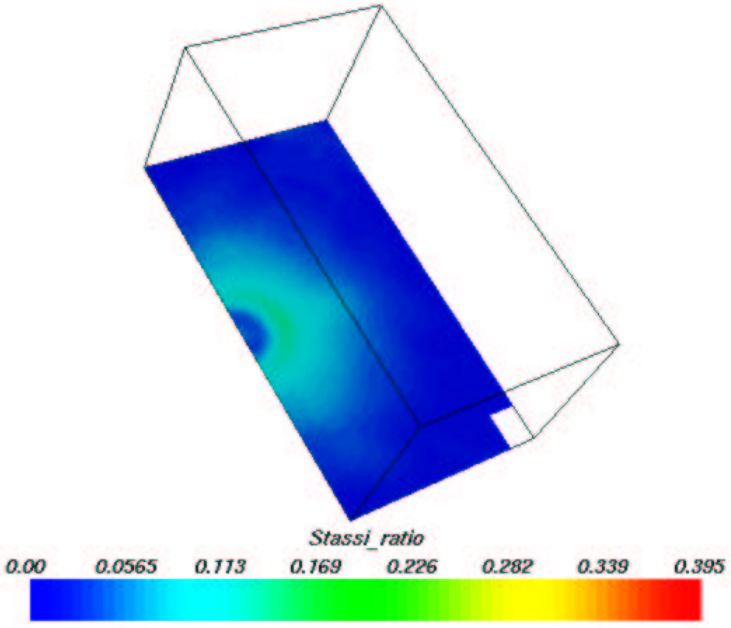

Figure 5.48: Stassi ratio on the central section

$t = 28\mu s$

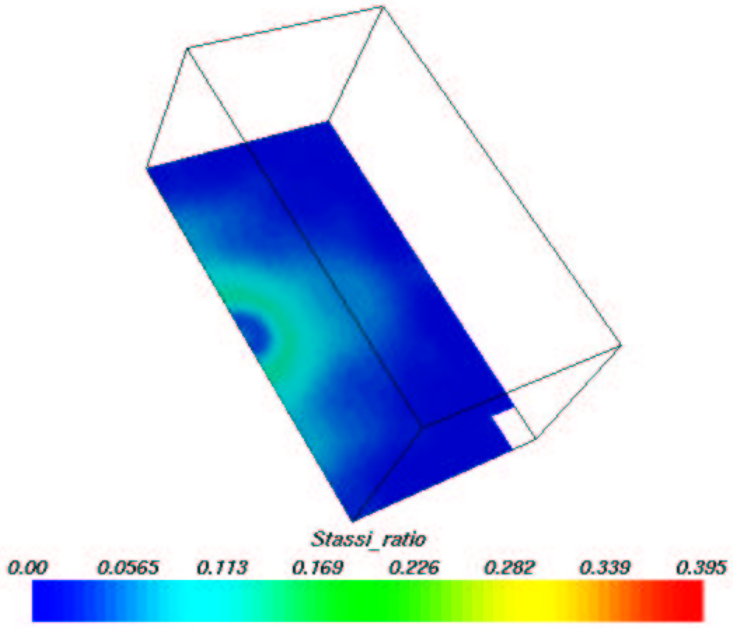

$t = 30\mu s$

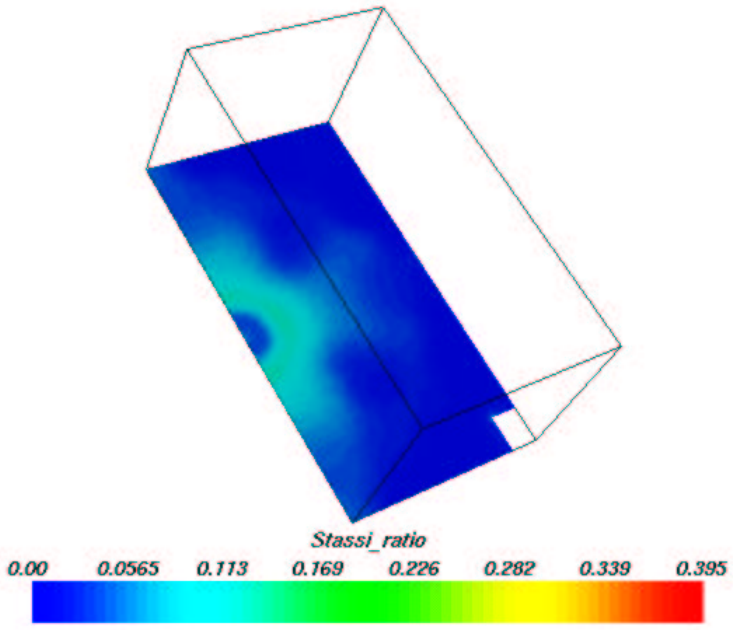

Figure 5.49: Stassi ratio on the central section

$t = 35\mu s$

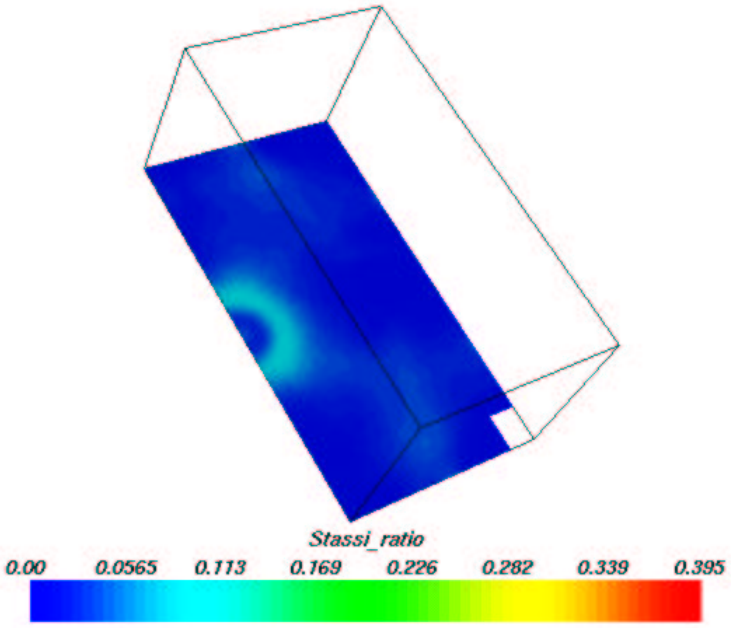

$t = 40\mu s$

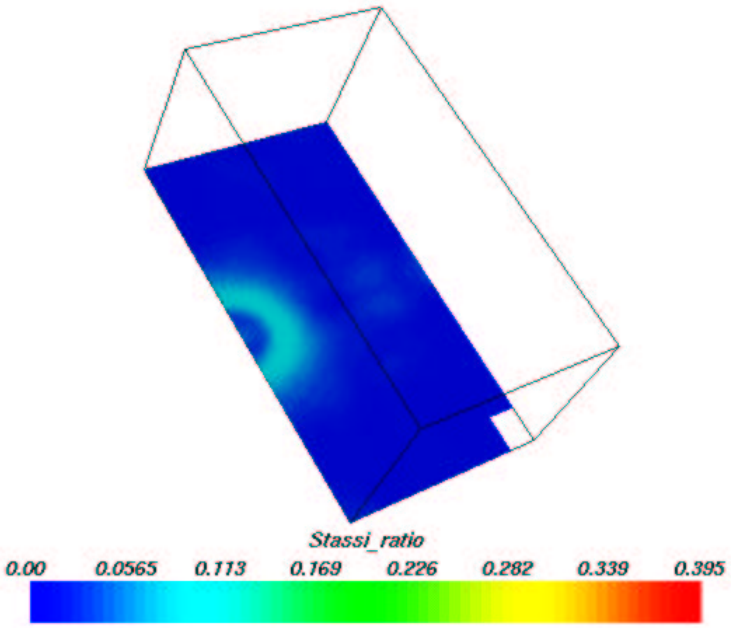

Figure 5.50: Stassi ratio on the central section

$t = 4\mu s$

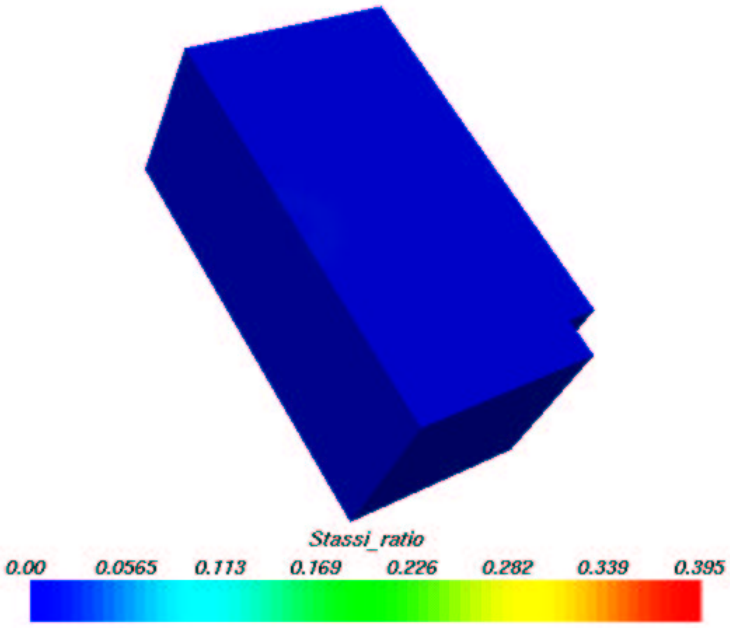

$t = 6\mu s$

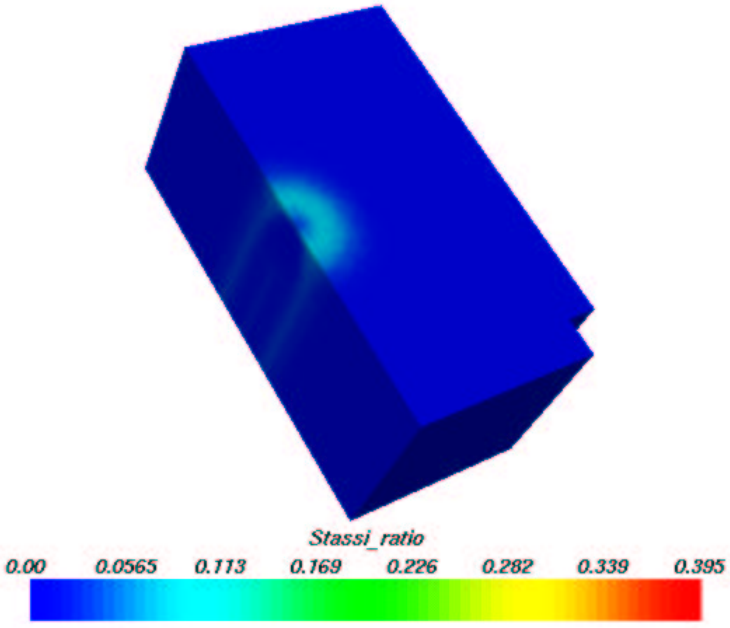

Figure 5.51: Stassi ratio on the outside surface

$t = 8\mu s$

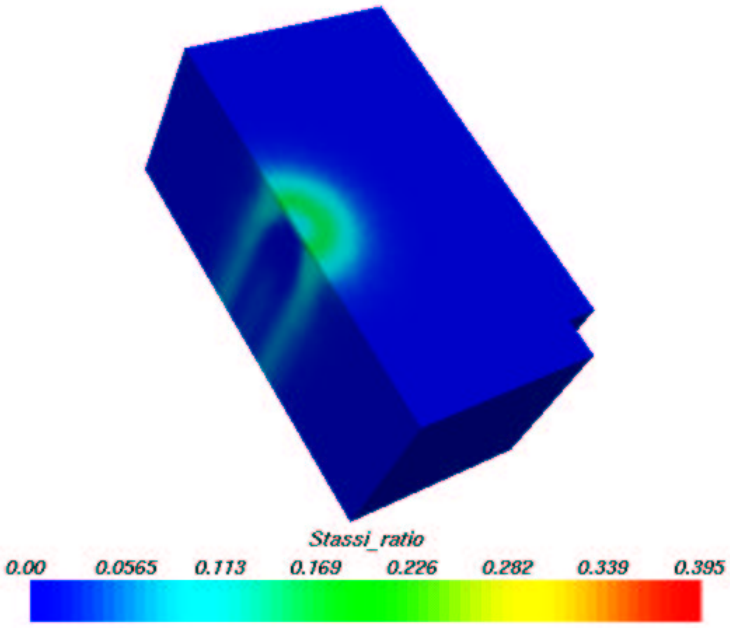

$t = 10\mu s$

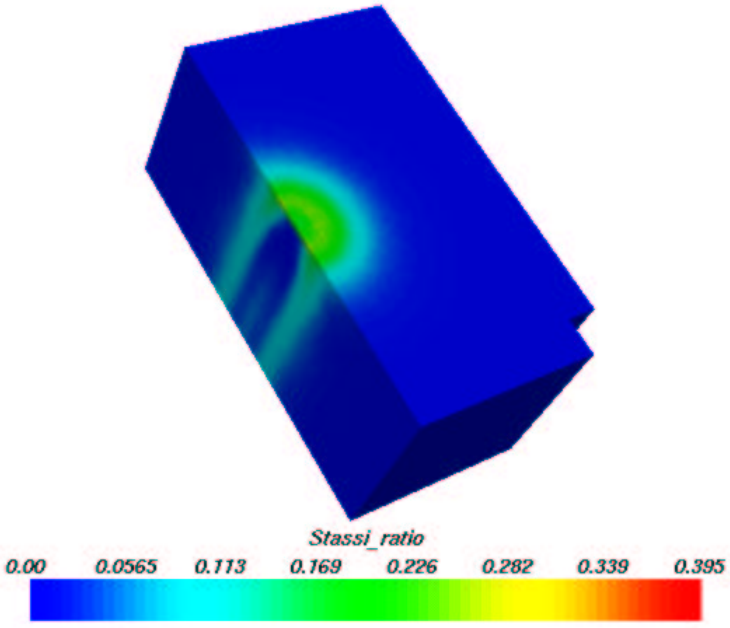

Figure 5.52: Stassi ratio on the outside surface

$t = 12\mu s$

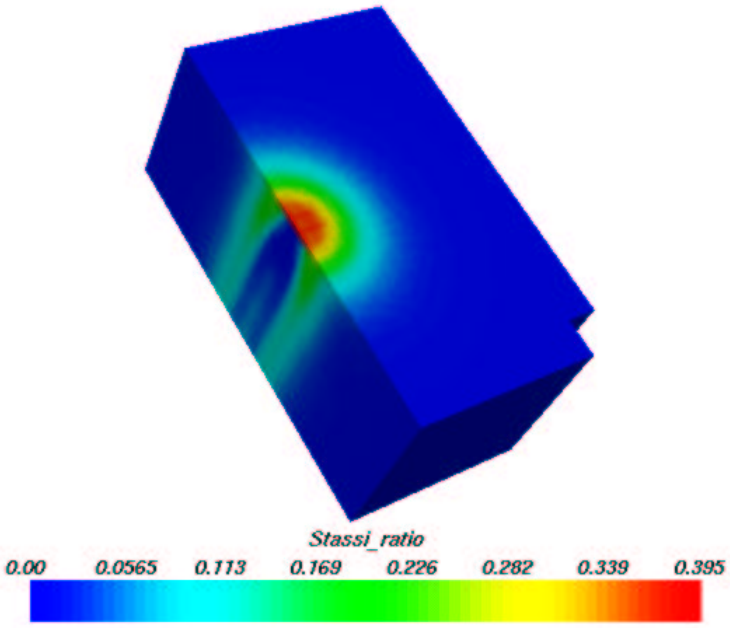

$t = 14\mu s$

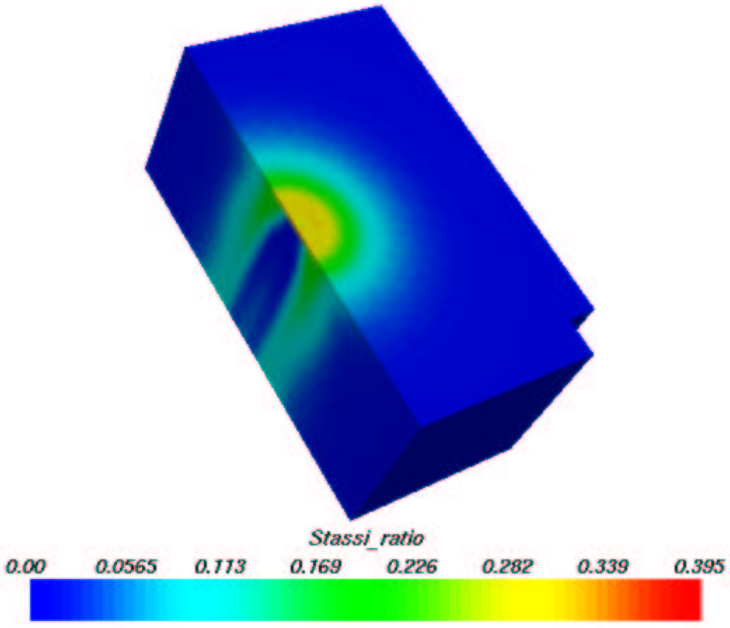

Figure 5.53: Stassi ratio on the outside surface

$t = 16\mu s$

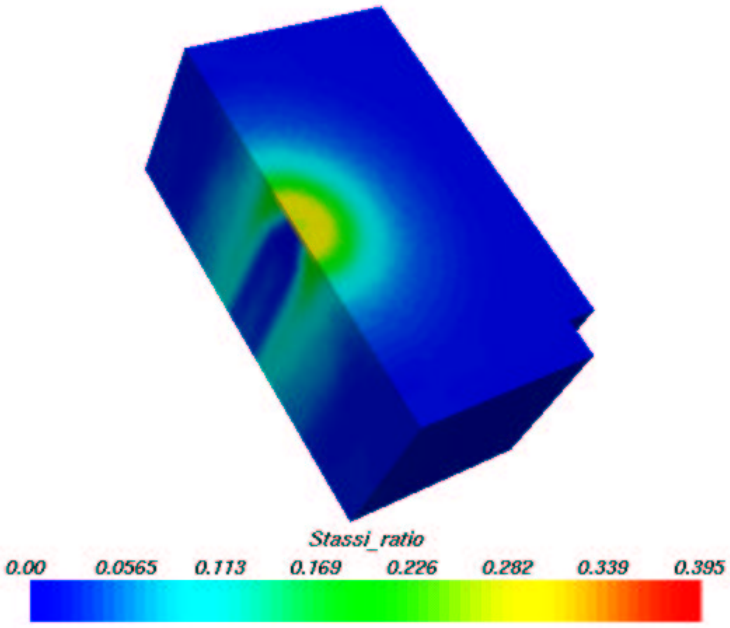

$t = 18\mu s$

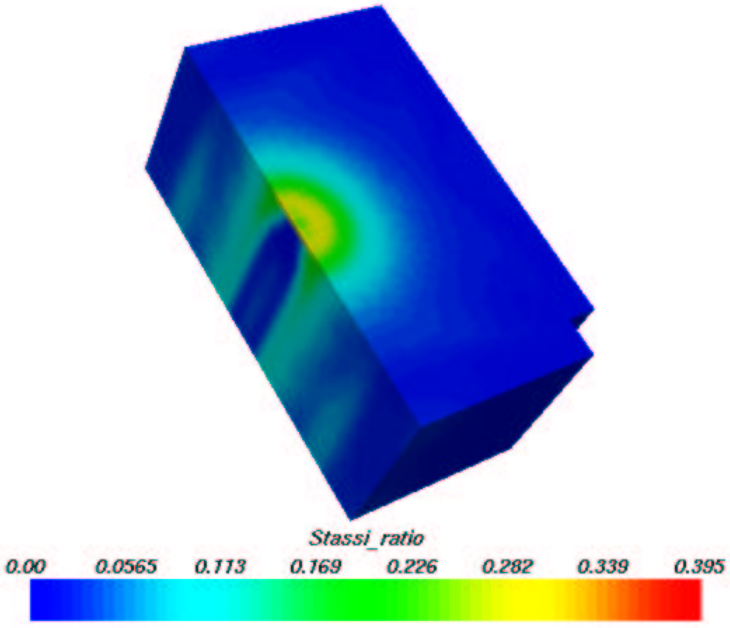

Figure 5.54: Stassi ratio on the outside surface

$t = 20\mu s$

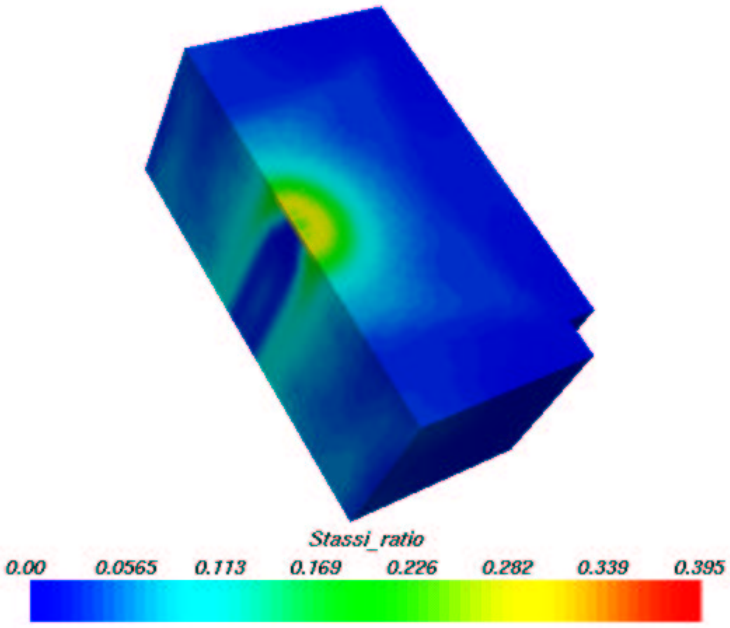

$t = 22\mu s$

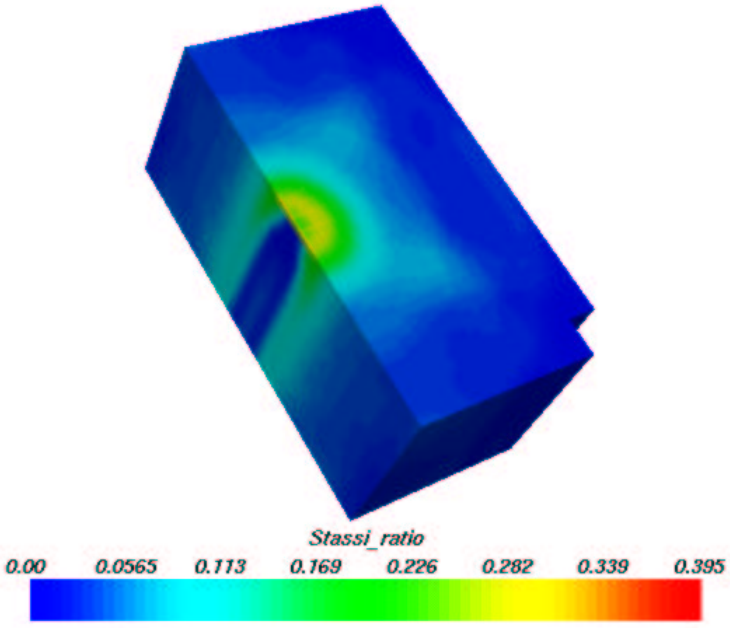

Figure 5.55: Stassi ratio on the outside surface

$t = 24\mu s$

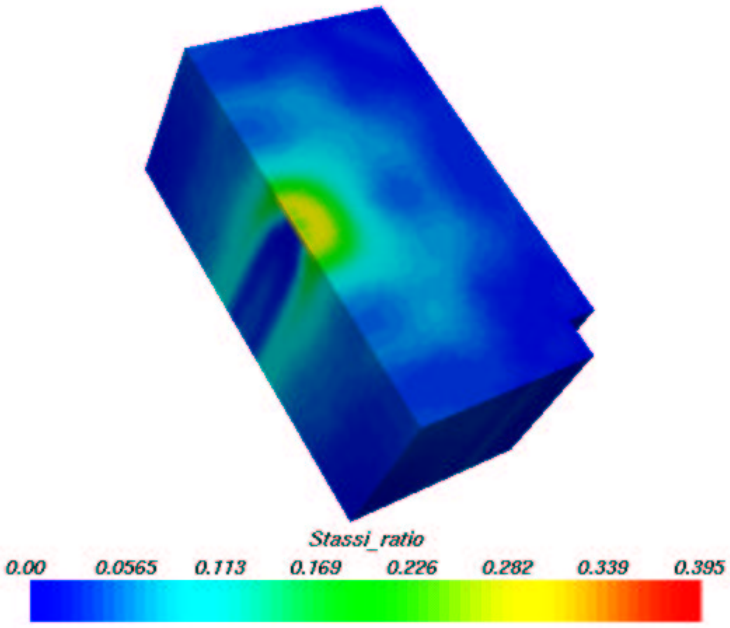

$t = 26\mu s$

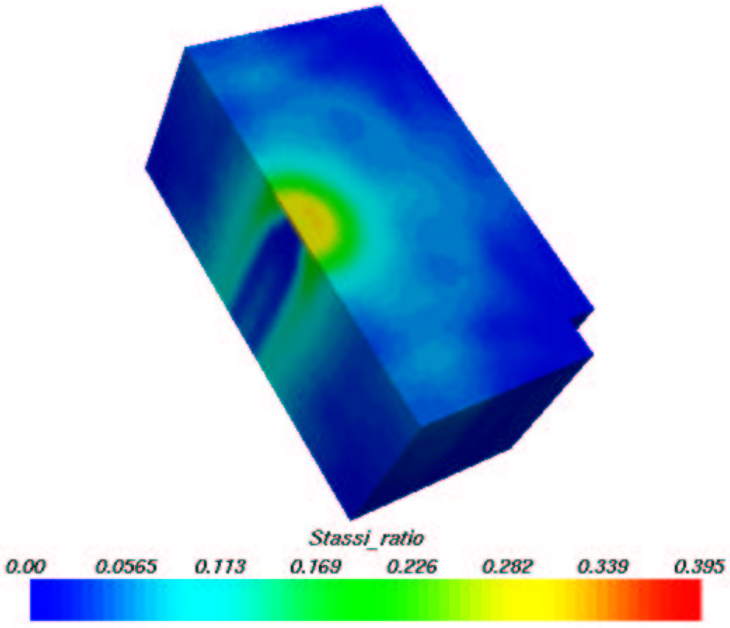

Figure 5.56: Stassi ratio on the outside surface

$t = 28\mu s$

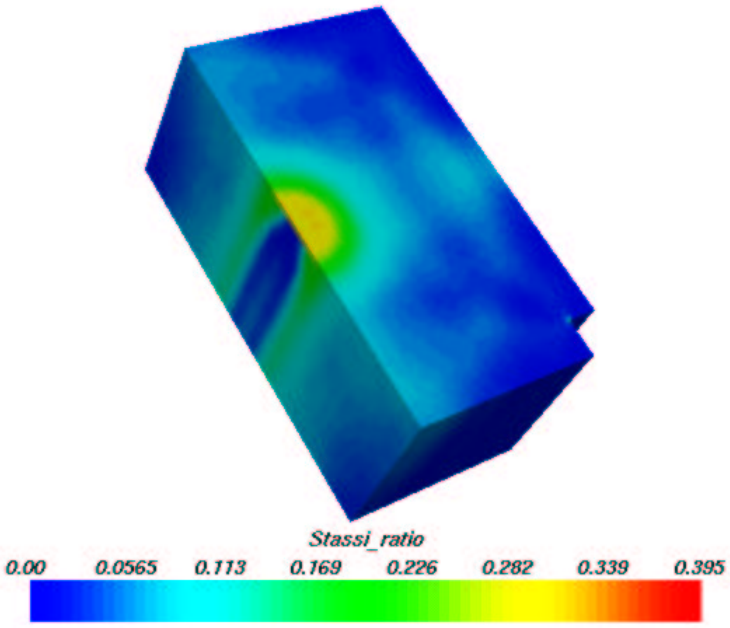

$t = 30\mu s$

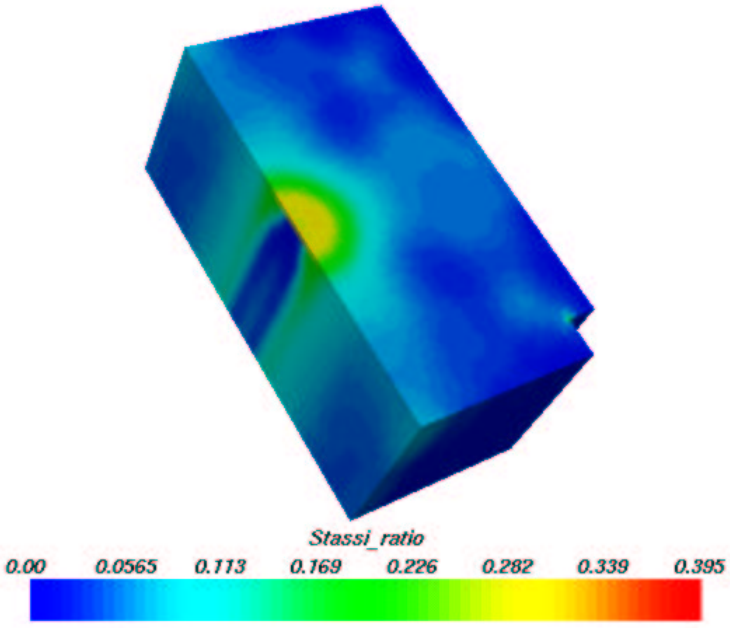

Figure 5.57: Stassi ratio on the outside surface

$t = 35\mu s$

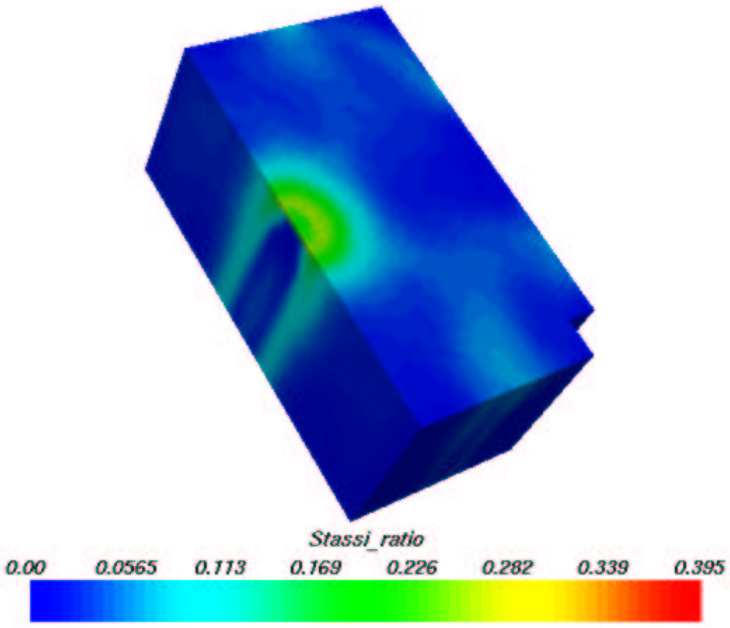

$t = 40\mu s$

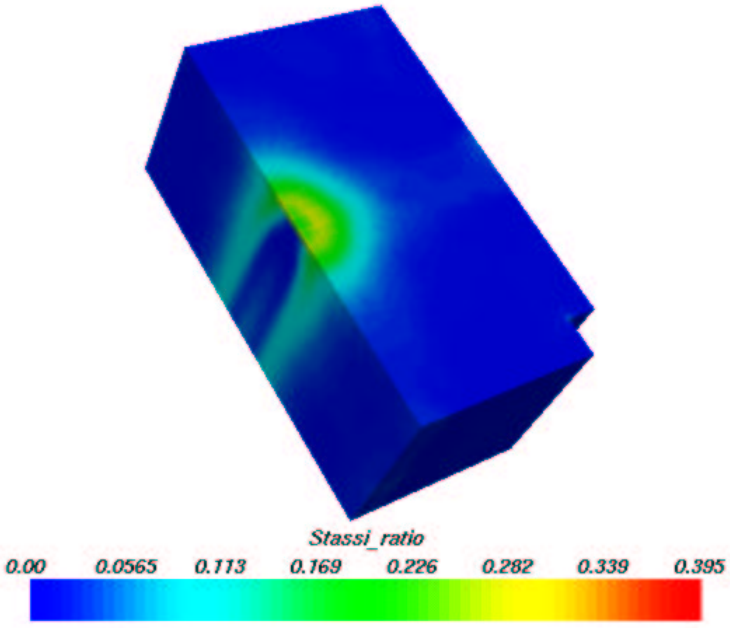

Figure 5.58: Stassi ratio on the outside surface

Chapter 6

Boron Nitride TDI 3D analysis

6.1 The model

The LHC Injection Beam Stopper (TDI) has already been described in some detail. During the design Graphite has been abandoned for the construction of this equipment and substituted by Boron Nitride; this material should guarantee better performances than those shown by graphite, that did not appear satisfactory from the results of the numerical analysis shown in the previous chapters.

The structure is thus composed by a set of 18 Boron Nitride absorbing blocks, followed by an Aluminum and a Beryllium-Copper blocks. The boron Nitride blocks are the most stressed; each of them have a constant section, almost rectangular, with a width of $58mm$ and an height of $54mm$. The length is constant as well and equal to $157.7mm$.

It was shown in the previous chapter that a non uniform mesh may be adopted with a limited influence on the quality of the simulation results, thus allowing to reduce the total number of spectral nodes, and unknowns, to be considered, to decrease the element size and increase the nodal density where more precision is required.

Thus the element size is kept approximately constant on each section, nearly equal to $2mm$, and is variable along the axis of the absorber block, in the direction of the beam; it is equal to $2mm$ near the front and back faces, and reaches a value approximately equal to $8mm$ near the center of each block. A total number of 26928 spectral elements is considered. The number of nodes depends on the spectral degree adopted, for spectral degree $N = 2$ the spectral nodes are 226519, while when $N = 4$ the number o nodes is 1767405, corresponding to over 7 million d.o.f.

Figure 6.1 shows the model adopted, with the spectral "macro" elements put in evidence. Spectral nodes inside each element are not shown.

The geometry of the block and the external boundaries may suggest to take advantage of symmetry conditions: unfortunately, the load conditions do not show this symmetry and thus a model size reduction could not be obtained.

As in the 3D simulations run on graphite, free boundaries are assumed on all the external surfaces of the blocks.

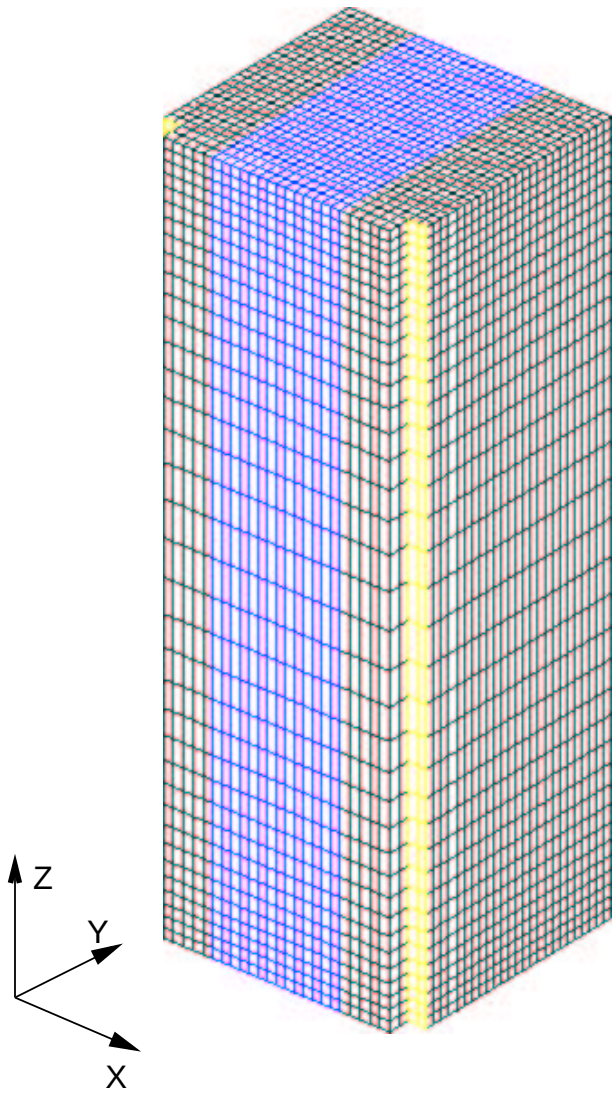

Figure 6.1: Boron Nitride absorber block, spectral element mesh

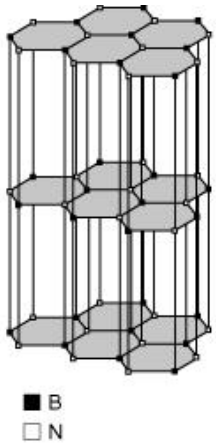

Figure 6.2: Scheme of the Hexagonal Boron Nitride crystal

6.2 Material properties

Boron Nitride is often referred to as "white graphite" because it has the same platy hexagonal structure of carbon graphite, and also some similar properties. It is a white solid material in the as produced hot pressed form. It is non-porous, and non-toxic and may be easily machined.

It is used in Nuclear applications because of its high neutron capture cross section, but it also presents high thermal conductivity, a low thermal expansion, and, most important for this application, a good thermal shock resistance.

The material is highly anisotropic in its electrical and mechanical properties due to the platy hexagonal crystals and their orientation during the hot press consolidation.

Figure 6.2 shows the scheme of the crystal: the platy structure is visible. The intrinsic material reference system is oriented as follows: axes 1 and 2 are parallel to the plane (the material is isotropic in the plane) and direction 3 is perpendicular to the plane.

The material is machined to build the absorber blocks so that the hot pressing direction (3) is coincident to the beam axis direction (Z in the model), so that the direction of maximum resistance is coincident with the maximum load direction.

The following tables contain the relevant thermal and mechanical properties adopted in the simulations; the values are relative to the hexagonal hot-pressed Boron Nitride, grade BN5000 from Sintec and are taken from the Fraunhofer Institut test results (Bericht Nr. B2074/2075/2076).

Most of these properties depend on the temperature value, with the exception of those in Table 6.1, such as Poisson ratios and the density at the reference temperature. The values of the Poisson ratios, difficult to obtain, are not provided from the test; the values in the table have been estimated on the basis of similar materials (the graphite data in particular).

Thermal properties are listed in Table 6.2, it is apparent that all of these are subjected

Property	Symbol	Units	Value
Density	ρ	kgm^{-3}	1910
Poisson ratio 12	ν_{12}	-	0.15
Poisson ratio 23	ν_{23}	-	0.15
Poisson ratio 31	ν_{31}	-	0.15

Table 6.1: Hexagonal Boron Nitride: properties not depending from temperature

Temperature	Expansion coefficient			Specific heat	Thermal conductivity		
T	α_1	α_2	α_3	c_p	k_1	k_2	k_3
$^\circ C$	$\mu m\, m^{-1} {}^\circ C^{-1}$			$J\, Kg^{-1} {}^\circ C^{-1}$	$W\, m^{-1} {}^\circ C^{-1}$		
100	-0.07	-0.07	1.03	1000	34	34	24
200	-0.52	-0.52	0.56	1210	33	33	23
300	-0.37	-0.37	0.92	1370	32	32	23
400	-0.11	-0.11	1.3	1490	31	31	22
500	0.1	0.1	1.57	1590	30	30	22
600	0.28	0.28	1.79	1700	30	30	21
700	0.45	0.45	2.11	1860	29	29	21
800	0.57	0.57	2.5	1950	28	28	20
900	0.51	0.51	2.28	2180	27	27	20
1000	0.52	0.52	2.26	2200	27	27	19
1100	0.76	0.76	2.32		26	26	19
1200	2.07	2.07	3.23		25	25	18
1300	3.04	3.04	3.93		24	24	18
1400					23	23	17

Table 6.2: Hexagonal Boron Nitride: properties not depending from temperature

to great variation depending on the temperature, but it is also evident a great anisotropy: quantities as the thermal expansion coefficient or the thermal conductivity along the hot pressing direction, marked with 3, is clearly different from the in-plane properties, those along the axis marked with 1 and 2.

The elastic moduli are listed in Table 6.3. Again, a clear link with the temperature value is evident, but the anisotropy is less significant for these quantities, since the elastic moduli along the principal direction are quite similar.

It is important to say that the experimental tests from the Fraunhofer institute only give a measure of the normal elastic moduli E_1, E_2 and E_3, while no data are available for the shear moduli G_{12}, G_{23} and G_{31}. These values are essential for a mechanical analysis, so they have been estimated from the following formula well suited for quasi isotropic behavior:

$$\frac{1}{G_{ij}} = \frac{1}{E_i} + \frac{1}{E_j} + \frac{\nu_{ij}}{E_i} \tag{6.1}$$

Table 6.4 presents the values of the rupture stress components. Here again is evident

Temperature	Young's modulus			Shear modulus		
T	E_1	E_2	E_3	G_{12}	G_{23}	G_{31}
$°C$	GPa			GPa		
20	34	34	38	14.8	15.5	15.5
350	46	46	41	20	19	19
700	10	10	15	4.3	5.1	5.1

Table 6.3: Hexagonal Boron Nitride: properties not depending from temperature

Temperature	Tensile strength			Compressive strength			Shear strength		
T	σ_{4p1}	σ_{4p2}	σ_{4p3}	σ_{c1}	σ_{c2}	σ_{c3}	σ_{s12}	σ_{s23}	σ_{s31}
$°C$	MPa			MPa			MPa		
20	75	75	75	110	110	99	75	75	75
350	95	95	69	111	111	100	95	95	95
700	37	37	27	59	59	69	37	37	37
1000	9	9	4				9	9	9

Table 6.4: Hexagonal Boron Nitride: properties not depending from temperature

a strict correlation between the stress values and the temperature. Compressive strength is higher than tensile strength, and similar results appear along the different directions: the material is almost isotropic, concerning strength properties.

The mechanical tests only gave results for the tensile and compressive strength. To estimate shear strength, coherently with the strength criteria adopted, we assumed that each component of the shear strength is equal to the tensile strength along the axes 1 and 2.

The material is checked for the failure with the maximum stress criteria: each component of the stress tensor is compared with the corresponding failure value, either in tension or in compression depending on the sign of the stress.

The maximum value of the ratio between the stress component and the limit value is assumed as a measure of how critic a stress state is. The maximum allowable value for the ratio is 0.66, that corresponds to an allowable stress of $\frac{2}{3}$ of the failure stress.

6.3 Load conditions

Each block has been loaded by the energy deposition of a train of four batches. The energy deposition per particle is the result of a Monte Carlo simulation and is introduced as input for the thermal and mechanical simulation.

The exact particle distribution in space and time, i.e. the energy density in the material and the time law of its deposition, has been exactly simulated: the reader may refer to the second chapter for details. The beam energy deposition starts at $t = 2.14\mu s$ and ends at $t = 10.0\mu s$.

Binning	R_{min}	R_max	NR	θ_{min}	θ_{max}	$N\theta$	Z_{min}	Z_{max}	NZ
-	mm	mm	-	rad	rad	-	mm	mm	-
1	0	62	155	$-\pi$	π	8	0	4150	415
2	0	62	155	$-\pi$	π	8	0	2850	285
3	0	62	155	$-\pi$	π	8	2850	3450	60
4	0	62	155	$-\pi$	π	8	3450	4150	70

Table 6.5: Monte Carlo simulation: mesh properties

Several load conditions have been considered: in a first test the beam load in concentrated at the center of the absorber blocks, the so called **Normal** conditions. In a second test (**Grazing**) the beam axis is chosen to graze the surface of the absorber block that faces the beam orbit, and the beam axis is assumed to be tangent to that surface. The third test considers the beam axis inside the absorber block, parallel to the surface facing the undisturbed beam orbit, and $4mm$ distant from the surface.

The power deposition on the spectral element model is calculated from the interpolation on each spectral node of the results of a Monte Carlo simulation run on Fluka, that gives the density of the energy deposited on the material by a single proton of the beam. The Monte Carlo simulation was run on a computational grid composed by 4 binnings in cylindrical coordinates. The properties of the Fluka mesh adopted are summarized in Table 6.5.

This discretization, together with an adequate statistic, should guarantee a sufficiently accurate description of the energy deposition in the radial direction, a good approximation along the axis, but should not result very accurate in the tangential direction around the beam axis.

First, a complete analysis of the 18 Boron Nitride blocks was run, with a spectral degree $N = 2$, in order to find the most stressed block; then, the same mesh has been used to check for the most critical load condition, checking the resistance of the most stressed block, when the beam hits at different distances from the internal surface, starting from the grazing condition in which the beam axis is tangent to the lower internal surface.

The same particle energy deposition results are used for all the simulations, since it is assumed that the results are not influenced by the presence of discontinuities in the material. The particle distribution refers to the case in which all the particle energy may be deposited inside the material: if this does not happen, as in the grazing case, only the portion of the energy deposition profile that actually falls inside the material is considered without any influence by the portion that falls outside the blocks.

Finally a very detailed mesh is used, with a spectral degree equal to 4, to simulate the three design conditions: centered beam, grazing and near surface load.

The results in terms of temperature and maximum stress found in the simulated period are shown for each Boron Nitride absorber block. Detailed results in terms of kinetic energy propagation, pressure and stress distribution are illustrated in greater

detail for the most stressed block.

6.4 Results analysis

6.4.1 Most stressed block

A thermo-mechanical analysis was run for all of the Boron Nitride blocks, in the centered beam conditions, to check for the block subjected to the most dangerous thermal loads and mechanical stresses.

The beam load acts on a set of 18 Boron nitride absorbing blocks, and it is necessary to simulate the behavior of each of the block separately, and check for the resistance of each of them, in fact it is not easy to decide a priori which block is the most stressed one. The simulations are run up to $t = 80\mu s$ and the most critical stress condition found in this time extent is verified in each point. The spectral degree is $N = 2$ and a time step $\Delta t = 1.0E - 7s$ was chosen.

Figure 6.3 display the Fluka energy deposition inside the absorber blocks due to a single proton, resulting from the interpolation on the spectral element model of the data obtained by the Monte Carlo simulation. It is evident that the beam is highly concentrated in the first three blocks, with a high value on the beam axis, maximum on the third block, and then gradually decreases in intensity and is less concentrated radially on the subsequent blocks.

Figure 6.4 shows the temperature increase due to the beam energy deposition inside the material at the end of the heating time in a central section of all the blocks.

In the first blocks the heated volume is highly concentrated around the beam axis, with the temperature that increases to reach the maximum in the third block. The energy deposited on the subsequent block is less concentrated around the axis and the maximum temperature decreases. The temperature follows the energy deposition profile given by the Fluka output, but is not proportional to it since the thermal capacity is not constant but depends on the material temperature.

Not surprisingly, the third block results the most stressed one, since the maximum temperature is reached and high values of radial temperature gradient around the beam axis are present. Figure 6.5 shows the maximum stress ratio found in the whole simulation: it turns out that the most stressed blocks are the first 5, and the third in particular. The stressed area is concentrated around the beam axis where the maximum temperature increase is reached. The last blocks do not show peaks: the material seems to be stressed more uniformly, due to the elastic wave propagation.

Figure 6.6 presents the maximum stress ratio in each block for an $80\mu s$ simulation.

The stresses resulting from the thermal load and the resulting stress wave propagation have been evaluated at each time step at each node of each absorber block. For all nodes the ratio between every component of the stress tensor and the corresponding rupture stress value is calculated, and the maximum is evaluated. The points on the graph represent the maximum value of these ratio for the block, considering all the

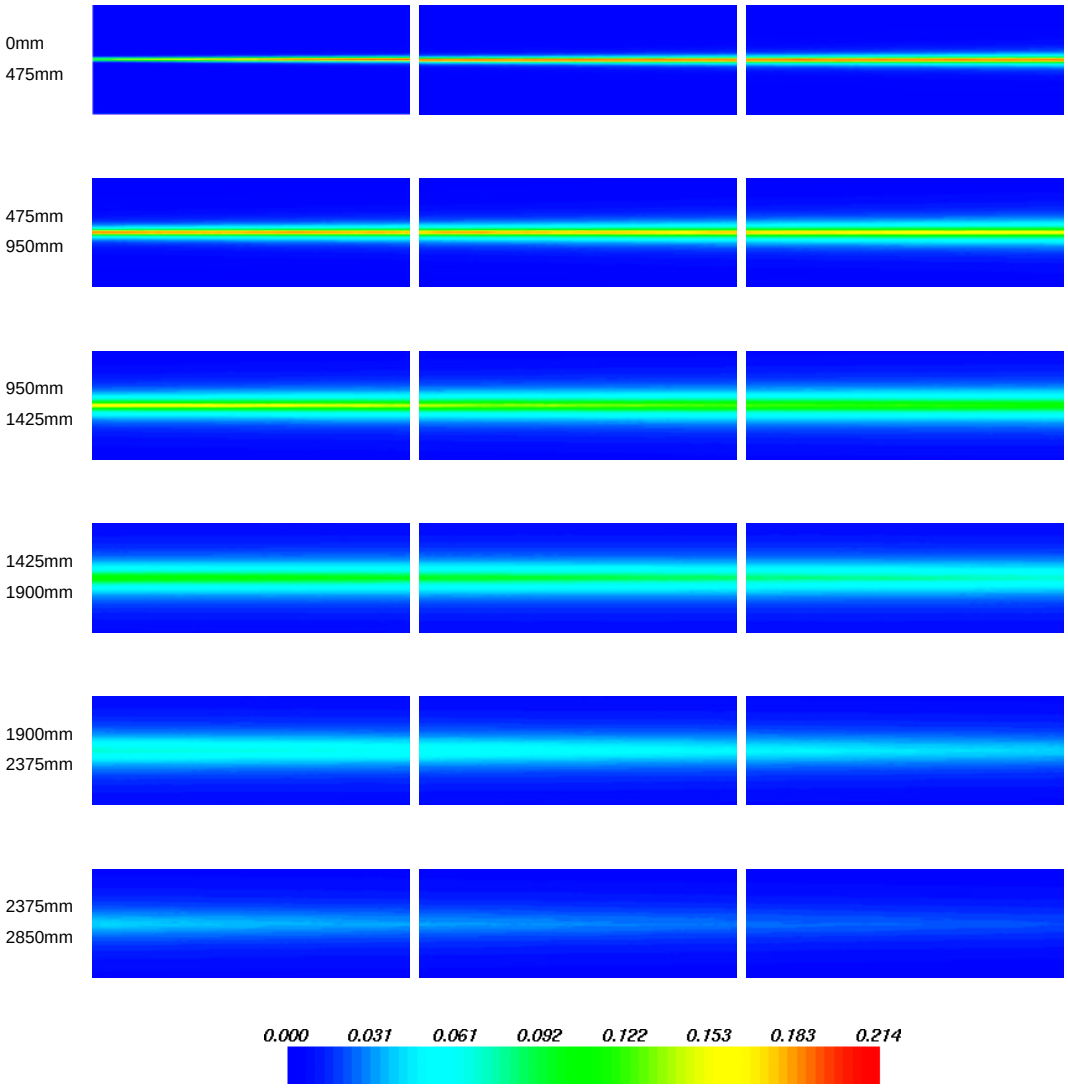

Figure 6.3: Proton energy deposition per unit volume ($\frac{GeV}{cm^3}$) in the boron nitride absorber blocks

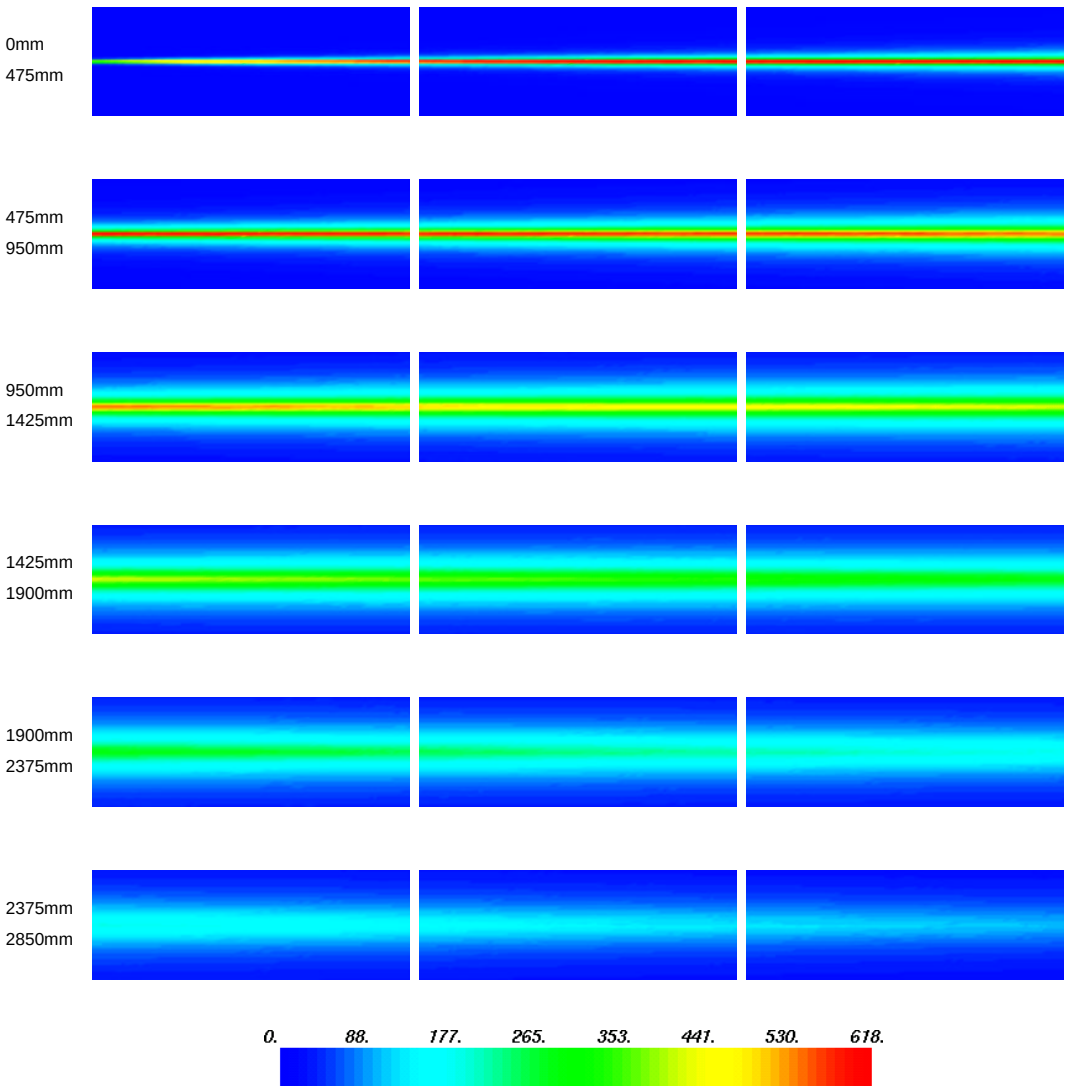

Figure 6.4: Temperature increase (K) in the boron nitride absorber blocks

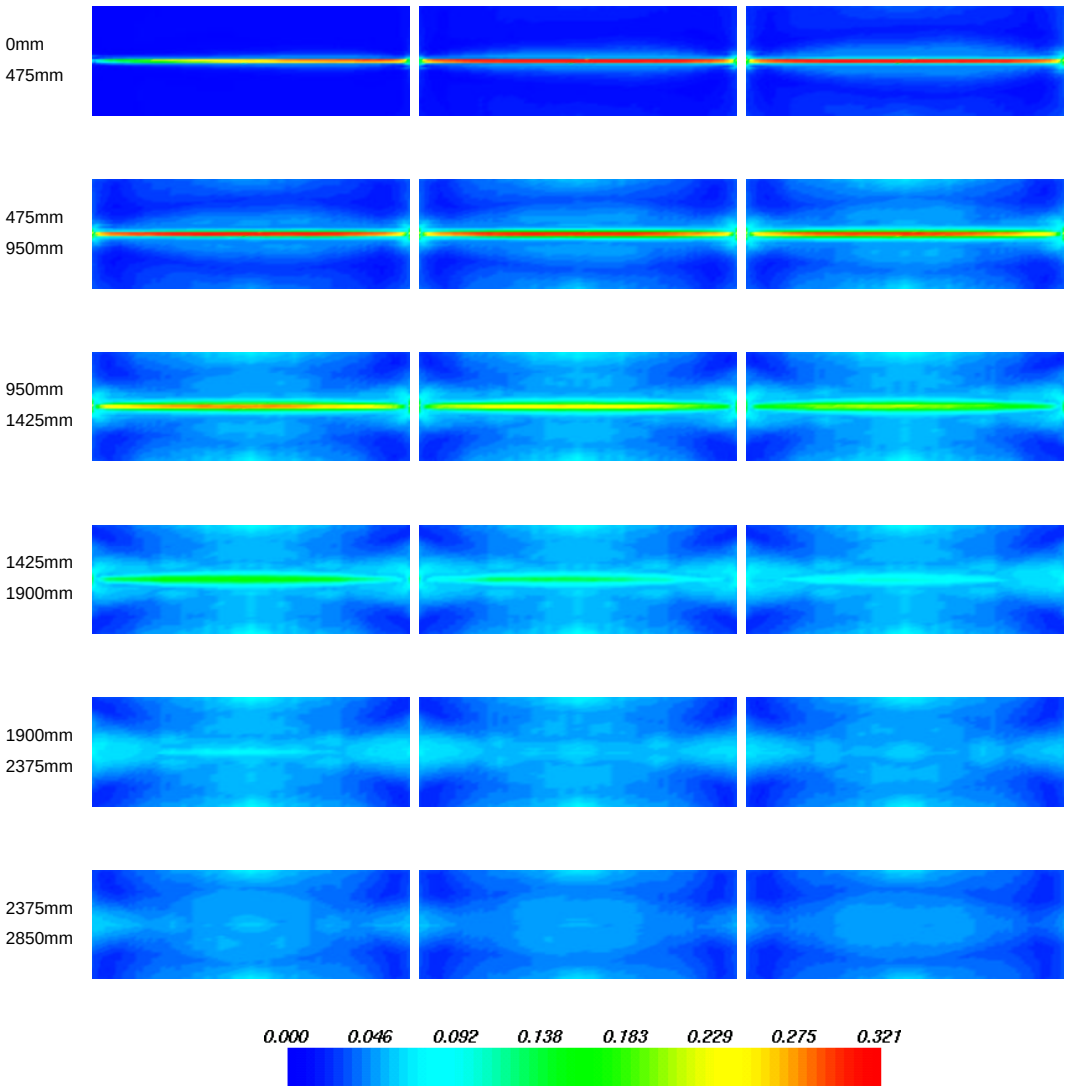

Figure 6.5: Maximum stress ratio (-) in the boron nitride absorber blocks

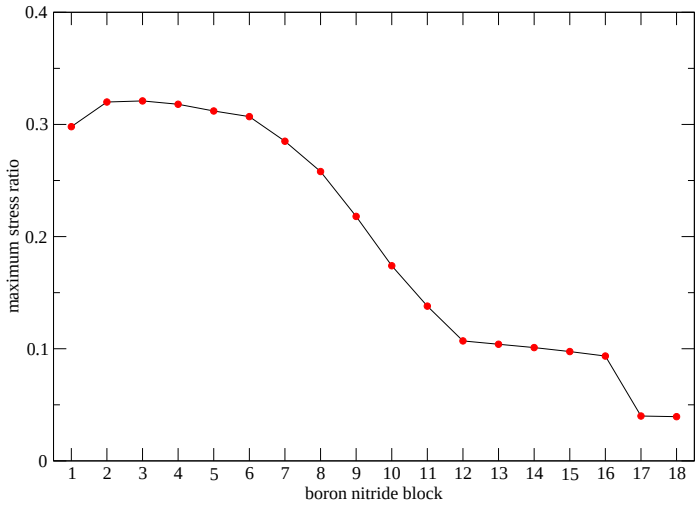

Figure 6.6: Maximum stress ratio in the boron nitride absorber blocks

stress components and all the point of the block during the simulation time.

The maximum stress ratio has approximately the same aspect of the temperature on the beam axis: the maximum value is found in the third block, as expected. The value of the ratio is 0.32, lower than the maximum allowable value of 0.66.

6.4.2 Most stressed condition

The particle beam may heat the absorber blocks at various distances from the lower internal surface: it is therefore interesting to verify, as in the case of the graphite block, if there exists a particular position for which the resulting stresses reach the maximum value.

Several numerical simulations were therefore run on the third block, with the beam axis being moved progressively inside the material starting from the tangent position ($0mm$), up to $5mm$ from the surface. The analyses were run adopting a spectral degree $N = 2$ for a total simulation time of $80\mu s$, a time step $\Delta t = 1.0E - 7s$ was chosen.

The graph in Figure 6.7 shows the maximum stress ratio value found in the block for the different beam positions. The results show that the maximum value is more or less constant for the different beam positions considered.

This is a clear difference with the graphite behaviour: its reason is not due to a different behavior of the two materials rather to failure criterion adopted.

In fact, the Stassi failure criterion was in fact adopted for graphite, it considers the influence of the internal pressure in the evaluation of an equivalent stress: hence, in the volume near the beam axis where a positive and high value of the internal pressure is

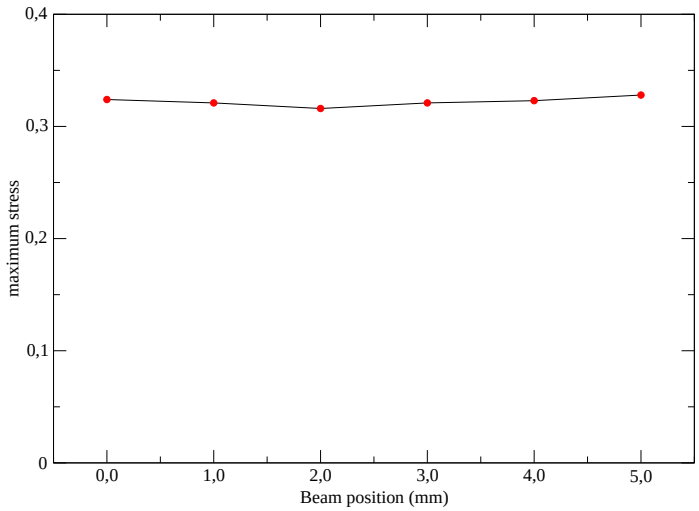

Figure 6.7: Maximum stress ratio for different hitting positions

found, the equivalent stress is lower and the characteristic annular form appears. When the beam approaches the internal surface there cannot be an high value of the internal pressure any longer, and according to the Stassi criterion the maximum equivalent stress increases; this was verified in the analysis of graphite.

As already mentioned the Stassi criterion is not applicable to this structure due to the anisotropic properties of the Boron Nitride. The maximum stress criterion was selected, which does not consider any effect due to the internal pressure. Therefore the maximum stress value, located on the points on the axis of the beam heated volume is only partly influenced by the proximity to the border of the block.

In these load conditions the maximum stress criterion is more severe than the Stassi criterion; the equivalent stress calculated on the basis of the maximum stress for the graphite is expected to be higher than its counterpart evaluated on the Stassi basis and presented in the previous chapters.

6.4.3 Detailed analysis. Beam distance: $27mm$

The third block results the most stressed one among the 18 Boron nitride Absorber blocks. The analysis has been therefore focused on this block, running more detailed simulations in the three design conditions selected. The spectral degree chosen for these analyses is $N = 4$ and the time step is fixed to $\Delta t = 2.0E - 8s$.

First the centered load conditions results are shown. Figure 6.8 and 6.9 display the temperature increase in the block, due to the energy deposition: the heated volume is almost cylindrical, very concentrated around the axis. Beam deposition starts at

$t = 2.14\mu s$ and ends at $t = 10\mu s$ with a quasi constant temperature rise. In all the following figures the model is oriented so that the beam exits form the surface of the picture, the block being viewed from the rear surface.

$t = 4\mu s$

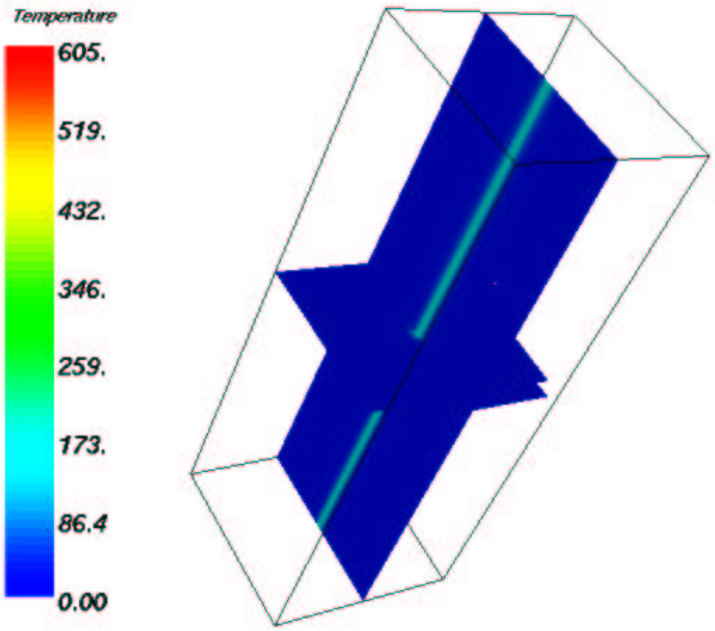

$t = 6\mu s$

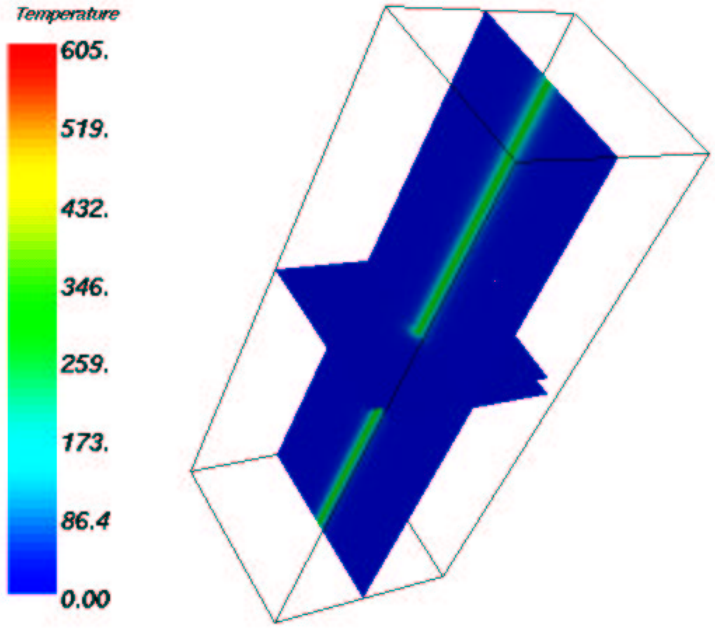

Figure 6.8: Temperature rise in the third boron nitride absorber block [K]

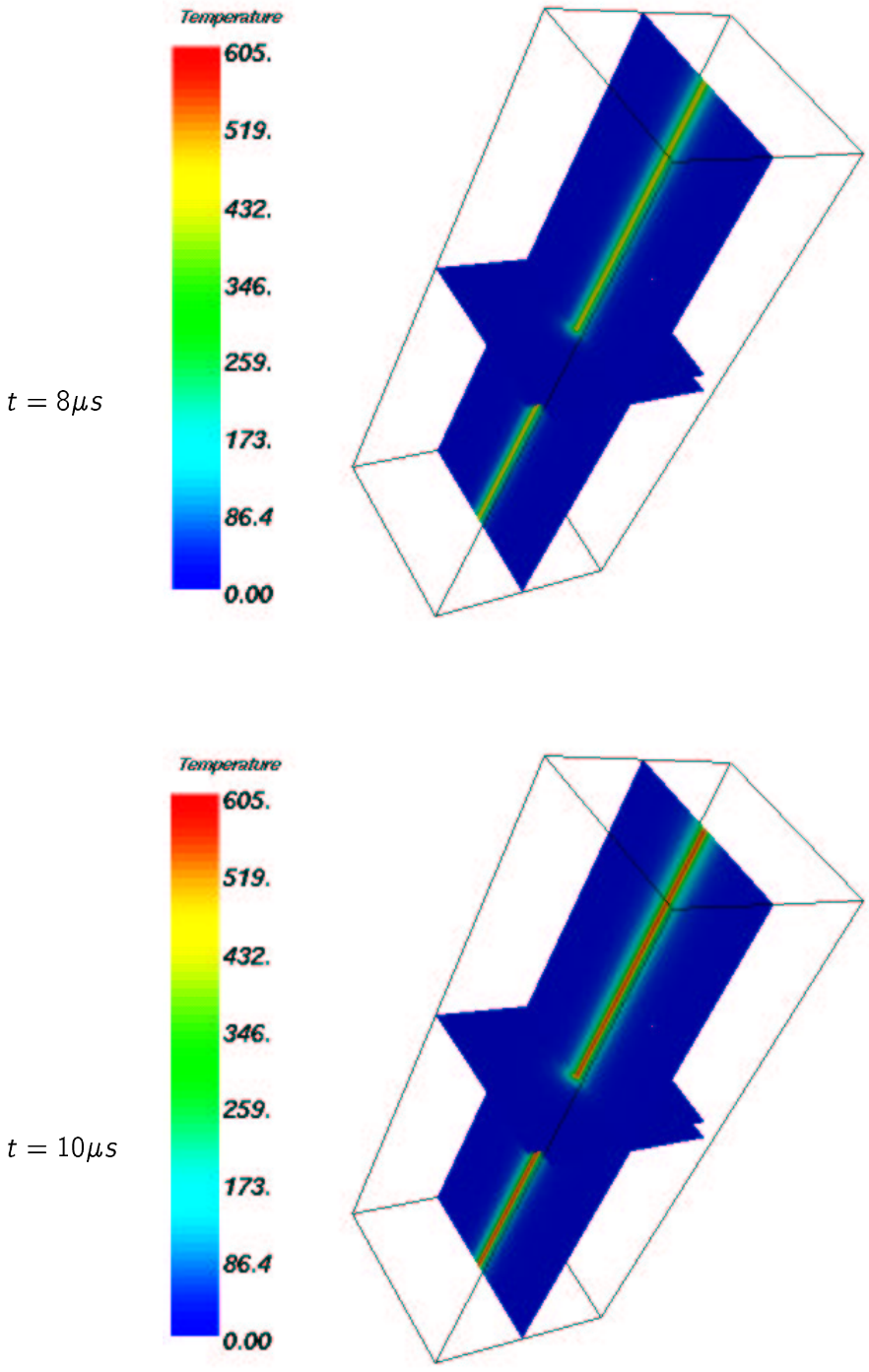

Figure 6.9: Temperature rise in the third boron nitride absorber block [K]

In Figures from 6.10 to 6.16, kinetic energy density on the the external surface is depicted.

The pictures show that the general behavior of the Boron Nitride absorber block is very similar to that found in the 3D analysis run on the graphite block. In the external surface views the propagation of a circular wave departing from the beam axis is clearly visible. After the end of the beam deposition at $t = 10\mu s$, the energy density maximum value reduces suddenly, and the propagation of the longitudinal wave becomes more evident (see Figure 6.12,6.13, 6.14); the radial wave is subjected to multiple reflections on the boundaries and its path becomes soon difficult to follow. In Figure 6.16 it is possible to see the longitudinal wave that after reflection comes back to the front and rear faces.

The results have shown that the wave propagation, clearly visible by the kinetic energy plots, is not evident when the pressure or equivalent stress plots are analyzed: therefore only the results at the end of the beam energy deposition are shown as an example in Figures 6.17, 6.18.

The difference with respect to the graphite results, where the propagation of the stress wave is more clearly visible, is partly due to the above mentioned different equivalent stress adopted, but also to the different material properties. We have also to mention that the load conditions are different with respect to the graphite simulation: a lower value of the mean radius of the heated volume results from the Fluka data interpolation in this block.

Finally, Figure 6.19, shows the maximum value of the stress ratio in each point of the block, and the time at which the value is reached. The results are quite similar to those shown in Figure 6.18: the most stressed volume is still concentrated around the beam axis, but also other parts of the volume are subjected to significant stresses, and the maximum value too is higher, due to the elastic stress wave.

Concerning the time results, it is interesting to see that the color plot is not continuous but is characterized by sharp separations between different parts of the block. This means that the maximum stress ratio is found at similar times for the points belonging to a particular part of the model, and the division between the parts is related to the path that the elastic wave follows through the block.

Stress ratio results indicate again that the stress condition appears safe according to the simulation. The maximum value of 0.32 found in the model corresponds to a safety factor of more than 3 over the rupture and of almost 2 over the allowable stress, giving enough margin for the approximations affecting numerical simulation.

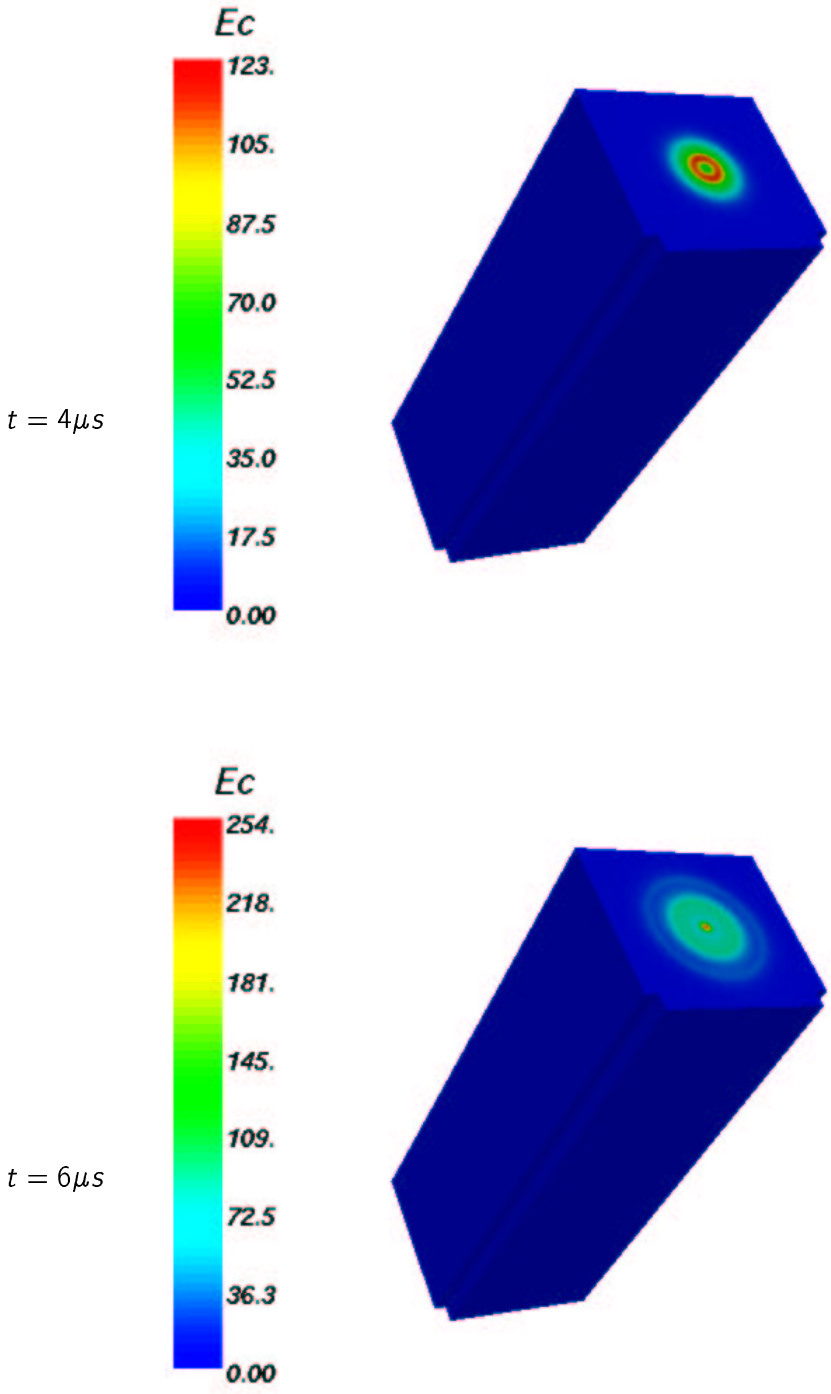

Figure 6.10: Kinetic energy density, centered beam $[J/m^3]$

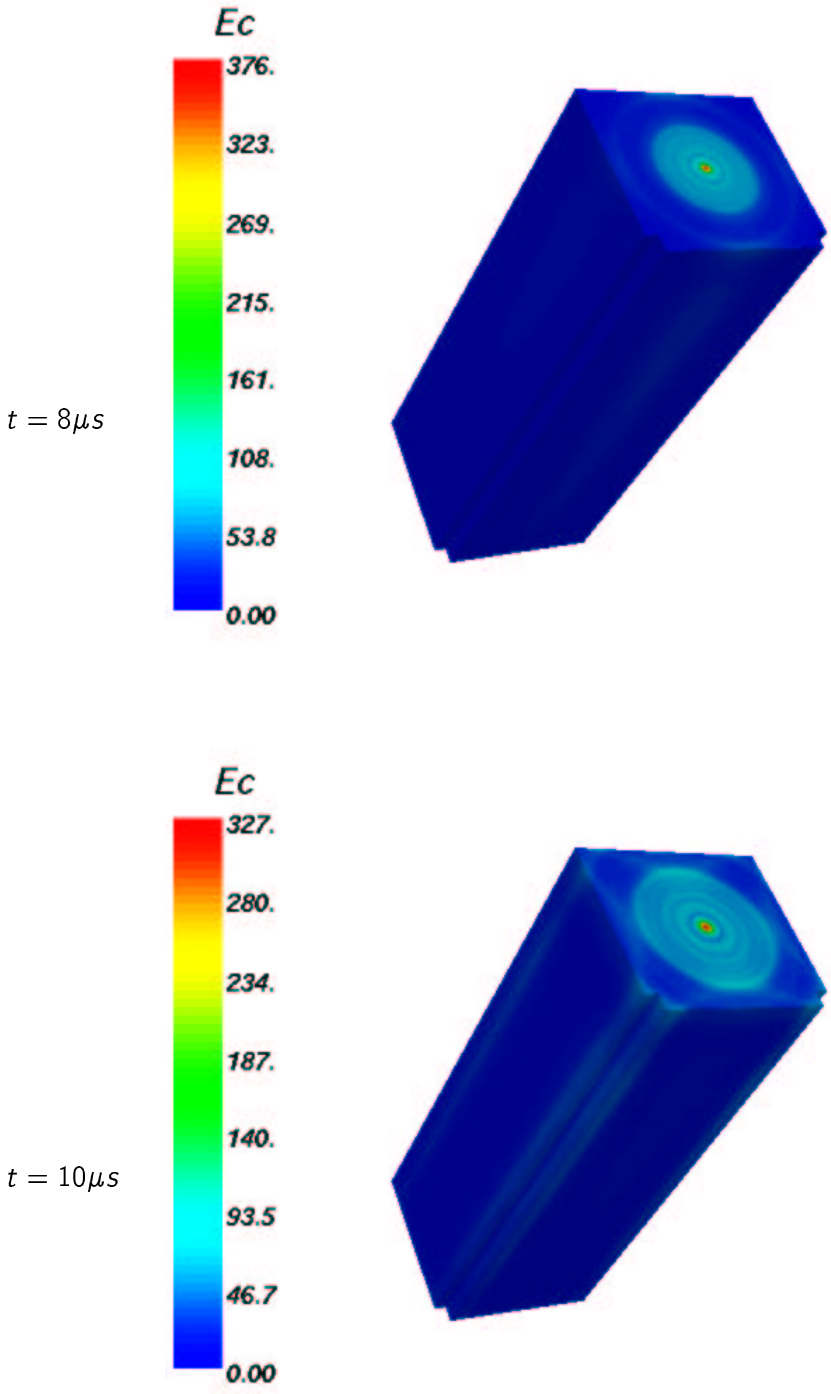

Figure 6.11: Kinetic energy density, centered beam $[J/m^3]$

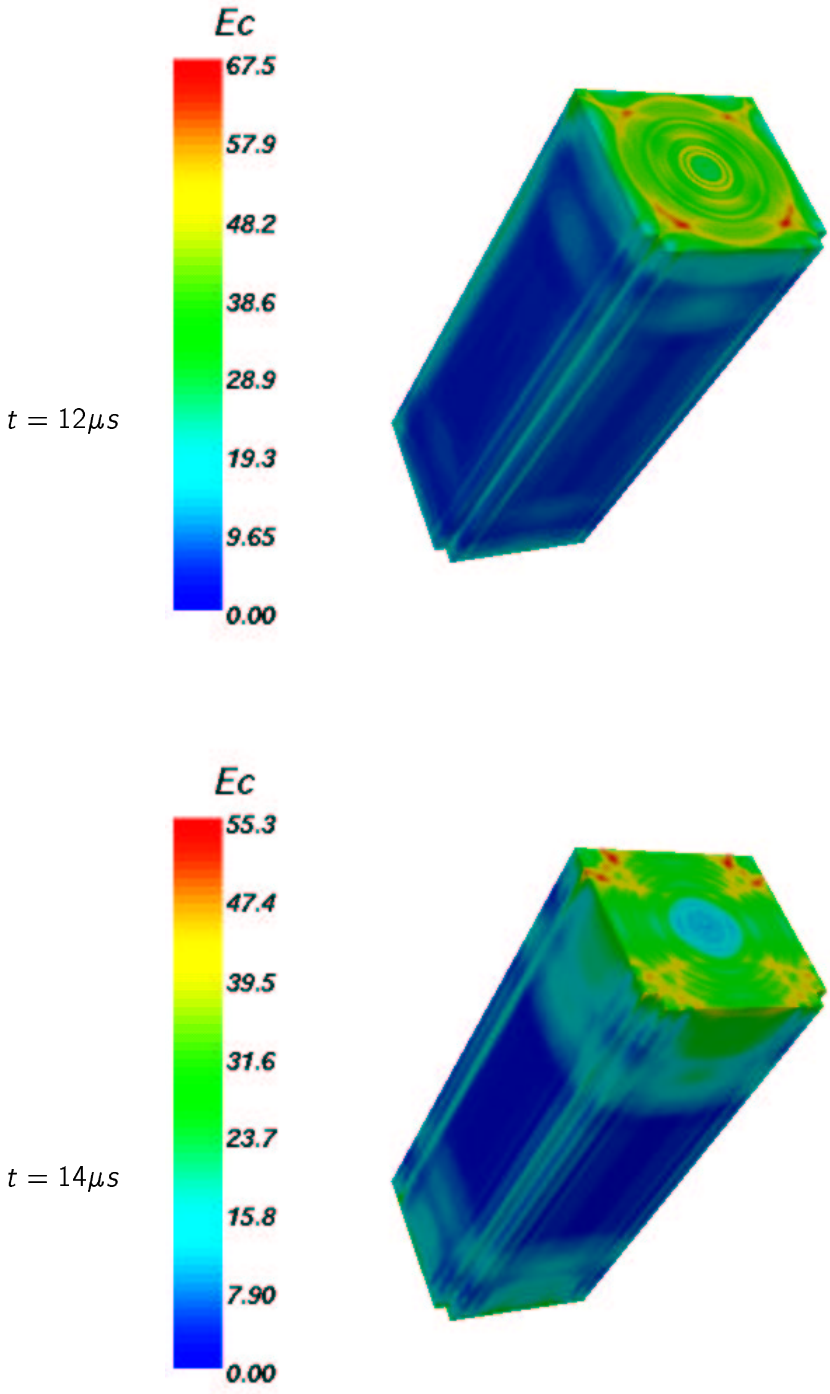

Figure 6.12: Kinetic energy density, centered beam $[J/m^3]$

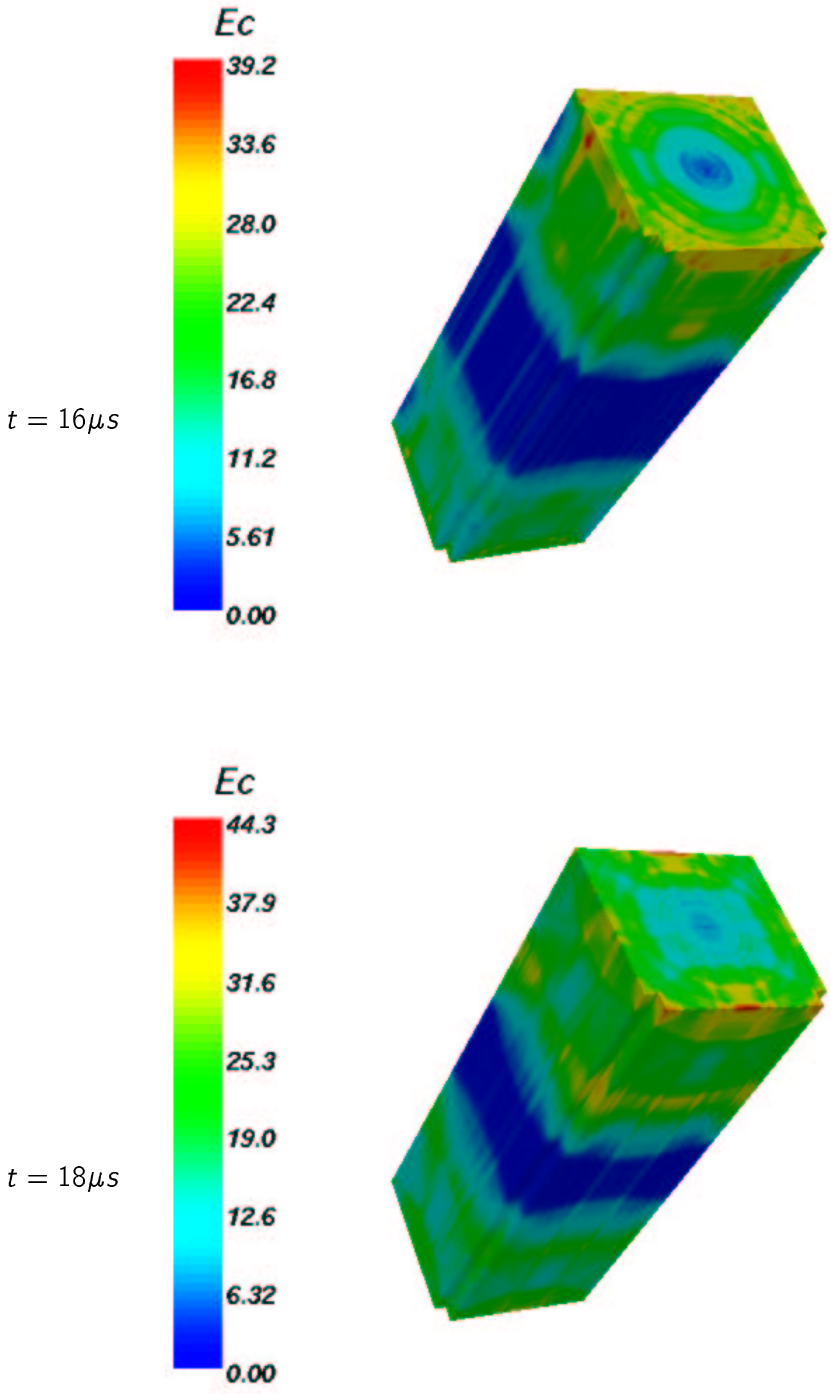

Figure 6.13: Kinetic energy density, centered beam $[J/m^3]$

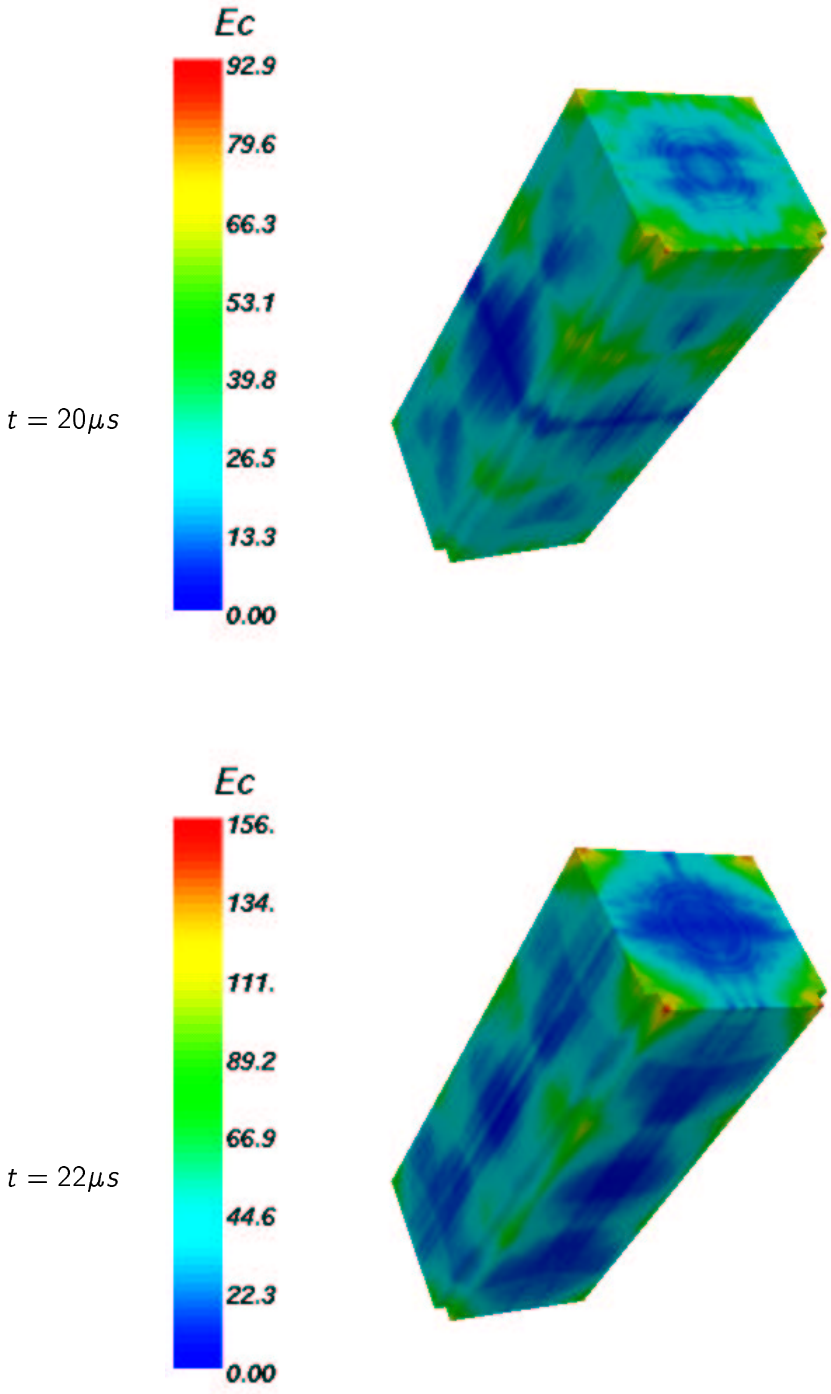

Figure 6.14: Kinetic energy density, centered beam $[J/m^3]$

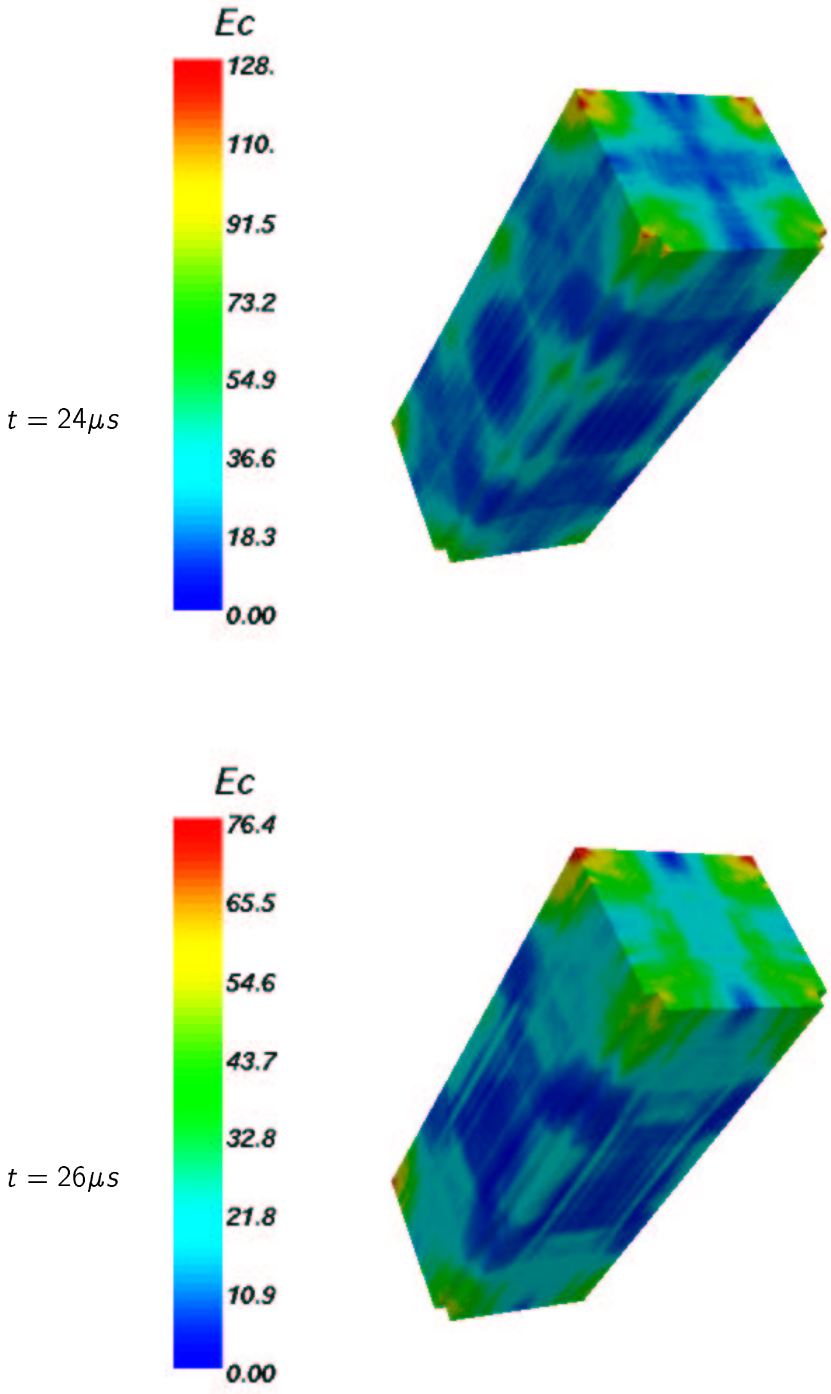

Figure 6.15: Kinetic energy density, centered beam $[J/m^3]$

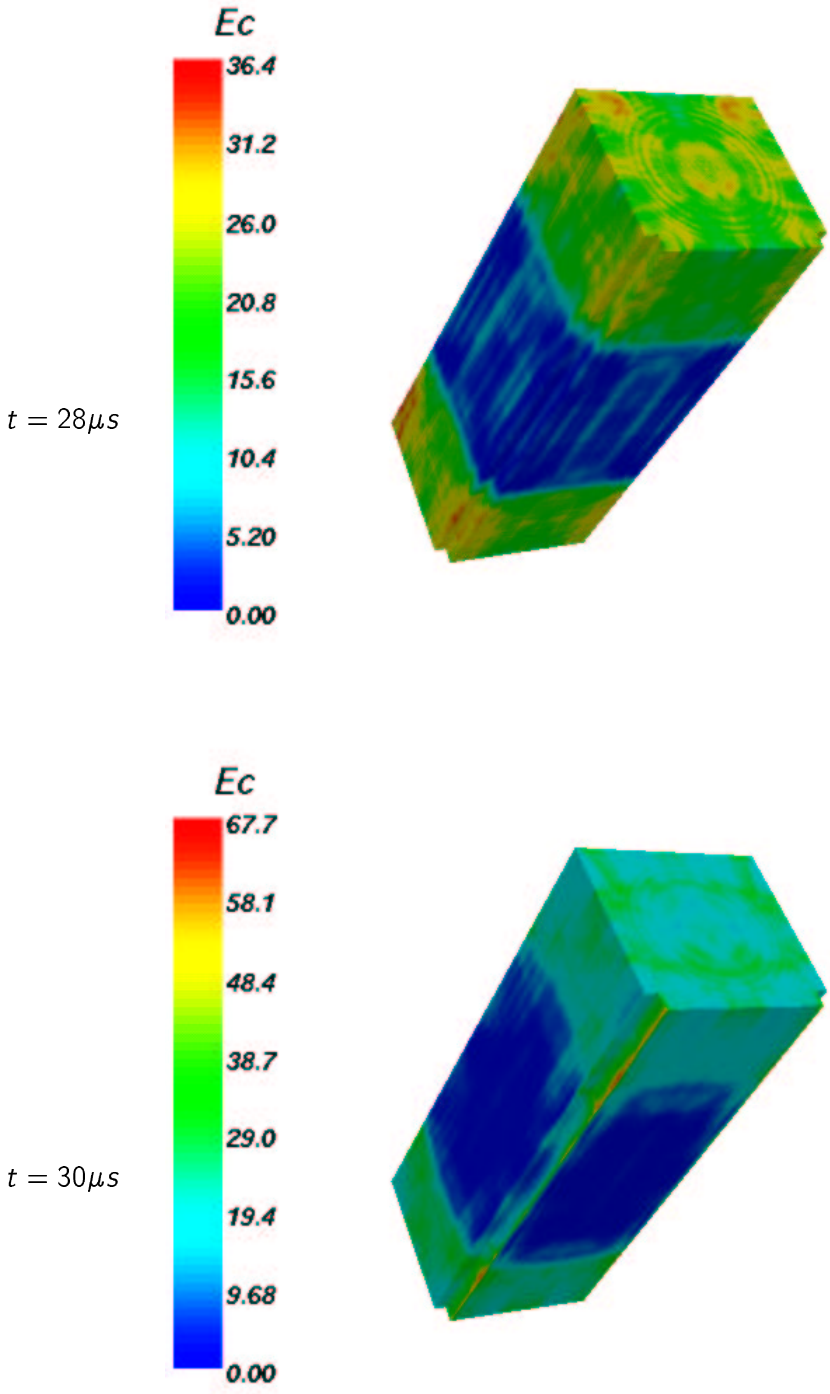

Figure 6.16: Kinetic energy density, centered beam $[J/m^3]$

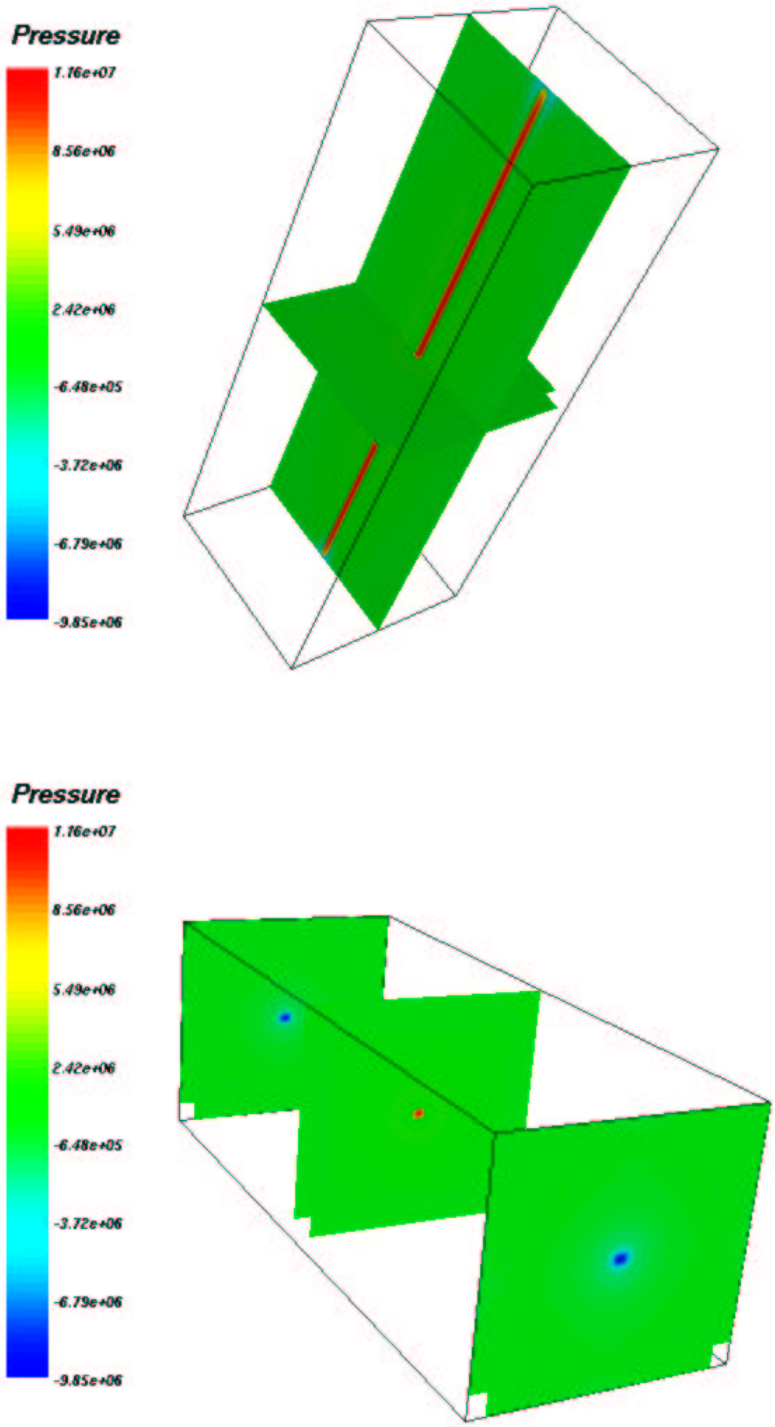

Figure 6.17: Internal pressure at $t = 10\mu s$, centered beam $[Pa]$

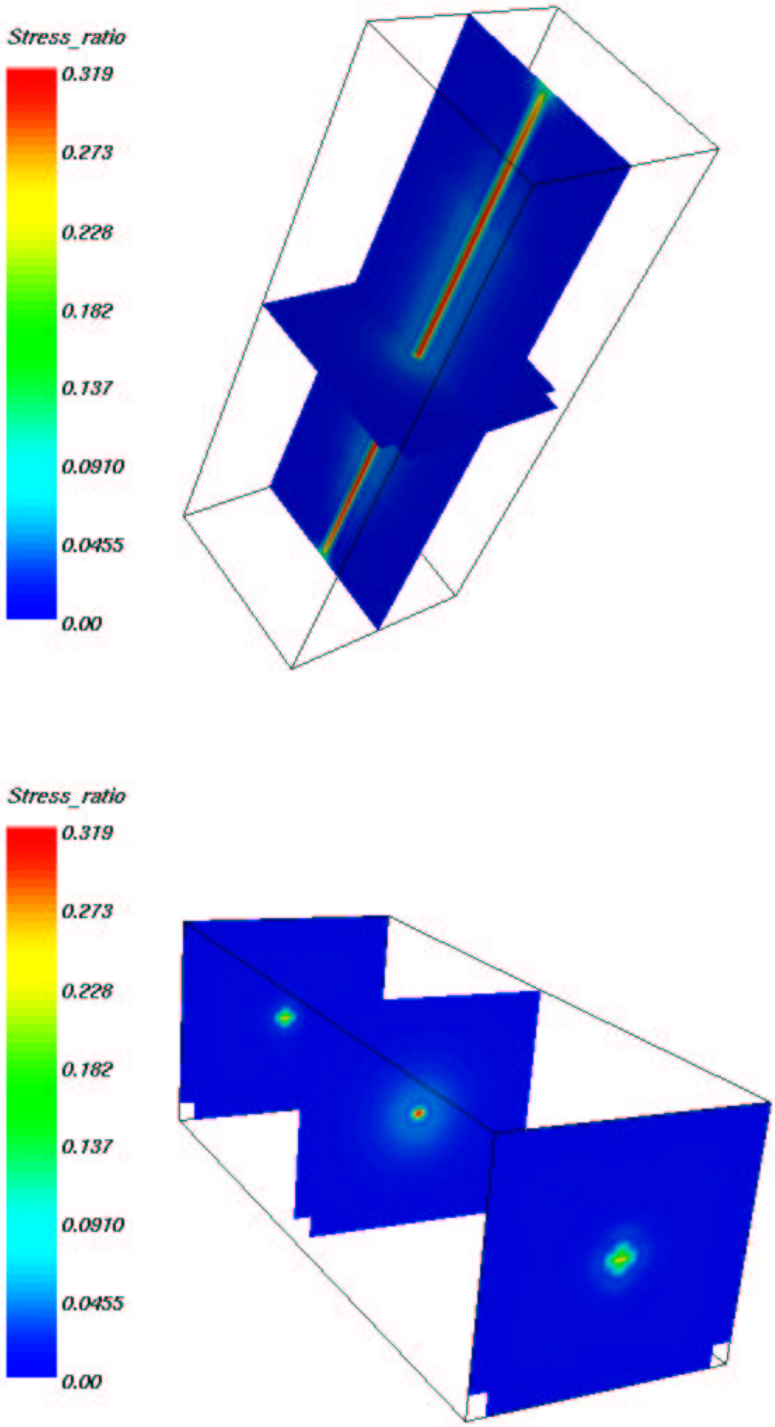

Figure 6.18: Stress ratio at $t = 10\mu s$, centered beam [−]

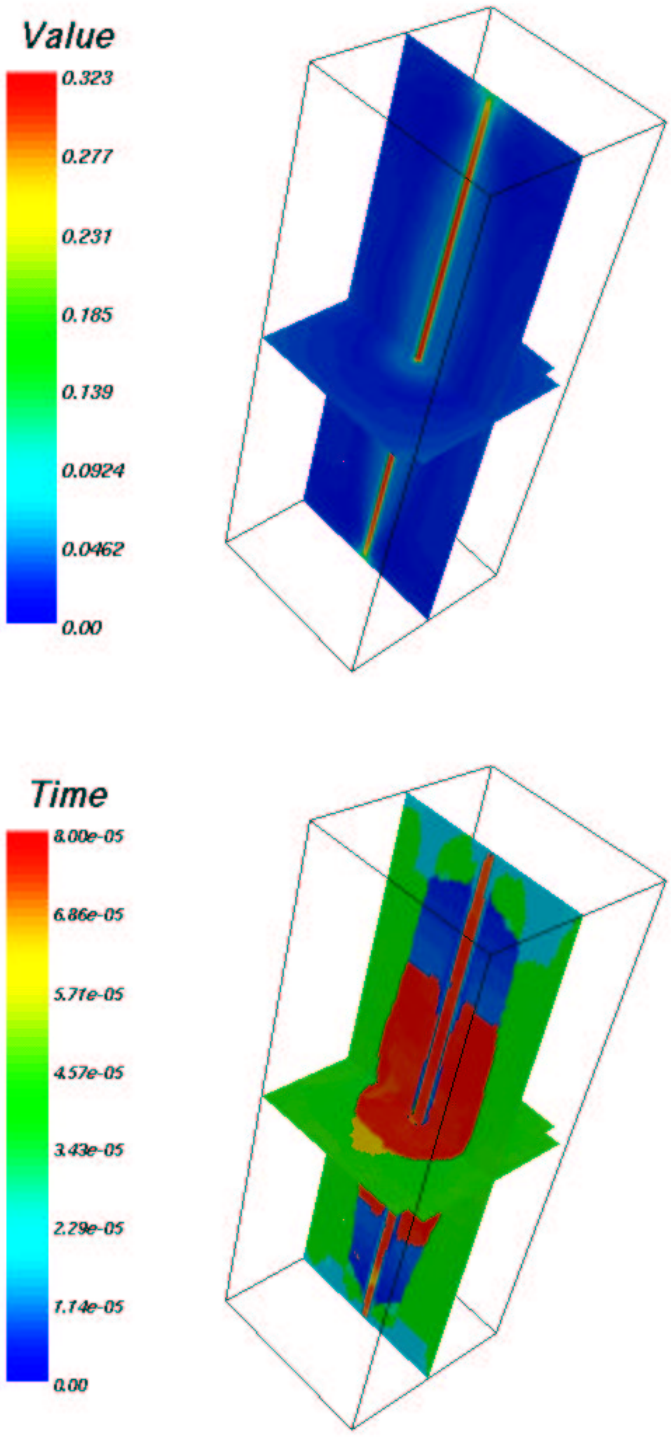

Figure 6.19: Max stress ratio, centered beam, value on top [-], time [s] on bottom

6.4.4 Detailed analysis. Beam distance: $0mm$

The grazing condition is now analyzed in detail. The mesh is the one already introduced, with a spectral degree $N = 4$. First the kinetic energy density is shown with an external view of the block: Figures from 6.20 to 6.26, exibit how the kinetic energy propagates inside the block, with an elastic wave moving radially from the beam axis and longitudinally from the front and rear faces.

Again, the maximum value of the kinetic energy density is subjected to a great variation in time, with very high values during the heating period. In the Figures 6.20 6.21 the kinetic energy density is concentrated at the edges of axis of the heated volume, where the material of the surface is pulled out by the thermal expansion. In figures 6.22 6.23 the radial and longitudinal wave propagation are more evident, with the first wave reflections on the block external faces. The kinetic energy distribution then becomes soon very difficult to be interpreted (see Figure 6.26 due to the multiple reflections of the stress wave).

The stress wave propagation cannot be clearly identified by the analysis of the pressure and equivalent stress plots; pressure and stress ratio results at the end of the beam loading period are shown in Figures 6.27 and 6.28.

The stress ratio is very similar to that found for the centered load conditions: the most critical condition is found again in the beam axis, and is related to the ratio of the longitudinal component of the stress tensor with the corresponding rupture stress. This is subjected to a limited influence by the surrounding material, and/or by the beam position: similar results are found in these two analyses and are continued from further simulations.

The internal pressure results also are similar to those concerning centered beam load; the results in Figure 6.27 represent the internal pressure in the material, defined as one third of the sum of the principal stresses, and therefore does not coincide with the external pressure on the external surface of the block that vanishes everywhere.

Figure 6.29 shows the maximum value of the stress ratio for each point of the block during the simulation time, and the instant at which this maximum value is reached. The maximum values are very similar to those found at $t = 10\mu s$. The influence of the stress wave is limited, the most stressed part of the model being again concentrated around the beam axis where the maximum temperature increase is reached.

The results of the maximum stress ratio indicate that the maximum equivalent stress is lower than the allowable stress value.

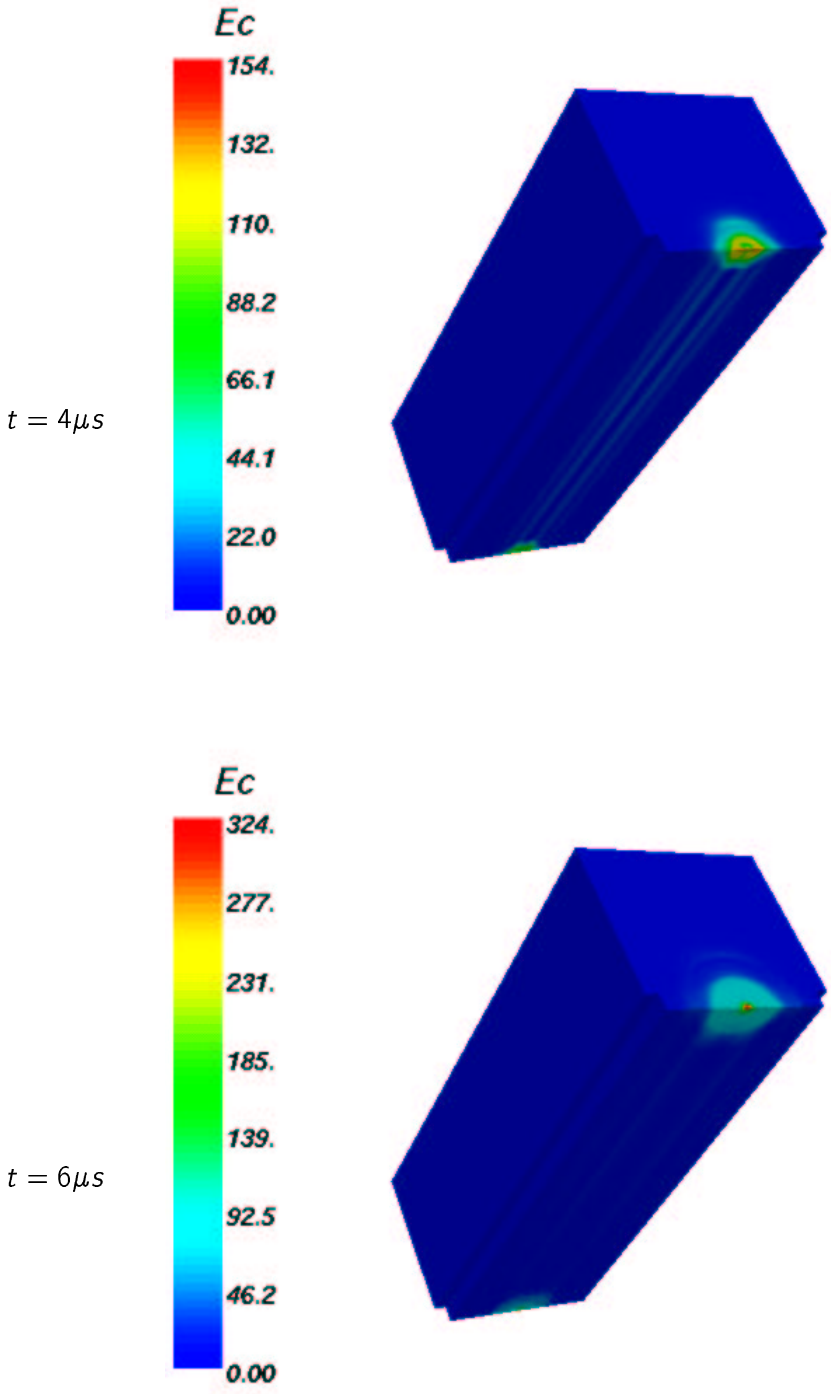

Figure 6.20: Kinetic energy density, beam distance $0mm$ $[J/m^3]$

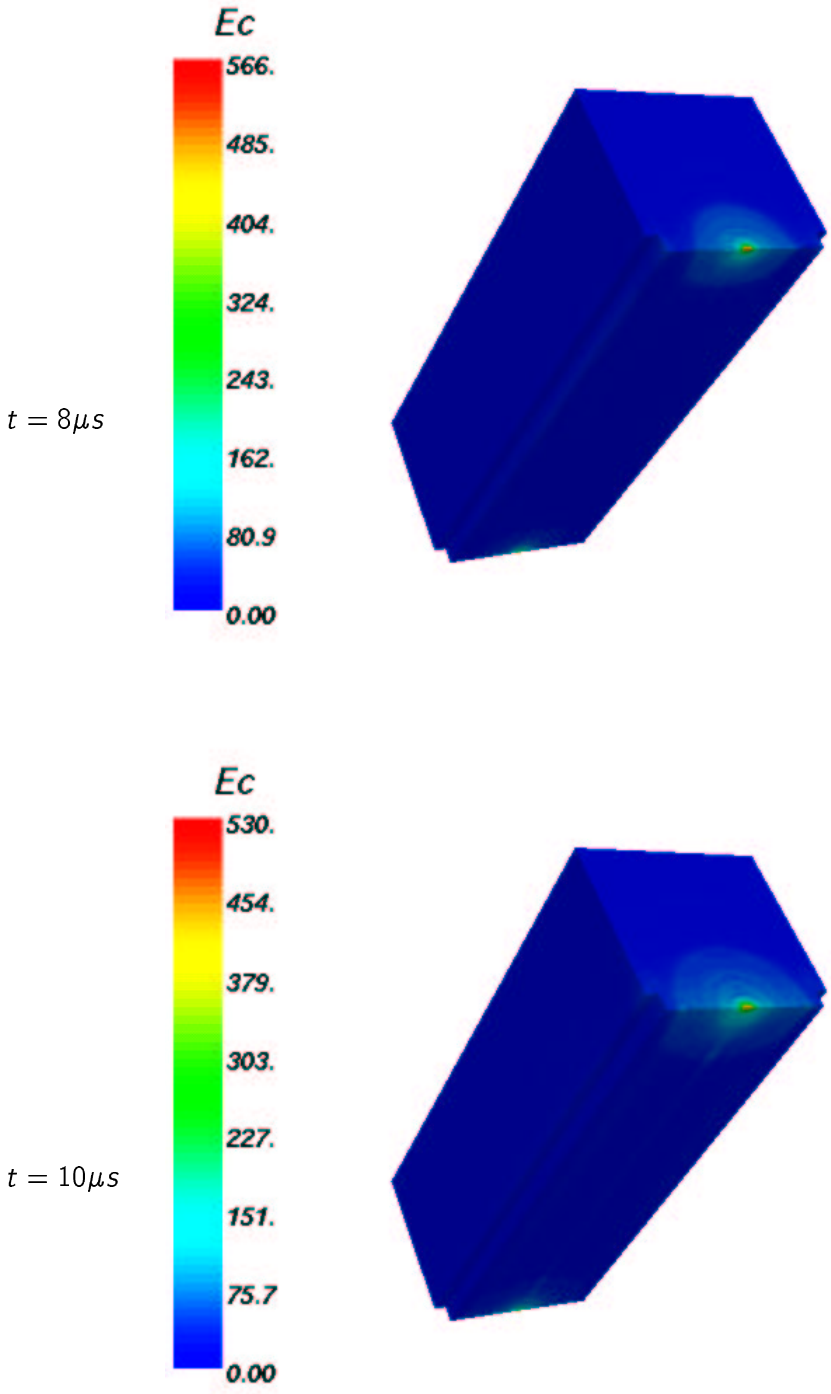

Figure 6.21: Kinetic energy density, beam distance $0mm$ $[J/m^3]$

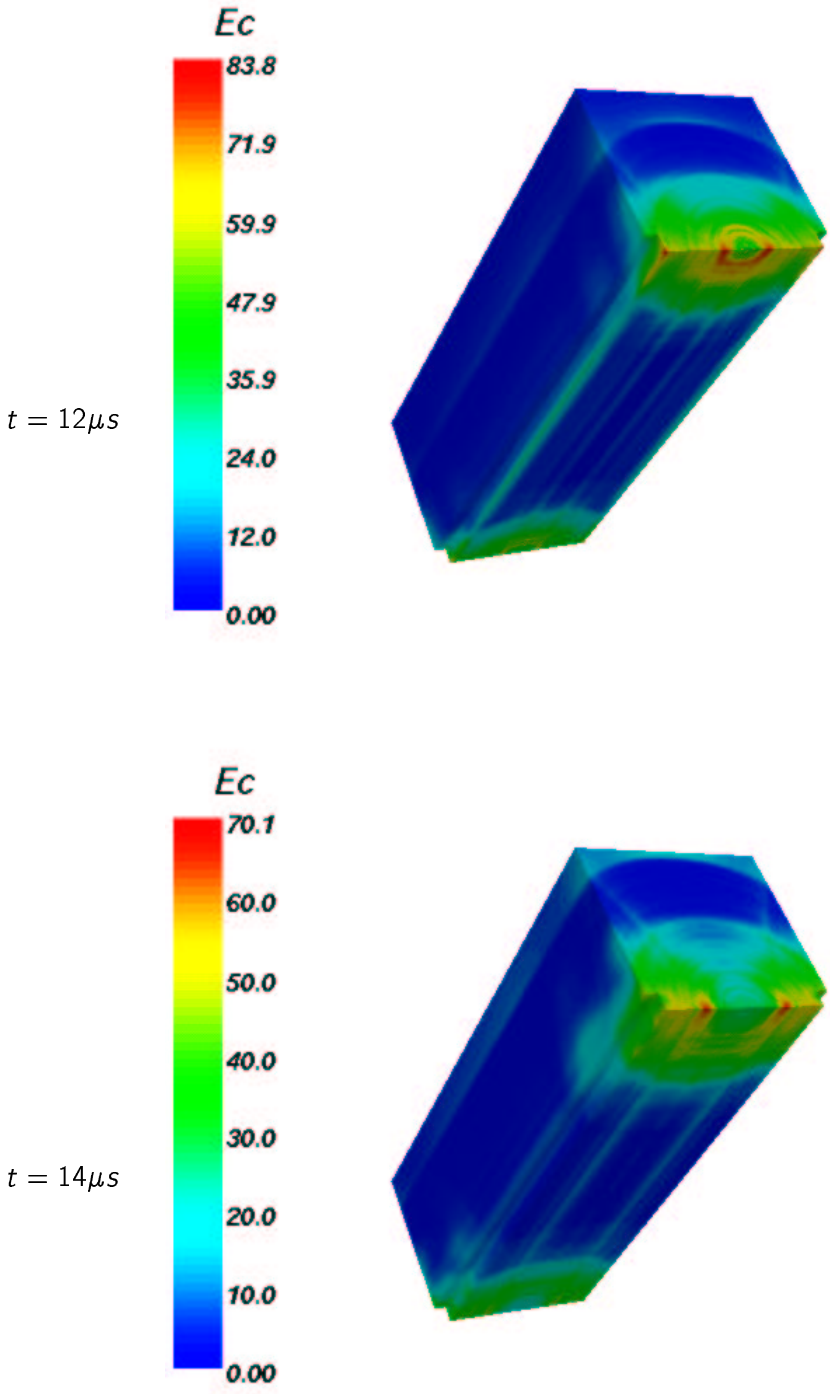

Figure 6.22: Kinetic energy density, beam distance $0mm$ $[J/m^3]$

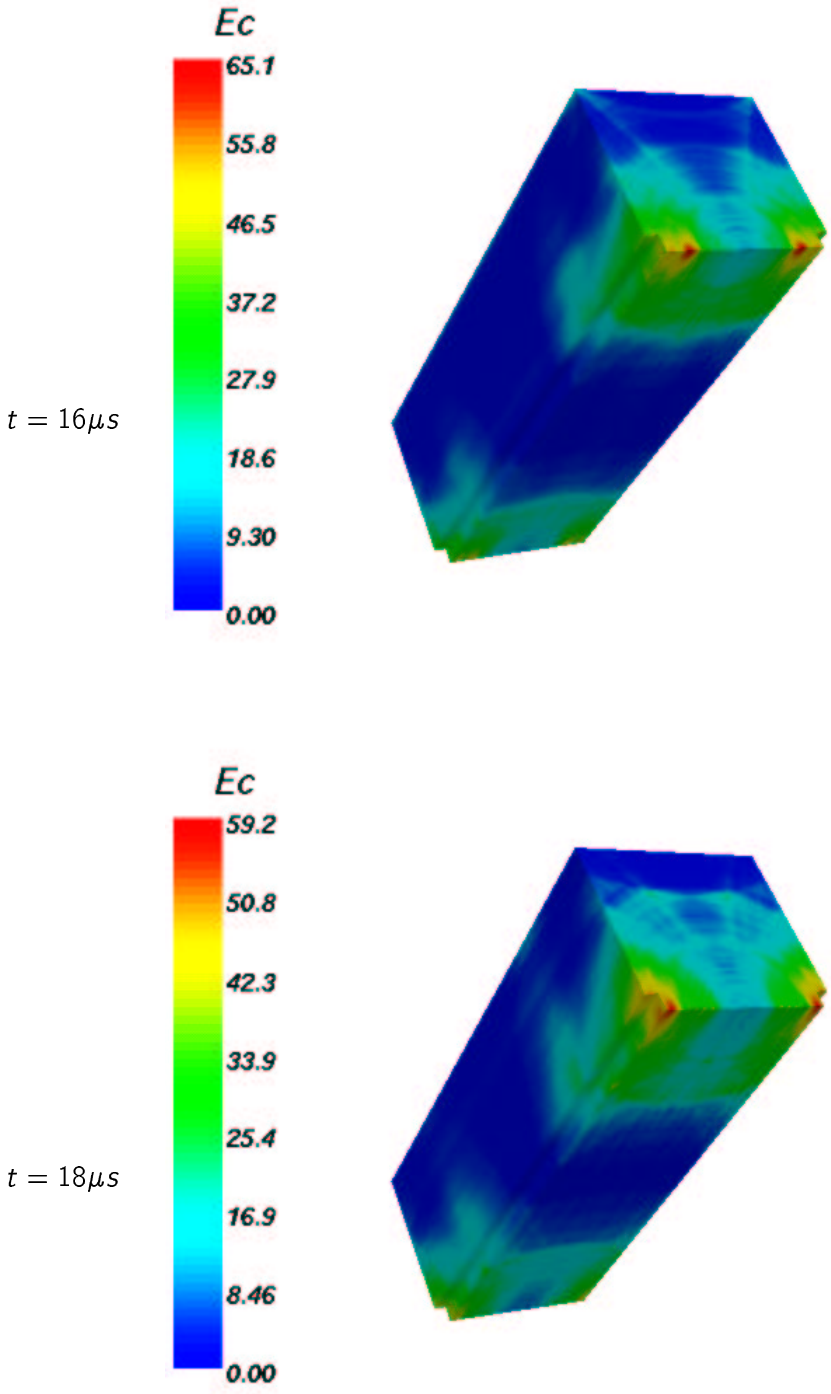

Figure 6.23: Kinetic energy density, beam distance $0mm$ $[J/m^3]$

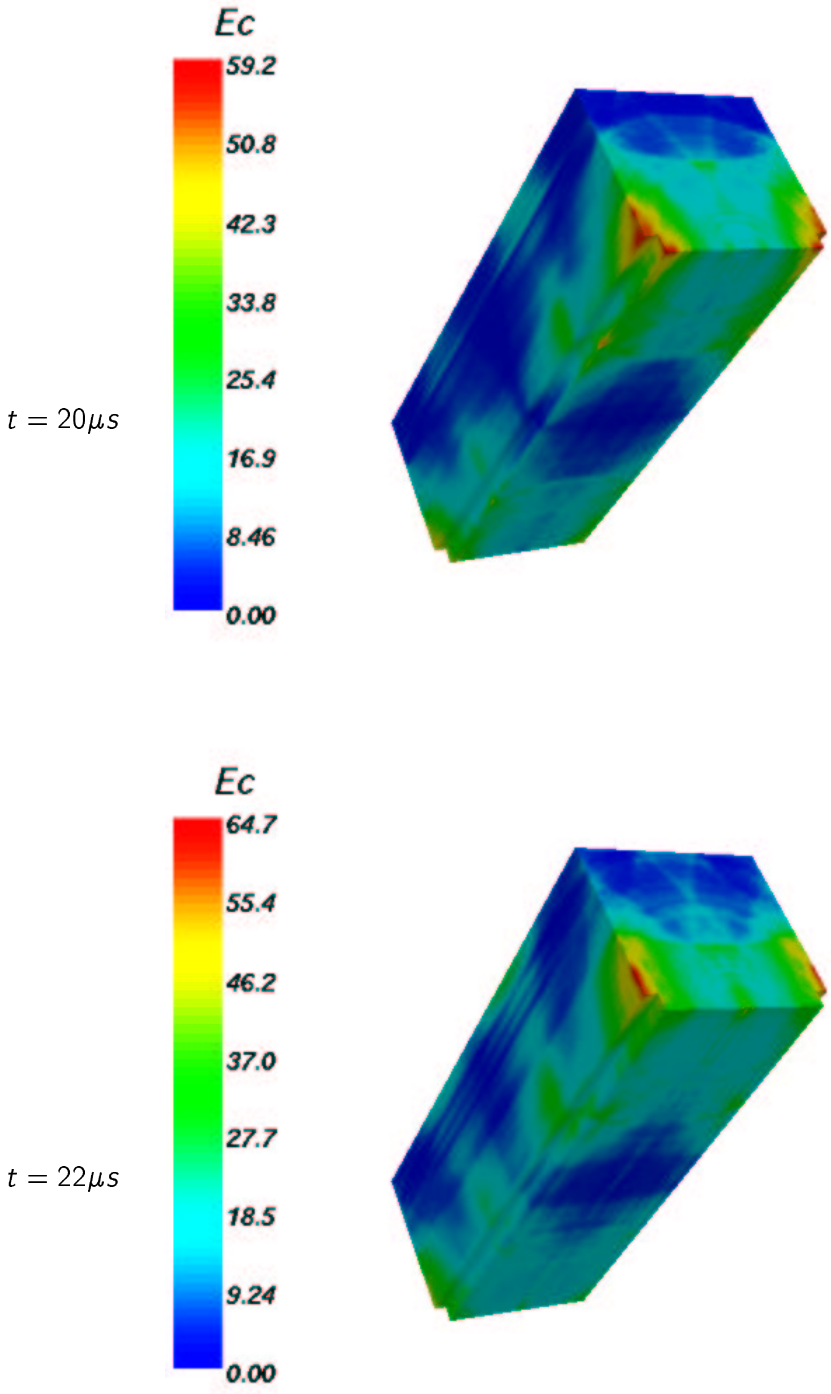

Figure 6.24: Kinetic energy density, beam distance $0mm$ $[J/m^3]$

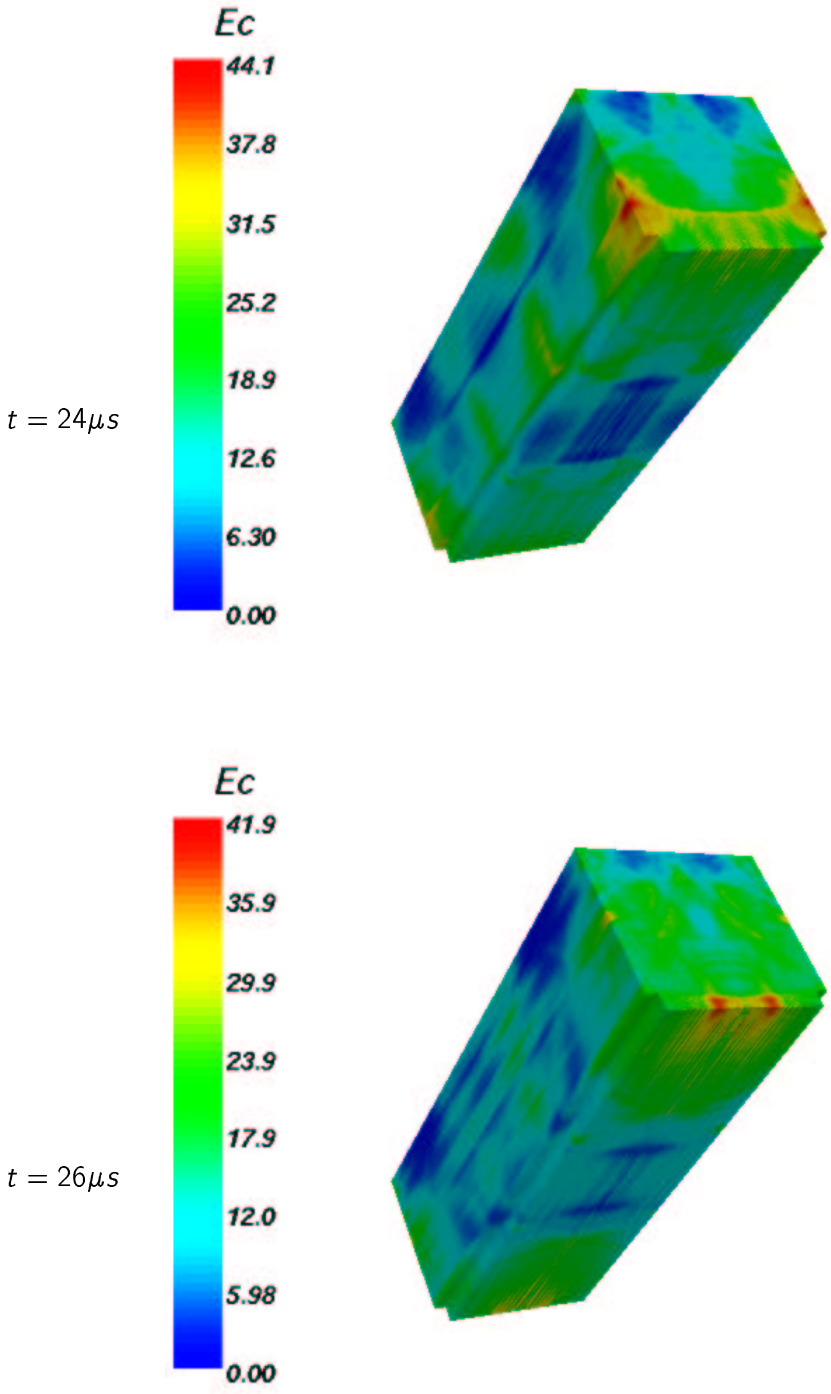

Figure 6.25: Kinetic energy density, beam distance $0mm$ $[J/m^3]$

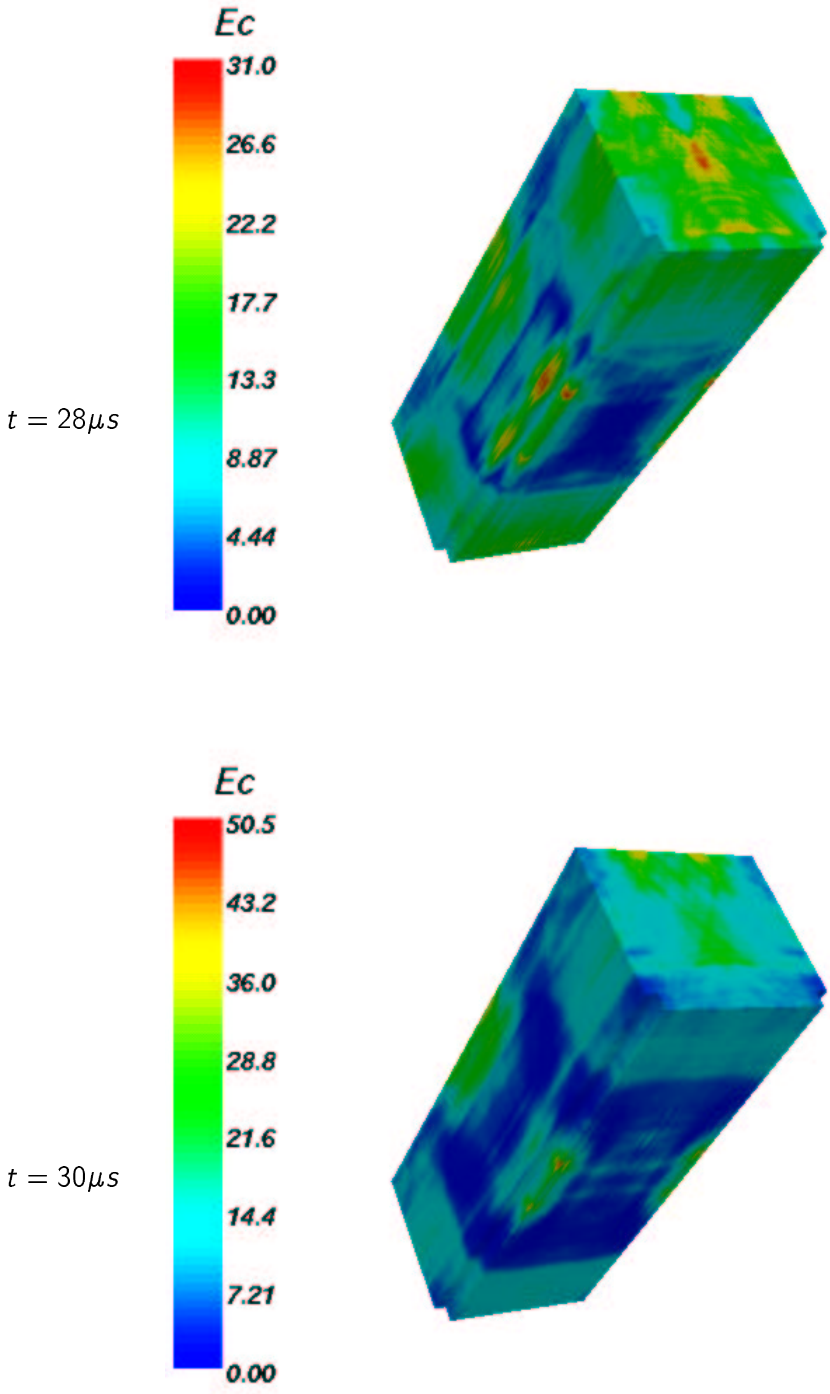

Figure 6.26: Kinetic energy density, beam distance $0mm$ $[J/m^3]$

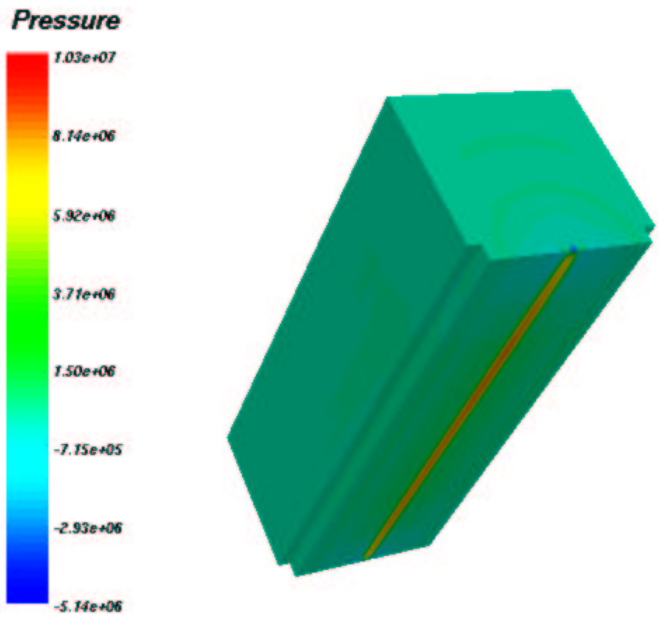

Figure 6.27: Internal pressure at $t = 10\mu s$, beam distance $0mm$ $[Pa]$

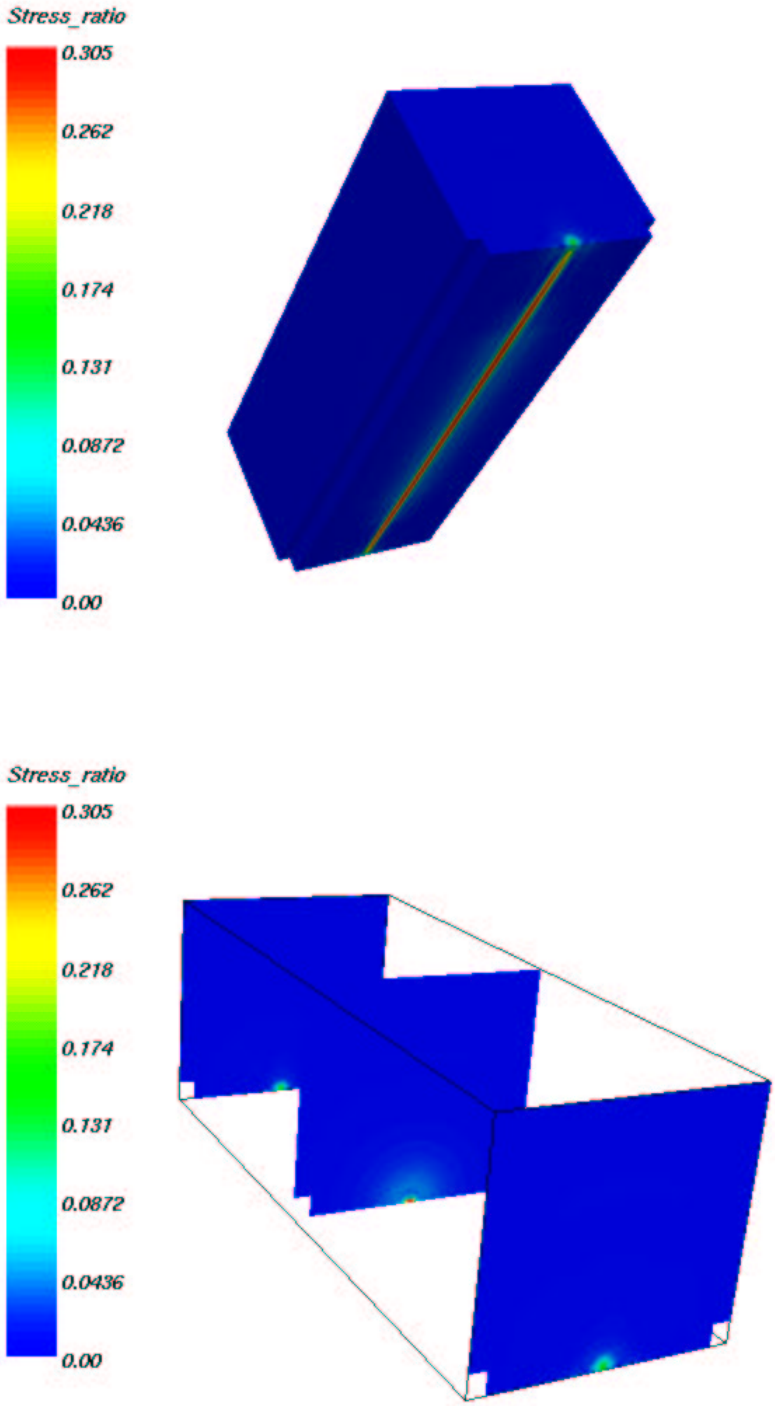

Figure 6.28: Stress ratio at $t = 10\mu s$, beam distance $0mm$ [−]

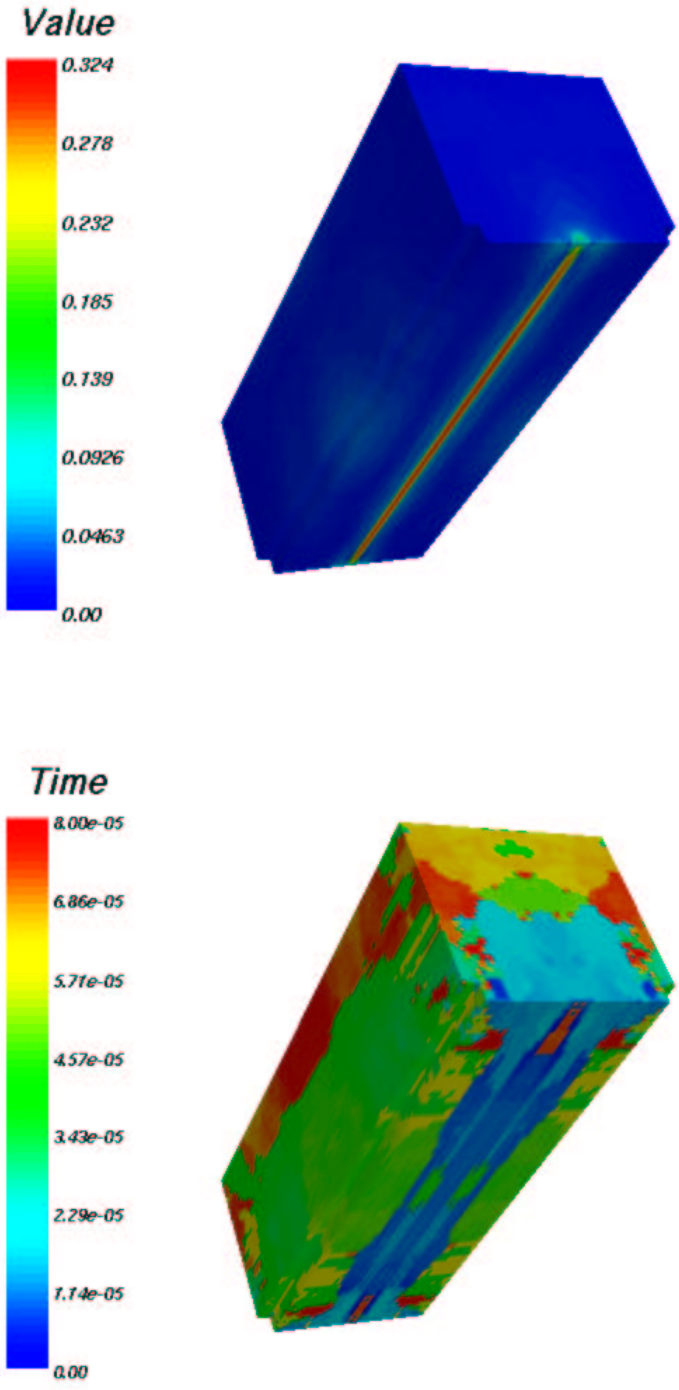

Figure 6.29: Max stress ratio, beam distance 0mm, value on top [-], time [s] on bottom

6.4.5 Detailed analysis. Beam distance: $4mm$

The near surface load condition is the last loading case analysed in detail. Here the beam axis is located inside the absorber block, $4mm$ distant from the lower surface. The spectral degree is $N = 4$ and the time step is again equal to $\Delta t = 2.0E - 8s$.

Figures from 6.30 to 6.36 show the kinetic energy density in the absorber block as appears on the external surface. The results are very similar to those of the grazing loading conditions. The wave profile is very similar but the maximum value is higher: in fact, almost the whole beam energy is deposited in the absorber block, therefore more energy has to be distributed inside the block.

Stress results are similar to those found for the grazing condition. Figure 6.37 shows the internal pressure and the stress ratio at the end of the beam loading period.

The maximum values of the stress ratio and the time at which this maximum value is reached for each point of the model are presented in Figure 6.38. Again the results do not differ significantly from those found in the other loading conditions: the maximum value is again on the beam axis, and is still lower than the allowable value of 0.66.

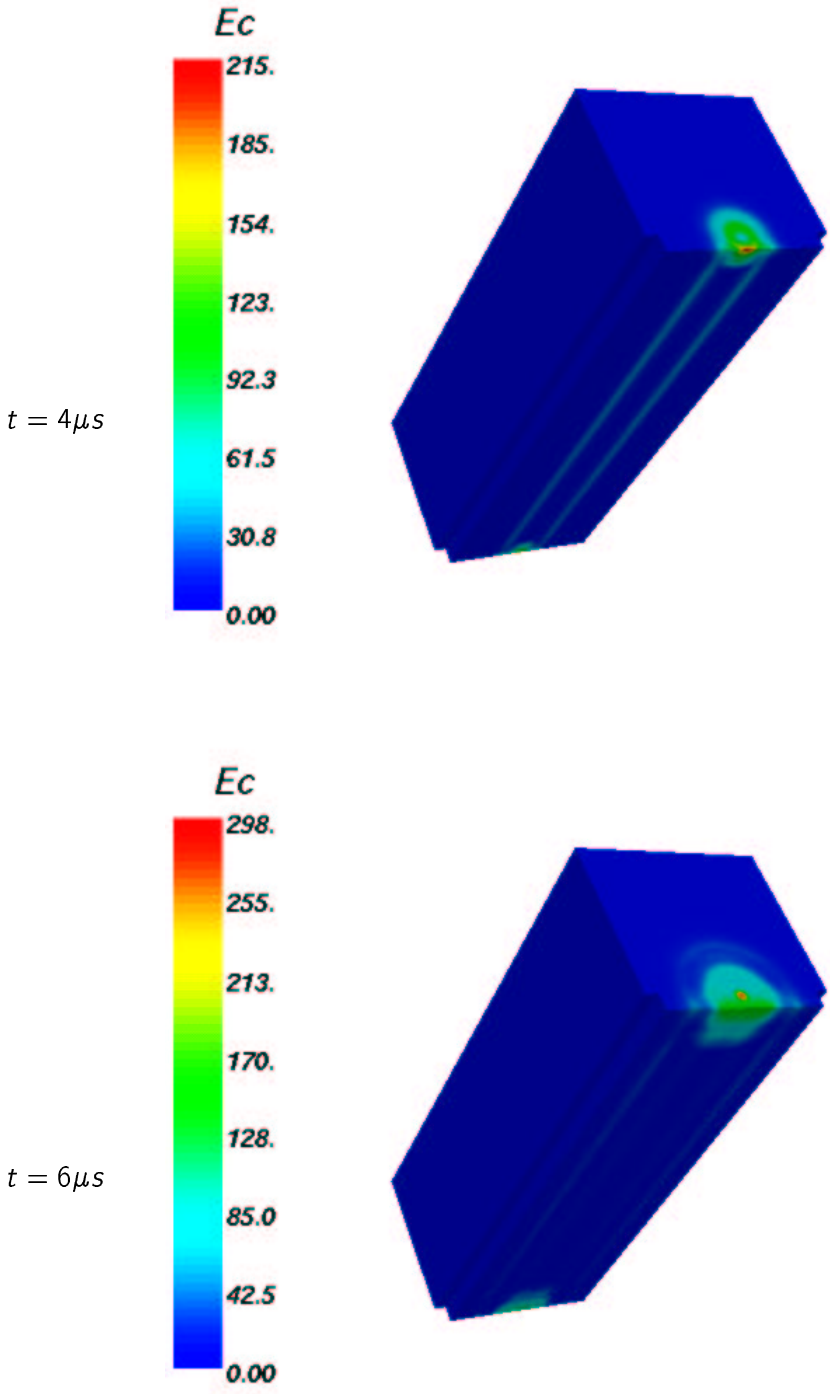

Figure 6.30: Kinetic energy density, beam distance $4mm$ $[J/m^3]$

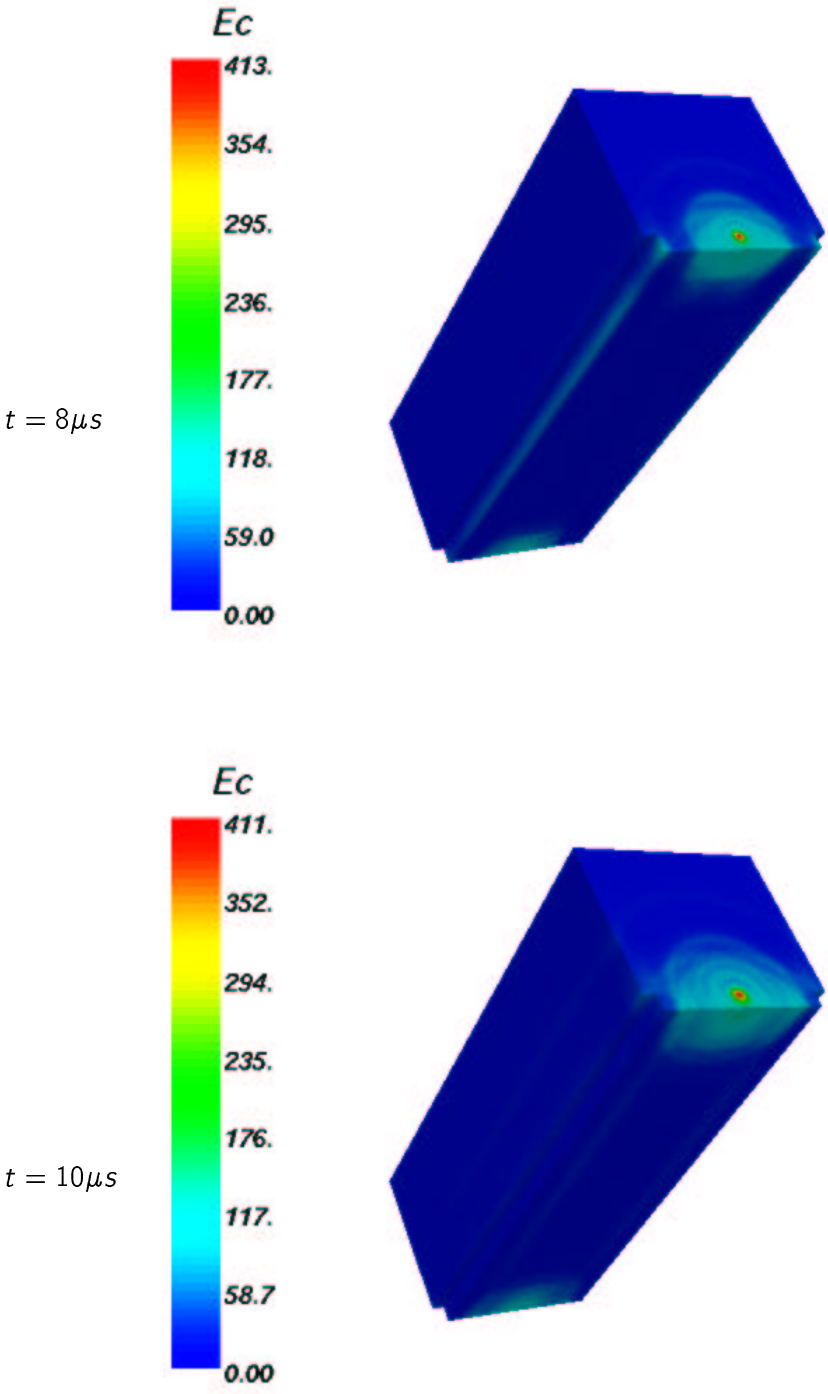

Figure 6.31: Kinetic energy density, beam distance $4mm$ $[J/m^3]$

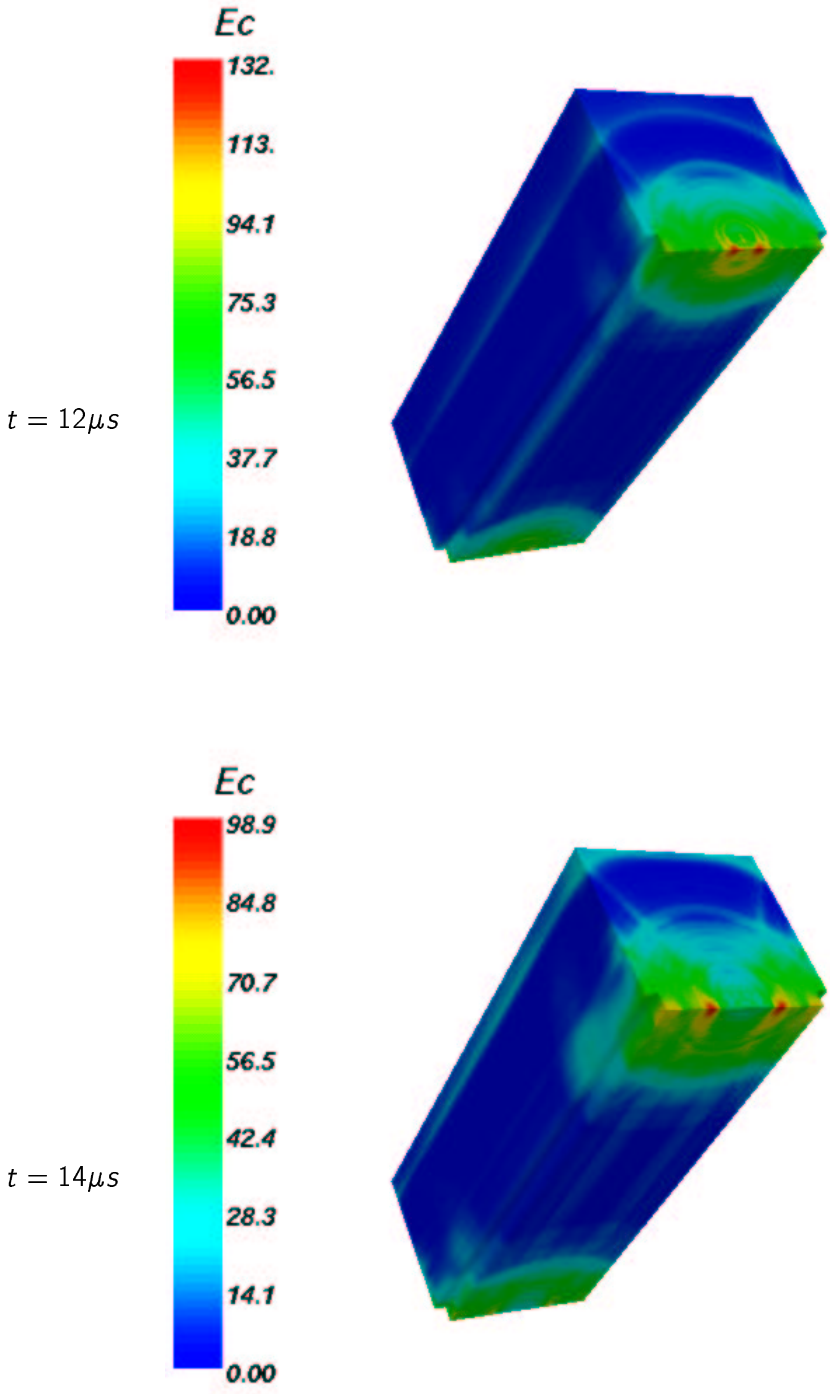

Figure 6.32: Kinetic energy density, beam distance $4mm$ $[J/m^3]$

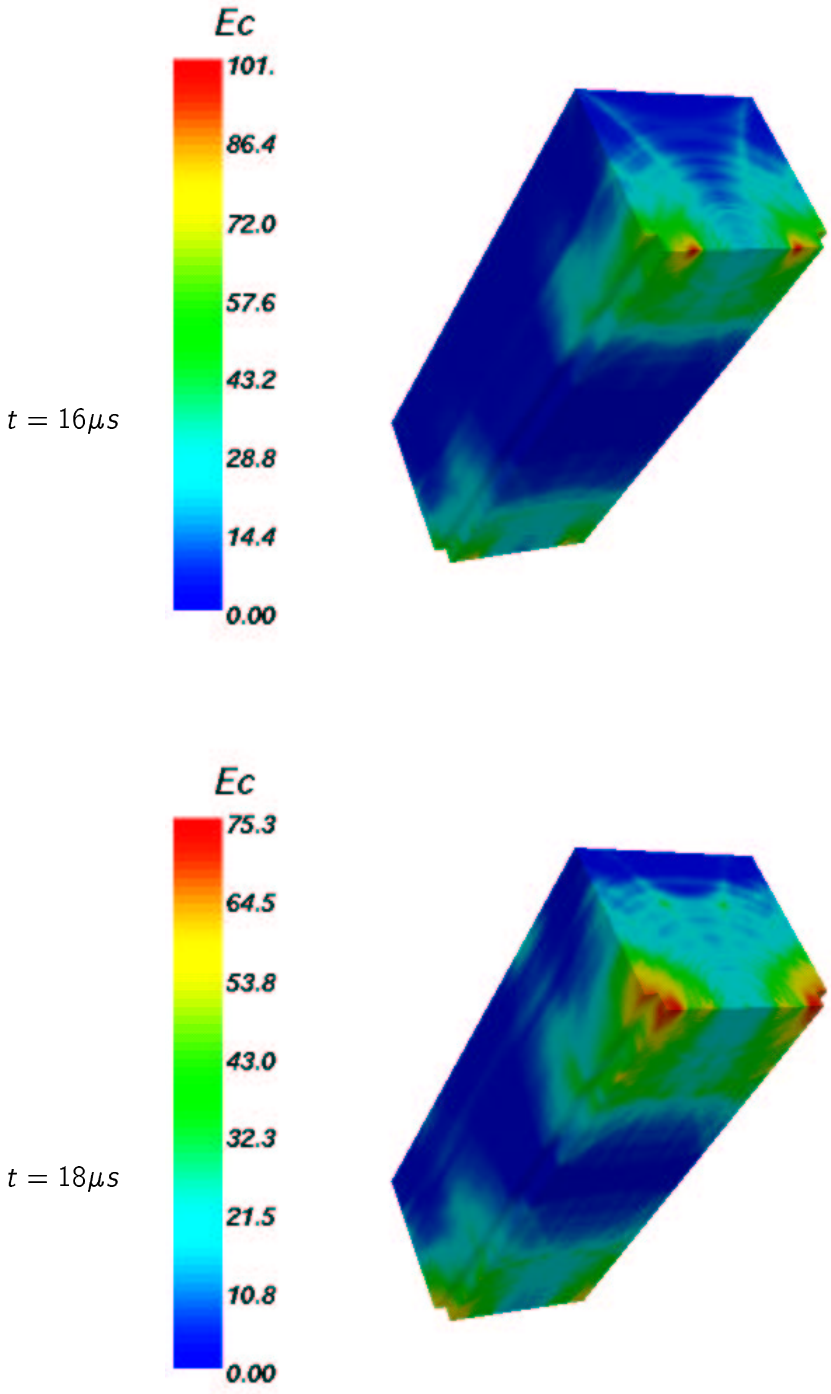

Figure 6.33: Kinetic energy density, beam distance $4mm$ $[J/m^3]$

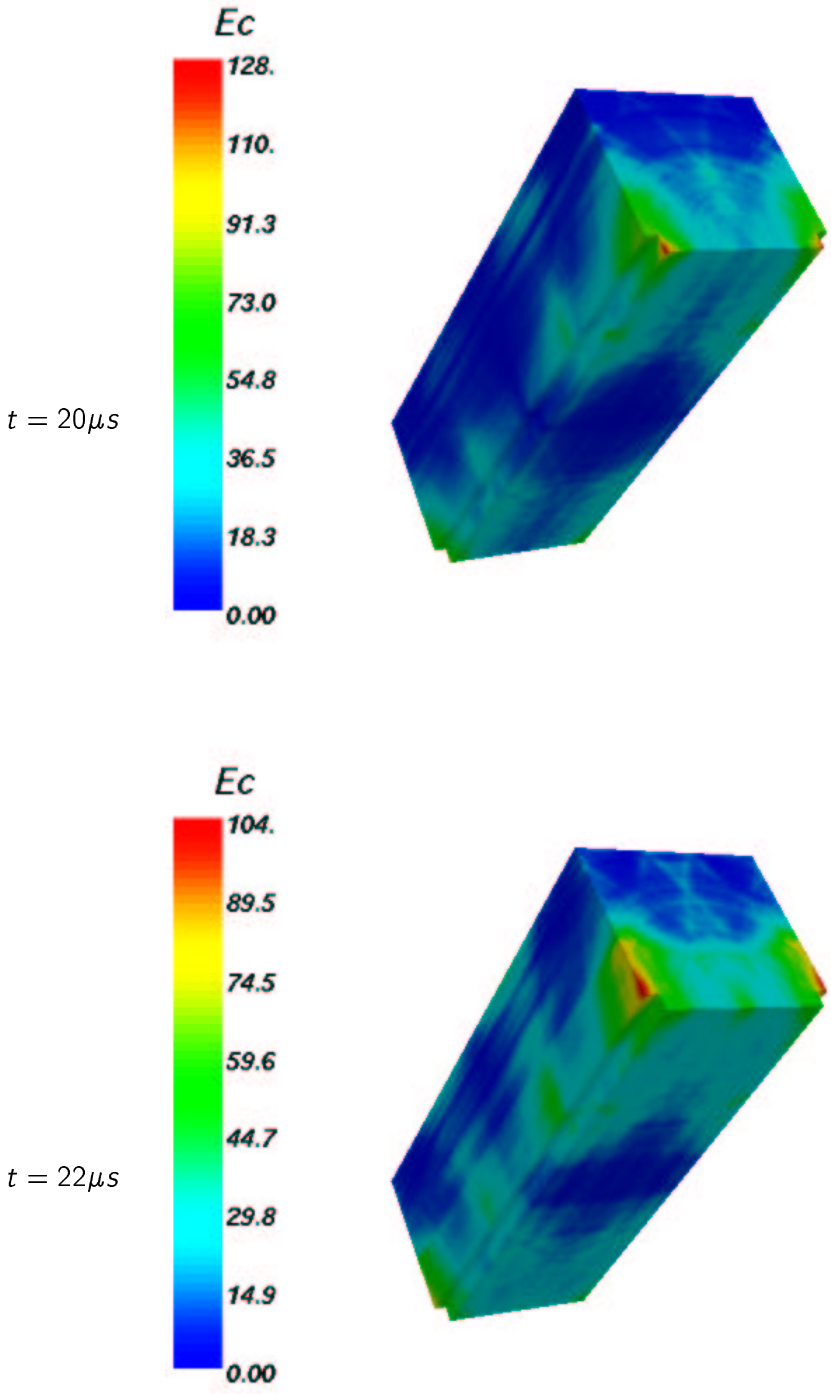

Figure 6.34: Kinetic energy density, beam distance $4mm$ $[J/m^3]$

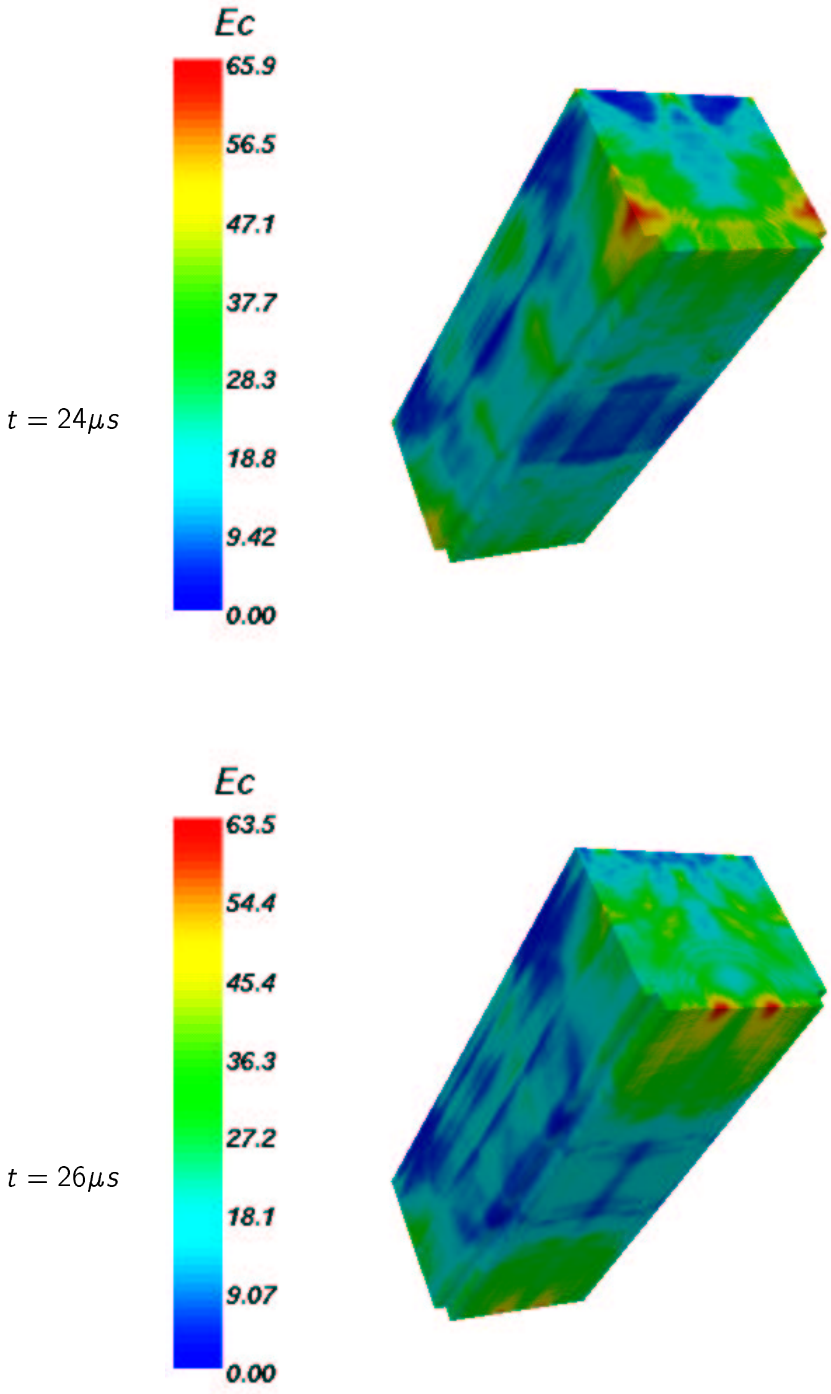

Figure 6.35: Kinetic energy density, beam distance $4mm$ $[J/m^3]$

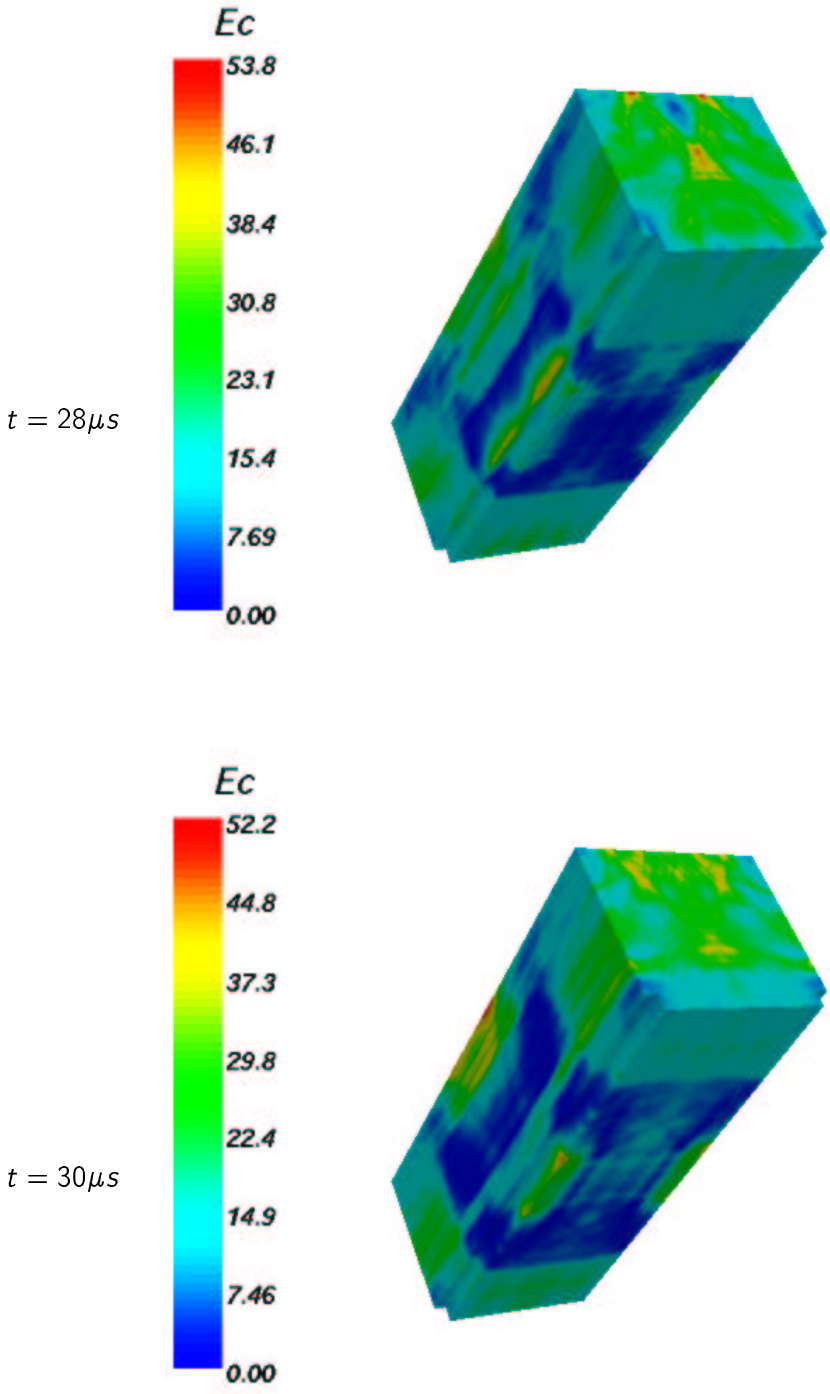

Figure 6.36: Kinetic energy density, beam distance $4mm$ $[J/m^3]$

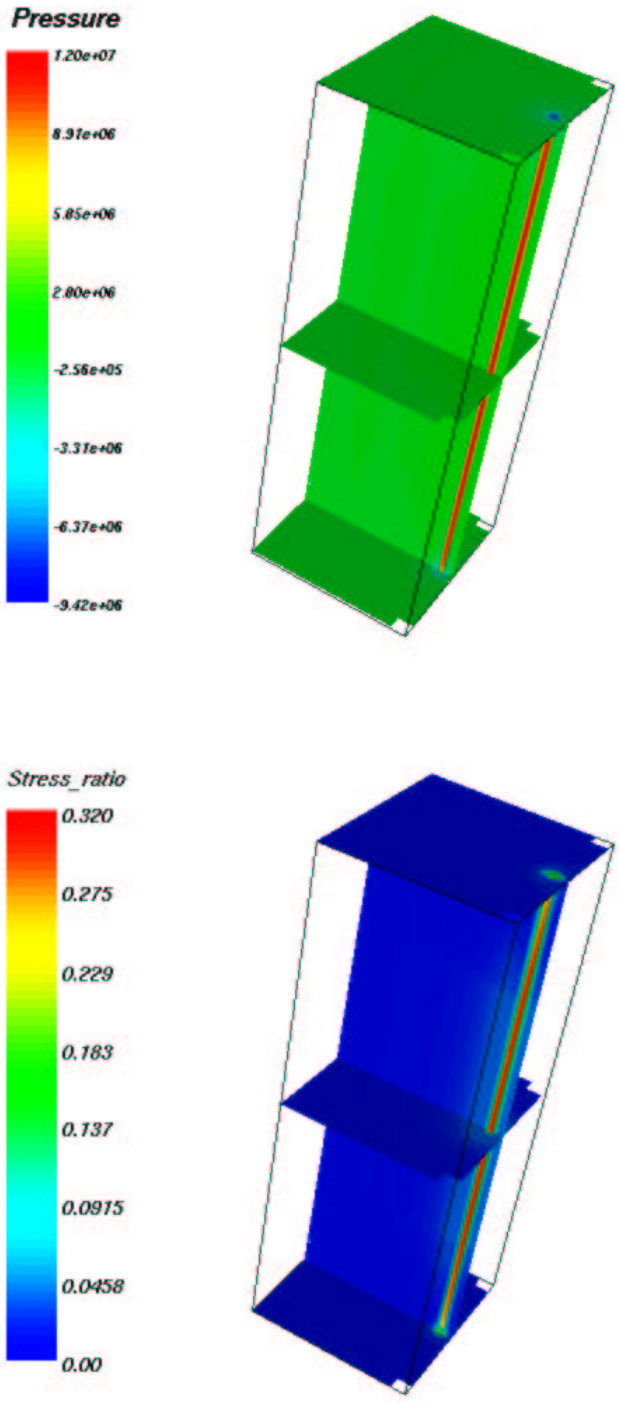

Figure 6.37: Internal pressure [Pa] and stress ratio [-] at $t = 10\mu s$, beam distance $4mm$

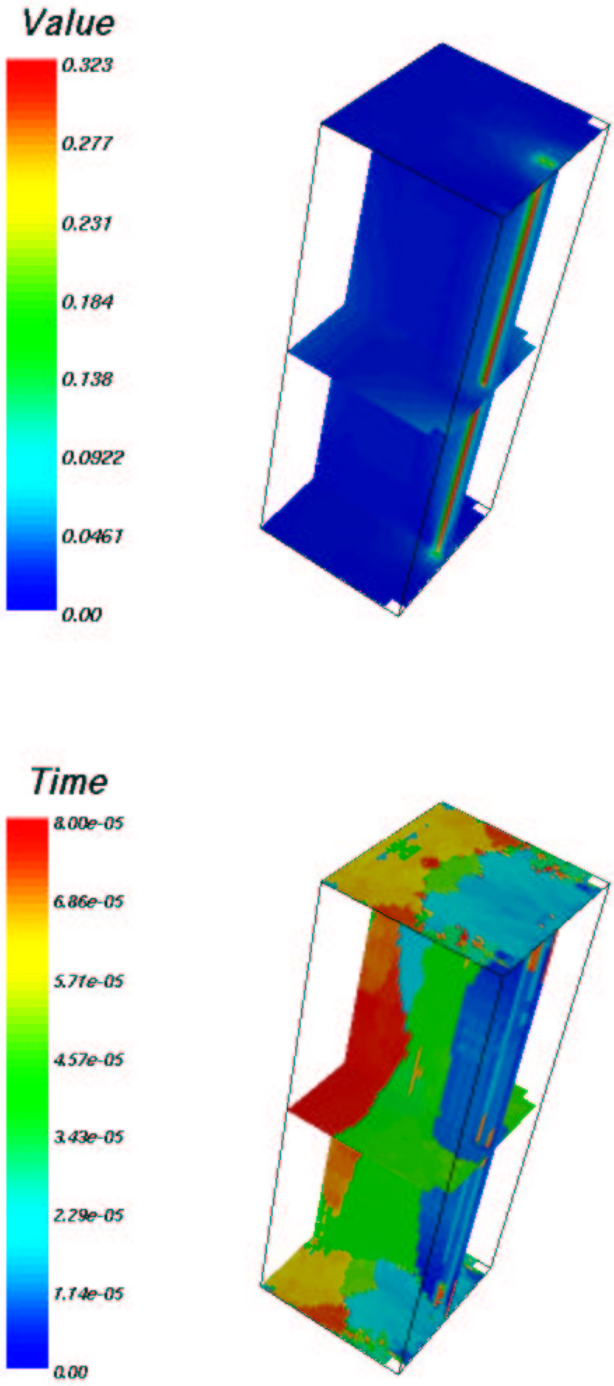

Figure 6.38: Max stress ratio, beam distance 4mm, value on top [-], time [s] on bottom

Chapter 7

Conclusions

In the frame of contract K777/SL a numerical analysis of the mechanical behavior of beam obstacles is presented, the load condition being those due to the high energy particle beam circulating in the new Large Hadron Collider (LHC).

By means of numerical simulation it has been possible to get a detailed view at the different mechanical phenomena that take place in this equipment under particular load conditions, to tune up a specifically designed high performance simulation code, and to verify the correctness of the design of the TDI beam stopper under several operating conditions.

The ELSE code, developed at CRS4, extended and modified for this particular problem has been the chosen tool for the numerical analysis. The code is based on the *spectral element method* a powerful numerical technique similar to the well known *finite element method*, and very efficient in the simulation of wave propagation.

Keeping the flexibility of FEM in dealing with complex geometries, it allows to reach accuracies beyond the standard methods and/or solving very large problems, since it uses a reacher set of functions, that results very efficient when solving wave propagation problems. It is an *h-p* method, meaning that the solution may be refined both reducing the mesh size as in finite element, but also increasing, at run time, polynomial order of the method.

The method is fully described in the second chapter, where the underlying theory is presented, together with details on the implementation of the ELSE code. The thermal-mechanical coupling is described as well, as other extensions developed for the problem at hand such as temperature dependent material properties, or the interface with a Monte Carlo code used to evaluate the atomic interaction of particles with beam obstacles and the resulting energy deposition.

The same chapter also gives a general description of the TDI beam obstacle design and of the load conditions to which it is subjected. The TDI (Injection Stoppers) for LHC are mobile obstacles intended to be used during the adjustment of the injection trajectory in order to protect the superconducting machine elements in the event of a malfunctioning of the injection kicker, by dissipating the energy of the particle beam that may hit it at several different positions.

The third chapters presents the results of the first conceptual and parametric studies and numerical simulations. The problem of an infinite solid being hit and heated by a particle beam is first analyzed. The particle beam is supposed to give an energy deposition characterized by a symmetry around the beam axis and by a constant distribution along the axis; a 2D analysis was therefore sufficient.

These simulations not only give the opportunity to compare and validate the numerical results with those obtained by analytical models, but were also useful to find out the relevant parameters in the beam load, and material properties that have significant influence on the stress distribution and stress wave propagation.

It may happen that the particle beam does not hit the absorber block in a central position, where the maximum efficiency in energy dissipation may be reached, but rather near the external faces, where the stress condition of the structure is worsened because of the effects of the stress wave reflections on the external surfaces. The problem was first studied in the third chapter by means of 2D numerical simulations on a semi-infinite plane model. The influence on the stress intensity of the distance from the free surface at which the beam hits the obstacle is evaluated and related to the beam and material characteristics.

The actual problem of the TDI beam obstacle design was then faced. The fourth chapter presents the results of several numerical 2D simulations run on a section of the TDI absorber block. These analyses have been run in parallel to the design of this equipment, and the results presented are relative to the material initially selected for the absorber blocks: graphite.

Several load conditions are analyzed on the boron nitride section, in particular the influence of the beam hitting position has been first evaluated. When the beam is not centered but is near to the lower surface of the block, the surface facing the undisturbed orbit of the particles, more dangerous stress states are found.

In fact, if the centered load conditions may be considered acceptable for the resistance requirements of a graphite absorber block, this is not true for a near surface load. According to the Stassi failure criterion, the resulting safety factor with respect to rupture resulted lower than 1.5 that may be considered acceptable, even within the limits of a 2D analysis.

The same chapter presents the results of the simulations run on a 2D model of a section not only of the absorbing structure, but also of the supporting structures surrounding it. This analysis was intended to evaluate the amount of energy that may pass through the block borders and the loading conditions and resulting stress values that are induced in the other structures.

The limited extension of the contact area, and the relevant differences in the material properties of the jaw with respect to the absorber block, reduces the amount of elastic energy transferred to the surrounding structure, with low values of the resulting stresses. The elastic energy is mostly contained in the absorber block, and the presence of the other parts of the structure only has a limited influence on the maximum stresses that may be reached inside the block.

The fifth chapter shows the results of a 3D simulation on the graphite absorber block. The simulation was limited to the absorber block only, due to the limits in the computational resources and to the fact that, as demonstrated by the 2D analysis, a little amount of energy was transferred to the supporting structure.

The 3D analysis allowed to put in evidence the propagation of a longitudinal wave inside the block with origin at the front and rear faces on the beam axis and travelling trough the whole length of the block giving rise to significant stress values. The analysis was run on the centered load condition. The results show that the maximum value of the equivalent stress according to the Stassi failure criterion is concentrated on the front and rear surfaces near the intersection with the particle beam axis. In these points a significant concentration of kinetic energy is also present and the material seems to be pulled out of the block by the quick thermal expansion.

The maximum values of the equivalent stresses are higher than those found in a 2D section. The beam loading conditions seem to be too severe for this design, and for the material adopted so far. It was decided to verify the performances of a different material: the hot pressed hexagonal boron nitride.

This ceramic material is similar in different aspects to graphite, but has better performances for the mechanical resistance to this particular load, due to the very low value of the thermal expansion coefficients and to the good values of the tensile and compressive strength.

The thermal, elastic and mechanical strength properties of this material have been provided by CERN, as result of a material testing campaign of the Fraunhofer Intitute. Anyway, a rule of thumb estimation of some of the required mechanical properties was necessary, since they have not been produced by the experiments.

The results of the complete thermo-mechanical analysis on the whole set of the 18 Boron-Nitride absorber blocks of the final design is presented in Chapter 6. The exact energy distribution resulting by the Monte Carlo simulation with Fluka is used to calculate the temperature increase in the different absorber blocks.

The load conditions in terms of particle energy space, time distribution, intensity and position of the beam axis, was provided by the CERN too.

First, a complete analysis of all the 18 blocks in the centered beam conditions was performed, to detect the block subjected to the most critical loading conditions. All the blocks have been examined separately in a $80\mu s$ long simulation, in order to examine the effect of multiple wave reflections. The third block, resulted the most critical, being subjected to the maximum temperature increase, exhibiting high values of temperature gradients and maximum values of the equivalent stress.

This block has been subjected to further investigation, and verified not only in the centered load case, but also in the grazing conditions, when the axis is tangent to the lower surface, and in a near surface condition, when the particle beam axis falls inside the absorber block but is close to the lower surface.

The benefits of the change of material are evident. In each of examined conditions the results of the simulations show that the maximum value of the equivalent stress

state is constantly lower than the allowable value, showing a safety factor nearly equal to 2 over the allowable stress.

Even if it may be partially due to the failure criterion chosen for this anisotropic material, from the load condition examined it resulted that the beam position has a limited influence on the most critic value of the stress state.

Bibliography

[1] Maggio, F., and A. Quarteroni, *Acoustic wave simulation by spectral methods*, East-West Journal of Numerical Mathematics, 2 (2), pp. 129-150, 1994

[2] Faccioli E., F. Maggio, A. Quarteroni, and A. Tagliani, *Spectral-domain decomposition methods for the solution of acoustic and elastic wave equations*, Geophysics, 61 (4), pp. 1160-1174, 1996

[3] Casadei F., E. Gabellini, G. Fotia, F. Maggio, and A. Quarteroni, *A hybrid spectral-element/finite-element method for complex wave propagation applications*, CRS4-TECH-REP-00/21, submitted to Computer methods in applied mechanics and engineering

[4] Fasso A., Ferrari A., Sala P.R. *Electron-photon transport in FLUKA: Status*, Proceedings of MonteCarlo 2000 Conference, Springer-Verlag, p. 159-164, 2001

[5] Fasso A., Ferrari A., Ranft J., Sala P.R. *FLUKA: Status and prospective for hadronic applications*, Proceedings of MonteCarlo 2000 Conference, Springer-Verlag, p. 955-960, 2001

[6] Sievers P., *Elastic stress waves in matter due to rapid heating by an intense high-energy particle beam*, CERN-LAB II/BT/74-2

[7] Massidda L. *Spectral methods in non stationary thermoelasticity: first results*, CRS4-TECH-REP-01/116

[8] Quarteroni, A., and A. Valli, *Numerical approximation of partial differential equations*, Springer Verlag, Berlin, 1994

[9] Buono S., G. Fotia, F. Maggio, and L. Massidda *Simulation of the elastic wave propagation induced by the PS beam into the TOF target at CERN*, CRS4-TECH-REP-01/57

[10] Massidda L. *Spectral methods in non stationary thermoelasticity: validation of ELSE code for fast heating problems and Beam Obstacles design*, CRS4-TECH-REP-

[11] Canuto, C., M.Y. Hussaini, A. Quarteroni, and T.A. Zang, 1988, *Spectral methods in fluid dynamics*, Springer Verlag, New York

[12] Zyczkowski M. *Combined loading in the theory of plasticity*, PWN-Varsaw, 1981

[13] ANSYS Inc. *ANSYS Theory Reference* ANSYS Rel. 6.1 Manuals

[14] Peraire S., Sala P.R. *Conceptual optimisation of the TDI and TCDD protections for LHC injection lines*, LHC Project Internal Report - CERN

[15] Zazula J. M. *On graphite transformations at high temperature and pressure induced by absorption of the LHC beam*, CERN-LHC Project Note 78/97